

Copyright  
by  
Siyavash Motealleh  
2009

The Dissertation Committee for Siyavash Motealleh Certifies that this is the approved version of the following dissertation:

**Mechanistic study of menisci motion within homogeneously and heterogeneously wet porous media**

**Committee:**

---

Steven L. Bryant, Supervisor

---

David A. DiCarlo, Co-Supervisor

---

Dave C. Herrick

---

Larry W. Lake

---

Mukul M. Sharma

---

Carlos Torres-Verdín

**Mechanistic study of menisci motion within homogeneously and  
heterogeneously wet porous media**

**by**

**Siyavash Motealleh, B.S.; M.S.**

**Dissertation**

Presented to the Faculty of the Graduate School of

The University of Texas at Austin

in Partial Fulfillment

of the Requirements

for the Degree of

**Doctor of Philosophy**

**The University of Texas at Austin**

**August 2009**

## Dedication

To my parents, Saiedeh Shahabi and Masoud Motealleh for their endless support, to my sisters, Sepideh and Maryam for being wonderful and caring and to my wife, Amanda, for her endless love and encouragement.

## **Acknowledgements**

I would like to express my gratitude to all the people who have supported me throughout my graduate career. First, I would like to thank my advisors, Steven Bryant and David DiCarlo for being instrumental in guiding me as a graduate student by fostering my understanding of pore level petrophysics and for setting an excellent example of how to think critically about building a fluid flow model. To my committee members, thank you for all the insightful discussions and helpful suggestions to improve my dissertation project.

I would like to acknowledge my officemates and people I had the pleasure of working with throughout the years; especially Cynthia Thane and Javad Behseresht for providing me with information regarding the dense random spherical pack. I am also grateful to Javad for assisting me with Matlab and Elena Rodriguez for being so helpful and patient with me and also for the great artwork in my office. Also, I want to acknowledge Mandana Ashouripashaki for providing experimental data for the fractionally wet medium and Masa Prodanovic for general assistance with my project and helpful discussions.

Above all, I would also like to thank my family for all their love and support during my PhD program. Maman and Baba, I appreciate all your words of wisdom and sacrifices you both made in order to provide me with the best educational opportunities. I am also so grateful to my wife Amanda Chadee for being so supportive during my graduate study and for keeping me smiling with her refreshing easy-going personality. You are rock my life!

# **Mechanistic study of menisci motion within homogeneously and heterogeneously wet porous media**

Publication No. \_\_\_\_\_

Siyavash Motealleh, PhD.

The University of Texas at Austin, 2009

Supervisors: Steven Bryant

David DiCarlo

Oil reservoirs and soil can be homogeneously wet (water-wet, oil-wet, neutral-wet) or heterogeneously wet (mixed wet or fractionally wet). The goal of this research is to model the detailed configuration of wetting and non-wetting phases within homogeneously and heterogeneously wet porous media. We use a dense random pack of equal spheres as a model porous medium. The geometry of the sphere pack is complex but it is known.

In homogeneously wet porous media we quantify the effect of low saturations of the wetting phase on the non-wetting phase relative permeability by solving analytically the geometry of the wetting phase. At low saturations (at or near the drainage endpoint) the wetting phase exists largely in the form of pendular rings held at grain contacts. Pore throats correspond to the constriction between groups of three grains, each pair of which can be in contact. Thus the existence of these pendular rings decreases the void area

available for the flowing non-wetting phase. Consequently, the existence of the pendular rings decreases the permeability of non-wetting phase. Our model explains the significant permeability reduction of the non-wetting phase with a small change in the wetting phase in a low permeability porous medium.

To model heterogeneously wet porous medium, we assume that the porous medium is fractionally wet where each grain is either oil-wet or water-wet. These water-wet or oil-wet grains are distributed randomly within the porous medium. We calculate analytically the stable fluid configuration in individual pores and throats of a fractionally wet medium. The calculation is made tractable by idealizing the configurations as locally spherical (menisci) or toroidal (pendular rings.) Because the calculation of the interface position is entirely local and grain-based, it provides a single, generalized, geometric basis for computing pore-filling events during drainage as well as imbibition. This generality is essential for modeling displacements in fractionally wet media. Pore filling occurs when an interface becomes unstable in a pore throat (analogous to the Haines condition for drainage in a uniformly wet throat), when two or more interfaces come into contact and merge to form a single interface (analogous to the Melrose condition for imbibition in uniformly wet medium), or when a meniscus in a throat touches a nearby grain (a new stability criterion).

The concept of tracking the fluid/fluid interfaces on each grain means that a traditional pore network is not used in the model. The calculation of phase saturation or other quantities that are conveniently computed in a network can be done with any approach for defining pore bodies and throats. The fluid/fluid interfaces are mapped from the grain-based model to the network as needed. Consequently, the model is robust as there is no difference in the model between drainage and imbibition, as all criteria are accounted for both increasing and decreasing capillary pressure.

# Table of Contents

List of Tables .....	xi
List of Figures .....	xii
<b>CHAPTER 1: INTRODUCTION</b> .....	<b>1</b>
1.1. INTRODUCTION .....	1
1.2. SIGNIFICANT CONTRIBUTIONS .....	3
1.3. LITERATURE REVIEW AND METHODOLOGY .....	5
1.3.1. Development of Pore-Based Network Modeling .....	5
1.3.2. Development of Direct Simulations .....	9
1.3.3. Extracting Pore Structure from Real Sediments .....	10
1.3.4. Development of Grain-Based Network Modeling .....	11
1.4. WETTABILITY .....	14
1.4.1. Heterogeneous Wettability .....	17
<b>CHAPTER 2: EFFECT OF LOW WETTING PHASE SATURATION ON NON-WETTING PHASE PERMEABILITY IN A UNIFORMLY WET ROCK</b> .....	<b>23</b>
2.1. ABSTRACT .....	23
2.2. INTRODUCTION .....	24
2.3. METHOD .....	25
2.3.1. Model of Pore Space .....	25
2.3.2. Terminology .....	28
2.3.3. Assumptions .....	28
2.3.4. Method for Computing Fluid Configurations in the Pore Space .....	29
2.3.5. Method for Computing Effective Permeability of Non-Wetting Phase .....	30
2.3.6. Method for Computing Geometry of Pendular Rings .....	32
2.4. SIMULATION .....	33
2.5. RESULTS AND DISCUSSION .....	35
2.5.1. Influence of Pore-Filling Wetting Phase on Gas Phase Permeability in Low-Porosity Rocks .....	35
2.5.2. Influence of Pendular Rings and Liquid Bridges on Gas Phase Permeability in Low-Porosity Rocks .....	39
2.6. MODEL VALIDATION .....	43
2.6.1. Comparison with Experimental Data for Tight Gas Sands .....	43
2.6.2. Comparison with Experimental Data for Vaporization of Water during Gas Injection .....	48



2.7. CONCLUSIONS.....	53
<b>CHAPTER 3: MECHANISMS OF MENISCUS MOTION IN 2D FRACTIONALLY WET</b>	
<b>POROUS MEDIA.....</b>	<b>55</b>
3.1. ABSTRACT.....	55
3.2. INTRODUCTION .....	55
3.3. TERMINOLOGY .....	59
3.4. MODEL/SIMULATION .....	60
3.4.1. Assumptions.....	60
3.4.2. Model of Pore Space .....	61
3.4.3. Grain-Based Mechanistic Criteria for Menisci Movement .....	62
3.4.4. Simulation .....	74
3.5. RESULTS .....	75
3.6. MODEL VALIDATION.....	81
3.7. DISCUSSION .....	85
3.8. SUMMARY .....	89
<b>CHAPTER 4: UNIFIED MODEL OF DRAINAGE AND IMBIBITION IN 3D FRACTIONALLY</b>	
<b>WET POROUS MEDIA.....</b>	<b>90</b>
4.1. ABSTRACT.....	90
4.2. INTRODUCTION .....	91
4.3. MODEL .....	92
4.3.1. Model of Pore Space .....	92
4.3.2. Assumptions.....	93
4.3.3. Terminology.....	94
4.3.4. Grain-Based Mechanistic Criteria for Menisci Movement .....	99
4.4. SIMULATION.....	122
4.5. RESULT .....	122
4.6. MODEL VALIDATION.....	128
4.6.1. Water-Wet Case .....	128
4.6.2. Fractional-Wet Case.....	130
4.7. DISCUSSION.....	140
4.7.1. Effect of Each Event Type on Drainage/ Imbibition within a Water-Wet Medium .....	140
4.7.2. Compare Occurrence of Each Event during Drainage /Imbibition within a Fractionally Wet Medium .....	147
4.7.3. Effect of Oil-Wet Grain Positions on Drainage/Imbibition Curves .....	153

4.7.4. Effect of Meniscus-4 <sup>th</sup> Grain Criterion on the Primary Drainage Curves of Fractionally Wet Media .....	158
4.7.5. Residual Phase Saturation .....	160
4.8. CONCLUSIONS.....	164
<b>CHAPTER 5: CONCLUDING REMARKS.....</b>	<b>166</b>
<b>APPENDIX A: TOROID APPROXIMATION FOR CALCULATING VOLUME AND CROSS-SECTION AREA OF PENDULAR RINGS/LIQUID BRIDGES .....</b>	<b>168</b>
A.1.CROSS-SECTION AREA .....	170
A.2.VOLUME .....	171
<b>APPENDIX B: EFFECT OF GRAIN SURFACE ROUGHNESS.....</b>	<b>172</b>
<b>APPENDIX C: STABILITY AND POSITION OF MENISCI WITHIN FRACTIONALLY WET POROUS MEDIA.....</b>	<b>176</b>
C.1. STABILITY OF A MENISCUS (HAINES CRITERION).....	176
C.2. POSITION OF A MENISCUS.....	185
C.3. STABILITY OF TWO ADJACENT MENISCI (MELROSE CRITERION).....	186
<b>APPENDIX D: VISUALIZATION OF MENISCI MOTION WITHIN FRACTIONALLY WET POROUS MEDIA.....</b>	<b>189</b>
D. 1. MENISCI MOTION IN A WATER-WET POROUS MEDIUM .....	190
D. 2. MENISCI MOTION IN A FRACTIONALLY WET POROUS MEDIUM .....	197
<b>NOMENCLATURE .....</b>	<b>204</b>
<b>REFERENCES .....</b>	<b>206</b>
<b>VITA .....</b>	<b>220</b>

## List of Tables

Table 1.1. Estimated value of interfacial tension and contact angle between, solid surface, oil layer surface, water phase, oil phase and air. ....	17
---	----

## List of Figures

Figure 1.1. (a) Schematic of the water droplet on the freshly cleaved mineral surface in the presence of air. (b) Schematic of the water droplet on the freshly cleaved mineral surface in the presence of the oil phase. ....	15
Figure 1.2. (a) Schematic of the water droplet on the oil layer surface in the presence of air. (b) Schematic of the water droplet on the oil layer surface in the presence of the oil phase. ....	16
Figure 1.3. Schematic of a fractionally wet porous medium (grain level scale).....	18
Figure 1.4. Schematic of a mixed wet porous medium (grain level scale).....	20
Figure 2.1. Schematic of one pore (Delaunay cell) in a model unconsolidated sediment whose center is at point X. Arrows indicate gaps and point contacts that can support liquid bridges and pendular rings of the wetting phase after the pore has drained. Point W is the center of a pore throat. ....	26
Figure 2.2. (a) Schematic of a throat UVT (Fig. 2.1) before cementation. After the throat has drained the narrow gaps support liquid bridges of the wetting phase. The other gap is too wide to support a stable liquid bridge. (b) Schematic of same throat after cementation. The isopachous cement (gray) reduces the area of the throat. The pendular rings are smaller than in (a), because a larger capillary pressure is required to drain this throat. They may nevertheless occupy a larger fraction of the throat area, which is also smaller than in (a). Moreover the third gap UT is now narrow enough to support a liquid bridge. (c) Schematic of throat shows the definition of inscribed radius, $r_c$ and equivalent radius, $r_e$ . (d) The presence of pendular rings and liquid bridges (blue) reduces the area open to flow of non-wetting phase (red). This reduces the equivalent radius, but in this throat the inscribed radius is not changed. Note that Fig. 2.2a and 2.2d are schematic of throat UVT before cementation. As a result, the gap UT is not narrow enough to support a liquid bridge.....	27
Figure 2.3. Schematic of a toroidal liquid bridge of wetting phase between two grains of radius $R$ . The vertices $O$ and $O'$ correspond to the sphere centers and line $OO'$ that joins the sphere centers is the axis of symmetry for the liquid bridge. For the toroid approximation, the surface of the liquid bridge has radii of curvature $r_1$ and $r_2$ . The grain centers are separated by distance $2h$ .....	32
Figure 2.4. Saturation of the wetting phase (contribution from pendular rings and liquid bridges only) at different curvatures. Each curve is the result of starting at a large value of curvature (drainage endpoint) and decrementing the curvature to a value somewhat larger than the percolation threshold for drainage. This is consistent with the early stages of imbibition from the drainage endpoint, well before the percolation threshold for imbibition.....	35
Figure 2.5. Throat size distribution for model rocks of low porosity ( $\phi=8\%$ ) and moderate porosity ( $\phi=22\%$ ). The peak in the low porosity rock at zero radii corresponds to throats closed by cementation. Average throat inscribed radius for high porosity is $0.214 R$ and for low	

porosity (excluding closed throats) is 0.143 $R$ . The radius of the spheres of the model sediment (before cement) is $R$ . Approximately 23% of originally open throats are closed in the low porosity model rock due to overgrowth cementation. ....	37
Figure 2.6. Same distribution of throat sizes as Fig. 2.5, excluding throats closed by cement in the low porosity sample. The log scale shows that the distribution is much broader in the more heavily cemented sample. ....	38
Figure 2.7. The reduction of effective gas permeability due to low water saturation occupying pores in the two model rocks. Filling pores with water has notably less effect on gas permeability in the low porosity rock. This permeability calculation does not account for pendar rings or liquid bridges. ....	39
Figure 2.8. Effective gas (non-wetting) phase permeability vs. water (wetting) phase saturation. The saturation consists entirely of pendar rings and liquid bridges. The effect of the saturation is more pronounced for model rocks with smaller porosities. The narrow range of saturations is physically consistent with the restriction to rings/bridges. ....	40
Figure 2.9. Coalescence fraction (number of throats closed by coalescence at corresponding wetting saturation divided by total number of open throats in the absence of wetting phase) versus wetting saturation for model rocks of different porosities. Coalescence does not occur in this range of saturations for the high porosity model rocks (29%, 32%), so these curves coincide with the saturation axis. The smaller the porosity, the sooner coalescence starts as the water saturation increases from zero (except in the sample with 8% porosity). Consequently the gas phase connectivity decreases sooner with a small influx of water in the low porosity model rocks. ....	41
Figure 2.10. Gas effective permeability for tight sandstones: experimental data [217] and trends of model predictions. Confining pressure increases the sensitivity of effective gas permeability to low water saturations. If water saturation increases exclusively by changing the number and size of pendar rings/liquid bridges (no pore-filling), the gas permeability (red line) decreases faster than observed. If water saturation increases exclusively by pore filling (no rings/bridges), the gas permeability decreases more slowly than observed. Rings and bridges are thus the main mechanism for water sensitivity at low saturations. ....	44
Figure 2.11. Experimental data [177] for gas effective permeability for low permeability rock. This graph has two data sets: gas relative permeability measured at irreducible water saturation at the overburden pressure (set A) and the gas relative permeability at 4000 psi confining pressure (set B). The trends and conclusions discussed in Fig. 8 are applicable to this data set as well. ....	45
Figure 2.12. Extensive growth of isopachous cement from adjacent grains can lead to the formation of slot-like pores between grains. The slots are held open by asperities arising from different crystallographic orientation of the grains. Thus the slot aperture can change considerably with confining stress. ....	47
Figure 2.13. (a) Picture of bead pack column (18 cm) used for the capillary controlled gravity drainage of high concentrate brine experiment. This picture was taken at the end of experiment and the bead pack column was exposed to heat (oven) for more than 48 hrs. The	

red indicator in the brine enhances visual contrast between grains and precipitated salts. (b) Enlarged view on the top part of the bead pack column. The white spots are the crust of salt that precipitated between the glass wall of the column and the grains (beads). The average bead size is 2 mm. ....	50
Figure 2.14. Schematic of pendular ring held at point contact between grain and wall. We adapt the toroid approximation for rings between two spheres, so that $r_1$ and $r_2$ are taken to be the radii of curvature of the meniscus. This approximation is reasonable for large values of mean curvature, when $r_1 \ll r_2$ . $r_h$ is radius (max) of the circle of projected pendular rings, and the calculated value is compared with observations (Fig. 2.13). ....	51
Figure 3.1. Schematic of a fractionally wet porous medium (grain level scale). ....	56
Figure 3.2. Schematic of a mixed wet porous medium (grain level scale). ....	57
Figure 3.3. (a) Schematic of a porous medium constructed with randomly distributed disks, the oil-wet membrane and water-wet membrane located at the left and right hand side of porous medium. (b) Schematic of network model extracted from porous medium (Fig. 3.3a). The pore space within porous medium can be divided to pore bodies and pore throats using Delaunay tessellation. ....	61
Figure 3.4. Schematic of a pore-filling under the Haines criterion. Originally the meniscus is located in the left hand throat (blue curve, location 1). The meniscus is an arc of a circle whose radius is set by the applied capillary pressure. Increasing the curvature causes the circle to become smaller, until it can pass through smallest opening of the throat (green curve, location 3). The green curve is unstable and the pore will be drained which results in locating two menisci at adjacent throats (purple curves, location 4). ....	63
Figure 3.5. Schematic of a pore-filling under the Melrose criterion. Two menisci are originally located at two adjacent throats (blue curve, location 1); by decreasing the curvature (capillary pressure), menisci move toward the pore. Different color curve shows the position of the menisci at different curvatures. Eventually these two menisci touch (green curve, location 3), the green curve is unstable and pore will be imbibed by wetting phase. The merged meniscus jumps to a new stable location, the purple curve (location 4). ....	64
Figure 3.6. Schematic of different configurations of a pore in the fractionally wet porous media. The throat is the void space (gap) within two pair of disks. In configuration a, and b the throats are uniformly wet, whereas in configurations c and d two of throats are fractionally wet and one of them is uniformly wet. ....	66
Figure 3.7. Schematic of a stable meniscus (blue) with a radius of $r$ , located on two disks with different contact angle ( $\theta_1, \theta_2$ ). The disks have different radii ( $R_1, R_2$ ) and are separated by a gap of width $D$ . $O$ is the center of meniscus, and $O_1$ and $O_2$ are the center of two disks which hold the meniscus. ....	67
Figure 3.8 Relation between maximum curvature for a stable meniscus versus the gap size of the fractionally wet throats holding the menisci, and the contact angle of disk 2. The region	

below the plotted surface is region of stable menisci and the region above the surface is the region of unstable menisci.....	69
Figure 3.9. Schematic of meniscus (blue) with radius of $r$ , located on two disks with zero contact angles ( $\theta_1=\theta_2=0^\circ$ ). The disks have same radius ( $R_1=R_2=R$ ) and are separated by a gap of width $D$ .....	70
Figure 3.10. Schematic of menisci (blue) with radius of $r$ , located on two disks with zero and $180^\circ$ contact angles ( $\theta_1=0, \theta_2=180^\circ$ ). The disks have same radius ( $R_1=R_2=R$ ). .....	71
Figure 3.11. Schematic of two menisci merging (Melrose event) in a uniformly wet porous medium. Three water-wet disks construct a pore and three throats, and originally the two menisci are located on the two adjacent throats. The angle $\alpha$ is defined by lines connecting the points of contact of the menisci on the center disk to the disk center. (a). Menisci move toward the pore by decreasing the curvature (b), until they touch (c) and the pore fills with water. This Melrose event happens during imbibition as the curvature is decreased (d). .....	73
Figure 3.12. Schematic of two menisci merging (Melrose event) in a fractionally wet porous medium, two water-wet disks and one oil-wet disk construct a pore and three throats where two of them are fractionally wet and one is uniformly wet. Originally two menisci located on the two adjacent throats which are fractionally wet (a). Menisci move toward the pore by increasing curvature (b), until they touch (c) and the pore fills with oil. This Melrose event happens during drainage as the curvature is increased (d). .....	74
Figure 3.13. Imbibition and drainage curves for a 2D porous medium when 50% of its disks are oil-wet. The porous medium was filled with oil phase initially; first, the water phase pushes the oil out by decreasing capillary pressure (primary imbibition), second the oil phase drains the water out of the porous medium by increasing capillary pressure (drainage), and finally the water phase pushes into the porous medium again and replaces the oil phase (secondary imbibition). In all of three curves presented in this figure, the curvature ranges from positive to negative value and crosses over the zero curvature. All of these three curves were produced from the same code. The difference is just starting and ending applied curvature.....	76
Figure 3.14. Schematic of drainage end point for the porous medium with 50% of disks are oil-wet (the same porous medium as Fig. 3.13). The blue color represent the trapped water phase and the white color is the oil phase. The dark brown disks are oil-wet disks and the yellow disks are the water-wet disks. The region outlined in cyan shows a shell of water-wet grains in which a blob of water phase is trapped, the region outlined in dark red shows an outer shell of oil-wet grains around the water-wet shell. This pattern is characteristic of trapped water in this class of porous media. ....	77
Figure 3.15. (a) Primary imbibition (PI), drainage (D) and secondary imbibition (SI) curves for a porous medium with 25% oil-wet disks. (b) Primary drainage (PD), imbibition (I) and secondary drainage (SD) curves for a porous medium with 75% oil-wet disks. The curves on the Figs. 3.15a and 3.15b are vertically symmetric, so if the Fig. 3.15b rotates $180^\circ$ , the curve will be match with curves on Fig. 3.15a.....	79

Figure 3.16. Comparison between primary drainage curves for the porous media with different fractions of oil-wet ( $\theta_{ow} = 180^\circ$ ) disks distributed randomly among water-wet ( $\theta_{ww} = 0^\circ$ ) disks. The porous media was originally filled with water. The oil phase pushes the water phase out as the capillary pressure (curvature) increases. As the fraction of oil-wet disks within the porous medium increases, the curvature which the oil phase percolates through the porous medium decreases.....	80
Figure 3.17. Comparison between primary imbibition curves for the porous media with different fractions of oil-wet disks; the contact angles on water-wet and oil-wet disks are $\theta_{ww} = 0^\circ$ and $\theta_{ow} = 180^\circ$ , respectively. The porous media was originally filled with oil. The water phase pushes the oil phase out as the capillary pressure (curvature) decreases. As the fraction of oil-wet disks within porous medium increases, the curvature which the water phase percolates through porous medium decreases.....	81
Figure 3.18. (a) Measured octane/water drainage curve for the fractionally wet media. The primary drainage curves move monotonically lower with increasing oil-wet fraction. (b) Shows the simulation result for drainage of fractionally wet media. The contact angles on water-wet and oil-wet disks are $\theta_{ww} = 0^\circ$ and $\theta_{ow} = 180^\circ$ , respectively. For the model, we multiply the curvature by the known interfacial tension and divide by the grains radii to obtain the capillary pressure in Pascal.....	83
Figure 3.19. (a) Measured air/water imbibition curve for the fractionally wet media. The primary imbibition curves move monotonically lower with increasing oil-wet fraction. (b) Shows the simulation result for imbibition of fractionally wet media. The contact angles on water-wet and oil-wet disks are $\theta_{ww} = 0^\circ$ and $\theta_{ow} = 180^\circ$ , respectively. For the model, we multiply the curvature by the known interfacial tension and divide by the grain radii to obtain the capillary pressure in Pascal.....	84
Figure 3.20. Water/air drainage curves for the fractionally wet media. Primary drainage curves do not show much change with changing oil-wet fraction.....	85
Figure 3.21. Comparison between primary drainage curves for porous media with different fraction of oil-wet ( $\theta_{ow} = 50^\circ$ ) disks distributed randomly among water-wet ( $\theta_{ww} = 0^\circ$ ) disks. If the oil-wet disks are not perfectly hydrophobic, as commonly occurs in experiments when the grains are treated chemically, the change in the capillary pressure curve is less dramatic.....	88
Figure 4.1. (a) Schematic of a dense random packing of equal spheres. The face 1 is used as the entry face during simulation. The exit face(s) can be only face 4 or all faces other than face 1. (b) Schematic of network of tetrahedra extracted from the sphere pack (Fig. 4.1a). The pore space within the sphere pack can be divided into pore bodies and pore throats using Delaunay tessellation. The network of pore bodies and pore throats is extracted from network of tetrahedra.....	93
Figure 4.2. Schematic of a pore (Delaunay cell) in a random packing of equal spheres.....	94
Figure 4.3. Schematic of a meniscus (brown triangular patch) located on three grains (spheres) with zero contact angles (fully water-wet). $O$ indicates the center of the meniscus and $O_1$ , $O_2$ , and $O_3$ indicate centers of spheres constructing the throat. The meniscus is the cap part of	



the yellow sphere, limited to inside of the tetrahedron $OO_1O_2O_3$ , where the vertices of the tetrahedron are the centers of the meniscus and three grains. ....	96
Figure 4.4. Schematic of a meniscus (yellow cap) located on three grains (spheres) with zero contact angles. $O_1$ , $O_2$ , and $O_3$ indicate centers of the grains constructing the throat. Point $P_2$ is the point where the meniscus touches grain 2. The filling angle of meniscus ( $\psi_2$ ) on grain 2 is the angle between line $\overline{O_2P_2}$ and plane $\triangle O_1O_2O_3$ .....	97
Figure 4.5. Schematic of a water-wet edge holding a pendular ring of the water phase. $O_1$ and $O_2$ indicate centers of grains constructing the edge. Points $P_1$ and $P_2$ are the points where the pendular rings touches grain 1 and grain 2 respectively. The contact angle between the water phase and grains is zero degrees. $\varphi_1$ and $\varphi_2$ are the filling angles of the pendular ring on grain 1 and grain 2 respectively. ....	98
Figure 4.6. Schematic of meniscus (blue curve) located on two disks with zero contact angles (fully water-wet). $O$ indicates the center of the meniscus and $O_1$ and $O_2$ indicate the center of disks constructing the throat. a) Curvature of the meniscus is smaller than the drainage critical curvature for the throat. (b) Curvature of the meniscus equals the drainage critical curvature. $O$ (center of meniscus) is located on line $\overline{O_1O_2}$ .....	101
Figure 4.7. Schematic of meniscus (blue curve) located on a fractionally wet throat. $O$ indicates the center of the meniscus and $O_1$ is the center of water-wet disk (contact angle= $0^\circ$ ) and $O_2$ is the center of oil-wet disk (contact angle= $180^\circ$ ) the center of disks constructing the throat. (a) Curvature of the meniscus is smaller than the drainage critical curvature for the throat. (b) Curvature of the meniscus equals the drainage critical curvature. $O$ (center of the meniscus) is located on line $\overline{O_1O_2}$ .....	102
Figure 4.8. Schematic of a meniscus (yellow cap in (a), brown cap in (b)) located on three grains (spheres) with zero contact angles (fully water-wet). $O$ indicates the center of the meniscus and $O_1$ , $O_2$ , and $O_3$ indicate the center of spheres constructing the throat. (a) Curvature of the meniscus is smaller than the drainage critical curvature for the throat. (b) Curvature of the meniscus equals the drainage critical curvature of the throat. $O$ (center of meniscus) is located on plane $\triangle O_1O_2O_3$ .....	103
Figure 4.9. Schematic of a meniscus (light brown cap in (a), brown hemisphere in (b)) located on a fractionally wet throat. $O$ indicates the center of the meniscus and $O_1$ and $O_3$ is the center of water-wet grains (contact angle= $0^\circ$ ) and $O_2$ is the center of oil-wet grain (contact angle= $180^\circ$ ). (a) Curvature of the meniscus is smaller than the drainage critical curvature for the throat. (b) Curvature of the meniscus equals the drainage critical curvature. $O$ (center of meniscus) is located on the plane of $\triangle O_1O_2O_3$ .....	104
Figure 4.10. Schematic of two menisci located on two adjacent throats. The red meniscus sits on throat 123 and the blue meniscus sits on throat 234. All grains make zero contact angles with the two menisci. The menisci are connected by a wedge of wetting phase between grains 2 and 3.....	106

Figure 4.11 (a) Schematic of merging of two menisci located on two adjacent throats. The red meniscus sits on throat 123 and the blue meniscus sits on throat 234. All grains make zero contact angles with the two menisci. Throat 123 and throat 234 share an edge composed of grain 2 and grain 3. (b) Plane A and plane B are on the same plane (the angle between plane A and plane B equal zero degree). The Haines imbibition critical curvature equals the curvature of this merged meniscus. ....	107
Figure 4.12. A meniscus (blue) does not touch a pendular ring (red) inside a pore; hence this is a stable configuration not satisfying the condition for a Melrose event. The pore is composed of four grains (1, 2, 3, and 4). The pendular ring (red) located on edge 13 composed of grain 1 and grain 3. The meniscus is located on throat 234 which is composed of three grains (2, 3, and 4).....	109
Figure 4.13. A 2D slice through the plane $\triangle AON$ , which $A$ is the center of grain 3 in Fig. 4.12, $D$ is the center of grain 1 in Fig. 4.12 and $N$ is the point, equidistant from the grain centers of throat 234. The grain 3 is common between edge 13 and throat 234. $\varphi$ is the pendular ring filling angle and $\psi$ is the meniscus filling angle. The meniscus and pendular ring do not touch, as a result the angle $\alpha$ is greater than summation of angle $\varphi$ and $\psi$ . This figure is modified from the figure presented in Ref. [78]. ....	110
Figure 4.14. The edge holding pendular ring ( $\overline{AD}$ ) is not located on the $\triangle AON$ plane. Planes $\triangle AON$ (brown) and $\triangle AOD$ (green) are not in the same plane. They intersected with a nonzero angle with each other. $A$ is the center of grain 3. Grain 3 is common between the edge holding a pendular ring (red) and the throat holding a meniscus (blue). $D$ is the center of grain 1. $O$ is the center of the meniscus. $N$ is the point that is equidistant from the grain centers of the throat holding the meniscus. ....	111
Figure 4.15. (a) A pendular ring (red) and a meniscus (blue) at the curvature of 2.85. The pendular ring and meniscus do not touch at this curvature. (b) A pendular ring (red) and a meniscus (blue) at curvature of 2.15. The pendular ring and meniscus touch at this curvature. The Gladkikh development of Melrose criterion predicts that the two interfaces touch at curvature of 2.85 which is an overestimate of the real critical curvature for the Melrose event. ....	112
Figure 4.16. (a) Fluid configuration when a meniscus (blue) touch a pendular ring (red) inside a pore. The gray plane is the plane $\triangle AON$ which connects the middle of throat 234 and the center of the meniscus and the center of grain common between throat 234 and edge 13. The blue line connect the center of grain 3 to the center of meniscus. The blue line passes through the touching point between the pendular ring and meniscus. The green line is the line normal to the gray plane ( $\triangle AON$ ). (b) Demonstrate development of new Melrose criterion. $\overline{AD}$ is the edge holding a pendular ring (red). $\overline{AA'}$ is the normal vector to plane $\triangle AON$ , where $A$ is the center of grain 3. $D'$ is the projection of the center of grain 1 (point $D$ ) on the plane $\triangle AON$ . $O$ is the center of the meniscus. $N$ is the point, equidistant from the grain centers of the throat holding the meniscus. $P$ is the point which the pendular ring and the meniscus touch each other on grain 3. $\varphi$ is the filling angle of the pendular ring and $\psi$ is the filling angle of the meniscus. ....	113

- Figure 4.17. A Melrose event occurs if the summation of  $\varphi_1$  and  $\psi$  (see Fig. 4.16) is bigger than  $\alpha$  (the angle between line  $\overline{AN}$  and  $\overline{AD'}$ ).  $D'$  is the projection of the center of grain 1 (point  $D$ ) on plane  $\triangle AON$ .  $O$  is the center of the meniscus.  $N$  is the point equidistant from the grain centers of throat holding the meniscus.  $P$  is the point at which the pendular ring and the meniscus touch each other on grain 3. Vector  $\vec{a}$  is indicated by a black vector, and vectors  $\vec{a}_1$ ,  $\vec{a}_2$  and  $\vec{a}_3$  are indicated by the white vectors. .... 115
- Figure 4.18. Stage of coalescence of pendular rings on a pore throat in 2D view. A 2D slice of a pore throat by the plane connecting center of grains ( $O_1$ ,  $O_2$ , and  $O_3$ ). (a) Curvature of pendular rings is smaller than the critical curvature for coalescence to occur. Summation of pendular rings filling angle ( $\varphi_1$  and  $\varphi_2$ ) is smaller than angle  $\alpha$ . (b) Curvature of pendular rings equal to the critical curvature for coalescence to occur. Summation of pendular rings filling angles ( $\varphi_1$  and  $\varphi_2$ ) equals to angle  $\alpha$ . (c) The coalescence occurs and the pore throat is closed by the wetting phase. .... 116
- Figure 4.19. The stages of coalescence of pendular rings on a pore throat in 3D view. (a) Curvature of pendular rings is smaller than the critical curvature for coalescence to occur. Summation of pendular rings filling angle is smaller than angle between two edges holding pendular rings (angle  $\alpha$ ). (b) Curvature of pendular rings equal to the critical curvature for coalescence to occur. Summation of pendular rings filling angles equals to angle  $\alpha$ . (c) The coalescence occurs and the pore throat is closed by the wetting phase. .... 117
- Figure 4.20. Fluid configuration within two pores (pore 1234, and pore 1256), before a meniscus–4<sup>th</sup> grain contact during imbibition. Throat 123 and throat 125 hold menisci which are colored dark blue and red, respectively. A light blue interface connects the two menisci. All grains are water-wet and they make a contact angles of 30° with the menisci. The water phase is located below the menisci, and the oil phase is located above. The fourth grain of pore 1234 (grain 4) which comes in contact with the meniscus in throat 123 is colored green. .... 118
- Figure 4.21. Reducing the curvature in Fig. 4.20 leads to this fluid configuration (different view point than Fig. 4.20) in which the meniscus (dark blue) touches the green fourth grain (grain 4). Grain 1 has been removed to expose the region of the meniscus and the fourth grain contact (this region is highlighted by red circle). .... 119
- Figure 4.22. Fluid configuration within two pores (pore 1234, and pore 1256), after the meniscus (dark blue) touches the 4<sup>th</sup> grain (grain 4) (cf. Fig. 4.21). (a) The water phase rises on the surface of grain 4, and as a result two pendular rings are formed on edge 14 and edge 24. (b) Grain 4 is removed in order to reveal rings (light blue) and meniscus (dark blue) contacts. .... 120
- Figure 4.23. The fluid configuration within two pores (pore 1234, and pore 1256), after the meniscus touches the 4<sup>th</sup> grain (grain 4) (final stage). Three new menisci (dark blue) are formed on the throat corresponding to pore 1234 (throat 124, throat 134, and throat 243). The light blue interface is not a pendular ring, but a surface that connects adjacent menisci. .... 121
- Figure 4.24. Imbibition and drainage curves for a porous medium with 50% of grains oil-wet. The porous medium was filled with the oil phase initially: first, the water phase pushes the oil

<p>out by decreasing capillary pressure (primary imbibition), second the oil phase drains the water out of the porous medium by increasing capillary pressure (drainage), and finally the water phase pushes into the porous medium and replaces the oil phase (secondary imbibition). In all three curves, the curvature ranges from positive to negative values and thus passes through zero curvature. All three curves are produced from the same code applying the same criteria for pore-filling events. The different behavior arises entirely from the different values of starting and ending applied curvature.....</p>	123
<p>Figure 4.25. (a) The primary drainage (PD), imbibition (I) and secondary drainage (SD) curves for a porous medium with 25% oil-wet grains. (b) The primary imbibition (PI), drainage (D) and secondary imbibition (SI) curves for a porous medium with 75% oil-wet grains. The curves on the Figs. 4.21a and 4.21b are vertically symmetric, so if the Fig. 4.25b rotates 180°, the curves will overlies the curves on Fig. 4.25a. ....</p>	125
<p>Figure 4.26. Comparison between primary drainage curves for the porous media with different fractions of oil-wet (<math>\theta_{ow} = 150^\circ</math>) grains distributed randomly among water-wet (<math>\theta_{ww} = 30^\circ</math>) grains. The porous media was originally filled with water. The oil phase pushes the water phase out as the capillary pressure (curvature) increases. ....</p>	126
<p>Figure 4.27. Comparison between secondary imbibition curves for the porous media with different fractions of oil-wet grains; the contact angles on water-wet and oil-wet grains are <math>\theta_{ww} = 30^\circ</math> and <math>\theta_{ow} = 150^\circ</math>, respectively. The imbibition curves start from drainage endpoint of the curves in Fig. 4.26. The water phase pushes the oil phase out as the capillary pressure (curvature) decreases. As the fraction of oil-wet grains within porous medium increases the value for curvature which the water phase percolates through porous medium decreases.....</p>	127
<p>Figure 4.28. Comparison between simulation results for a fully water-wet medium and Haines experimental data for packing of glass beads. The contact angles on water-wet grains are <math>\theta_{ww} = 0^\circ</math>. The imbibition curve starts from the drainage endpoint of the drainage curves. The drainage curve is a primary drainage curve.....</p>	129
<p>Figure 4.29. (a) Measured octane/water drainage curve for the fractionally wet media. The primary drainage curves move monotonically lower with increasing oil-wet fraction. (b) Simulation results for drainage of fractionally wet media. The contact angles on water-wet and oil-wet grains are <math>\theta_{ww} = 30^\circ</math> and <math>\theta_{ow} = 150^\circ</math>, respectively. For the model, we multiply the curvature by the known interfacial tension and divide by the grains radii to obtain the capillary pressure in Pascal .....</p>	131
<p>Figure 4.30. (a) Measured octane/water drainage curve for the fractionally wet media. The primary drainage curves move monotonically lower with increasing oil-wet fraction. (b) Simulation results for drainage of fractionally wet media. The contact angles on water-wet and oil-wet grains are <math>\theta_{ww} = 0^\circ</math> and <math>\theta_{ow} = 120^\circ</math>, respectively. For the model, we multiply the curvature by the known interfacial tension and divide by the grains radii to obtain the capillary pressure in Pascal .....</p>	133
<p>Figure 4.31. Measured PCE/water drainage curve for the fractionally wet media [153]. The primary drainage curves move monotonically lower with increasing oil-wet fraction. The value of water saturation is normalized. The apparent water phase saturation is zero at the minimum</p>	

measured water saturation. The apparent water phase saturation is unity at the maximum measured water saturation.....	134
Figure 4.32. (a) Measured octane/water imbibition curve for the fractionally wet media. The primary imbibition curves move monotonically lower with increasing oil-wet fraction. (b) Simulation results for imbibition of fractionally wet media. The contact angles on water-wet and oil-wet grains are $\theta_{ww} = 30^\circ$ and $\theta_{ow} = 150^\circ$ , respectively. For the model, we multiply the curvature by the known interfacial tension and divide by the grains radii to obtain the capillary pressure in Pascal. ....	135
Figure 4.33. (a) Measured octane/water imbibition curve for the fractionally wet media. The primary imbibition curves move monotonically lower with increasing oil-wet fraction. (b) Simulation results for imbibition of fractionally wet media. The contact angles on water-wet and oil-wet grains are $\theta_{ww} = 0^\circ$ and $\theta_{ow} = 120^\circ$ , respectively. For the model, we multiply the curvature by the known interfacial tension and divide by the grains radii to obtain the capillary pressure in Pascal. ....	137
Figure 4.34. (a) Measured air/water imbibition curve for the fractionally wet media [204]. The primary imbibition curves move monotonically lower with increasing oil-wet fraction. The value of water saturation is normalized. The minimum measured water saturation equate to a value of zero for the apparent water phase saturation. The maximum measured water saturation equate to the value of one for the apparent water phase saturation. (b) Simulation result for imbibition of the fractionally wet media. The contact angles on water-wet and oil-wet grains are $\theta_{ww} = 0^\circ$ and $\theta_{ow} = 110^\circ$ , respectively. For the model, we multiply the curvature by the known interfacial tension and divide by the grains radii to obtain the capillary pressure in Pascal. ....	139
Figure 4.35. Compares the simulation results for imbibition of a water-wet medium when only generalized Haines imbibition events occur (light blue curve), only Melrose events (red curve) occur, both generalized Haines imbibition and Melrose events occur (green curve). The imbibition starts from the drainage end point. Here we ignore the trapping of the oil phase. ....	142
Figure 4.36. (a) Fraction of each event (i.e. Melrose and generalized Haines imbibition) during imbibition of a water-wet medium. (b) Total events during imbibition versus the water phase saturation.....	143
Figure 4.37. Compares the simulation results for primary imbibition of a water-wet medium (purple curve) with secondary imbibition of a water-wet medium (green curve). Haines imbibition event can occur in both primary and secondary imbibition. During secondary imbibition, pendular ring exist. Consequently, the Melrose events can occur. In contrast, in primary imbibition, no Melrose event occurs due to the lack of existence of pendular rings. During primary imbibition, the meniscus-4 <sup>th</sup> grain event occurs at a small value of dimensionless curvature.....	145
Figure 4.38. Compares the simulation results for the primary imbibition of a water-wet medium with and without accounting for the coalescence of pendular rings. (a) We ignore the trapping of the oil and water phases. (b) We take into account the trapping of the oil and water phases.....	146

Figure 4.39. (a) $P$ - $S$ curve for drainage of a fractionally wet medium with 25% oil-wet grains. The contact angles on water-wet and oil-wet grains are $\theta_{ww} = 30^\circ$ and $\theta_{ow} = 150^\circ$ , respectively. (b) Fraction of each events occur during drainage of the fractionally wet medium with 25% oil-wet grains.....	148
Figure 4.40. (a) $P$ - $S$ curve for drainage of a fractionally wet medium with 75% oil-wet grains. The contact angles on water-wet and oil-wet grains are $\theta_{ww} = 30^\circ$ and $\theta_{ow} = 150^\circ$ , respectively. (b) Fraction of each event during drainage of the fractionally wet medium with 75% oil-wet grains.....	149
Figure 4.41. (a) $P$ - $S$ curve for imbibition of a fractionally wet medium with 25% oil-wet grains. The contact angles on water-wet and oil-wet grains are $\theta_{ww} = 30^\circ$ and $\theta_{ow} = 150^\circ$ , respectively. (b) Fraction of each events occur during imbibition of the fractionally wet medium with 25% oil-wet grains.....	151
Figure 4.42. (a) $P$ - $S$ curve for imbibition of a fractionally wet medium with 75% oil-wet grains. The contact angles on water-wet and oil-wet grains are $\theta_{ww} = 30^\circ$ and $\theta_{ow} = 150^\circ$ , respectively. (b) Fraction of each events occur during imbibition of the fractionally wet medium with 75% oil-wet grains.....	152
Figure 4.43. $P$ - $S$ curve for the primary drainage of different realization of the fractionally wet media with 25% oil-wet grains. The contact angles on water-wet and oil-wet grains are $\theta_{ww} = 30^\circ$ and $\theta_{ow} = 150^\circ$ , respectively.....	153
Figure 4.44. (a) CDF and (b) histograms for Haines critical curvature for drainage of two realizations of the media with 25% oil-wet grains. The CDF and histogram for the realization 1 and realization 2 are similar. The contact angles on water-wet and oil-wet grains are $\theta_{ww} = 30^\circ$ and $\theta_{ow} = 150^\circ$ , respectively.....	155
Figure 4.45. (a) Histograms for Haines critical curvature for drainage in a fully water-wet medium. The peak at the value of 11.5 is corresponding to the throats that have three point contacts between its grains. (b) Histograms for Haines critical curvature of the medium with 25% oil-wet grains. The peak at critical curvature of 11.5 associates with the throats defined by three water-wet grains that touch each other. The peak at critical curvature of 3.5 associates with throat composed of two water-wet grains and one oil-wet grain that touch each other. The peak at critical curvature of zero associates with throat composed of two oil-wet grains and one water-wet grain that touch each other. The contact angles on water-wet and oil-wet grains are $\theta_{ww} = 30^\circ$ and $\theta_{ow} = 150^\circ$ , respectively.....	156
Figure 4.46. CDF of Haines critical curvature of a fully water-wet medium (blue curve) and the medium with 25% oil-wet grains (red curve). 50% of throats within the medium with 25% oil-wet grains have Haines critical curvature smaller than 3.5. 50% of throats within the fully water-wet medium have Haines critical curvature smaller than 6.5. The value of 50% corresponds to the bond percolation threshold of the random sphere pack [143].....	157
Figure 4.47. (a) Primary drainage curves for the porous media with different fractions of oil-wet ( $\theta_{ow} = 150^\circ$ ) grains distributed randomly among water-wet ( $\theta_{ww} = 30^\circ$ ) grains. The meniscus-4 <sup>th</sup> grain event is not considered. (b) Primary drainage curves for the porous media with	

different fractions of oil-wet ( $\theta_{ow} = 150^\circ$ ) grains distributed randomly among water-wet ( $\theta_{ww} = 30^\circ$ ) grains. The meniscus-4th grain event is considered. ....	159
Figure 4.48. Shows the difference in the trapped phase saturation at the end of drainage and imbibition for a water-wet medium with two different boundary conditions. The red curve shows the result for drainage/imbibition when only one side of the medium is open as an exit side. The blue curve shows the result for drainage/imbibition when five sides of the medium are open as the exit sides. ....	161
Figure 4.49. Comparison between primary drainage curves for the porous media with different fractions of oil-wet ( $\theta_{ow} = 150^\circ$ ) grains distributed randomly among water-wet ( $\theta_{ww} = 30^\circ$ ) grains. The water phase gets trapped when disconnected from the bulk phase. ....	162
Figure 4.50. Compares the residual water phase saturation at the end of primary drainage for porous media with different fraction of oil-wet ( $\theta_{ow} = 150^\circ$ ) grains distributed randomly among water-wet ( $\theta_{ww} = 30^\circ$ ) grains. The marker 'O' shows the average value of the residual water saturation for primary drainage of different realization of fractionally wet media. The bar shows the maximum and minimum values for residual water saturation achieved for simulation of 10 realizations. ....	163
Figure A.1. Schematic of a toroidal liquid bridge of the wetting phase between two grains with radius $R$ . The contact angle between the pendular ring and grains is $\theta$ . The vertices $O$ and $O'$ correspond to the sphere centers. Line $\overline{OO'}$ that joins the sphere centers is the axis of symmetry for the liquid bridge. For the toroid approximation, the surface of the liquid bridge has radii of curvature $r_1$ and $r_2$ . The grain centers are separated by distance $2h$ . Point $N$ is the equidistance from grain centers. ....	168
Figure B.1. Capillary pressure (divided by interfacial tension to yield curvature) exhibits a power law dependence on wetting phase saturation in our model rocks. The exponents have magnitudes between 0.53 and 0.6, corresponding to fractal dimension $D_L$ between 0.1 and 0.34. ....	173
Figure B.2. As fractal dimension increases corresponding to increasingly rough grain surfaces, Eq. B.2 predicts that gas relative permeability is less sensitive to small saturations of water. We assume $k_{rg,max} = 1$ for all curves. At a fractal dimension of 1.7, which corresponds to a strongly water-wet rock [151], the gas phase permeability is almost independent of water saturation for $S_w < 0.1$ . This indicates that the pore space associated with surface roughness in this rock makes a negligible contribution to the gas phase permeability. Thus, when water occupies that pore space, it contributes to $S_w$ but does not change $k_{rg}$ . For comparison, a fractal dimension 0.334 corresponds to our high porosity model rock; Eq. B.2 predicts greater sensitivity to low $S_w$ than observed in experiments or predicted by our model. ....	174
Figure C.1. Schematic of a meniscus (blue) with radius of $r$ , located on two disks with different contact angle ( $\theta_1, \theta_2$ ). The disks have different radii ( $R_1, R_2$ ). $L_1$ and $L_2$ are distance of center of meniscus from center of disk 1 and disk 2 respectively. $P_1$ and $P_2$ are the contact point of the meniscus with the disk 1 and disk 2 respectively. ....	177

Figure C.2. Schematic of a meniscus (blue) with radii of $r$ , located on two disks with zero contact angles ( $\theta_1=\theta_2=0$ ). The disks have same radius ( $R_1=R_2=R$ ) and are separated by a gap of width $D$ .....	180
Figure C.3. Stable and unstable values for radii of menisci located on the water-wet throat composed of two equal size disks. The area above the blue line is the region of stable menisci. The area below the blue line is the region of unstable menisci. The slope of blue line is one and its intercept is zero. ....	181
Figure C.4. Schematic of a meniscus (blue) with radii of $r$ , located on two disks with zero and $180^\circ$ contact angles ( $\theta_1=0, \theta_2=180^\circ$ ). The disks have same radius ( $R_1=R_2=R$ ). ....	182
Figure C.5. Stable and unstable values for radii of menisci located on the fractionally wet throat composed of two equal size disks with zero and $180^\circ$ contact angles ( $\theta_1=0, \theta_2=180^\circ$ ). The area above the blue line is the region of stable menisci. The area below the blue line is the region of unstable menisci. The slope of blue line is one and its intercept is one. ....	183
Figure C.6. Surface of minimum radii of stable menisci at different gap size of fractionally wet throats. The fractionally wet throats are composed of two equal size disks, where the contact angle of disk 1 and menisci remains constant at zero degree ( $\theta_1=0^\circ$ ) and the contact angle of disk 2 and menisci varies between 0 and $180^\circ$ ( $0^\circ \leq \theta_2 \leq 180^\circ$ ). The region above the plotted surface is the region of stable menisci. The region below the plotted surface is the region of unstable menisci.....	184
Figure C.7. Two menisci are located at adjacent throats (throat 1 ( $\overline{O_1O_2}$ ) and throat 2 ( $\overline{O_1O_3}$ )). The menisci and grains make zero contact angles. $\beta_1$ and $\beta_2$ are the filling angle of meniscus 1 and meniscus 2 respectively. (a) The points $p_1$ and $p_2$ , contact points between meniscus 1 and meniscus 2 with disk 1, are distinct. As a result, two menisci are separated by angle $\alpha$ . (b) Points $p$ is the contact point between meniscus 1, meniscus 2 and disk 1. The angle $\alpha$ equal zero. Two menisci merge and become a single meniscus. This situation results in occurrence of the Melrose event. ....	187
Figure C.8. Two menisci are located at adjacent throats (throat 1 ( $\overline{O_1O_2}$ ) and throat 2 ( $\overline{O_1O_3}$ )). The menisci and water-wet grains make zero contact angles and the menisci and oil-wet grains make $180^\circ$ contact angles. $\beta_1$ and $\beta_2$ are the filling angle of meniscus 1 and meniscus 2 respectively. (a) The points $p_1$ and $p_2$ (contact points between meniscus 1 and meniscus 2 with disk 1) are distinct. As a result, two menisci are separated by angle $\alpha$ . (b) Points $p$ is the contact point between meniscus 1, meniscus 2 and disk 1. The angle $\alpha$ equal zero. Two menisci merge and become a meniscus. This situation results in occurrence of the Melrose event.....	188
Figure D.1. Schematic of a water-wet porous medium at the beginning of primary drainage. The porous medium is filled with the water phase (blue). The oil phase (white) is connected to the oil-wet membrane.....	189



Figure D.2. (a) Schematic of a water-wet porous medium and fluid/fluid interfaces (menisci) during primary drainage. The dimensionless curvature of the interface equals 2.6. (b) Change of the water phase saturation versus change of applied curvature from value of -2 to 2.6. ....	190
Figure D.3. (a) Schematic of a water-wet porous medium and fluid/fluid interfaces (menisci) during primary drainage. The dimensionless curvature of the interface equals 7.8. The value of curvature is normalized by radius of disks composing the porous medium. The pores highlighted by red triangles are filled by the oil phase, whereas they were filled with water phase in the Fig. D.2a. (b) Change in the water phase saturation with change in the applied curvature from value of -2 to 7.8. Two red circle highlight the $S_w$ change correspond to filling event of two pores highlighted in Fig. D.3a. ....	191
Figure D.4. (a) Schematic of a water-wet porous medium and fluid configuration at drainage end point. The dimensionless curvature of the interface equals 13.8. The red boxes (box A and B) highlight the trapped water phase in a throat. The trapped water phase in the pores is indicated by red arrows. (b) Change in the water phase saturation with change in the applied curvature from value of -2 to 13.8. ....	192
Figure D.5. Schematic of a water-wet porous medium and fluid/fluid interface (menisci) during secondary imbibition. (a) The fluid configuration before the Melrose event: Two menisci touch inside a pore highlighted by the red box. (b) The fluid configuration after the Melrose event: a pore highlighted by the red box is filled with a water phase and a meniscus locates on a new pore throat. ....	193
Figure D.6. (a) Schematic of a water-wet porous medium and fluid/fluid interfaces (menisci) during secondary imbibition. The dimensionless curvature of the interface equals 3.6. The red box A highlights two pores in which a Melrose event occur within. The red box B highlights a frozen meniscus corresponded to the trapped water phase (b) Change of water phase saturation versus change of applied curvature for the primary drainage and the secondary imbibition. In the secondary imbibition the value of the curvature changed from 13.8 to 3.6. ....	194
Figure D.7. (a) Schematic of a water-wet porous medium and fluid/fluid interfaces (menisci) during secondary imbibition. The dimensionless curvature of the interface equals 3.4. The red box B highlights a meniscus in which get unfrozen after reconnection of trapped water phase to bulk water phase (b) Change in the water phase saturation with change in the applied curvature for primary drainage and secondary imbibition. In the secondary imbibition the value of the curvature changed from 13.8 to 3.4. ....	195
Figure D.8. (a) Schematic of a water-wet porous medium and fluid/fluid interfaces (menisci) during secondary imbibition. The dimensionless curvature of the interface equals 0.8. (b) Change in the water phase saturation with change in the applied curvature for primary drainage and secondary imbibition. In the secondary imbibition the value of the curvature changed from 13.8 to 0.8. The red box shows that the water phase saturation ( $S_w$ ) does not change while the applied curvature decreases from 3.4 to 0.8. ....	196
Figure D.9. (a) Schematic of a water-wet porous medium and fluid/fluid interfaces (menisci) during secondary imbibition. The dimensionless curvature of the interface equals 0.6. (b) Change in the water phase saturation with change in the applied curvature for primary drainage and secondary imbibition. In the secondary imbibition the value of the curvature changed from 13.8 to 0.4. ....	196

Figure D.10. Schematic of a fractionally wet porous medium at the beginning of primary drainage. The porous medium is filled the with the water phase (blue). The oil phase (white) is connected to the oil-wet membrane.....	197
Figure D.11. (a) Schematic of a fractionally wet porous medium and fluid/fluid interfaces (menisci) during primary drainage. The dimensionless curvature of the interface equals 2.4. (b) Change of the water phase saturation versus change of applied curvature from value of -2 to 2.4.....	198
Figure D.12. (a) Schematic of a fractionally wet porous medium and fluid/fluid interfaces (menisci) during primary drainage. The dimensionless curvature of the interface equals 2.6. (b) Change of the water phase saturation versus change of applied curvature from value of -2 to 2.6.....	199
Figure D.13. (a) Schematic of a fractionally wet porous medium and fluid configuration at drainage end point. The dimensionless curvature of the interface equals 13.8. (b) Change of the water phase saturation versus change of applied curvature from value of -2 to 13.8.....	200
Figure D.14. (a) Schematic of a fractionally wet porous medium and fluid/fluid interfaces (menisci) during secondary imbibition. The dimensionless curvature of the interface equals 0.2. (b) Change in the water phase saturation with change in the applied curvature for primary drainage and secondary imbibition. In the secondary imbibition the value of the curvature changed from 13.8 to 0.2.....	201
Figure D.15. (a) Schematic of a fractionally wet porous medium and fluid/fluid interfaces (menisci) during secondary imbibition. The dimensionless curvature of the interface equals -0.8. (b) Change in the water phase saturation with change in the applied curvature for primary drainage and secondary imbibition. In the secondary imbibition the value of the curvature changed from 13.8 to -0.8. ....	202
Figure D.16. (a) Schematic of a fractionally wet porous medium and fluid/fluid interfaces (menisci) during secondary imbibition. The dimensionless curvature of the interface equals -1.2. (b) Change in the water phase saturation with change in the applied curvature for primary drainage and secondary imbibition. In the secondary imbibition the value of the curvature changed from 13.8 to -1.2. ....	203

# CHAPTER 1: INTRODUCTION

## 1.1. INTRODUCTION

Macroscopic multiphase fluid-rock properties (e.g. relative permeability) have a significant impact on processes within the agricultural and oil industries such as water infiltration and enhanced oil recovery. The macroscopic properties of porous media are affected by the physics of pore-scale displacement. Hence, numerous studies have been conducted to model the macroscopic properties of porous media based on pore level petrophysics [15, 26, 28, 29, 38, 40-43, 57, 58, 62, 67-69, 77, 79-82, 94, 95, 107, 108, 126, 139, 140, 150, 158-161, 180, 181, 183, 187, 188, 195-199, 205-208]. Most of these studies on predicting macroscopic properties of a porous medium used a network model to upscale pore level displacements, whereas several other studies use a direct simulation [84, 137, 152, 157, 212].

In network models, the pore space is divided into pore bodies (sites) and pore throats (bonds). The pore throats connect the pore bodies to each other. In a traditional pore-based network model, a number of pore-level petrophysical properties are defined through *ad hoc* parameters such as the coordination number of pore bodies, and the distribution of pore and throat-sizes. Consequently, the predictive capability of these network models is limited by the presence of *ad hoc* parameters. In contrast, in a grain-based network model, many features of the network model including the relation between pore bodies and pore throats are extracted from the geometry of the porous medium.

In this study we use a grain-based network model extracted from a simple but physically representative model of a porous medium. Our model consists of a dense random packing of equal spheres in which the coordinates of the spheres center are

known. Such a sphere pack can be generated by computers [47] or measured experimentally [72].

The advantage of this approach lies in its flexibility and simplicity. For instance, the fluid rock interaction properties (i.e. wettability) may be assigned to the entire (or partial) surface of a grain. These options result in different models of heterogeneously wet porous media (i.e. fractionally wet and mixed wet porous media). In addition, we can create simple sedimentary rock models by simulating geological processes such as overgrowth cementation where we uniformly increase the size of spheres in the sphere pack without moving their centers.

This model demonstrates predictive capability despite its simplicity. The pore-level petrophysical features are extracted directly from the geometry of the model porous medium. As a result, there are no *ad hoc* parameters for this model. We test the model prediction directly against experimental results. An unsuccessful match between experimental results and the model prediction indicates that the model failed to consider some important pore level physics of the real porous media. In contrast, the successful prediction of the experimental results increases our confidence that the model can be used as a reliable approximation of real porous media.

This chapter provides an overview of the history of wettability studies and pore-scale modeling. First, we compare grain-based network modeling to both pore-based network modeling and direct simulation. Second, we review the physics of wettability and its effect on macroscopic properties of porous media.

## 1.2. SIGNIFICANT CONTRIBUTIONS

By adopting a grain-based approach for modeling of fluid flow within the porous media, we:

1. Extended the application of grain scale modeling to model fluid flow within low porosity and low permeability rocks at small wetting phase saturations.
2. Calculated and demonstrated the importance of pendular rings in reduction of gas permeability at low water saturation in low permeability rocks.
3. Explained the effect of CO<sub>2</sub> injection into deep saline aquifers on the absolute permeability of the reservoir in the near wellbore region dried out by the CO<sub>2</sub>.
4. Calculated and demonstrated the importance of pendular rings for imbibition within uniformly wet media.
5. Obtained the first mechanistic model of capillary controlled displacement in a fractionally wet medium.
6. Generalized Haines and Melrose criteria previously developed for uniformly wet media by solving analytically for the stability and position of menisci (fluid/fluid interfaces) within fractionally wet media.
7. Proposed a new mechanistic criterion for movement of menisci (fluid/fluid interfaces) within uniformly and fractionally wet media. The "meniscus 4<sup>th</sup> grain" criterion explains the difference between primary and secondary imbibition within water-wet media. This criterion is general enough to be applied for drainage and imbibition of fractionally wet media.

8. Developed a grain-based and mechanistic model for the simulation of capillary controlled fluid displacement process (i.e. drainage and imbibition) by analytically solving for the stability and position of menisci within the porous media. Because the calculation of interface position is entirely local (grain-based), it provides generalized criteria that applies to drainage as well as to imbibition events within fractionally and uniformly wet media. Our grain-based model is in contrast with traditional pore network models which use different *ad hoc* criteria for modeling of drainage and imbibition.
  
9. Unified drainage and imbibition algorithm by introducing concept of types of pore/throat filling events, applying to the grain-based model.

## **1.3. LITERATURE REVIEW AND METHODOLOGY**

### **1.3.1. Development of Pore-Based Network Modeling**

The motivation behind pore scale modeling is the ability to predict macroscopic properties by relating the macroscopic properties to pore level features. Leverett [126] was one of the first to link a macroscopic property of a porous medium to the pore scale properties of that medium. He unified capillary pressure curves using a single characteristic length scale (i.e. pore throat size). Although Leverett's study did not provide a pore level mechanism for capillary displacement, he hypothesized that a relationship exists between macroscopic properties and pore level events. Hence, his work was the foundation for future study on pore level petrophysics.

#### ***Bundle of tubes model***

Leverett's hypothesis became the foundation of many future studies. One such study was by Purcell [165]. He simulated the capillary displacement in the pore space by using a bundle of tubes model. He used this model to relate the permeability of the porous medium to the porosity and capillary pressure curve of that medium and analytically solved the capillary displacement in the bundle of capillary tubes. The advantage of the bundle of tube model lies in its simplicity and its analytical tractability. Hence, this model has been used to study the effect of pore level physics on the macroscopic properties by several authors [44, 46, 56, 169, 190, 192, 193, 209].

The bundle of tubes model cannot explain a number of macroscopic properties of a porous medium observed by experiment. For instance, the bundle of tubes model does not show a hysteresis between drainage and imbibition for the capillary pressure curve. Hence, the bundle of tubes model failed to capture geometrical and physical features of a real porous medium. The major weakness of the bundle of tubes model is the lack of

interconnectivity between tubes (the pore space). In spite of this weakness, the bundle of tubes model had a huge impact on pore scale modeling as this model was the first to connect capillary displacement at the pore level to the macroscopic properties of a porous medium.

To overcome this weakness, Fatt [67] constructed a network of tubes which interconnected. In Fatt's network model [67-69], each tube represents a bond or a pore throat and the junction of tubes (node) represents a site or a pore body. Although Fatt's network model did not capture all geometrical and physical features of a real porous medium, his work built a foundation for network models that were used in studies of numerous phenomena, such as interfacial area, dispersion, electrical properties, dynamic effect of multiphase flow, non-Darcy flow behavior, relative permeability, and three phase flow [6, 32, 48, 56, 71, 73, 93, 104, 132-136, 145, 166, 167, 189, 210, 211, 216]. Fatt identified several weaknesses in his network model. For instance, he stated that in his model the pore is either filled with the wetting or non-wetting fluid, whereas in a real porous media, two phases can co-exist in a pore during two phase flow through the porous medium. Moreover, Fatt selected regular networks for his study although he stated that "the photometric graphs of sandstone thin section shows the pores are connected in an irregular network"[67].

### ***Site and bond percolation***

Fatt computed numerically the macroscopic properties of a porous medium by simulating the pore level events. As a result, the choice of regular and small networks was due to the limitation of numerical computation ability at that time (1957). To overcome this limitation many authors used percolation theory to upscale the transport phenomena from pore scales to core scales. Percolation theory was first introduced in 1941-3 as an analytical tool to describe solution gel transition in polymer solutions [76,



186]. In 1957, Broadbent and Hammersley used percolation theory to describe the transport phenomena in randomly disordered media [33, 34]. Later, Larson [116] introduced the percolation theory to flow in porous media. The percolation theory applied to the network of bonds (pore throats) and sites (pore bodies). Berkowitz and Balberg [22] gave an excellent review on the application of percolation theory in modeling of fluid flow through porous media.

Although the ability to find analytical solutions using percolation theory allowed researchers [49, 97-99, 103, 105, 114, 115, 117, 119, 129, 170, 171] to apply this theory to large network models and resolve one of limitation of Fatt's network model, still percolation theory could not be applied to an irregular network model. More importantly, in the percolation theory, no spatial correlation exists between bonds or sites within the network model.

### ***Invasion percolation***

The application of percolation theory in transport through porous media concerns the displacement of one fluid by another in a porous medium. However, percolation theory fails to take in to account the essence of the two phase flow through porous media. In a porous medium, the invading fluid only occupies pores that are connected to the inlet of the porous medium. Yet, traditional percolation theory cannot differentiate between a pore connected to inlet and a pore disconnected from inlet: the criterion for invading or occupying a pore is purely stochastic.

A new version of percolation called invasion percolation was introduced to resolve the lack of influence of neighboring pores in percolation theory. The invasion percolation initially was introduced to account for the dynamic properties of fluid flow through porous media [220].

The general idea of invasion percolation is the same idea behind Fatt's network model: Pores that are connected to the inlet through previously invaded pores are the only candidates for subsequent invasion, and the invading fluid can occupy a pore if that pore is connected to outlet through defending fluid. Hence the algorithm for invasion percolation can be solved only by numerical solution. The advancement of numerical computation ability has allowed researchers to use invasion percolation method to study dynamic or capillary controlled displacement within porous media [49, 62, 83, 120, 122-125, 220]. In our study, we also adopt the invasion percolation approach to model the two phase flow through a porous medium.

#### ***Development of triangular shape pore***

In Fatt's network model, a pore or a pore throat is represented by a circular tube. Hence fluids cannot co-exist in a pore during multiphase flow through the porous medium. To overcome this weakness, tubes with angular cross sections can be used in the network model rather than circular tubes. This improvement allows simultaneous flow of more than one fluid in a tube (i.e. pore throat or pore body). For instance, the wetting fluid can flow in the corner, while the non-wetting fluid occupies the central portion of the tube. Initially, Singhal and Somerton [182] solved numerically for two phase flow through a tube with triangular cross-sections. Later on, tubes with angular cross-sections used in the study of the trapping of the oil phase and the study of flow through two dimensional media [12, 13, 118, 121]. The capability of two phase flow in a tube with single angular cross-section results in massive use of this configuration as an idealized pore throat in pore network models [3-5, 26, 28, 100, 158-162, 187, 188, 205-208].

The usage of traditional pore network model with idealized pore throats and pore bodies reduces the problem of 3D fluid flow in pore space to 2D fluid flow through tubes. The benefit of using idealized pore shape is the simplicity of fluid flow calculation in

tubes compared to calculation of 3D fluid flow in pore space. One of the disadvantages of the traditional pore network model is its need to divide pore space to network of idealized pores and throats. The pore space in a sedimentary rock is simply space where grains do not exist. It can be difficult to define which part of pore space is a pore and which part of pore space is a throat. In addition, to convert the pore space into the idealized pore throats and pore bodies, the geometry of grains is sacrificed.

### **1.3.2. Development of Direct Simulations**

Instead of network modeling, other approaches have been used to simulate fluid flow on the pore scale. The Stokes equations are a set of partial differential equation (PDE) which characterizes Newtonian fluid flow given the correct boundary conditions. The fluid flow within porous media can be simulated by solving the PDE (Stokes equation) within digitized image of the pore space extracted from image of the porous medium [1, 137]. Either finite element or finite difference methods can be used to solve the Stokes equation. But the use of finite element or finite difference method in highly complicated geometry inside a porous medium is hard. A relatively simpler approach is use of lattice Boltzmann method [91] to solve the Stokes equation. With the increase in numerical computation powers, lattice Boltzmann method recently become popular for simulation of single and multiphase flow within porous media [50, 84, 137, 152, 157, 212]. However, this approach is still computationally expensive and in practice it can simulate fluid flow within of order 1000 pores (e.g. a porous medium with dimension much less than millimeter). The clear advantage of lattice Boltzmann method over pore network modeling is its independence from dividing the pore space into idealized pore bodies and pore throats. In direct simulation methods, there is no need to transform pore space to the network of pores and pore throats.

### 1.3.3. Extracting Pore Structure from Real Sediments

For both direct simulation method and pore network method, a three dimensional description of the pore space is necessary. In direct simulation method the flow equation will be solve directly for the pore space and in pore network method, a network of pores and throats will be extracted from the pore space. Several authors [2, 21, 25, 101, 102, 127, 128, 201, 214, 221] have used statistical information to generate the 3D image of pore space. The statistical information (i.e. porosity and two-point correlation function) can be measured from 2D thin-sections. The 3D image of pore obtained from this approach has the same statistical properties as thin-sections. The advantage of this approach is its ability to build wide varieties of porous media. Biswal *et al.* [24] compared the properties of pore structure derived from statistical approach using thin-section obtains from Fontainebleau sandstone with properties of pore space obtained from microtomography of that sandstone. They find that the statistical approach cannot capture the long-range connectivity imposed by the geological processes that formed the porous media. Consequently, the pore space created by this approach has a different long-range connectivity than the corresponding porous media.

The other method for mapping the pore structure is using 3D imaging techniques such as nuclear magnetic resonance [109] or X-Ray microtomography [7, 54, 55, 64, 75, 130, 131, 176]. The advantage of these methods are their ability to give the image of pore space and map the pore structure directly from real porous media, independent of statistical interpretation. As a result, several authors use this method to study the fluid flow within a porous material [8, 164, 174, 175, 203, 218, 219]. The disadvantage of this method is its expensive and laborious procedure for acquiring the image of porous media. A real porous medium (e.g. core) must be available in order to extract the pore space image out of it. Obtaining cores from the subsurface is hard and expensive. In addition,

this method is not general in that the pore space extracted from image of a real porous medium is only specific to that porous medium.

In summary, in all of the above approaches, the map of pore space is obtained from either laborious experimental measurement (e.g. imaging technique) or statistical information gathered from a real porous medium. In the former case, the approach is expensive and specific to the medium that the image was taken from. In the latter case, the computer generated porous medium only represents the real porous medium in some statistical parameters.

The fluid flow within these pore spaces is simulated either by direct simulation method or by using network of idealized pores and pore throats. The former approach is computationally expensive and currently can apply to very small porous medium. The latter approach uses several *ad hoc* parameters which should be defined before the simulation.

#### **1.3.4. Development of Grain-Based Network Modeling**

A different approach is the grain-based model. A *physically representative network* model of a porous medium can be built based on the geological process by which the sedimentary rock was made. The analytical solution for the stable interface locations within pore space of that medium can be calculated. In the grain-based model, the fluid flow (i.e. movement of interface) is simulated based on analytical solution for the stable position of interface on the grains. As a result, this model is independent of the approach of dividing pore space into the pore bodies and pore throats. Consequently, the network of pores and pore throats is an intermediate tool and the fluid flow simulation depends only on the geometry of the grains.

Considering a random packing of equal spheres as a model of sediment was suggested first by Slichter [184] in 1899 and later by Hackett and Strettan [86] in 1928.

Spheres within a random packing of equal spheres simplify the geometry of grains within a real sediment, but the random packing of equal spheres captures many of the essential features of a real sediment (e.g. pore structure, pore connectivity). Although a random sphere pack is a simplified version of the real sediment, still it has complex geometry. Consequently, it was not used as a quantitative grain-scale model until 1971 when Mason [141] used a random packing of equal sphere as a model of a packed bed of particles. He extracted pores and pore throats from the pore space of this packing and quantified their sizes. The coordinates of the centers of the spheres within this packing were measured by Finney [72].

### ***Finney pack***

Finney constructed a spherical conglomerate of about 8000 equal size spheres. He determined geometry of grain space in his packing by measuring the spatial locations of spheres within the packing. These data allow a complete analytical description of both pore and grain space. This description provides the boundary conditions needed to calculate many macroscopic properties and transport coefficients of engineering interest [38, 194]. The *Finney pack* is often used as a form of validation for computer generated mono-dispersed spheres packing [47, 51, 138, 168].

### ***Computer generated spheres packing***

There are two main algorithms for generating a sphere pack by computers: 1. Sequential addition algorithm [168, 185, 213]. 2. Cooperative rearrangement algorithm [53, 138]. The former approach is based on the packing of spheres under influence of gravity force and it tends to create loose sphere packs. The latter approach distributes the centers of spheres randomly within the packing and allows the radii of spheres to vary in order to create denser sphere packs. If the growth of spheres causes overlaps between

spheres, the overlaps will be removed by moving the spheres or shrinking the spheres. The computer generated sphere packs can be mono dispersed or random packing of spherical particles with different sizes [168, 179]. The computer generated packing also can be a pack of non-spherical particles [106].

Oren and Bakke and co-workers [15, 24, 155, 156] developed a reconstruction algorithm to generate a packing of spheres of different size. They compute the grain size distribution from analysis of the thin-section of real sediment rock.

#### *Network models extracted from a random sphere pack*

Mellor [143] used Delaunay tessellation of the sphere centers in order to subdivide the pore space within *Finney pack* to network of pore bodies and pore throats. The extraction of a *physically representative* network model from a random spheres pack (*Finney pack*) gives an excellent tool to researchers to study fluid flow properties within the porous medium. The next major advance came with work of Bryant and co-workers [36-38, 42] who used *Finney packs* and simulated the geological process that form the real sedimentary rocks (e.g. cementation and compaction) to model broader groups of porous media. They showed that in contrast with traditional network models, a *physically representative* network model extracted from a real porous medium (*Finney pack*) has pore scale correlation of geometric features, and this correlation affects transport properties. They also simulate single phase flow within the porous media and predict the permeability of model rocks. The predicted permeability of rock models have good agreement with measured permeability of sandstone.

Several other authors developed pore network models for uniformly wet porous media based on the grain geometry and location [39-41, 79-81, 140]. Bryant and Johnson [41] simulate drainage processes which allow trapping of wetting phase in the uniformly wet porous media. They concluded the Haines criterion and relatively simple, local

evaluation of trapping can yield physically representative wetting phase configuration. Gladkikh and Bryant [80] modeled imbibition for uniformly wet porous media in new way. For first time, they used dynamic criterion for the imbibition of a single pore originally suggested by Melrose [144]. Their pore network model is based directly on the location and geometry of the grains that construct the porous media. Their prediction of macroscopic properties is consistent with experimental data presented in the literature. The successful predications of fluid flow properties of the uniformly wet rock by using *physically representative* network model encourage us to extend the use of this approach to study the fluid flow within heterogeneously wet rocks.

Toumelin [195] used a realistic pore network model extracted from *Finney pack* to predict macroscopic properties of a saturated rock with various wetting condition (e.g. heterogeneously wet rocks). However, the fluid configuration in his model is based on heuristic arguments rather than actual calculations. He showed the effects of the wetting condition on the macroscopic properties (e.g. NMR response, Electromagnetic Measurement)

#### **1.4. WETTABILITY**

In a sedimentary rock containing immiscible fluids, the grains are wetted by the fluid that has smaller energy of interaction with the grain surfaces [63]. Wettability of porous media is the subject of wide investigation as the water distribution in the pore space will vary with the wettability and thus alter the transport and availability of the water and the other phases co-existing in the pore space [10, 11]. Fluid distribution at the pore scale is important because this affects the macroscopic porous medium/fluid properties such as capillary pressure curves and relative permeability curves.

Many minerals within sedimentary rocks have a tendency to be wetted by water, but if there is a layer of organic matter (e.g. asphaltene, carboxylic acids, and humic



acids) on the grain surface, the grain surface can become water-repellent [10, 11, 61, 163]. In addition, some porous media (e.g. soils) can be a mixture of organic and inorganic material. The wettability of organic matter ranges from neutral-wet to water-repellent [60, 66, 202]. Schematically we can understand the difference between a water-wet and water-repellent grain by looking at the interfacial tensions between the solid, liquid, and gas phases on a flat surface. Fig. 1.1 depicts a freshly cleaved mineral surface, which is a high energy surface due to the ionic bonds that were broken [59]. The interfacial tension between the freshly cleaved mineral surface and air ( $\sigma_{AS}$ ) is very large (approximately 1000 mN/m, exact numbers are difficult when dealing with interfacial tensions between solids and fluids). With water being polar, the interfacial tension between water and solid ( $\sigma_{WS}$ ) is much less than both  $\sigma_{AS}$  and  $\sigma_{WA}$  (the surface tension of water). Using the balance of forces at the contact line to obtain Young's relation shows that the water phase either spreads or has a very low contact angle with mineral surfaces in the presence of air (Fig. 1.1a) or (Fig. 1.1b) oil.

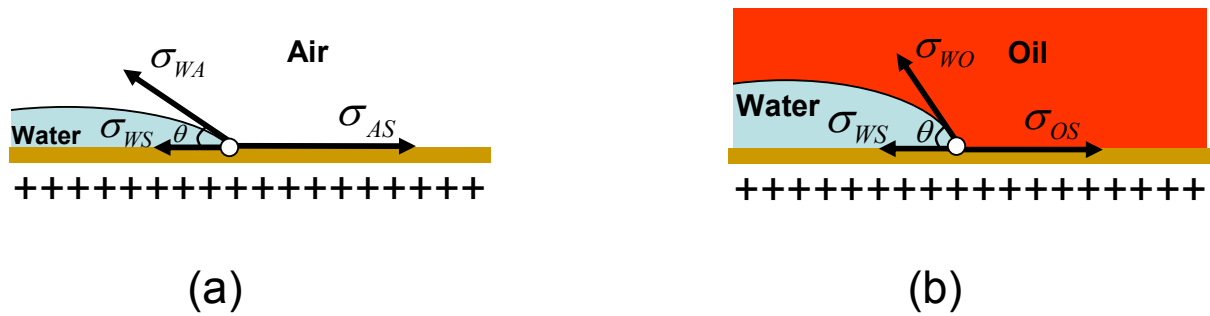


Figure 1.1. (a) Schematic of the water droplet on the freshly cleaved mineral surface in the presence of air. (b) Schematic of the water droplet on the freshly cleaved mineral surface in the presence of the oil phase.

When the grain surface gets contaminated by organic matter, or if the grain consists entirely of organic matter, the surface is then non-polar or low energy, with only van der Waals forces between the surface molecules. This simplest way to envision this

surface is that it is covered by a thin solid layer of non-polar molecules, or equivalently, it is covered by a solid layer of oil (Fig. 1.2). Fig. 1.2a and 1.2b show the force balance and the contact angles measured through the water phase for the water in presence of air (Fig. 1.2a) and oil (Fig. 1.2b).

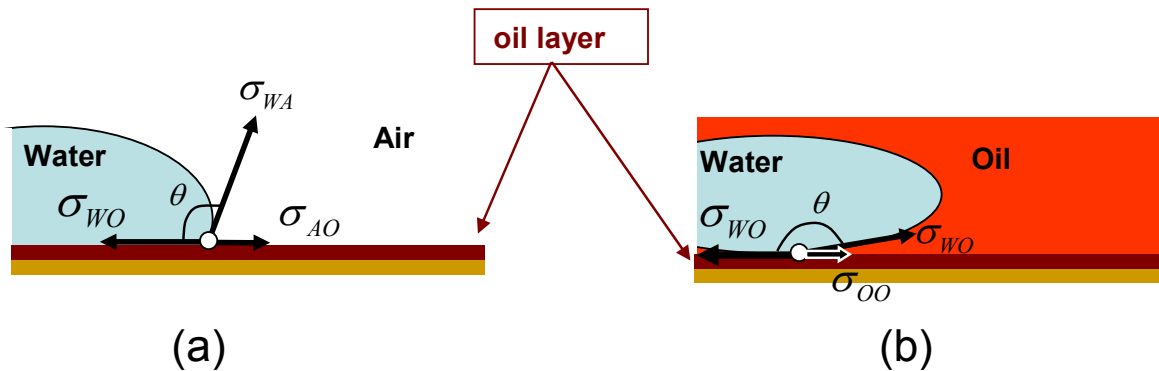


Figure 1.2. (a) Schematic of the water droplet on the oil layer surface in the presence of air. (b) Schematic of the water droplet on the oil layer surface in the presence of the oil phase.

From these simple descriptions, the contact angles for the different surfaces and fluid pairs are estimated in Table 1.1. Basically, mineral surfaces are water-wet in the presence of oil or air. The water-repellent surfaces are neutral-wet (or slightly gas wet) in the presence of air and they are oil-wet in the presence of oil. The contact angles are only rough estimates, surface roughness and pinning of the contact line will lead to contact angle hysteresis especially for contact angles near  $90^\circ$  [148]. Thus for simplicity we will call the water-repellent surfaces oil-wet.

Table 1. 1. Estimated value of interfacial tension and contact angle between, solid surface, oil layer surface, water phase, oil phase and air.

Contact angle (degree)	Interfacial tension (mN/m)	Interfacial tension (mN/m)	Interfacial tension (mN/m)	Related Fig.
$\theta \approx 0$	$\sigma_{AS} \approx 1000$	$\sigma_{WS} < \sigma_{AS}$	$\sigma_{WA} = 72$	Fig. 1.1a
$\theta \approx 0$	$\sigma_{OS} \approx 1000$	$\sigma_{WS} < \sigma_{OS}$	$\sigma_{WO} = 50$	Fig. 1.1b
$90 \leq \theta < 115$	$\sigma_{AO} \approx 20$	$\sigma_{WO} \approx 50$	$\sigma_{WA} = 72$	Fig. 1.2a
$\theta \approx 180$	$\sigma_{OO} \approx 0$	$\sigma_{WO} \approx 50$	$\sigma_{WO} = 50$	Fig. 1.2b

#### 1.4.1. Heterogeneous Wettability

Reservoirs can be partly oil-wet and partly water-wet due to wettability alteration, which occurs on the part of the reservoir rock that is exposed to the crude oil [172]. This is referred to in the literature variously as heterogeneous wettability [113], fractional wettability [200] and mixed wettability [5, 206, 209, 211]. Here, we identify two categories of heterogeneous wettability: fractional wettability and mixed wettability.

##### *Fractional wettability*

Fractionally wet porous media have been used as a model for water-repellent soil [30, 31, 204]. In terms of a soil or a porous medium, "fractionally wet" is taken to mean that each grain in the porous medium is either water-wet or oil-wet. The wettability may have a spatial structure (e.g., oil-wet grains may clump together), but for simplicity, it is usually taken that the water-wet and oil-wet grains are distributed randomly within the porous medium. This is depicted schematically in Fig. 1.3.

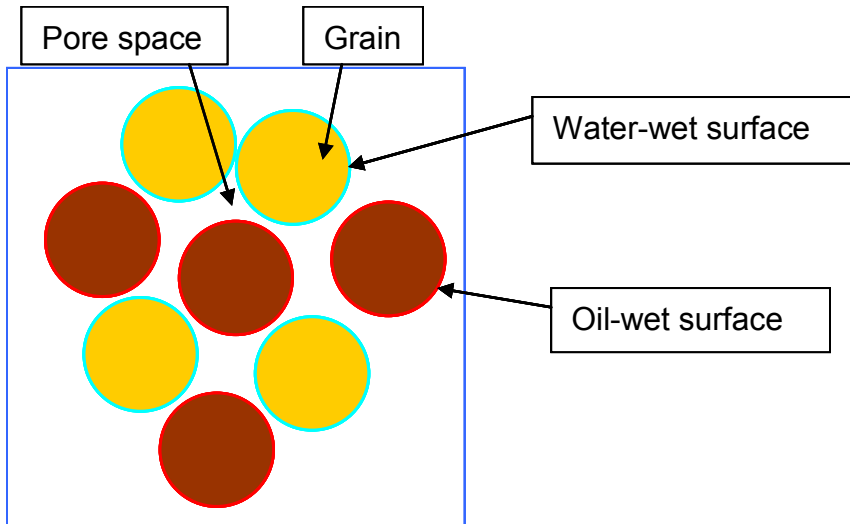


Figure 1.3. Schematic of a fractionally wet porous medium (grain level scale).

Fractionally wet porous media occur naturally in certain soils, and they are the simplest heterogeneously wet media that can be reliably reproduced experimentally. In field soils, the fractional wettability may come about as the humic acids may coat grains of different sizes and mineralogies differently. In the laboratory, fractionally wet porous media are easily prepared by mixing different fractions of oil-wet grains and water-wet grains. Because of this fractionally wet media has been the focus of most experimental measurements [19, 31, 90, 153, 178, 204].

Brown and Fatt [35] were the first to construct fractionally wet porous media. They mixed different fraction of oil-wet and water-wet sand grains to build several fractionally wet porous media. The authors showed that “wettability” of the model rock could be measured by Nuclear Magnetic Relaxation method (NMR).

In another study Fatt and Klikoff [70] investigated the effects of fractional wettability on the capillary pressure curves and relative water permeability curves. Their method involved sand packs composed of mixtures of water-wet and oil-wet (silicon-treated) sands. They mixed different “fractions” of water-wet sands with the oil-wet

sands to build several fractionally wet porous media. They concluded that porous media with different fractional wettability have different macroscopic properties.

### *Mixed wettability*

In a mixed wet porous medium, individual grains may have both water-wet and oil-wet patches. This can arise because different mineral surfaces on the grain (micas or quartz), or it may occur because different portions of a grain come into contact with the reservoir oil.

Salathiel [172] performed several experiments on mixed wet porous media. He found that rocks with mixed wettability show low residual oil saturation. He proposed a model to explain low residual oil saturation of mixed wet porous media by the mechanism of surface film drainage. He postulated pore-level configuration of oil and water phase in the mixed wet porous media. He suggested that as crude oil displaces water from initially water-wet rocks (first migration), oil displaces water from larger pores but capillary force retains water in small pores and at grain contacts as rings. The asphaltic components of the crude oil are deposited onto those rock surfaces that are in direct contact with oil, making their surfaces oil-wet. As a result, the surfaces of the grains within the small pores, which were never filled with oil, remain water-wet. Similarly, the surfaces of the grains where the pendular ring forms remain water-wet (Fig. 1.4). This mechanism of wettability alteration causes a single grain to have both water-wet and oil-wet patches. The oil-wet surfaces make continuous paths that span from pore to pore, which allow oil to be drawn along the grain surfaces by the viscous force of the waterflood. Therefore, this model explains the low residual oil saturation in the mixed wet porous media.

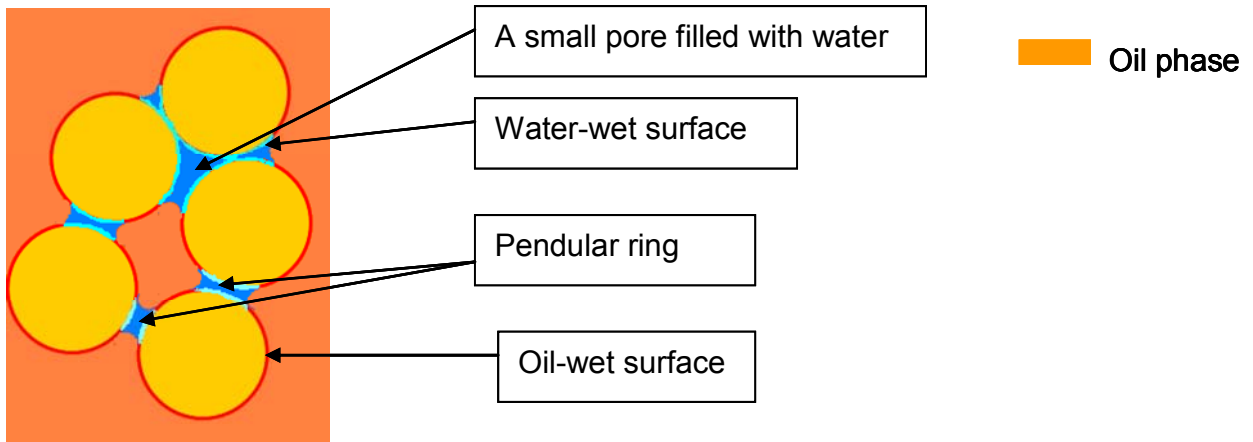


Figure 1.4. Schematic of a mixed wet porous medium (grain level scale).

Heiba *et al.* [92] studied the fluid (water and oil) distribution in the “mixed wet” porous media by applying a pore network model. They defined “mixed wet porous media” as a network of large and small pores. The large pores are oil-wet, and the small pores are water-wet. From our definition, which is based on grains rather than pores, different parts of a single pore in a mixed wet porous medium can be oil-wet or water-wet. Hence their definition of “mixed wettability” does not correspond to our definition of “mixed wettability”.

Mohanty and Salter [147] also used a pore network model to study multi-phase flow in mixed wet rocks. They described their model as “the pore space is a network of pore bodies interconnecting by pore throats”. They assumed that some of the pores and throats are water-wet and some are oil-wet, and distributed this wettability randomly. This random distribution of wetting surfaces fails to agree with the grain-based model proposed by Salathiel for mixed wettability.

McDougall and Sorbie [142] investigated waterflood performance in heterogeneously wet porous media. They modeled mixed wet rock as porous media composed of small pores (water-wet) and big pores (oil-wet). They also modeled

fractionally wet porous media by choosing certain fractions of pores water-wet and oil-wet, independent of the pore sizes. Their model also fails to represent the mixed wettability model suggested by Salathiel (1973).

Kovscek *et al.* [112] were first to propose a pore network model that represents the mixed wet porous media which was suggested by Salathiel (1973). They used a bundle of star-shaped pores with different sizes (small, intermediate, and big). They hypothesize that the grain surface of small pores, big pores, and the corners of intermediate pores remain water-wet after first oil migration, while the remainder of the surface of the intermediate pore changes to oil-wet due to rupturing of the thin water film. They suggest that oil does not enter small pores, nor the corners of big and intermediate pores. They assume that the pore wall curvature of a big pore is so small that high capillary pressure is necessary to overcome critical disjoining pressure. “The disjoining pressure is the force that tends to disjoin or separate the two interfaces. A negative disjoining pressure attracts the two interfaces [96]”. When the capillary pressure exceeds the critical disjoining pressure the thin water film ruptures. The disjoining pressure depends on the mineralogy of the rock, salinity of the brine, etc [16-18]. Hence it is difficult to quantify the disjoining pressure at which the water film will be ruptured. Therefore several authors adapted this model to more convenient pore-network-models [5, 26, 27, 159].

Blunt [26] generalized the model suggested by Kovscek *et al.* He constructed a network of pores and throats with square cross-sections. He believed that after primary drainage (oil invading to the water-wet rock), oil drains water from the center of the pores while water remains in the corner of the pores due to capillary force. The wettability alteration changes the portion of the pore walls that directly contact oil. This model allows a single pore to contain both water-wet and oil-wet patches. He randomly changed

the wettability of the surface of the center part of the pores to the oil-wet. He suggested that the oil/water contact at the surface of pore's corner is pinned until the differential pressure between water and oil is high enough to overcome the capillary force exerted from the oil-wet part of the pore. He [27] later modified his model by building a network of pores and throats with triangular cross-sections.

Piri and Blunt [159] improved the pore network model proposed by Blunt. They built a random network of pores and throats with triangular, rectangular and circular cross-sections to represent the pore space observed in the sandstone.

All above pore network models are based on the random network of pores and throats with different shape (triangular, square, circular, star-shape, etc), and have failed to incorporate grain sizes and locations. One important concept that is not considered in the above models is that "pore is the space where grains do not exist". Therefore, we base our network model on the locations of the grains instead of distributing pores and throats with the different shapes.



## **CHAPTER 2: EFFECT OF LOW WETTING PHASE SATURATION ON NON-WETTING PHASE PERMEABILITY IN A UNIFORMLY WET ROCK**

### **2.1. ABSTRACT**

Field experience in unconventional gas reservoirs indicates that well deliverability can vary dramatically, even between closely spaced wells. A possible explanation lies in laboratory experiments which show that a small increase in water saturation can decrease the gas phase permeability significantly. Conversely, drying out the water saturation during gas cycling in reservoirs or during injection of CO<sub>2</sub> into deep saline aquifers affects petrophysical properties such as absolute permeability and capillary pressure. The precipitation of salts from the evaporating brine is one contributor to these effects.

In this chapter, we use a grain-based network model to study the effect of low saturations of the wetting phase on non-wetting phase relative permeability. We also show how certain porosity-reducing processes magnify this effect. To compute phase geometry and permeability, we use a physically representative network model. The network is extracted from a model rock, built from a dense random packing of spheres modified geometrically to simulate various rock-forming processes. At low saturations (at or near the drainage endpoint) the wetting phase exists largely in the form of pendular rings held at grain contacts. Pore throats correspond to the constriction between groups of three grains, each pair of which can be in contact. Thus the existence of these pendular rings decreases the void area available for flowing non-wetting phase. Because the hydraulic conductance of the throat varies with the square of the void area, the effect on permeability is disproportionate to the volume occupied by the rings. The same approach quantifies the reduction in permeability by salt precipitation during drying.

Convention holds that connate water has little effect on oil or gas permeability because it occupies the smaller pores. Comparing predictions for unconsolidated model rocks with those for cemented model rocks allows one to reconcile this view with the sensitivity reported in the field and the laboratory.

## **2.2. INTRODUCTION**

In tight gas sandstone the productivity of a well is sometimes quite different from that of a nearby well. Wells can also be very sensitive to small amounts of water, whether from an aquifer associated with the reservoir, from hydraulic fracturing or from other completion operations. Although the effect of water saturation on the effective permeability to gas has been the subject of numerous experiments [45, 52, 111, 173, 215, 217], a fully mechanistic explanation has not yet been offered as to why the effect appears larger in tight gas reservoirs. A related phenomenon is the dehydration of near-wellbore formation during gas injection. Gas cycling in reservoirs or injection of CO<sub>2</sub> into deep saline aquifers can lead to precipitation of salts as the resident water evaporates into the dry injected gas. The precipitation can reduce the permeability of the formation and thus reduce injectivity of the well [222]. This chapter provides insight into the reduction of permeability due to drying, because the spatial distribution of precipitated salts must be related to the geometric configuration of the wetting phase. Low wetting saturation is mainly irreducible wetting phase that exists in two morphologies [41]. One is volumes of water held in the smallest pores. The other is pendular rings held at grain contacts or liquid bridges held between two grains separated by a gap. The former forces gas to flow around the filled pores, decreasing the average connectivity of the gas phase. The latter reduces the area open to gas (the non-wetting phase) as it passes through a pore

throat. It is possible to quantify the effects of these topological and geometrical changes on gas phase permeability with the methods described below.

## **2.3. METHOD**

### **2.3.1. Model of Pore Space**

The geometry of pore space in porous media is very complex, and a large number of pores must be modeled to obtain reasonable predictions of macroscopic behavior. Direct simulation of flow within pore space is now possible, but physically representative network models of pore space provide an inexpensive alternative. Bryant *et al.* [42] proposed a method for obtaining simple network models that are physically representative of clastic rocks. The approach was demonstrated with a network extracted from a model rock, built from a dense random packing of equal spheres constructed by Finney [72]. Finney determined geometry of grain space in his packing by measuring the spatial locations of several thousand spheres. These data allow a complete analytical description of both pore and grain space. This description provides the boundary conditions needed to calculate many macroscopic properties and transport coefficients of engineering interest [38, 194]. This approach has been further developed by several researchers, including Bakke and Øren [15], Jin *et al.* [107] and Al-Aroush *et al.* [9].

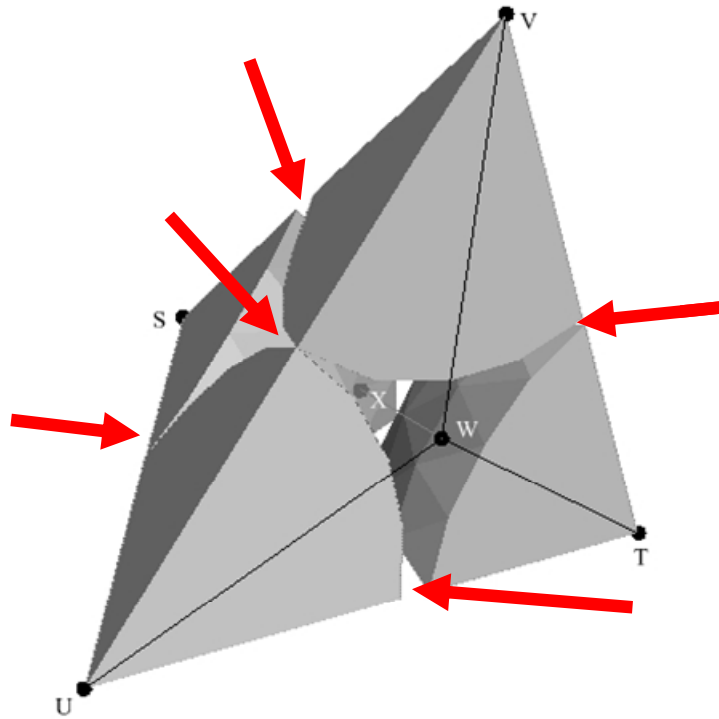


Figure 2.1. Schematic of one pore (Delaunay cell) in a model unconsolidated sediment whose center is at point X. Arrows indicate gaps and point contacts that can support liquid bridges and pendular rings of the wetting phase after the pore has drained. Point W is the center of a pore throat.

Delaunay tessellation of the sphere centers can be used to subdivide pore space by grouping four nearest sphere centers together. The tessellation yields tetrahedra, Fig. 2.1. Each face of a tetrahedron corresponds to a pore throat. The geometry of the throats is the primary control on permeability. Each edge of the tetrahedron corresponds to a grain-grain contact (if the spheres touch) or a gap between grains (if the spheres do not touch). The contacts/gaps can support pendular rings/liquid bridges of wetting phase, depending on the capillary pressure. The geometry of these rings/bridges and the geometry of the throats provide the link between low water saturations and effective permeability to the gas phase.

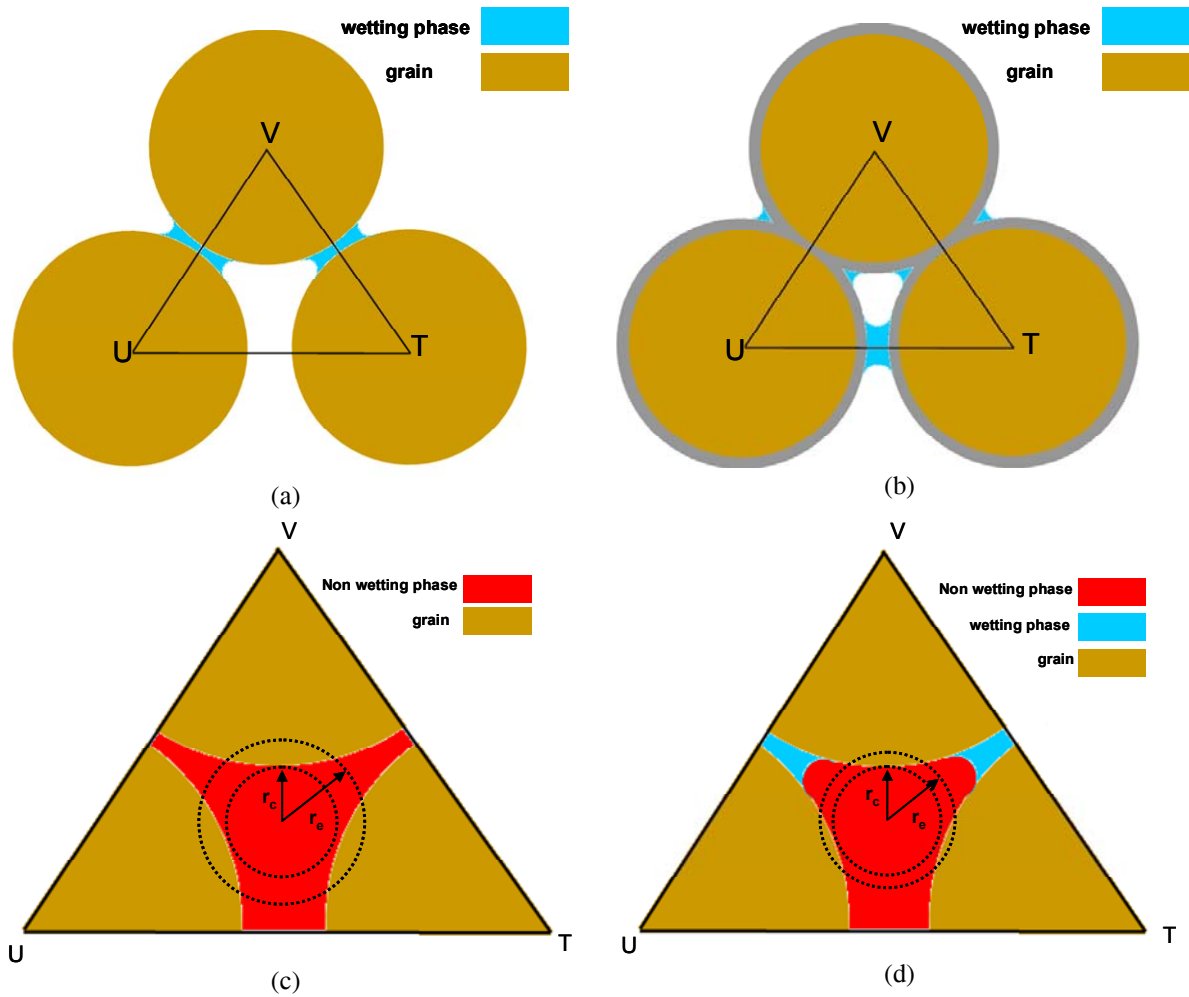


Figure 2.2. (a) Schematic of a throat UVT (Fig. 2.1) before cementation. After the throat has drained the narrow gaps support liquid bridges of the wetting phase. The other gap is too wide to support a stable liquid bridge. (b) Schematic of same throat after cementation. The isopachous cement (gray) reduces the area of the throat. The pendar rings are smaller than in (a), because a larger capillary pressure is required to drain this throat. They may nevertheless occupy a larger fraction of the throat area, which is also smaller than in (a). Moreover the third gap UT is now narrow enough to support a liquid bridge. (c) Schematic of throat shows the definition of inscribed radius,  $r_c$  and equivalent radius,  $r_e$ . (d) The presence of pendar rings and liquid bridges (blue) reduces the area open to flow of non-wetting phase (red). This reduces the equivalent radius, but in this throat the inscribed radius is not changed. Note that Fig. 2.2a and 2.2d are schematic of throat UVT before cementation. As a result, the gap UT is not narrow enough to support a liquid bridge.

This model of rock can be modified geometrically to simulate various rock-forming processes [38]. Here we consider only isopachous quartz cementation. The simplest model of this process treats the quartz cement as a coating of uniform thickness on all sediment grains. We implement this “onion-skin” model numerically by increasing the radius of each sphere in the packing, holding the centers of the spheres fixed. See Fig. 2.2b. The morphology of wetting phase held in the crevices associated with cemented grain contacts is qualitatively similar to the morphology of pendular rings in the uncemented material. For convenience we will use the terms "pendular ring" or "ring/bridge" to refer to any of these morphologies.

### 2.3.2. Terminology

In this chapter, we study the fluid displacement within uniformly wet media. Hence we define capillary pressure to be the pressure of the non-wetting phase (e.g. gas phase) minus pressure of the wetting phase (e.g. water phase).

$$P_c = P_{nw} - P_w. \quad (2.1)$$

This macroscopic capillary pressure is proportional to the curvature of the microscopic interfaces through the Young Laplace equation,

$$P_c = \sigma_{ow} \left( \frac{1}{r_1} + \frac{1}{r_2} \right) = 2C\sigma_{ow}, \quad (2.2)$$

where  $r_1$ ,  $r_2$  are radii of curvature and  $C$  is defined as the mean curvature. The curvature is essentially a scaled capillary pressure. We report the value of the curvature as dimensionless curvature by normalizing the grains radii to be unity.

### 2.3.3. Assumptions

In this chapter, we assume that grains within rock models are strongly water-wet. Hence, we take in to account the existence of the thin water films on the surface of the grains. As a result, pendular rings or liquid bridges can grow even though they are

surrounded by non-wetting phase (i.e. gas phase). We also ignore the gas compressibility and gas slippage in this chapter. We treat the gas phase as incompressible non-wetting phase.

#### **2.3.4. Method for Computing Fluid Configurations in the Pore Space**

Physically representative network models are especially useful for computing geometry of multiple fluid phases, because each network element (throat, pore body) corresponds to a particular set of grains in the porous medium. The Delaunay tessellation defines a network of pore bodies and pore throats. With this network, it is possible to simulate drainage to irreducible wetting phase saturation [41] and imbibition from a drainage endpoint [80]. In this work, for evaluating the effect of rings/liquid bridges on the effective permeability of non-wetting phase, we do not explicitly model either process. Instead, we focus upon the consequences for hydraulic conductivity when low water saturations occur as pendular rings/liquid bridges. This morphology can account for wetting saturations in the range of  $1\% < S_w < 10\%$ .

At irreducible saturation the wetting phase also occupies (fills completely) small pores isolated during drainage [41]. We briefly consider the influence of this second morphology in low porosity sandstones below. The main result is that small changes in wetting phase saturation in this morphology do not affect significantly the relative permeability of non-wetting phase. Hence we simply compute the geometry of rings/bridges for several values of curvature (equivalently, applied capillary pressure) at all contacts/gaps in the packing.

In this chapter, we do not consider the process that might lead to the presence of the rings and bridges. Many processes are possible. Different saturations might arise in different locations in a reservoir because different capillary pressures prevailed when gas emplacement was complete. This would correspond to different endpoints on a drainage

curve. On the other hand, small amounts of water may imbibe into part of a formation as a result of completion or production operations. This would correspond to imbibition from a drainage endpoint. Here, we simply vary the capillary pressure across a physically reasonable range, thereby causing the curvature and volume of each ring/bridge to vary. This in turn causes saturation to vary. We do not address the interesting question of whether a connected path exists through which wetting phase can move to accommodate these saturation changes (see Chapter 4). Rather, we frame the problem as follows: if changes in low wetting phase saturation occur in low permeability rocks, can they quantitatively explain disproportionately large changes in the gas phase permeability?

### 2.3.5. Method for Computing Effective Permeability of Non-Wetting Phase

The hydraulic conductance of each pore throat is computed from the geometry of the void area and the rings/bridges that obstruct the area. The geometry of throats controls the advancement of the non-wetting phase into the pore space (drainage). The wetting fluid forms pendular rings and liquid bridges after non-wetting phase pushes through a throats (Fig. 2.2a, b). The rings and bridges reduce the area available for flow of the non-wetting phase. In analogy with the Hagen-Poiseuille equation (Eq. 2.1), the hydraulic conductance of an irregularly shaped pore throat is taken to be proportional to the fourth power of the effective radius of that throat (Eq. 2.2).

$$q = \frac{\pi r_{ef}^4}{8\mu L} \Delta P, \quad (2.1)$$

$$g_{hydr} = \frac{\pi r_{ef}^4}{8\mu L}. \quad (2.2)$$

In the Eq. 2.1 and Eq. 2.2,  $q$  is the flow rate,  $\mu$  is the viscosity of displaced fluid,  $L$  is the distance between center of two neighboring pores,  $\Delta P$  is the pressure difference between two neighboring pores,  $r_{ef}$  is the effective radius of the throat that connects two neighboring pores, and  $g_{hydr}$  is hydraulic conductance of that throat.



Bryant *et al.* [42] show that the effective radius of a throat can be estimated by the average of the inscribed radius and the equivalent radius, Fig. 2.2c, d. The inscribed radius is the radius of the biggest circle that can be inscribed into the throat. The equivalent radius is the radius of circle that has the same area as the throat. Therefore the equivalent radius is proportional to square root of the throat area. The presence of pendular rings decreases the void area of throat available for non-wetting to pass through and thus decreases the hydraulic conductance.

We use the approach of Bryant and Blunt [40] and Bryant *et al.* [42] to compute permeability to the gas phase in the network. Briefly, a constant pressure drop is imposed across the phase of interest (here the non-wetting phase). We assume incompressible fluid and steady state flow. Hence, according to Kirchoff's law, net flow rate into/out of any pore is zero (Eq. 2.3).

$$\sum_{k=1}^z q_k = 0, \quad (2.3)$$

where  $z$  is the number of neighboring pores and  $q_k$  equals to

$$q_k = g_{i,NBR(i,k)} \left( P_i - P_{NBR(i,k)} \right). \quad (2.4)$$

In Eq. 2.4,  $g_{i,NBR(i,k)}$  is hydraulic conductance of the throat that connects pore  $i$  and its  $k^{th}$  neighbor pore.  $P_i$  is the pressure value in the pore  $i$  and  $P_{NBR(i,k)}$  is the pressure value in the  $k^{th}$  neighbor of pore  $i$ . Substituting Eq. 2.4 in to Eq. 2.3 leads to

$$\sum_{k=1}^z g_{i,NBR(i,k)} P_{NBR(i,k)} - \sum_{k=1}^z g_{i,NBR(i,k)} P_i = 0. \quad (2.5)$$

Eq. 2.5 can be written for all of pores within the medium which leads to a system of simultaneous equations for the pressures in each pore body. The overall flow rate is calculated from the value of pressures in pore bodies. The ratio of overall flow rate through the network to the imposed pressure drop yields permeability to the non-wetting

phase. We report this as a relative permeability by normalizing to the single-phase permeability of the model rock.

### 2.3.6. Method for Computing Geometry of Pendular Rings

The geometry of pendular rings and liquid bridges depends on the geometry of the grains supporting the ring/bridge and the curvature of the gas/water interface (Fig. 2.3). There are two approaches for calculation of the pendular ring (liquid bridge) volume and cross-sectional area: the toroid approximation and the exact nodoid calculation [74]. (See Appendix A for detail calculation of volume and cross-section area of the ring/bridge based on toroid approximation)

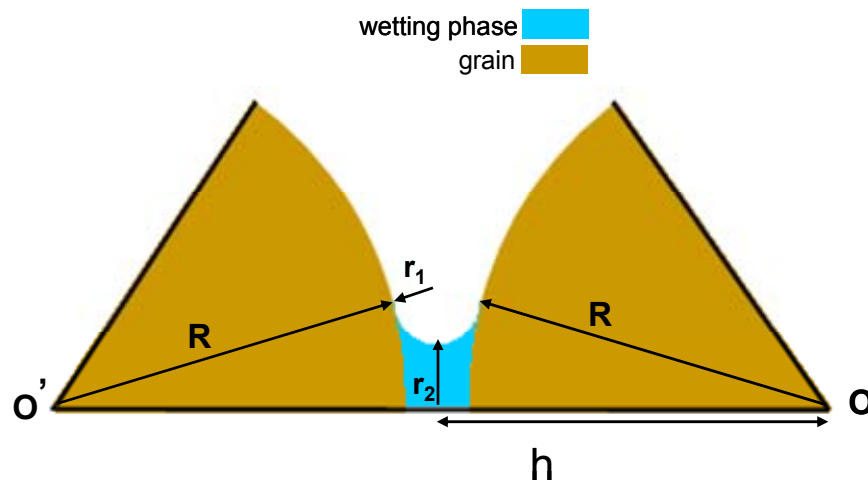


Figure 2.3. Schematic of a toroidal liquid bridge of wetting phase between two grains of radius  $R$ . The vertices  $O$  and  $O'$  correspond to the sphere centers and line  $OO'$  that joins the sphere centers is the axis of symmetry for the liquid bridge. For the toroid approximation, the surface of the liquid bridge has radii of curvature  $r_1$  and  $r_2$ . The grain centers are separated by distance  $2h$ .

In the toroid approximation, the wetting phase is a volume of revolution about line  $OO'$  joining the grain centers, with normal and tangential radii of curvature  $r_1$  and  $r_2$ , respectively. At the midpoint of the toroid the mean curvature is  $C = 1/r_1 - 1/r_2$ . The

toroid does not have constant curvature, because the tangential radius of curvature varies with distance along line  $OO'$ .

An interface controlled by capillary forces will have constant curvature everywhere, as prescribed by the Young-Laplace equation. For the case of wetting phase held between equal spheres, this condition produces a surface known as the nodoid. Gladkikh [78] shows that toroid model is a good approximation of the nodoid for calculating the properties of pendular rings relevant to our application (e.g. volume, cross section area).

## 2.4. SIMULATION

The porosity of the non-cemented Finney pack is 36%. Since we are interested in low porosity and permeability media, in our simulation we reduce porosity and permeability of the model medium by uniformly growing cement over grain spheres. For example, a cement thickness of  $0.16 R$ , where  $R$  is the radius of the Finney spheres, yields a porosity of 11%.

We start the imbibition simulation from an assumed (rather than directly simulated) drainage end point specified by a (large) value of mean curvature  $C$ . We assume that at drainage end point wetting phase exists only in the form of pendular rings and liquid bridges. At any value of applied curvature pendular rings exist at all grain contacts, but liquid bridges will be stable only at gaps narrower than a threshold that depends on the curvature. If the applied curvature exceeds the critical curvature of the gap, the liquid bridge cannot exist. The simulation proceeds by decreasing the applied curvature incrementally. The number of gaps which can support liquid bridges thus increases. In addition, the volumes of already existing pendular rings and liquid bridges increase. It is possible for the pendular rings or liquid bridges to grow big enough to

touch each other. This situation is thermodynamically unstable and coalescence of the rings/bridges will occur. This effect is important, because the coalescence corresponds to snap off (disconnection) of the non-wetting phase in the pore throat. This effect is included in the network model calculation of phase permeability by setting the throat conductivity to zero.

Fig. 2.4 shows the trend of saturation increase with mean curvature decrease for model sandstones of different porosities. For each model rock, the range of curvatures shown is significantly larger than the drainage percolation threshold. At any particular curvature value, the models with lower porosity (higher cementation) have higher volume fraction occupied by pendular rings and liquid bridges. The range of saturations is smaller than typical irreducible wetting phase saturations in cemented porous media. This is because these calculations do not include the pore-filling morphology of wetting phase [41].

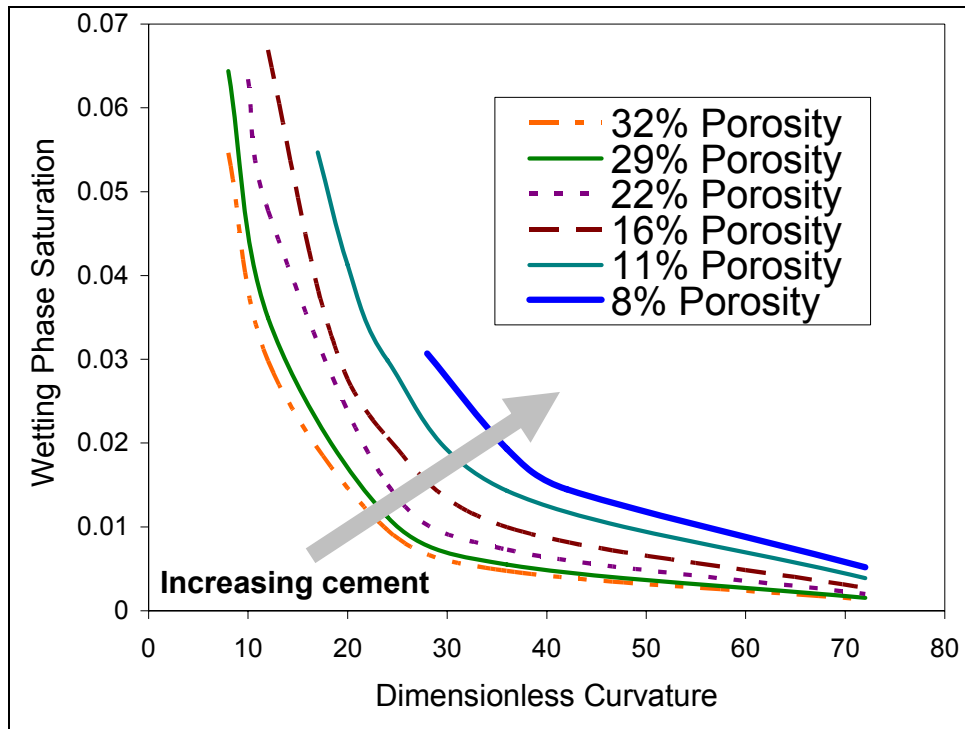


Figure 2.4. Saturation of the wetting phase (contribution from pendular rings and liquid bridges only) at different curvatures. Each curve is the result of starting at a large value of curvature (drainage endpoint) and decrementing the curvature to a value somewhat larger than the percolation threshold for drainage. This is consistent with the early stages of imbibition from the drainage endpoint, well before the percolation threshold for imbibition.

## 2.5. RESULTS AND DISCUSSION

### 2.5.1. Influence of Pore-Filling Wetting Phase on Gas Phase Permeability in Low-Porosity Rocks

In this section we justify our emphasis on the pendular ring/liquid bridge morphology for low water saturations. Conventional wisdom has long held that the wetting phase occupies smaller pores and thus at low saturations it should have relatively little effect on non-wetting phase permeability. In the low porosity model sandstones

described above, the effect of wetting phase in pores is indeed small. Moreover, as shown in this section, the effect in these model rocks is smaller than the effect in moderate to high porosity model rocks. This counterintuitive conclusion is the consequence of the broader throat size distribution, which extends to much smaller pores, in the lower porosity rocks. Consequently any wetting liquid that fills pores is much more likely to occupy small pores which are accessed by very small throats. These small throats contribute very little to overall permeability. (In the calculations presented in this section, rings and bridges do not contribute to the saturation nor do they affect the gas phase permeability. Though not possible to arrange in nature, studying this situation in a model provides useful insight.)

In our perfectly sorted model rocks with moderate to high porosity (greater than 20%), there is a distinct lower limit in the throat size distribution, corresponding to the throat defined by three initially touching grains around which cement has grown. This lower limit is apparent for the moderate porosity sample in Fig. 2.5 and 2.6. In the low porosity model rock, the distribution of throat sizes extends much more broadly, including a significant fraction of closed throats (Fig. 2.5 and 2.6). In both samples, the smallest pore throats correspond to the smallest pores. In high porosity rocks, however, the smallest pore throats are not so much smaller than the average throat size (about one third the average throat size in the 22% porosity model rock, Fig. 2.5 and 2.6). Thus when these throats are drained, their addition to the connected paths open for flow of gas makes a small but measurable contribution to the gas phase relative permeability, Fig. 2.7. Conversely, removing these throats when water imbibes into the smallest pores reduces the overall permeability of the gas phase by a small but noticeable amount.

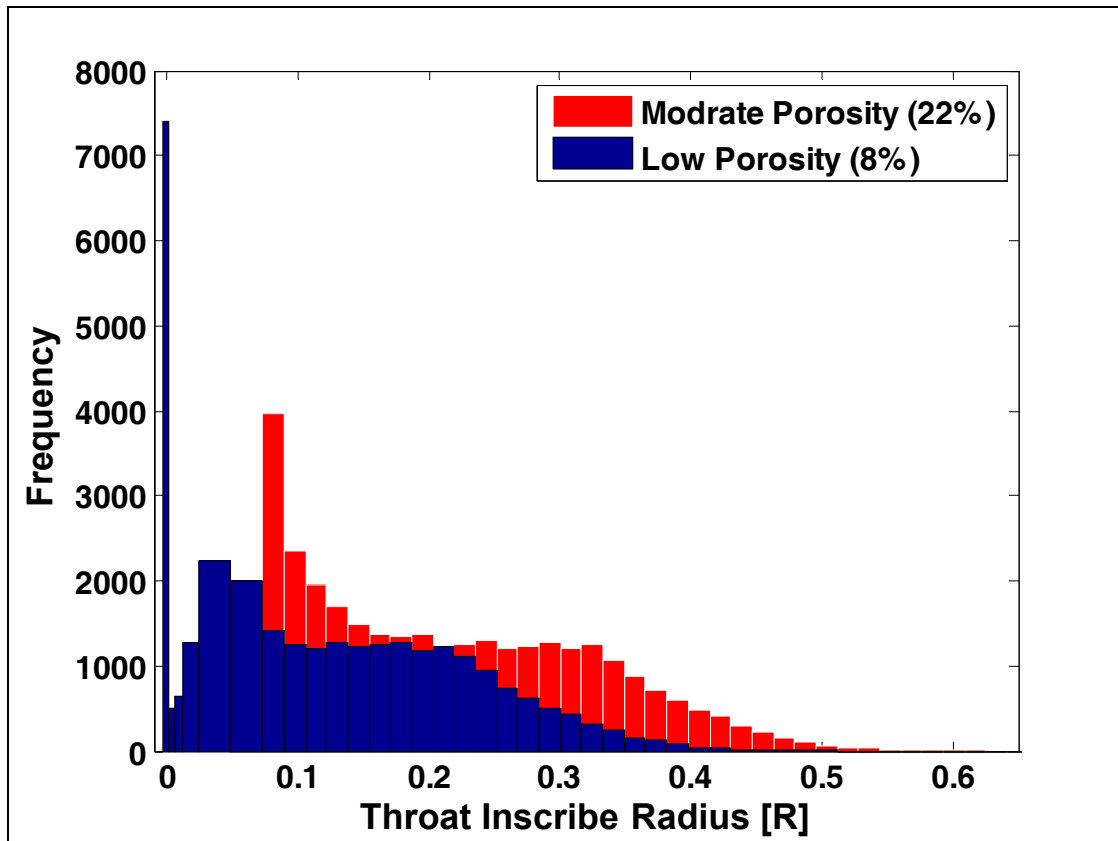


Figure 2.5. Throat size distribution for model rocks of low porosity ( $\phi=8\%$ ) and moderate porosity ( $\phi=22\%$ ). The peak in the low porosity rock at zero radii corresponds to throats closed by cementation. Average throat inscribed radius for high porosity is  $0.214 R$  and for low porosity (excluding closed throats) is  $0.143 R$ . The radius of the spheres of the model sediment (before cement) is  $R$ . Approximately 23% of originally open throats are closed in the low porosity model rock due to overgrowth cementation.

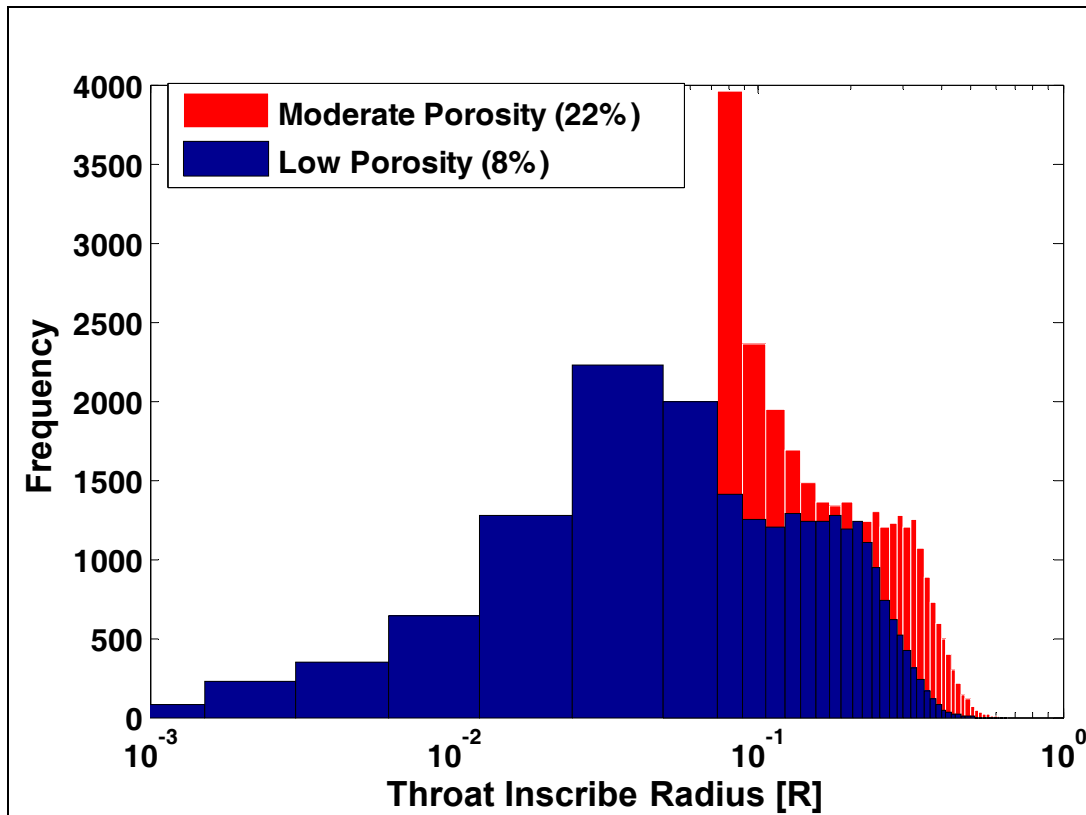


Figure 2.6. Same distribution of throat sizes as Fig. 2.5, excluding throats closed by cement in the low porosity sample. The log scale shows that the distribution is much broader in the more heavily cemented sample.

In low porosity rock at low wetting saturation the situation is different. The wetting phase occupies pores accessed through throats much smaller than average: the smallest open throats are one to two orders of magnitude smaller than average throat size in the 8% porosity model rock. Consequently draining these pores has much smaller effect on gas phase permeability than drainage at the corresponding saturation in the higher porosity model rocks. For the same reason, imbibition of water into these pores and occupation of the associated throats does not reduce effective gas phase permeability very much. From this discussion we conclude that the sensitivity of the effective gas permeability to the water saturation reported in the literature cannot be explained by



investigation of the pore-filling morphology of wetting phase. Hence our hypothesis is that the sensitivity of the effective gas permeability is due to the effect of geometry of pendular rings/liquid bridges on the gas permeability.

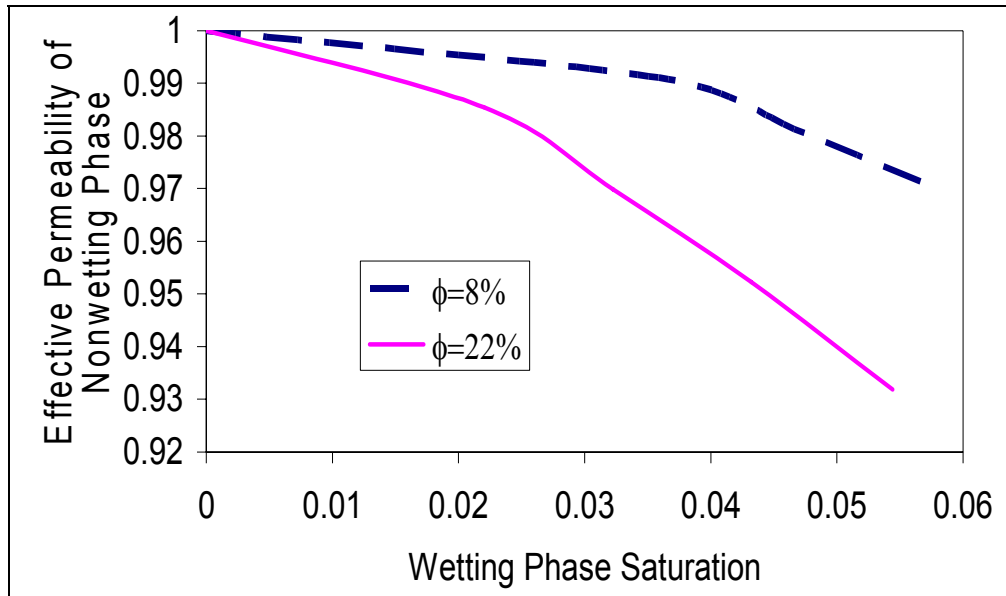


Figure 2.7. The reduction of effective gas permeability due to low water saturation occupying pores in the two model rocks. Filling pores with water has notably less effect on gas permeability in the low porosity rock. This permeability calculation does not account for pendular rings or liquid bridges.

The calculation of effective permeability presented in Fig. 2.7 is done at drainage end point, considering only the effect of pores filled with water phase. That is, the effect of pendular rings and liquid bridges that we discuss below is deliberately excluded from these calculations.

### 2.5.2. Influence of Pendular Rings and Liquid Bridges on Gas Phase Permeability in Low-Porosity Rocks

Fig. 2.8 shows the trend of gas phase relative permeability as a function of water saturation for model rocks with different porosities. For porous media of porosity 29%

and higher, the trend is the same: the effective permeability to gas decreases linearly as saturation increases, and the trends have the same slope. A model rock with 22% porosity also follows this trend until saturation 0.04, at which point it exhibits a somewhat faster decrease in effective permeability. The model rock cemented to 16% porosity shows the same qualitative behavior as the sample with 22% porosity, but the saturation at which the slope changes is 0.01 (see also Fig. 2.9). With further porosity decrease, the trends show steeper slopes across the entire saturation range in Fig. 2.8. The smaller the porosity, the steeper the slope.

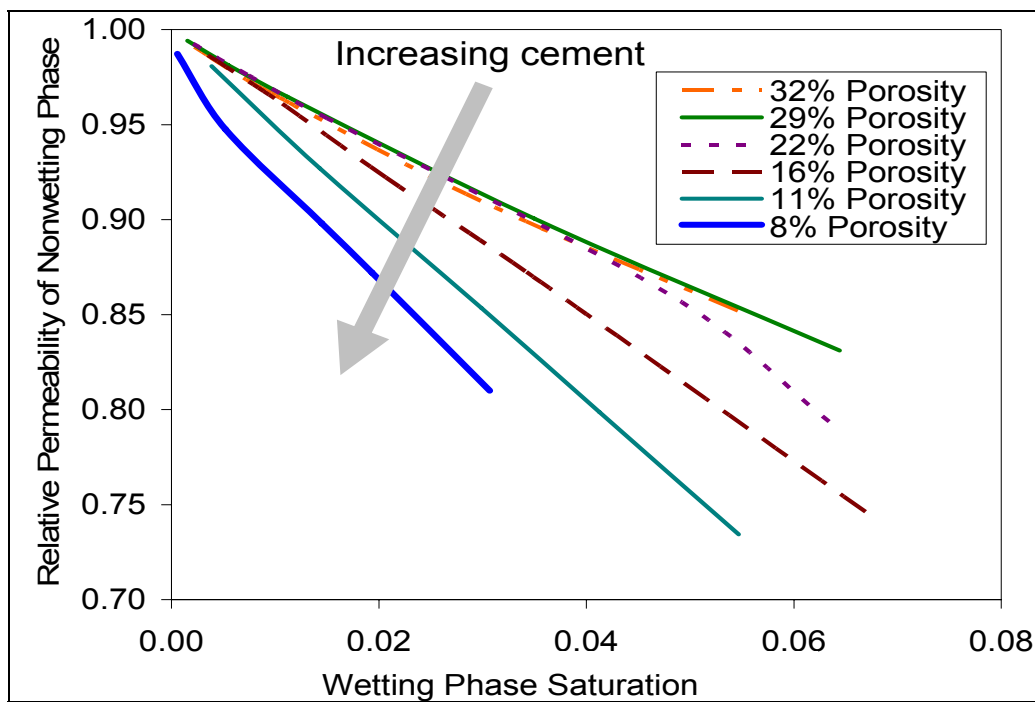


Figure 2.8. Effective gas (non-wetting) phase permeability vs. water (wetting) phase saturation. The saturation consists entirely of pendular rings and liquid bridges. The effect of the saturation is more pronounced for model rocks with smaller porosities. The narrow range of saturations is physically consistent with the restriction to rings/bridges.

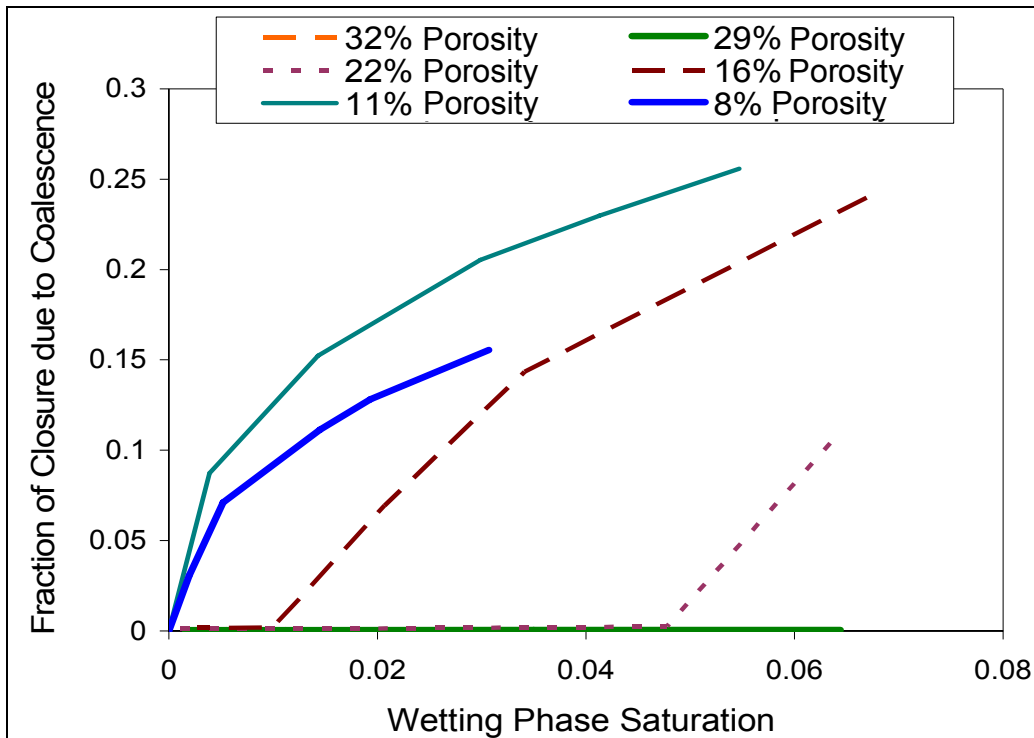


Figure 2.9. Coalescence fraction (number of throats closed by coalescence at corresponding wetting saturation divided by total number of open throats in the absence of wetting phase) versus wetting saturation for model rocks of different porosities. Coalescence does not occur in this range of saturations for the high porosity model rocks (29%, 32%), so these curves coincide with the saturation axis. The smaller the porosity, the sooner coalescence starts as the water saturation increases from zero (except in the sample with 8% porosity). Consequently the gas phase connectivity decreases sooner with a small influx of water in the low porosity model rocks.

These differences are the consequence of two simultaneous phenomena: growth of the rings/bridges as curvature decreases, and coalescence when neighboring rings/bridges come into contact. The thickness of cementation overgrowth for media with porosity above 29% is quite small, thus in these samples the dominant phenomenon that affects the non-wetting phase permeability is growth of the rings. In fact, the imbibition percolation threshold is reached in these model rocks before any coalescence occurs [80]. With increased cementation (lower porosity), grain contacts grow closer together, and

rings can coalesce at a higher curvature. With heavily cemented media (porosity 11% or less), a significant fraction of throats are closed to gas flow by coalescence. This is shown in Fig. 2.9. Note that the saturation at which coalescence starts for samples of intermediate porosities corresponds to the saturation at which the slope changes in Fig. 2.8.

Consequently, at small porosities, an increase in wetting phase saturation has two effects on gas permeability. It reduces the cross-sectional area available for gas flow in open throats (Fig. 2.2c, d), and it increases the number of throats completely blocked to gas flow. The cross-sectional area reduction affects the conductivity of both large throats and small throats, and therefore it reduces the overall hydraulic conductivity of the porous medium. The blockage of small throats by wetting phase reduces the connectivity of the porous medium. It is true that low water saturation is able to close only small throats, not large throats. But the large throats do not percolate in low porosity media. That is, a connected flow path for the gas phase involves a significant fraction of small throats. Hence, the blockage of small throats reduces the connectivity of adjacent pores and consequently makes the percolated path for gas flow appreciably more tortuous. Hence, in the low porosity media, the connectivity reduction, reducing effective gas permeability more significantly than in high porosity media.

Fig. 2.8 suggests that the contribution of connectivity reduction is comparable in magnitude to the contribution of conductivity reduction. The slope of the  $k_{rg}$  vs.  $S_w$  curves changes as the contribution of throat disconnection increases, i.e. as porosity decreases or as  $S_w$  increases at moderate porosity. The change in slope is not extreme, so neither contribution dominates.

## 2.6. MODEL VALIDATION

### 2.6.1. Comparison with Experimental Data for Tight Gas Sands

Measurements of effective permeability to gas at low water saturation (less than 0.05) are sparse. Nevertheless the model predictions provide insight into the reported trends. Ward and Morrow [217] plot effective permeability versus water saturation for tight sandstones (Fig. 2.10). Their plot is compiled from several sources and includes differences in permeability, porosities and applied confining pressure.

We observe two different trends for the experimental data. For small confining pressure, the effective permeability decreases with slope of -0.5 at low water saturation (see blue curve interpolation on Fig. 2.10). At large confining pressure, the slope is steeper, about -2, the black curve on Fig. 2.10. We have included slopes from our simulation for comparison. The red line (slope -5) is the prediction for the model rock of 8% porosity when only pendular rings/liquid bridges affect saturation and gas permeability. The green line is the trend when only pores filled with water affect saturation and gas permeability.

The model is qualitatively consistent with the data, in that it bounds the observed sensitivity of the gas phase permeability to low water saturation. Quantitatively, the predicted trend for rings/bridges is considerably stronger than observed, while the trend for filled pores is weaker than observed.

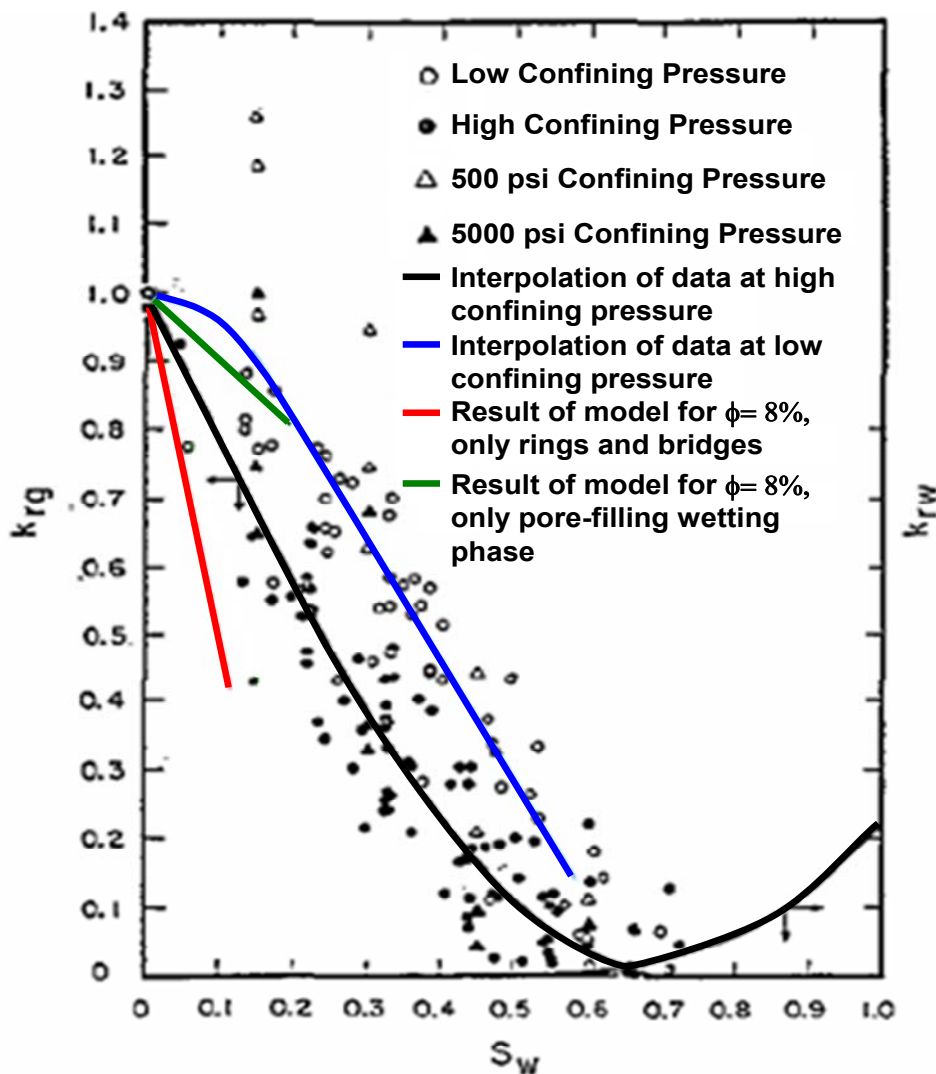


Figure 2.10. Gas effective permeability for tight sandstones: experimental data [217] and trends of model predictions. Confining pressure increases the sensitivity of effective gas permeability to low water saturations. If water saturation increases exclusively by changing the number and size of pendular rings/liquid bridges (no pore-filling), the gas permeability (red line) decreases faster than observed. If water saturation increases exclusively by pore filling (no rings/bridges), the gas permeability decreases more slowly than observed. Rings and bridges are thus the main mechanism for water sensitivity at low saturations.

We also validate our simulation result with experimental data gathered by Shanley *et al.* [177]. Relative gas permeability was measured in low permeability rocks at *insitu* overburden pressure (Fig. 2.11). While the scatter in the data is large, the trend falls between the limits predicted by the rings/bridges-only model and the filled-pores-only model.

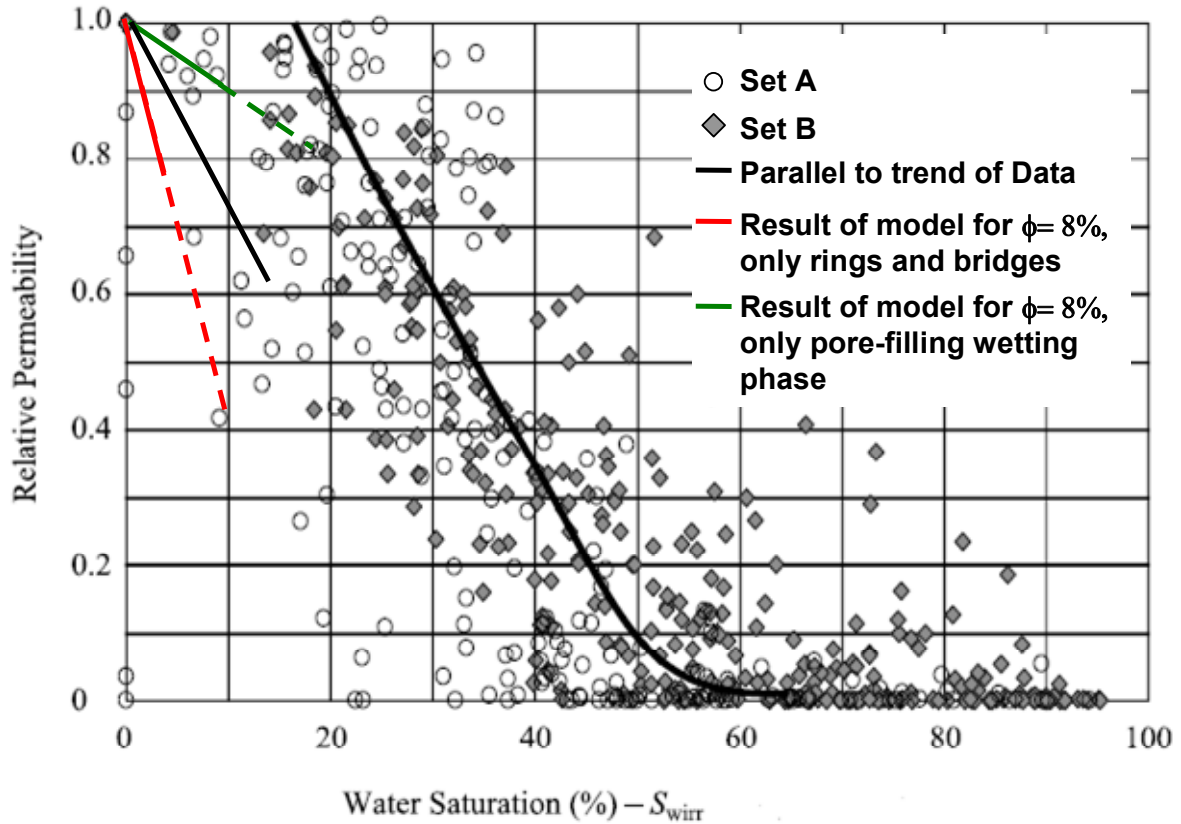


Figure 2.11. Experimental data [177] for gas effective permeability for low permeability rock. This graph has two data sets: gas relative permeability measured at irreducible water saturation at the overburden pressure (set A) and the gas relative permeability at 4000 psi confining pressure (set B). The trends and conclusions discussed in Fig. 8 are applicable to this data set as well.

While both experimental data and simulation result for rings/bridges-only model show similar trend, the slopes are different. The simulation result shows greater sensitivity than is typically observed. This is consistent with three idealizations in the

model. First, some throat shapes may occur in real rocks which are not represented in our model. Our model accounts only for throat area reduction with one possible throat shape (Fig. 2.2b). Real rocks have varied throat shapes and some of them can be effectively closed by applying high confining pressure. One of such shapes is slit shape shown on Fig. 2.12, which may arise when extensive isopachous cementation occurs. Cement rims growing toward each other with different orientations form a rough aperture held open by asperities. When small confining stress is applied, the two thin gaps between the top sphere and the lower spheres will be open. At low wetting phase saturations, some of the wetting phase will be contained in these slots. However, the effect of that volume of wetting phase on gas phase permeability will be small, because little gas would flow through the slots even when completely dry. At larger stresses, the slots may close. At low  $S_w$ , a greater fraction of wetting phase will be in pendular rings and liquid bridges, leading to greater effect on permeability per unit volume wetting phase.



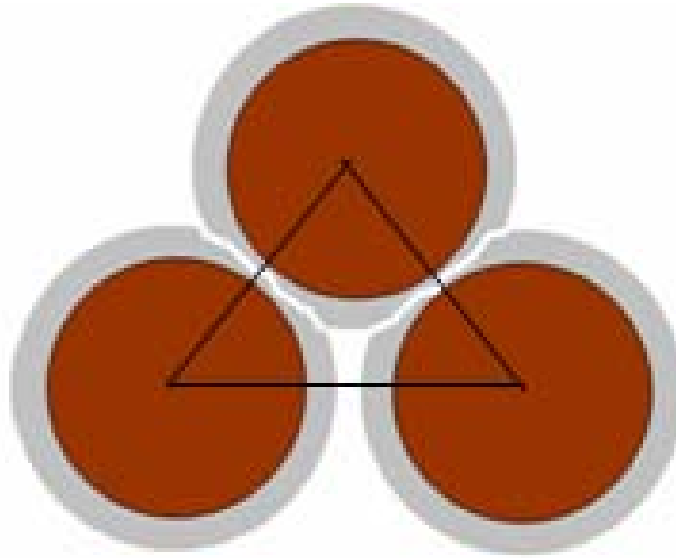


Figure 2.12. Extensive growth of isopachous cement from adjacent grains can lead to the formation of slot-like pores between grains. The slots are held open by asperities arising from different crystallographic orientation of the grains. Thus the slot aperture can change considerably with confining stress.

Second, we use smooth spheres in our model, but the surfaces of grains in rocks are rough. Some wetting phase can reside in small cavities associated with rough surface grains, enough to comprise the dominant part of  $S_w$  at low water saturations. However, if gas were present in these cavities, it would also be present in pore throats, whose characteristic size is much larger than the cavities. Flow along and through these cavities would make a very small contribution to total flow rate. Hence the water saturation associated with roughness does not affect significantly the effective gas permeability. The fractal roughness model of Moulu *et al.* [151] confirms this analysis, as discussed in Appendix B. Accounting for surface roughness in our model would thus reduce the apparent sensitivity of gas phase permeability to small values of water saturation. This is consistent with the measurements in Fig. 2.10. We conclude that only pendular rings and

coalesced throats affect permeability, while these features combined with wetting phase associated with roughness, slot pores, etc., determine saturation.

Third, our model for rings/bridges accounts only for wetting phase as pendular rings or liquid bridges. We ignore the pore-filling morphology which contributes to wetting saturation but has little effect on gas phase permeability at low  $S_w$  [150]. Therefore accounting for both morphologies (pore-filling and pendular ring) would decrease the sensitivity of gas phase permeability to wetting phase saturation. This is because over the saturation range of the experiments, the water phase exists in both the pore-filling and the pendular ring/liquid bridge morphologies. In a drainage simulation that fully accounts for the displacement physics, (see Chapter 4), it is possible to compute the relative amounts of water in the two morphologies. Bryant and Johnson [41] report roughly equal amounts in pores and in rings/bridges at the drainage endpoint in unconsolidated samples. If this ratio also applies in low porosity samples, then the slope of the model curves would be fall halfway between the two limits (red and green lines in Fig. 2.10). This would agree well with the experiments at high confining pressure.

### **2.6.2. Comparison with Experimental Data for Vaporization of Water during Gas Injection**

We further compare our simulation results with the data from vaporization of water during dry gas injection. Zuluaga and Lake [222] report core flood experiments that show noticeable permeability reduction (of order 20%), which is attributed to precipitation of salt from irreducible water saturation. In a typical experiment, irreducible saturation was established with a solution of 5 volume % NaCl. The porosity of the core was 16%, and the irreducible water saturation was 0.19. The solid salt initially present thus occupies the equivalent of almost 1% of pore volume ( $0.05 \times 0.19 \approx 0.01$ ). Hundreds

of pore volumes of dry methane were then injected, evaporating but not displacing the brine. After all the water was removed, an 18% permeability reduction was observed.

As with the water saturation in low porosity sandstones, the permeability reduction is remarkably large considering the small volume of salt. For example, if the salt were precipitated uniformly in the pore space, the Kozeny-Carman equation might be expected to apply; but we find  $\frac{k}{k_0} = \left(\frac{\phi}{\phi_0}\right)^3 \left(\frac{1-\phi_0}{1-\phi}\right)^2 \approx 0.97$ . This underestimates the observed reduction. To explain the observation, we propose that the grain scale distribution of salt is not uniform, that it can be understood in terms of pendular rings and that causes the disproportionate permeability change, just as it does for low  $S_w$  in tight gas sandstones.

As the wetting phase evaporates, the gas/water interface retreats toward grain contacts. The precipitated salt is thus presumably confined to the same part of pore space as the pendular rings and liquid bridges. Under this assumption, the volume occupied by salt would have the same effect on permeability as an equivalent volume of pendular rings. But according to our model, pendular rings and liquid bridges forming only 1% saturation, the minimum volume occupied by the salt, would cause only 3% permeability reduction (Fig. 2.8). To obtain the observed permeability reduction of 18%, salt would have to occupy the volume equivalent to a wetting phase saturation of about 5%.

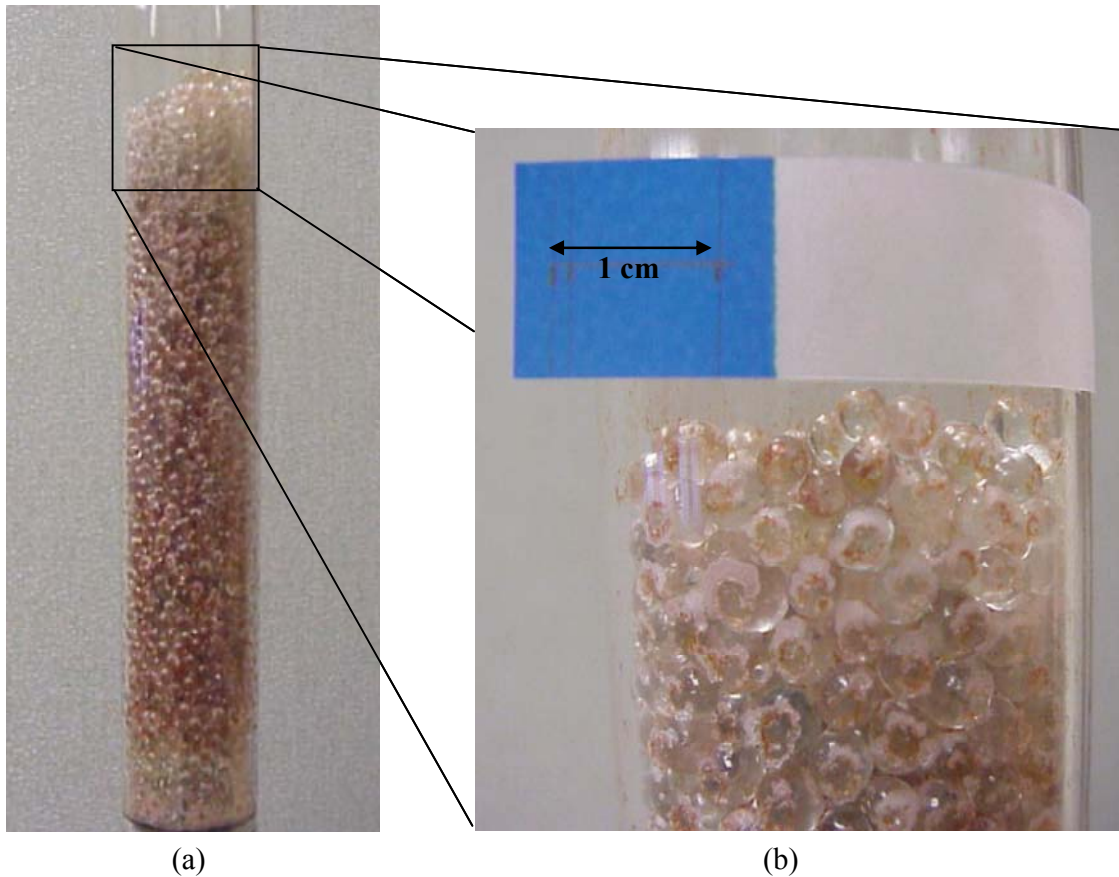


Figure 2.13. (a) Picture of bead pack column (18 cm) used for the capillary controlled gravity drainage of high concentrate brine experiment. This picture was taken at the end of experiment and the bead pack column was exposed to heat (oven) for more than 48 hrs. The red indicator in the brine enhances visual contrast between grains and precipitated salts. (b) Enlarged view on the top part of the bead pack column. The white spots are the crust of salt that precipitated between the glass wall of the column and the grains (beads). The average bead size is 2 mm.

Observations of evaporating brine (in bulk and in bead packs) help reconcile the difference between the theoretical minimum salt volume (1% of pore space) and the salt volume needed to explain the permeability reduction (5% of pore space). A column was packed with glass beads and filled with brine (Fig. 2.13a). The salt concentration of brine is 23% by weight, or 9% solid content by volume. We displaced brine with air at very

slow flow rate (capillary controlled gravity drainage process), then placed the column in an oven with temperature of  $75^{\circ}\text{C}$  for more than 48 hours. Evaporation of water results in the formation of salt crusts within the porous medium, which are visible through the wall of the glass column. Pictures of precipitated salt between beads and the wall of the glass column are shown in Fig. 2.13b. The precipitated salts at the point contacts look like rings (doughnut shape). Bernal and Mason [23] observed the same shape for dried ink at the point contacts between spheres in a packed column. Thus salt precipitates at the outer edge of the pendular rings, not the inner core.

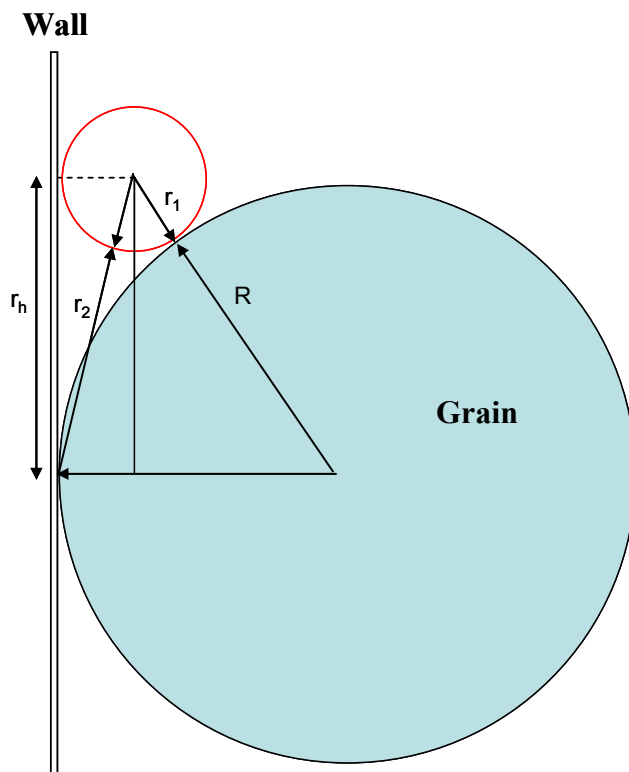


Figure 2.14. Schematic of pendular ring held at point contact between grain and wall. We adapt the toroid approximation for rings between two spheres, so that  $r_1$  and  $r_2$  are taken to be the radii of curvature of the meniscus. This approximation is reasonable for large values of mean curvature, when  $r_1 \ll r_2$ .  $r_h$  is radius (max) of the circle of projected pendular rings, and the calculated value is compared with observations (Fig. 2.13).

We measured the inner radius of the rings by an image processing technique and compared with calculated radius  $r_h$  of the circle of projected pendular rings on the wall at the point contact between grains and the wall (Fig. 2.14). By knowing the diameter of the beads and applied curvature, we calculated the cross sectional area (and its corresponding radius) of brine that is held as pendular rings at the contact points between beads and wall of glass column. We use average diameter of beads as bead diameter (beads are assumed to be uniform in size). The applied capillary pressure and the corresponding curvature are calculated from the measured distance above free water level (bottom of the bead pack). The value of calculated  $r_h$  is comparable to the value of the measured inner radius of the rings. For instance the average measured inner radius of rings at 12.5 cm from bottom of the column (free water level) is 0.61 mm, while the calculated  $r_h$  for the applied curvature at this level is 0.65 mm (the bead size is 2 mm).

Our observations show that salts precipitate from saturated brine solution outward from the pendular rings. The salt crust has small permeability and thus acts as seal for gas flow. Therefore the effect of these salt crusts on the reduction of area available for gas to flow is slightly more than the effect of the pendular rings themselves. Salt precipitation begins only after the brine becomes saturated. For the experiments reported by Zuluaga and Lake [222], this occurs when the wetting phase saturation is reduced to about 6%. At this point, much of the wetting phase will exist as pendular rings and liquid bridges. Evaporation from this point onward leaves a salt crust outwards toward the center of the pore throat. We hypothesize that capillarity draws brine into the crust, and as that brine evaporates, the crust grows. In this fashion, an accretion of porous salt is built in the same vicinity in pore throats as the rings and bridges. The reduction in effective permeability should therefore be comparable to that caused by a wetting phase saturation of 6%. The reduction predicted in this way (Fig. 2.8) is very close to the observed value.

## 2.7. CONCLUSIONS

Low wetting saturation can have significant effect on effective permeability of porous media, especially as isopachous cement decreases the porosity below 20%. Using a physically representative network model to compute phase permeability, we quantified the effect in simple model rocks at very low saturations (less than 6% wetting phase) by considering the geometry of pendular rings and liquid bridges held at grain contacts and near-contacts. The rings/bridges reduce the area open to flow of gas phase. This reduces the effective radius of these throats and thus reduces the effective permeability to the gas phase. For small porosity, the rings/bridges can coalesce in throats as wetting phase saturation increases, causing snap off of the gas phase. This reduces the connectivity of the gas phase and thus amplifies the reduction in effective permeability. Coalescence occurs much less often in model rocks of larger porosity. This difference contributes to the greater sensitivity of tight gas sandstones to water saturation in low porosity-low permeability rocks.

We contrasted this result with the effect when water only occupies pores in the model rocks. For this pore-filling wetting phase morphology, the model predicts that low porosity rocks exhibit less sensitivity of gas phase relative permeability to low water saturations than moderate or high porosity rocks. This is because the mechanism of porosity reduction, quartz overgrowth cementation, causes the pore throat size distribution to be much broader in low porosity samples than in moderate or high porosity samples. The entrance of water into the low porosity model rocks thus removes relatively much smaller throats from the network of connected gas phase. This finding reinforces the importance of rings/bridges as the primary mechanism for water sensitivity in tight gas sandstones.

The predicted trends of gas phase permeability vs. water saturation for the two morphologies, rings/bridges and filled pores, bracket the trends apparent in measurements reported in the literature. The predictions presented here thus provide bounds on the sensitivity of gas phase permeability. In practice, the net effect of increasing the water saturation from small values will depend on the relative amounts of water held in the two morphologies.

The model suggests one mechanism for the sensitivity of gas effective permeability in tight gas sandstones to confining stress. At small stress, crack-like or slit-like pore throats are open but contribute little to permeability. Thus when they contain wetting phase, the reduction in effective permeability is slight. At large stress, these slits are closed, and low wetting phase saturation exists only in the corners of triangular throats like those in our model. More generally, the wetting phase held in crevices associated with surface roughness contributes volume at small values, but does not affect gas phase permeability. Our rings/bridges-only model accounts only for wetting phase held in pendular rings and predicts greater sensitivity than observed. Incorporating surface roughness in the manner of Moulu *et al.* [151] would thus improve the predictions, indicating that pendular rings are the main pore-space feature affecting gas phase permeability but not the only feature affecting .

The model also provides a quantitative explanation for the disproportionately large reduction in gas permeability caused by injection of dry gas into a brine-saturated core. The salt precipitated from the initial brine saturation builds porous obstructions corresponding to the locations of pendular rings/liquid bridges. In this manner, a small volume of solid salt can obstruct a large enough volume of pore space to reduce permeability.



## **CHAPTER 3: MECHANISMS OF MENISCUS MOTION IN 2D FRACTIONALLY WET POROUS MEDIA**

### **3.1. ABSTRACT**

Oil reservoirs and soil are often heterogeneously wet (mixed wettability or fractional wettability). In mixed wet reservoirs the mechanism of wettability alteration means that a single grain can have patches that are water-wet and patches that are oil-wet. In fractionally wet porous media, each grain is either oil-wet or water-wet. Here we develop a mechanistic model of capillary controlled fluid movement in fractionally wet media. The model calculates the position of stable interfaces between grains of arbitrary wettability. Pore filling occurs when the interface becomes unstable in a pore throat (Haines condition), or when two or more interfaces come into contact and merge to form a single interface (Melrose condition). The model is robust and general in the sense that both filling mechanisms are considered simultaneously during arbitrary sequences of changes in capillary pressure. The model is demonstrated on 2D porous media consisting of randomly distributed oil-wet and water-wet disks, and capillary pressure–saturation curves are obtained. The model results compare favorably with the drainage/imbibition experiments on fractionally wet media. Most notably, a distinctive shift in the drainage/imbibition curves occurs as the fraction of oil-wet grains increases beyond a threshold value.

### **3.2. INTRODUCTION**

In a rock containing immiscible fluids, the rock is wetted by the fluid that has smaller surface energy of interaction with the rock [63]. Wettability of reservoir rocks is the subject of wide investigation because understanding rock wettability helps petrophysicists to estimate fluid distribution within the pore space of the rock [10, 11].

Fluid distribution at the pore scale is important because this affects the macroscopic rock/fluid properties such as capillary pressure curves and relative permeability curves.

Many rock minerals have a tendency to be wetted by water and thus, reservoir rocks are typically water-wet before they are filled with oil. However, chemical species within the oil that are charged can change the wettability of the reservoir rocks to oil-wet during geological time [172]. Reservoirs can be partly oil-wet and partly water-wet due to wettability alteration, which occurs on the part of the reservoir rock that is exposed to the crude oil [172]. This is referred to in the literature collectively as heterogeneous wettability [113], fractional wettability [200] and mixed wettability [5, 206, 209, 211].

Here, we identify two categories of heterogeneous wettability: Fractional wettability and mixed wettability. In the case of fractional wettability the grains that construct the porous medium are either water-wet or oil-wet. The water-wet and oil-wet grains are distributed randomly within the porous medium. This is depicted schematically in Fig. 3.1.

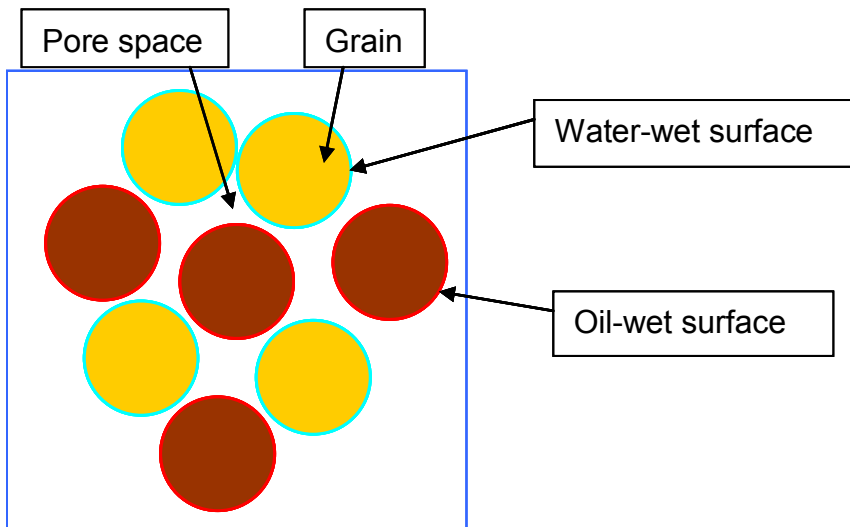


Figure 3.1. Schematic of a fractionally wet porous medium (grain level scale).

In the laboratory, the fractionally wet porous media are prepared by mixing different fraction of the oil-wet grains and water-wet grains. Fractionally wet porous media occur naturally in certain soils, and they are the simplest heterogeneously wet media that can be reliably reproduced experimentally. Because of this, fractionally wet media has been the focus of most experimental measurements [19, 31, 90, 178, 204].

In contrast for mixed wet porous media, the grains may have both water-wet and oil-wet patches. This can occur from different mineral surfaces on the grain (micas or quartz), or it may occur from different portion of the grains coming in contact with reservoir oil. In nature, oil invades the water-wet rock due to density differences between oil and water (first migration). During first migration water is displaced from large pores, and remains in both small pores and as rings at the grain contacts due to capillary force. It is theorized that wettability alteration occurs only on the surfaces of grains that directly contact the oil phase; therefore the surfaces of the grains within the small pores, which were never filled with oil, remain water-wet. Similarly, the surfaces of the grains where the pendular ring forms remain water-wet (Fig. 3.2). This mechanism of wettability alteration causes single grains to have both water-wet and oil-wet patches [172].

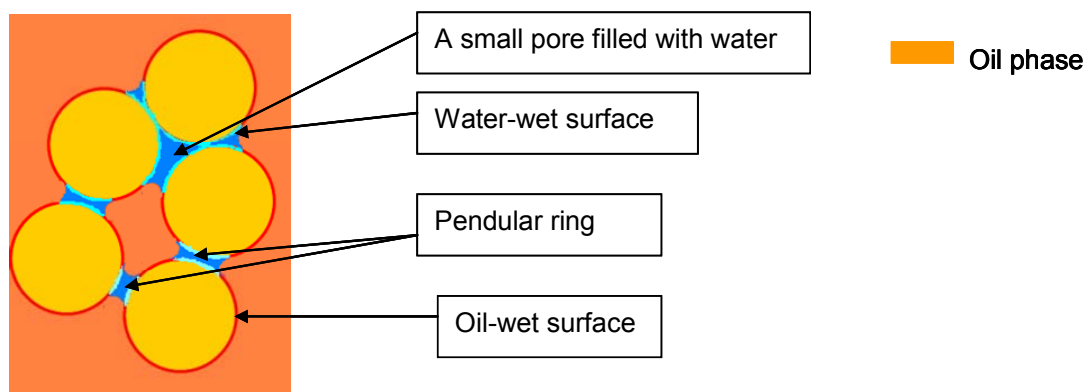


Figure 3.2. Schematic of a mixed wet porous medium (grain level scale).

Brown and Fatt [35] were the first to construct heterogeneously wet porous media. They mixed different fraction of oil-wet and water-wet sand grains to build several fractionally wet porous media. The authors showed that “wettability” of the model rock could be measured by Nuclear Magnetic Relaxation method (NMR).

McDougall and Sorbie [142] investigated waterflood performance in heterogeneously wet porous media. They modeled mixed wet rock as porous media composed of small pores (water-wet) and big pores (oil-wet). They also modeled fractionally wet porous media by choosing certain fractions of pores water-wet and oil-wet, independent of the pore sizes. They use the invasion percolation theory to model the capillary displacement of water and oil phase. Other researchers [26, 92, 147, 159, 204] have studied the mixed wet and fractionally wet porous medium using pore network modeling. Their pore network models are typically based on a lattice of random pores and throats with different shape (triangular, square, circular, star-shape, etc). The shapes are inspired by naturally occurring throats, which retain wetting phase at grain contacts after the throat has drained. In cylindrical throats, fluids cannot co-exist during multiphase flow through the porous medium. This weakness was overcome by considering angular cross section throats. The angular cross sections throats represent a useful advance over traditional cylindrical throats by retaining wetting phase in the corners of their throats. However, a concept not considered in the above models is that ‘pore is the space where grains do not exist’. In other words, the pore shapes are not fundamental; rather, the grain shapes are the “primitives” from which pore shapes are derived. Moreover, wettability is strictly speaking a property of grains, not of pores. A grain-based approach to this class of fluid displacements therefore seems natural.

This chapter is part of a broader effort to understand the mechanisms of meniscus movement in heterogeneously wet media, then to use that understanding to develop

purely mechanistic and geometric criteria for pore level events. We need to validate our simulation result (drainage and imbibition curves), and hence the geometric criteria on which the simulation relies, against experimental data. The criteria applied in fractionally wet porous media are not fundamentally different from criteria applied in mixed wet porous media. The experimental data for fractionally wet media are more readily available due to the simplicity of the experimental set up. The comparison between experimental data and simulation result is also easier in fractionally wet media because independent variable is simply the percentages of oil-wet and water-wet grains. In contrast in a mixed wet porous medium, the configuration of oil-wet and water-wet surfaces (wettability map) is very complicated, depending on pore geometry, the history of primary drainage, etc. For the purpose of validating mechanisms, then, the fractionally wet medium is preferred.

To understand the physics of menisci motion within fractionally wet porous media, we restrict ourselves to two-dimensional media in this chapter. This greatly simplifies the presentation and implementation of the concepts. In addition, the development of a model in two-dimensional media gives us the advantage of visualization of the menisci motion within a fractionally wet medium (see Appendix D for more details). The extension to three dimensions is presented in Chapter 4.

### **3.3. TERMINOLOGY**

Because the solid surfaces in a heterogeneously wet porous medium consist of surfaces with different wettability, discrimination between wetting and non-wetting phase is ambiguous. Hence we define capillary pressure to be the pressure of the non-aqueous phase (oil) minus pressure of the aqueous phase (water or brine).

$$P_c = P_o - P_w. \quad (3.1)$$

This macroscopic capillary pressure is proportional to the curvature of the microscopic interfaces through the Young Laplace equation,

$$P_c = \sigma_{ow} \left( \frac{1}{r_1} + \frac{1}{r_2} \right) = 2C\sigma_{ow}, \quad (3.2)$$

where  $r_1, r_2$  are radii of curvature and  $C$  is defined as the mean curvature. The curvature is essentially a scaled capillary pressure. Thus when the pressure of oil phase exceeds the water phase pressure, the capillary pressure and curvature are positive and consequently the interface curves toward the oil phase, and when the capillary pressure and curvature are negative the interface curves toward the water phase. These curved interfaces are referred to as menisci. We report the value of the curvature as dimensionless curvature by normalizing the grains radii to be unity.

Along these lines and following Morrow [149], we define drainage to be when the water saturation is decreasing, and imbibition to be when the water saturation is increasing.

### 3.4. MODEL/SIMULATION

#### 3.4.1. Assumptions

In this chapter, we do not take into account the existence of thin wetting films on the surface of grains. In addition, we assume that in a two-dimensional medium, the fluid/fluid interface (meniscus) with a constant curvature is represented by the arc of a circle, because this shape minimizes the surface free energy. We do not explicitly solve for the minimum surface energy. Instead, we developed our model based on the finding of studies regarding the stability of a fluid/fluid interface within the porous media [87, 88, 144].

### 3.4.2. Model of Pore Space

To study the movement in menisci through fractionally wet porous media, we create 2D porous media made up of equally sized disks. The disks cannot overlap but otherwise are randomly located. Each disk can be made either water or oil-wet.

To facilitate movement of water and oil through the network we also create an oil-wet membrane made of smaller sized oil-wet disks on the right hand side, and a similar water-wet membrane on the left hand side of the model (Fig. 3.3a).

We use the approach of Bryant *et al.* [42] to obtaining simple network models from 2D porous media. We use a Delaunay tessellation of the disks centers to subdivide the pore space into pore bodies and pore throats. The tessellation yields triangles, with each edge of the triangle corresponding to a pore throat. The space inside each triangle (excluding the disks) is the pore body (Fig. 3.3b).

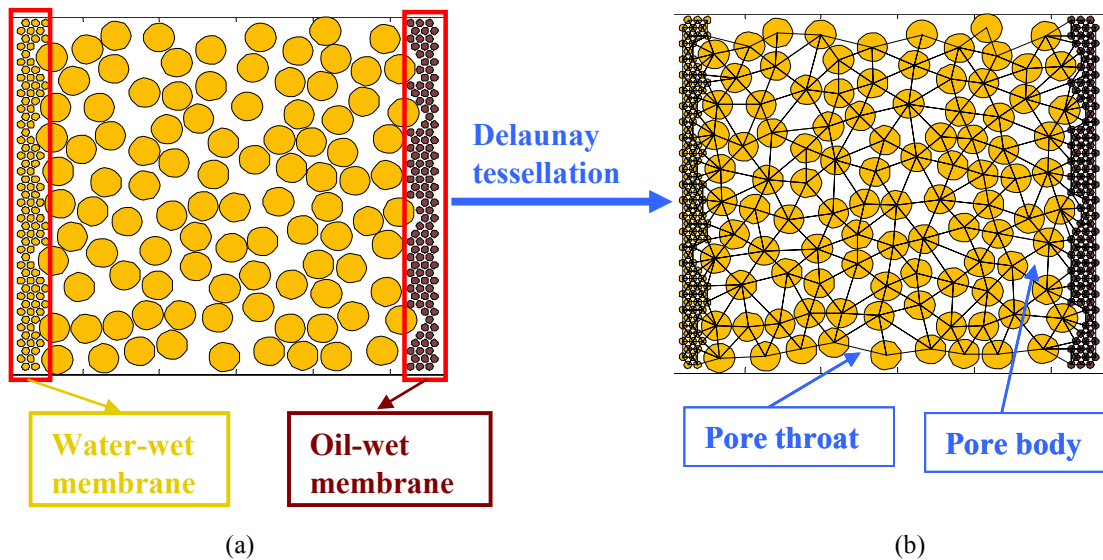


Figure 3.3. (a) Schematic of a porous medium constructed with randomly distributed disks, the oil-wet membrane and water-wet membrane located at the left and right hand side of porous medium. (b) Schematic of network model extracted from porous medium (Fig. 3.3a). The pore space within porous medium can be divided to pore bodies and pore throats using Delaunay tessellation.

### 3.4.3. Grain-Based Mechanistic Criteria for Menisci Movement

The essential features of a grain-based approach are (i) the locations of the grains and (ii) the wettability (contact angle) of each grain. The former data allow an unambiguous identification of pores and throats, without recourse to sampling a distribution or specifying a shape. The latter data lead to criteria for stable configurations of a meniscus (fluid /fluid interface). The fundamental event in a grain-based approach is the filling of an individual pore, just as in traditional pore network models. However we establish criteria for such events in terms of grain locations and contact angles, rather than in terms of the geometry of idealized throats. For invasion of a pore by a single meniscus passing through a throat, the grain-based and pore network models arrive at essentially the same result, namely the criterion for a Haines jump. For invasion of a pore by the merger of two or more menisci (Melrose mergers), the grain-based approach offers a significant advantage. The correct geometry and location of meniscus are readily determined in a grain-based model. We are unaware of any systematic way to account for these phenomena in a traditional pore network model. Haines jumps and Melrose mergers both occur during any cycle of drainage or imbibition in a fractionally wet medium. We conclude that a grain-based approach is essential for obtaining a mechanistic understanding of such displacements. This assertion is supported by the successful prediction of imbibition curves in uniformly wet media [80].

#### *Haines Events*

Pores can fill through two different mechanisms, Haines events [88] and Melrose events [144]. These can be most easily understood in uniformly water-wet media. Fig. 3.4 shows a schematic of a Haines event. During drainage of a water-wet porous medium, as the capillary pressure increases, the curvature of the meniscus increases. In a 2D medium, the meniscus is an arc of a circle whose radius is set by the applied capillary pressure. As



a result of capillary increase, the meniscus gradually moves to the right into ever narrower parts of the throat (Fig. 3.4). At location 3, the throat can no longer hold the meniscus, and it jumps to displace the fluid from the pore behind the throat. The criterion for this 2D Haines event is given by the smallest circle that will fit in the throat; for curvatures greater than the curvature of this circle, the meniscus will pass through the throat.

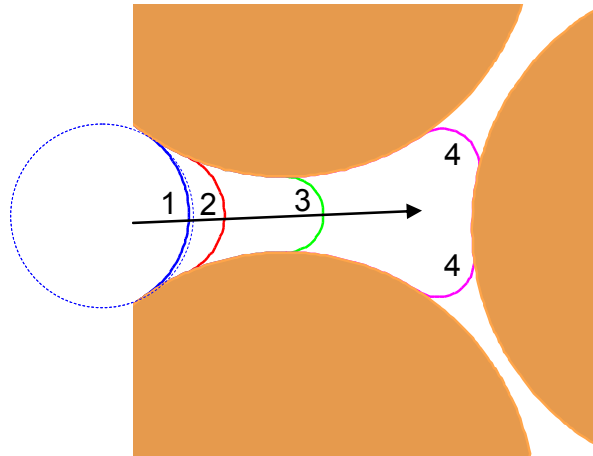


Figure 3.4. Schematic of a pore-filling under the Haines criterion. Originally the meniscus is located in the left hand throat (blue curve, location 1). The meniscus is an arc of a circle whose radius is set by the applied capillary pressure. Increasing the curvature causes the circle to become smaller, until it can pass through smallest opening of the throat (green curve, location 3). The green curve is unstable and the pore will be drained which results in locating two menisci at adjacent throats (purple curves, location 4).

In other words, when the circle gets small enough to pass through the gap, then the throat cannot hold the meniscus and the Haines event occurs. In the water-wet medium, The Haines event only occurs during drainage, while the capillary pressure increases.

### ***Melrose Events***

A Melrose event [144] is the irreversible jump that occurs after two separate menisci come into contact and merge into a single meniscus. Fig. 3.5 shows a Melrose

event in a uniformly water-wet medium during imbibition (curvature decreasing). The details are as follows. The decrease in the curvature causes advancement of the menisci from the upper and lower throats on the right (location 1) toward the pore (locations 2 and 3). Continued advancement results in the merging of menisci at location 3 to form a single meniscus. This configuration is not stable. Upon an infinitesimal decrease in curvature, the wetting phase fills the pore space completely and makes a new meniscus in the throat of neighboring pores, location 4. Thus, the criterion for a Melrose event is the touching of two separate interfaces. For a pore with multiple throats, several different Melrose events are theoretically possible, depending on which pairs of throats contain the merging menisci. In the water-wet medium, Melrose event only occur during imbibition, while the capillary pressure decreases.

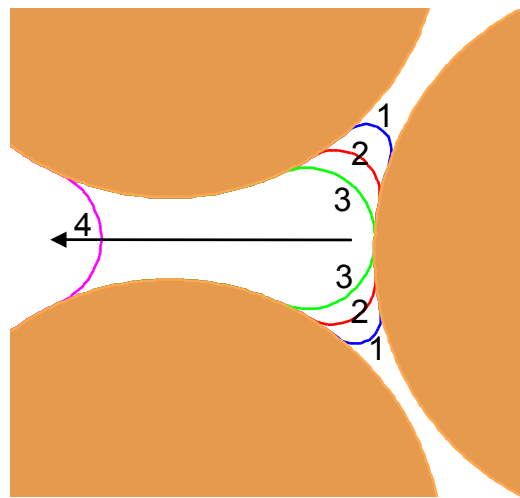


Figure 3.5. Schematic of a pore-filling under the Melrose criterion. Two menisci are originally located at two adjacent throats (blue curve, location 1); by decreasing the curvature (capillary pressure), menisci move toward the pore. Different color curve shows the position of the menisci at different curvatures. Eventually these two menisci touch (green curve, location 3), the green curve is unstable and pore will be imbibed by wetting phase. The merged meniscus jumps to a new stable location, the purple curve (location 4).

Fig. 3.4 and 3.5 also illustrate the geometric cause of hysteresis in a drainage and imbibition cycle. The critical location of the meniscus during drainage (location 3 in Fig. 3.4) is quite different from the critical location during imbibition (location 3 in Fig. 3.5). Hence the curvature (and capillary pressure) at which each event occurs is quite different.

### ***Shape of Water/Oil Interface (Meniscus) on the Fractionally Wet Throat***

In the fractionally wet porous medium, the configuration of the oil-wet and water-wet surface dictates the fluid distribution within porous medium. Within a two-dimensional network of disks, three neighboring disks construct a pore. Each pore has three throats constructed from pairs of adjacent disks (Fig. 3.6). There are four configurations of grains defining a pore in the fractionally wet porous medium:

- Three water-wet disks, in which all throats are water-wet. (Fig. 3.6a)
- Three oil-wet disks, in which all throats are oil-wet. (Fig. 3.6b)
- Two water-wet disks and one oil-wet disk, in which one water-wet and two fractionally wet throats. (Fig. 3.6c)
- Two oil-wet disks and one water-wet disk, in which one oil-wet and two fractionally wet throats. (Fig. 3.6d)

The task is to determine the Haines and Melrose events that can occur in each type of pore. This reduces to two more basic exercises: computing the critical curvature for a single meniscus in a throat, and computing the critical curvature for two menisci in adjacent throats. The solution to the first exercise, which we summarize next, is the foundation for the second. We treat curvature (or capillary pressure) as the independent variable. This is driven by the common experimental procedure of incrementing capillary pressure, waiting for equilibrium and repeating. To determine when Melrose and/or Haines criteria are met in the corresponding simulation, it is necessary to calculate the position of all of the menisci within the porous medium at a prescribed curvature.

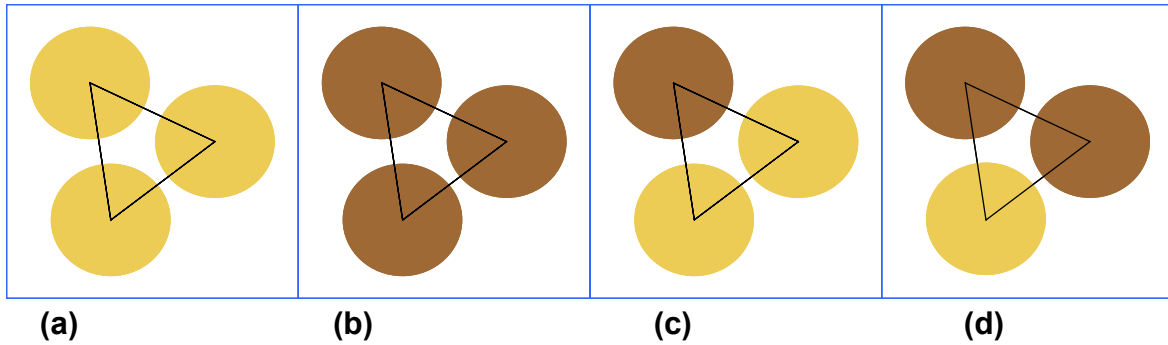


Figure 3.6. Schematic of different configurations of a pore in the fractionally wet porous media. The throat is the void space (gap) within two pair of disks. In configuration a, and b the throats are uniformly wet, whereas in configurations c and d two of throats are fractionally wet and one of them is uniformly wet.

### ***Stability of Meniscus in Fractionally Wet Throat, Analogy to Haines Criterion***

We generalize the classical Haines criterion by solving for the stable interface in fractionally wet media. Here we demonstrate how the position of one meniscus is found between a pair of 2D disks of arbitrary and unequal contact angles and radii, separated by an arbitrary gap width ( $D$ ) (Fig. 3.7).

For a meniscus with constant curvature, the geometry of the meniscus is defined by the center of the meniscus  $(x_0, y_0)$ , the radius of the meniscus, and the intersections with the solid surface. The intersections of the meniscus with the disks are forced to be at the contact angle of each surface. These constraints yield a trigonometry problem to be solved for the center of meniscus (for more details, see the Appendix C). Fig. 3.7 shows the schematic of menisci positioned on the two disks with different contact angles  $(\theta_1, \theta_2)$ .

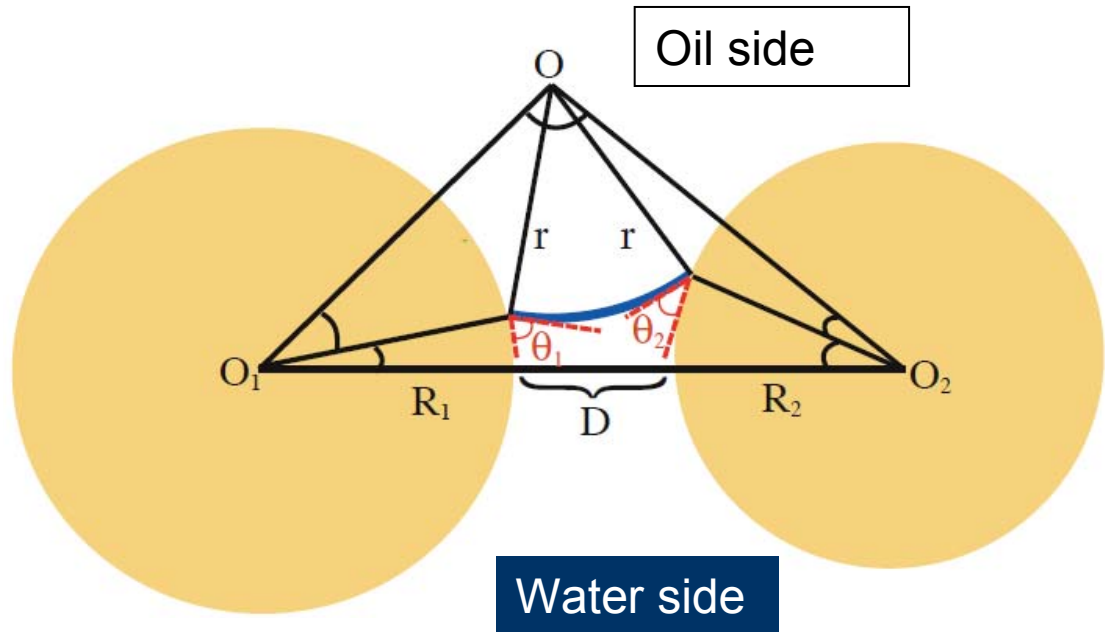


Figure 3.7. Schematic of a stable meniscus (blue) with a radius of  $r$ , located on two disks with different contact angle ( $\theta_1, \theta_2$ ). The disks have different radii ( $R_1, R_2$ ) and are separated by a gap of width  $D$ .  $O$  is the center of meniscus, and  $O_1$  and  $O_2$  are the center of two disks which hold the meniscus.

In the configuration of Fig. 3.7,  $R_1, R_2$  (radii of disk 1 and 2), contact angles ( $\theta_1, \theta_2$ ), the gap width ( $D$ ), and the radius of the meniscus  $r$  are given. A solution for the center of the meniscus exists if the following condition is met.

$$\frac{(D + R_1 + R_2)^2 - (L_1 - L_2)^2}{2L_1L_2} \leq 2, \quad (3.3)$$

where  $L_1$  and  $L_2$  are the distances from the center of each disk to the center of the meniscus (i.e.  $O$ ). In other words,  $L_1$  and  $L_2$  are length of  $\overline{OO_1}$  and  $\overline{OO_2}$  respectively. The

value of  $L_1$  and  $L_2$  are given by

$$L_1 = \sqrt{R_1^2 + r^2 + 2R_1r \cos(\theta_1)}, \quad (3.4)$$

$$L_2 = \sqrt{R_2^2 + r^2 + 2R_2r \cos(\theta_2)}, \quad (3.5)$$

respectively.

If condition of Eq. 3.3 is met, the meniscus can exist between the grains, and the meniscus is stable. If this condition is not met, the meniscus cannot exist. Thus Eq. 3.3 implies a critical value of curvature for the throat that holds the meniscus, namely the largest value for which the meniscus is stable on the throat. As shown above, this critical curvature is one for which the meniscus will first pass through the throat. The meniscus is stable when the curvature of meniscus is smaller than critical curvature of the throat. If the curvature of meniscus gets larger than the critical curvature, the condition of Eq. 3.3 is no longer satisfied. As a result, the meniscus will pass through the throat and a Haines event will occur.

We solve an inequality of Eq. 3.3 for fractionally wet throats at different curvature of meniscus, gap size, and contact angle of disk 2 ( $\theta_2$ ) with meniscus. The fractionally wet throat composes of two equal size disks. The contact angle of disk 1 with the meniscus remains constant ( $\theta_1 = 0^\circ$ ) while the contact angle of disk 2 ( $\theta_2$ ) varies. The gap sizes are normalized such that a value of 1 corresponds to the radius of the disks.

As a result of above exercise, we map the region in which a meniscus is stable on a fractionally wet throat. Fig. 3.8 shows the relation between maximum curvature for a stable meniscus versus the gap size of the fractionally wet throat holding the meniscus, and the contact angle of disk 2. In Fig. 3.8, the region below the plotted surface is region of stable menisci and the region above the surface is the region of unstable menisci. For instance, a meniscus with dimensionless curvature of 5 is stable on the fractionally wet throat with normalized gap size of 0.2, when both disks make zero contact angle with the meniscus. However, a meniscus with the same curvature is not stable if contact angle of disk 2 change to  $180^\circ$ . Fig. 3.8 also shows how fast the region of stable meniscus gets smaller as the gap size or contact angle of disk 2 increases.

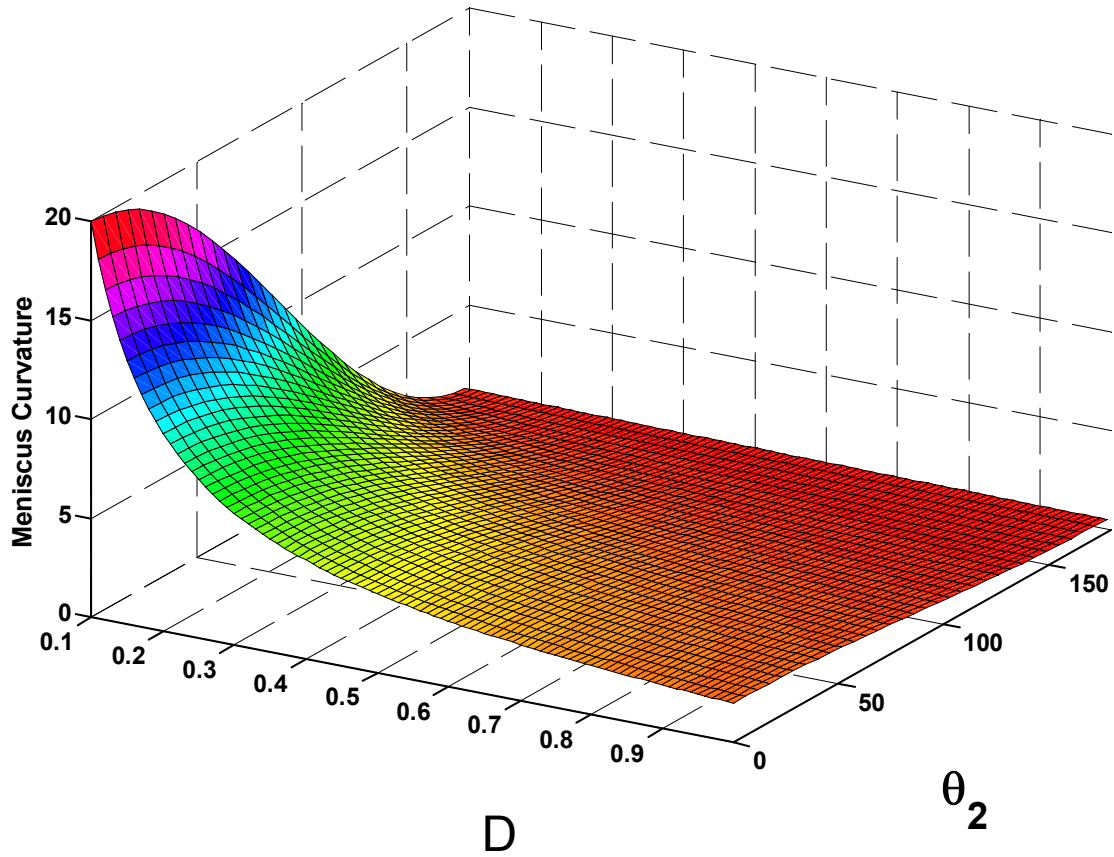


Figure 3.8 Relation between maximum curvature for a stable meniscus versus the gap size of the fractionally wet throats holding the menisci, and the contact angle of disk 2. The region below the plotted surface is region of stable menisci and the region above the surface is the region of unstable menisci.

Eq. 3.3 is a general criterion for any two disks with different contact angles and different radii. We illustrate this for two specific cases that occur frequently in the fractionally wet medium. Fig. 3.9 shows the schematic of a meniscus positioned on two disks of equal size with zero contact angles  $\theta_1 = \theta_2 = 0^\circ$ .

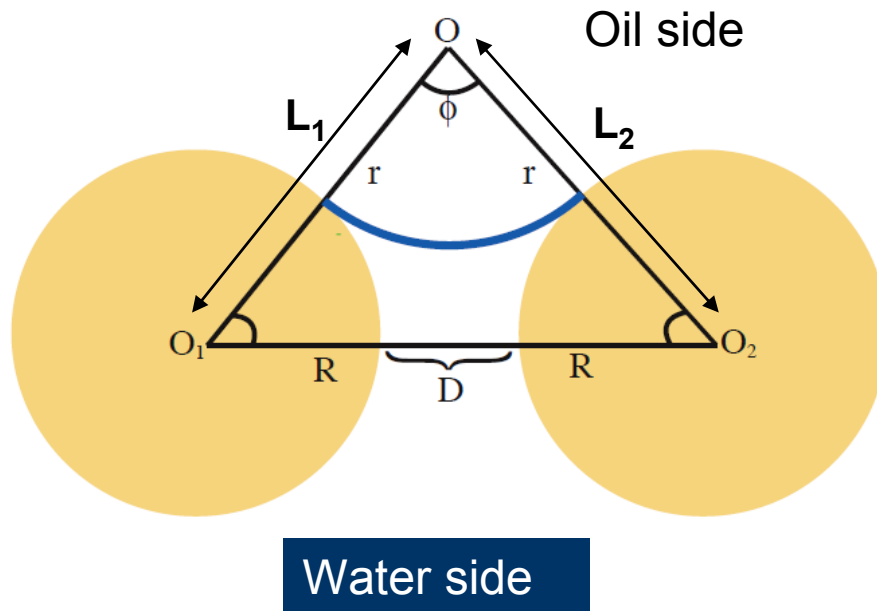


Figure 3.9. Schematic of meniscus (blue) with radius of  $r$ , located on two disks with zero contact angles ( $\theta_1=\theta_2=0^\circ$ ). The disks have same radius ( $R_1=R_2=R$ ) and are separated by a gap of width  $D$ .

In Fig. 3.9, the distances from center of each disk to the center of meniscus are equal:

$$L_1 = L_2 = r + R . \quad (3.6)$$

Substituting Eq. 3.6 in Eq. 3.3 reduces the criterion of stable meniscus to

$$r \geq \frac{D}{2} . \quad (3.7)$$

In Fig. 3.9, the meniscus will be stable if the radius of meniscus is bigger than half of the gap. Eq. 3.7 defines a minimum radius of curvature stable for given gap width ( $D$ ). The radius of meniscus and the curvature of meniscus are inversely proportional. Hence, it is instructive to rewrite Eq. 3.7 in terms of curvature, yielding a criterion for the maximum curvature (capillary pressure) allowable for the meniscus to be stable:

$$C \leq \frac{2}{D} . \quad (3.8)$$



Thus as soon as the curvature of the meniscus exceeds the critical value of  $\frac{2}{D}$ , the radius of the meniscus becomes smaller than half the gap size, the meniscus becomes unstable, and a Haines' jump occurs. In other words, this is exactly the same criterion for the Haines event during drainage of a water-wet medium. As mentioned before, when the circle, in which the meniscus is the arc part of that circle, gets small enough to pass through the gap, then throat is unable to hold the meniscus and the Haines event occurs. The curvature of this circle is the Haines criterion for this throat.

The other specific case of interest is when two disks have the same radii and opposite wetting preference. Fig. 3.10 shows the schematic of a meniscus positioned on two disks of equal size with  $0^\circ$  and  $180^\circ$  contact angles ( $\theta_1=0^\circ$ ,  $\theta_2=180^\circ$ ).

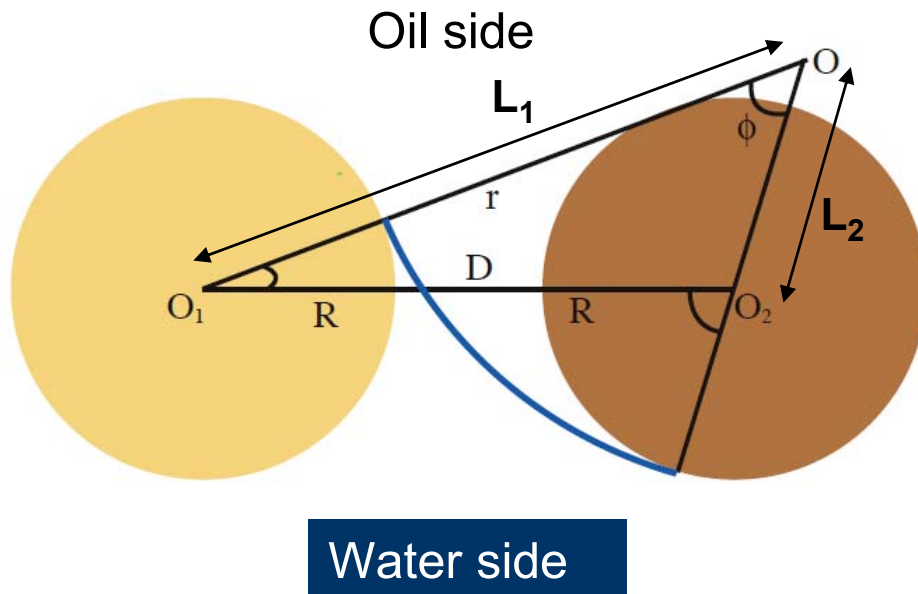


Figure 3.10. Schematic of menisci (blue) with radius of  $r$ , located on two disks with zero and  $180^\circ$  contact angles ( $\theta_1=0$ ,  $\theta_2=180^\circ$ ) The disks have same radius ( $R_1=R_2=R$ ).

Regarding Fig. 3.10, we can observe that

$$L_1 = r + R, \quad L_2 = r - R. \quad (3.9)$$

Substituting Eq. 3.9 into Eq. 3.3 leads to

$$r \geq \frac{D}{2} + R. \quad (3.10)$$

Typical values of  $D$  are three to ten times smaller than  $R$ . Thus comparing Eq. 3.10 to Eq. 3.6 shows that the minimum radius of a stable meniscus is much larger if one of disks is oil-wet (contact angle equals to  $180^\circ$ ). This means that the maximum value of curvature for a stable meniscus is much smaller when one of the disks is oil-wet. Therefore, the meniscus will become unstable in such a throat at a relatively small value of curvature, while menisci on water-wet throats remain stable. Thus, in a large collection of oil-wet and water-wet disks, the range of curvatures for which menisci are stable in all the throats in the domain is very small. This statement is true for positive applied curvature.

### ***Stability of Two Merging Menisci in Fractionally Wet Media, Analogy to Melrose Criterion***

The Haines criterion obtained above applies to a single meniscus between a pair of grains. We now consider two menisci at adjacent throats in a single pore. To understand the Melrose event geometrically, first consider a uniformly wet pore, shown in Fig. 3.11. The pore has three uniformly wet throats. Originally, two menisci are located at adjacent throats (Fig. 3.11a). Decreasing the curvature causes the menisci to move toward the pore (i.e. to the right) (Fig. 3.11b). The angle  $\alpha$  subtended by the points of contact of the menisci on the center disk decreases as curvature decreases. The moment the menisci touch, they become unstable and merge into a single meniscus (see Appendix C for detail of numerical implication of this criterion). They leave the center disk so the pore will be filled with water (Fig. 3.11c). This series of events occurs during an imbibition as the curvature and capillary pressure are decreased (Fig. 3.11d).

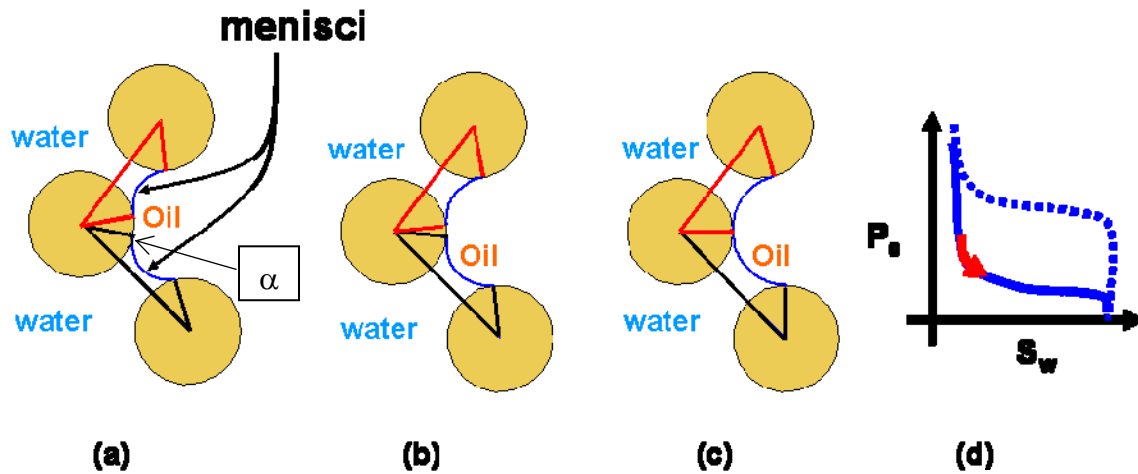


Figure 3.11. Schematic of two menisci merging (Melrose event) in a uniformly wet porous medium. Three water-wet disks construct a pore and three throats, and originally the two menisci are located on the two adjacent throats. The angle  $\alpha$  is defined by lines connecting the points of contact of the menisci on the center disk to the disk center. (a). Menisci move toward the pore by decreasing the curvature (b), until they touch (c) and the pore fills with water. This Melrose event happens during imbibition as the curvature is decreased (d).

The same kind of event (merging two menisci) can occur by increasing curvature in a fractionally wet pore (Fig. 3.12). This is an important generalization of the Melrose event. In Fig. 3.12, we show a single pore made up of two water-wet disks and one oil-wet disk. The pore has one uniformly wet throat and two fractionally wet throats. Originally two menisci are located at adjacent fractionally wet throats (Fig. 3.12a). This time they move toward the pore as curvature increases (Fig. 3.12b). The moment they touch, they get unstable and merge to a single meniscus, (Fig. 3.12c). These series of event occurs in drainage as the curvature and capillary pressure are increased (Fig. 3.12d).

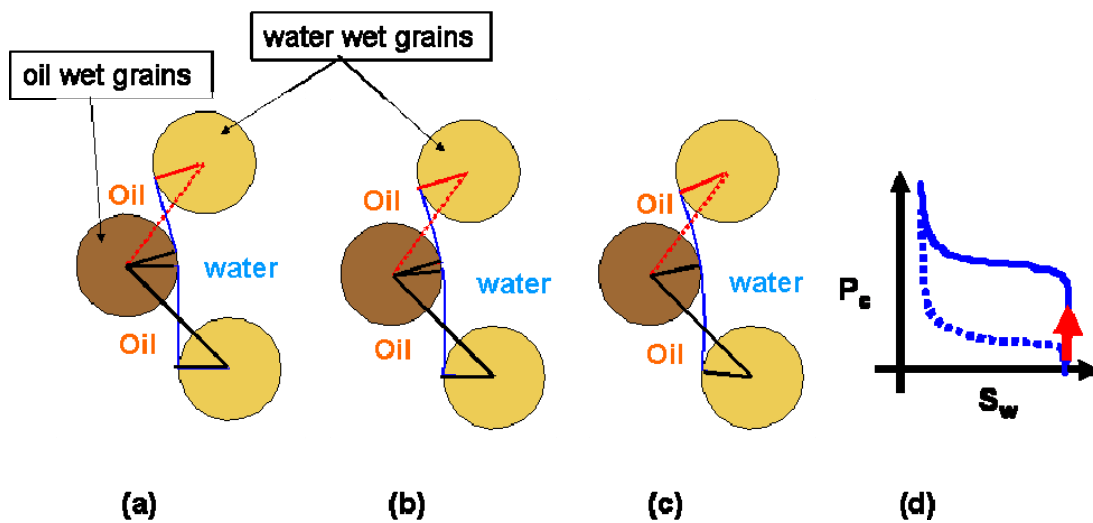


Figure 3.12. Schematic of two menisci merging (Melrose event) in a fractionally wet porous medium, two water-wet disks and one oil-wet disk construct a pore and three throats where two of them are fractionally wet and one is uniformly wet. Originally two menisci located on the two adjacent throats which are fractionally wet (a). Menisci move toward the pore by increasing curvature (b), until they touch (c) and the pore fills with oil. This Melrose event happens during drainage as the curvature is increased (d).

### 3.4.4. Simulation

In order to simulate drainage and imbibition, we apply the criteria developed above to each pore throat and pore body in the domain. The network of pore throats and pore bodies is extracted from the geometry and position of the grains within the domain. The main difference between our grain-based simulation and traditional pore network simulation is the development of the grain-based and mechanistic criteria. As a result, our model is independent of the approach of dividing pore space into the pore bodies and pore throats. Pore space can be divided into a network of pore bodies and pore throats by any approach (e.g. Delaunay tessellation [38, 42], Voronoi tessellation [103, 105], and medial axis [130, 154] methods). The pore network in our model functions as a tool to track the position of the menisci within the pore space, but all pore-filling criteria are

based on the grains position and geometry. For instance, two menisci which are not located in the same pore (e.g. they are located in two neighboring pores), still can merge if they touch each other on a disk. The disk (grain) should be common between two throats that hold the two menisci. When the two menisci touch; Melrose event occurs and both pores will be filled by invading fluid.

We simulate the menisci motion using the invasion percolation algorithm, changing curvature in small increments then computing the stable meniscus locations in all pores. At any given curvature (capillary pressure) all pores that are connected to the inlet (via invading fluid) will be in list of candidates for invasion. We check the candidate pores for criteria of invasion (Melrose or Haines criteria). If a candidate meets the criteria of invasion and it also connected to the outlet, we invade the candidate and add the neighboring pores to list of candidates. We continue until no candidate remains in the list. Candidates that are not connected to the outlet are labeled “trapped” and removed from further consideration of events. We increase or decrease the curvature incrementally and repeat the procedure above.

### **3.5. RESULTS**

Result of simulating fluid configuration within a porous medium is discussed in detail in Appendix D. In this section, we focus on the result for drainage and imbibition for a fractionally wet porous medium. Fig. 3.13 shows the imbibition and drainage curves for a porous medium with 50% of disks are oil-wet. The porous medium is composed of 500 equal size disks (excluding membrane disks). For this and subsequent figures, the curvature is dimensionless such that a curvature of 2 corresponds to the curvature of the disks surface. The radii of the disks are normalized to have value of unity. Initially the porous medium was filled with oil (Fig. 3.13, point  $P_0$ ), so the first process is primary imbibition where the water phase imbibes to the porous medium until residual oil phase

saturation. Then the drainage starts from imbibition end point (Fig. 3.13, point  $P_1$ ) with increasing capillary pressure and decreasing water saturation. Finally, the secondary imbibition starts from drainage endpoint (Fig. 3.13, point  $P_2$ ) and proceeds to a new value of residual oil phase saturation (Fig. 3.13, point  $P_3$ ). The model allows seamless movements of interfaces and filling events even through the zero capillary pressure level. Both Haines and Melrose events can occur with a change in the capillary pressure. All menisci are tested for both types of events depending on their local circumstances. Thus, the critical curvature for local events is dynamic and cannot be pre-calculated. This is unlike traditional invasion percolation models of capillary displacement.

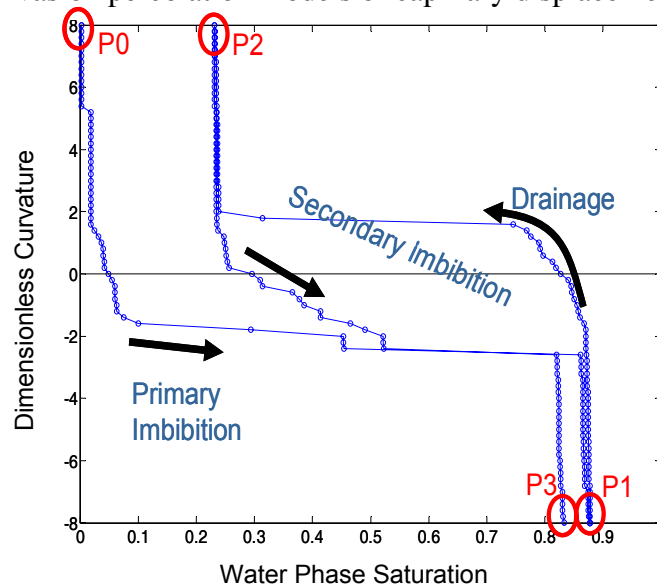


Figure 3.13. Imbibition and drainage curves for a 2D porous medium when 50% of its disks are oil-wet. The porous medium was filled with oil phase initially; first, the water phase pushes the oil out by decreasing capillary pressure (primary imbibition), second the oil phase drains the water out of the porous medium by increasing capillary pressure (drainage), and finally the water phase pushes into the porous medium again and replaces the oil phase (secondary imbibition). In all of three curves presented in this figure, the curvature ranges from positive to negative value and crosses over the zero curvature. All of these three curves were produced from the same code. The difference is just starting and ending applied curvature.

Fig. 3.14 shows the fluid configuration corresponding to point ( $P_2$ ) at the drainage curve in Fig. 3.13. One can see the water trapped inside the porous medium in disconnected blobs. The region outlined in cyan shows a shell of water-wet grains in which a blob of water phase is trapped, the region outlined in dark red shows an outer shell of oil-wet grains around the water-wet shell. This pattern is characteristic of trapped water in this class of porous media. From the figure, it can be observed that the water phase trapped in the cluster of water-wet grains surrounded by oil-wet grains.

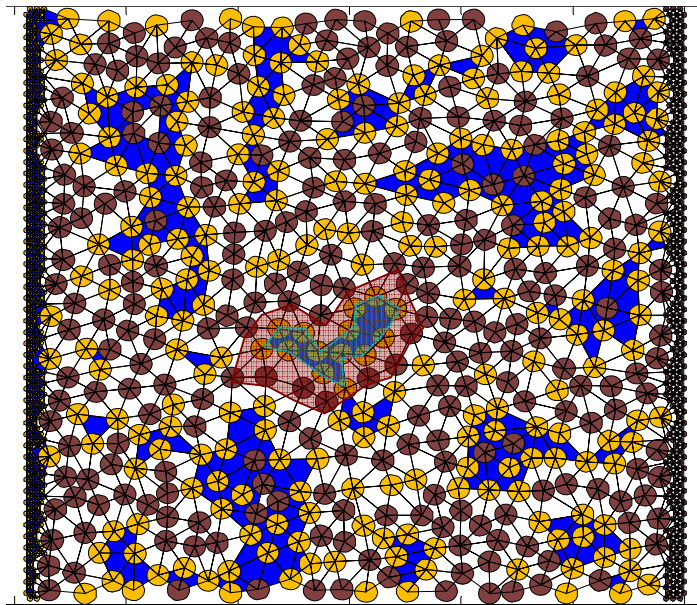


Figure 3.14. Schematic of drainage end point for the porous medium with 50% of disks are oil-wet (the same porous medium as Fig. 3.13). The blue color represent the trapped water phase and the white color is the oil phase. The dark brown disks are oil-wet disks and the yellow disks are the water-wet disks. The region outlined in cyan shows a shell of water-wet grains in which a blob of water phase is trapped, the region outlined in dark red shows an outer shell of oil-wet grains around the water-wet shell. This pattern is characteristic of trapped water in this class of porous media.

Our modeling approach considers both Haines and Melrose events on imbibition and drainage, as it is necessary for mixed wet or fractionally wet media. This gives the

model an inherent robustness in the sense that all grains, throats, and pore bodies are considered equivalent, just with a different contact angle for each grain. This robustness can be seen by considering a 25% oil-wet medium, and the equivalent 75% oil-wet medium in which all of the oil-wet grains are made water-wet and vice-versa. By reversing the wettability of each grain, the capillary pressure curve should also be reversed. Fig. 3.15a shows the 25% oil-wet capillary pressure curve obtained with the model, and Fig. 3.15b shows the 75% oil-wet capillary pressure curve. The symmetry is evident, as the drainage in the 25% oil-wet medium is identical to the imbibition in the 75% water-wet medium. This shows that the model is performing as expected. Note that this symmetry is only seen if each grain's wettability is reversed. If the position of the grains is different, or the pattern of the oil-wet grains is different, the model will show slightly different capillary pressure curves.

We emphasize that by checking Haines and Melrose criteria for all pores, the algorithm has generalized the notion of simulating drainage and imbibition. The very same code is used for all paths shown in Fig. 3.15; the only difference inside the code between drainage and imbibition is the sign of the increment in curvature. In contrast, traditional pore network models have algorithms specific to drainage and different algorithms for imbibition; only the machinery of invasion percolation is common to both. Applied to uniformly wet media, our algorithm correctly finds only Haines events during drainage and only Melrose events during imbibition.



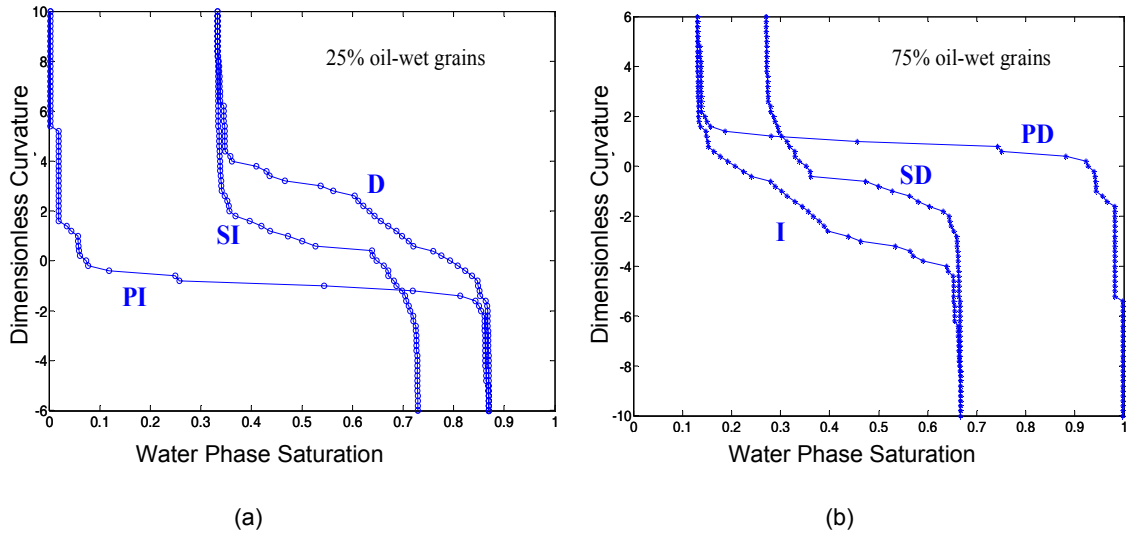


Figure 3.15. (a) Primary imbibition (PI), drainage (D) and secondary imbibition (SI) curves for a porous medium with 25% oil-wet disks. (b) Primary drainage (PD), imbibition (I) and secondary drainage (SD) curves for a porous medium with 75% oil-wet disks. The curves on the Figs. 3.15a and 3.15b are vertically symmetric, so if the Fig. 3.15b rotates 180°, the curve will be match with curves on Fig. 3.15a.

We can now use the model to study how the drainage and imbibition curves vary with the change of oil-wet fraction. Fig. 3.16 shows the primary drainage curves for porous media with different fraction of oil-wet disks. As before, the oil-wet disks have a contact angle of 180° and the water-wet disks have a contact angle of 0°. As expected, with increasing oil-wet fraction in the media, the drainage curves move to lower capillary pressures. More interestingly, the movement is not linear. Small (10%, 20%) percentages of the oil-wet fraction do not significantly change the position of the drainage curve from the complete water-wet case. Large changes in the curve are only seen once a threshold of approximately 40% oil-wet grains is achieved. Likewise, when the medium is primarily oil-wet (> 80%), the changes in the drainage curve are minor.

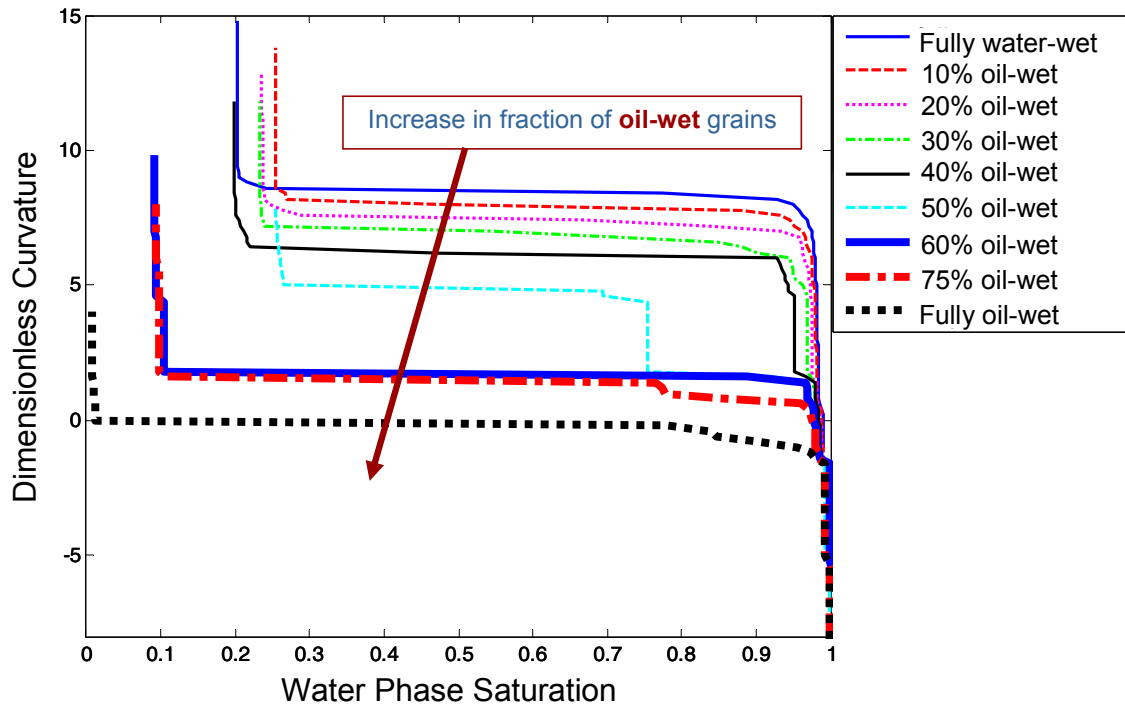


Figure 3.16. Comparison between primary drainage curves for the porous media with different fractions of oil-wet ( $\theta_{ow} = 180^\circ$ ) disks distributed randomly among water-wet ( $\theta_{ww} = 0^\circ$ ) disks. The porous media was originally filled with water. The oil phase pushes the water phase out as the capillary pressure (curvature) increases. As the fraction of oil-wet disks within the porous medium increases, the curvature which the oil phase percolates through the porous medium decreases.

Fig. 3.17 shows the model results for the primary imbibition curves for porous media with different fraction of oil-wet disks. Again, the curves tend to lower capillary pressures with increasing oil-wet fraction. Also, the change in capillary pressure is minor for the first 20-30% of oil-wet grains. The change is large for oil-wet percentages around 50%, and the change is small when the oil-wet fraction is greater than 70-80%.

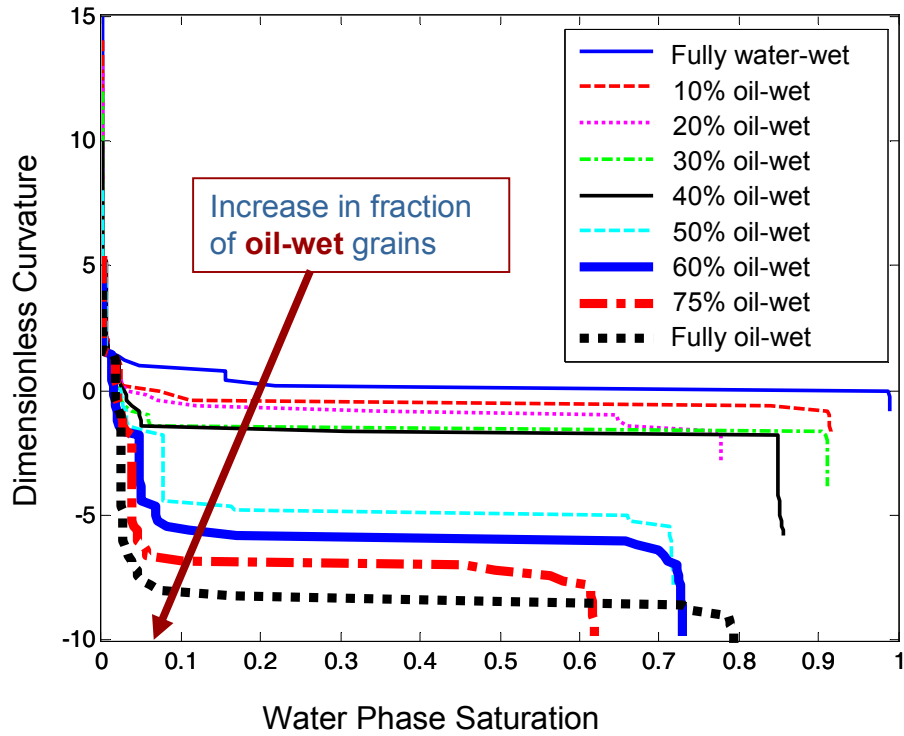


Figure 3.17. Comparison between primary imbibition curves for the porous media with different fractions of oil-wet disks; the contact angles on water-wet and oil-wet disks are  $\theta_{ww} = 0^\circ$  and  $\theta_{ow} = 180^\circ$ , respectively. The porous media was originally filled with oil. The water phase pushes the oil phase out as the capillary pressure (curvature) decreases. As the fraction of oil-wet disks within porous medium increases, the curvature which the water phase percolates through porous medium decreases.

### 3.6. MODEL VALIDATION

Ashouripashaki [14] performed laboratory experiments to obtain air/water and octane/water pressure-saturation curves for primary drainage, and primary imbibition into fractionally wet sand packs. The primary imbibition was performed only on water/air system. Water-wet sands (grain size  $d_{50} = 0.35\text{mm}$ ) was used as the water-wet grains; the oil-wet grains were made by tumbling the clean sand in a 5% OTS (octatrchlorosilane) in ethanol solution for 5 hours. After tumbling, the sand grains were rinsed in ethanol 5-6

times to remove the excess OTS, followed by air drying the sand. Fractionally wet packs were made by mixing prescribed proportions of the water-wet and oil-wet grains.

The experiments were performed in 60 cm long columns (2.54 cm inner diameter), which were filled with the fractionally wet sand. The columns consisted of separate 3 and 1 cm long sections of polycarbonate tubing that were held together with polyolefin shrink tubing. For drainage, the column was filled from below with water and flushed for 1 hour to remove entrapped air. Primary drainage was then performed by attaching a constant head tank to the outlet at the bottom of the column, and air (or octane) was allowed to enter the top at atmospheric pressure. Primary imbibition starts with an air-dry column, and the attachment of the constant head tank at the bottom of the column. For imbibition, the height of the constant tank was chosen such that the water would rise roughly halfway through the column. Each column was allowed to equilibrate for 1 week. After this, the capillary pressure in each section was obtained assuming capillary gravity equilibrium. The water content was obtained by sectioning the column and obtaining the water saturation through the section's wet and dry weight.

Fig. 3.18a shows the measured  $P$ - $S$  curves (pressure saturation curves) for primary drainage for 5 different sands of varying oil-wet fraction. The primary drainage measured for octane/water system. The drainage curves move monotonically lower with increasing oil-wet fraction. We simulate the primary drainage for a media with the same fraction of oil-wet grains as experimental data (e.g. 0, 25%, 50%, etc.). We multiply the dimensionless curvature by the known interfacial tension and divide by grain size to obtain the capillary pressure in Pascal for simulation results. Fig. 3.18b shows the simulation results for 2D fractionally wet porous media. The trend with increasing oil-wet fraction and the overall capillary pressure match between experimental data and simulation results are very good. The simulation prediction tends to be flatter than the

experiments and this is likely due to the fact that it is a two-dimensional media in contrast with the 3D experimental media

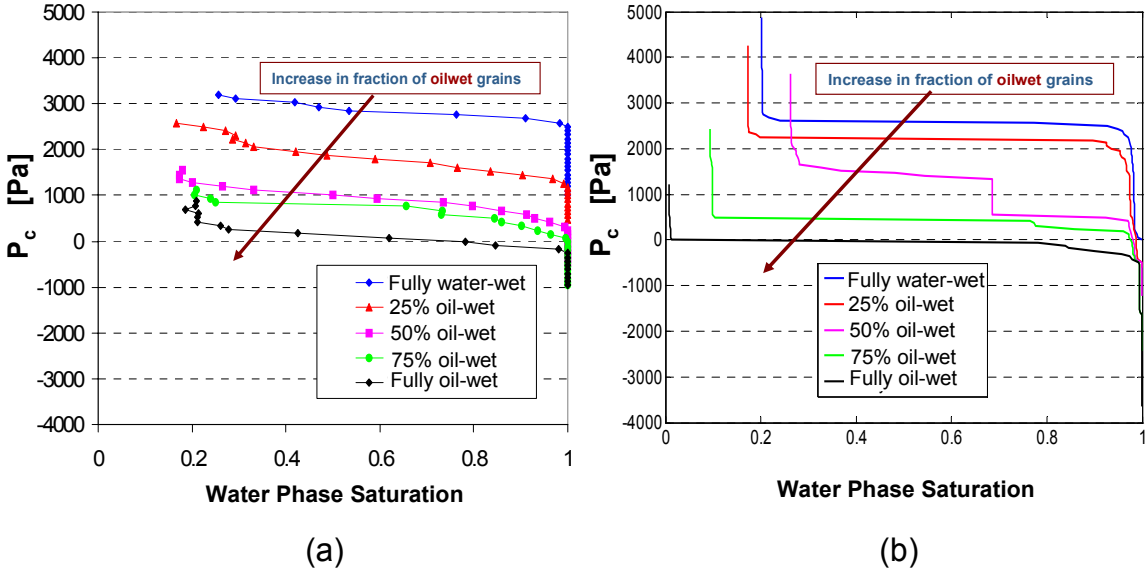


Figure 3.18. (a) Measured octane/water drainage curve for the fractionally wet media. The primary drainage curves move monotonically lower with increasing oil-wet fraction. (b) Shows the simulation result for drainage of fractionally wet media. The contact angles on water-wet and oil-wet disks are  $\theta_{ww} = 0^\circ$  and  $\theta_{ow} = 180^\circ$ , respectively. For the model, we multiply the curvature by the known interfacial tension and divide by the grains radii to obtain the capillary pressure in Pascal.

Fig. 3.19a shows the measured  $P$ - $S$  curves for primary imbibition for 5 different sands of varying oil-wet fraction. The primary imbibition was measured for air/water system. The imbibition curves move monotonically lower with increasing oil-wet fraction. We simulate the imbibition for a medium with the same fraction of oil-wet grains as experimental data. We multiply the dimensionless curvature by the known interfacial tension and divide by grain radii to obtain the capillary pressure in Pascal for simulation results. Fig. 3.19b shows the simulation results for 2D fractionally wet porous media.

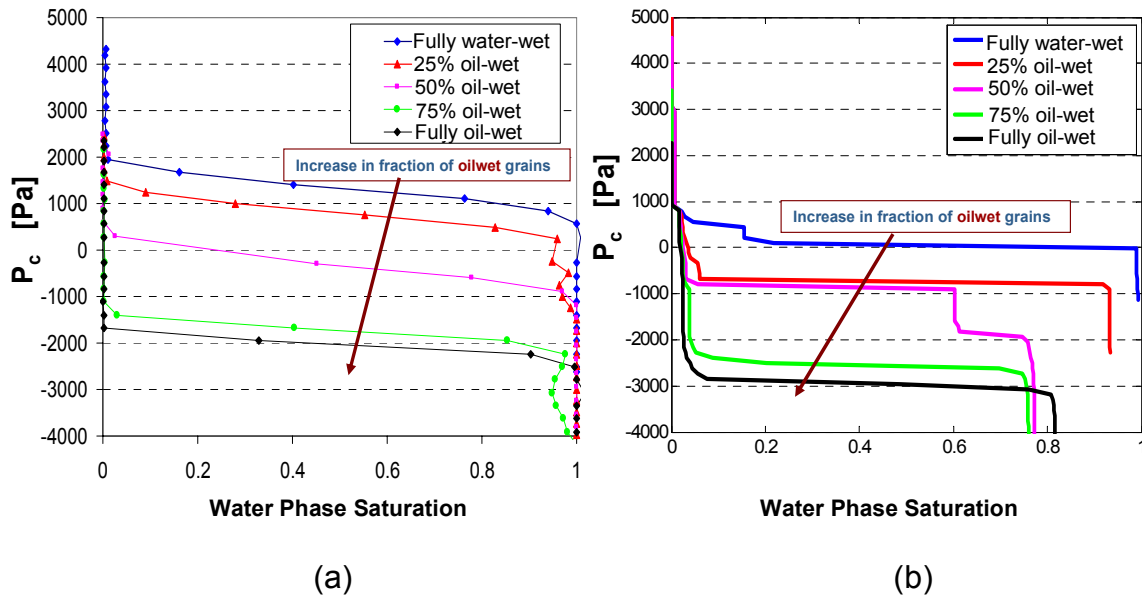


Figure 3.19. (a) Measured air/water imbibition curve for the fractionally wet media. The primary imbibition curves move monotonically lower with increasing oil-wet fraction. (b) Shows the simulation result for imbibition of fractionally wet media. The contact angles on water-wet and oil-wet disks are  $\theta_{ww} = 0^\circ$  and  $\theta_{ow} = 180^\circ$ , respectively. For the model, we multiply the curvature by the known interfacial tension and divide by the grain radii to obtain the capillary pressure in Pascal.

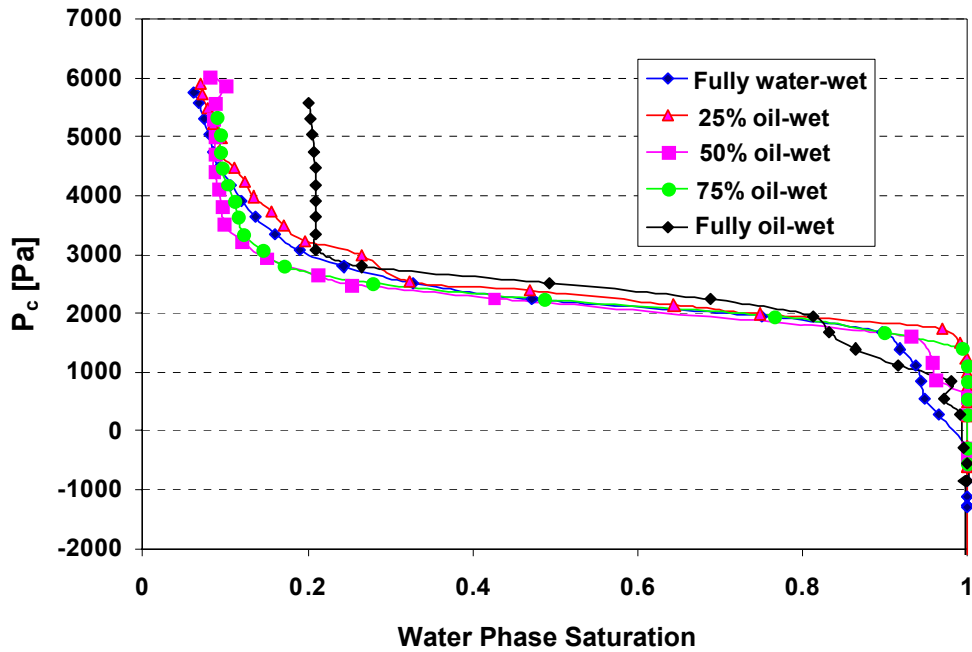


Figure 3.20. Water/air drainage curves for the fractionally wet media. Primary drainage curves do not show much change with changing oil-wet fraction.

Fig. 3.20 shows the measured  $P$ - $S$  curves for primary drainage for 5 different sands of varying oil-wet fraction. The primary drainage measured for air/water system. Unlike the primary drainage in octane/water system, the drainage curve is not sensitive to the fraction of oil-wet grain within the medium. In the drainage experiment data for air/water system, there is no distinct difference between applied capillary pressures in which the air breakthrough the porous medium.

### 3.7. DISCUSSION

The model developed in this paper consists of 2D disks as it is the simplest to observe the actual mechanics of the menisci movement. Clearly, the trapped phases will change in a 3D rather than a 2D model. Still there are many parallels between the  $P$ - $S$  curves obtained from this 2D model and those obtained from experiments in 3D porous media.

The most obvious parallels are seen between the experimental data for drainage curves in octane/water system (Fig. 3.18a) and simulation results for primary drainage of fractionally wet media (Fig. 3.18b and Fig. 3.16). The capillary pressure corresponding to the percolation threshold decreases monotonically in all of those figures. When the capillary pressure is increased, the water saturations go from near saturated to near completely unsaturated at a specific capillary pressure; this capillary pressure correspond to the percolation threshold. The invading fluid breaks through the porous medium when the capillary pressure reaches percolation threshold value. The percolation threshold changes nonlinearly with fraction of oil-wet grains in both experimental data and simulation results. Looking at the model results (Fig. 3.16), starting from 0% oil-wet fraction, the transition capillary pressure (percolation threshold) decreases only slightly up to about 40% oil-wet fraction; between 40% and 60% oil-wet fraction there is a large decrease in the transition capillary pressure; finally between 60% and 100% the transition capillary pressure decreases only slightly. In experimental data (Fig. 3.18a), a moderate change of the transition capillary pressure between 0% and 25% oil-wet fraction; a moderate change of the transition capillary pressure between 25% and 50% oil-wet fraction; a slight change between 50% and 75%, and finally a moderate change between 75% and 100%.

Despite this difference between experimental data and simulation result, the overall match is satisfactory. For instance, in both experimental data and simulation result, all of drainage curve (except 100% oil-wet) located above zero capillary pressure. In both experimental measurement and simulation results, small portion of the drainage curves for the fully oil-wet (100% oil-wet) medium locate below zero capillary pressure and most of the curves locate above the zero capillary pressure.



In the imbibition curves, Figs. 3.17 (model) and 3.19a (experiment), the transition capillary pressure (percolation threshold) decreases monotonically with increasing oil-wet fraction in both figures. More interestingly, the transition capillary pressure does not change linearly with oil-wet fraction in either figure. Looking at the model results (Fig. 3.17), starting from 0% oil-wet fraction, the transition capillary pressure decreases only slightly up to about 40% oil-wet fraction; between 40% and 60% oil-wet fraction there is a large decrease in the transition capillary pressure; finally between 60% and 100% the transition capillary pressure decreases only slightly. Looking at the experimental results (Fig. 3.19a), the same pattern is observed: a slight change of the transition capillary pressure between 0% and 25% oil-wet fraction; a large change between 25% and 75%, and finally a slight change between 75% and 100%.

The simplest explanation is in terms of percolating clusters of like wettability grains. The model suggests that the capillary pressure curve shows minor changes until 40% of the grains are oil-wet. Above this threshold, there are enough oil-wet grains to percolate across the model, allowing a rapid change in the capillary pressure curve. The experimental data are not obtained for as many fractions as the model, so the exact percentage of oil-wet grains needed to percolate is unknown (it is somewhere between 25% and 50%). It is likely that the 2D model and 3D experiments would lead to different percolating fractions, but the general nature of the curves would be similar.

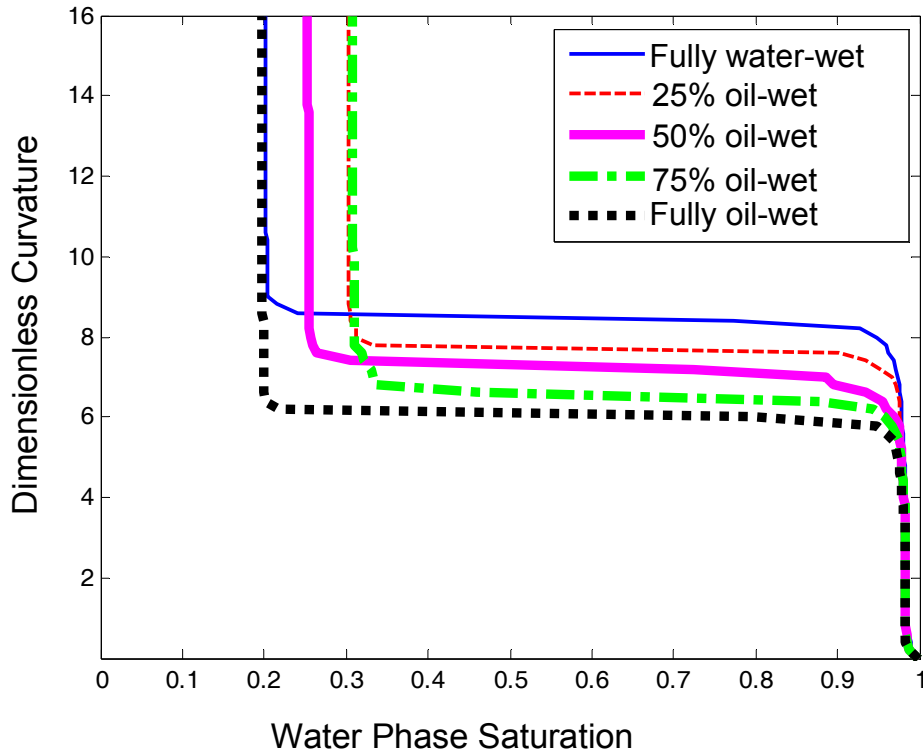


Figure 3.21. Comparison between primary drainage curves for porous media with different fraction of oil-wet ( $\theta_{ow} = 50^\circ$ ) disks distributed randomly among water-wet ( $\theta_{ww} = 0^\circ$ ) disks. If the oil-wet disks are not perfectly hydrophobic, as commonly occurs in experiments when the grains are treated chemically, the change in the capillary pressure curve is less dramatic.

For the drainage curves of air/water system, the match between experimental data and model results is not as straightforward, mainly because there is no observed change in the transition capillary pressure for the experiments. Similar experimental behavior was observed for water/air systems with the oil-wet grains being silanized versions of the water-wet grains [19, 204]. In this case, it is most likely a result of the contact angle not being  $180^\circ$  for drainage from the oil-wet grains. Ustohal *et al.* [204] estimates a receding (draining) contact angle of  $50^\circ$  for silanized sand, far from the  $180^\circ$  that the model results in Fig. 3.16 show. The model is robust enough to handle different contact angles in calculating the movement of the menisci. Fig. 3.21 shows the model results for drainage

from fractionally wet media, where the contact angle of the water-wet grains is  $0^\circ$  and the contact angle of the oil-wet grains is  $50^\circ$ . As in Fig. 3.16, the transition capillary pressure decreases with increasing oil-wet fraction, but the change in capillary pressure is much less. The fit with the experiments in Fig. 3.20 is better, suggesting that careful, independent measurement of contact angle is necessary for evaluating behavior of fractionally wet media in air/water system.

### 3.8. SUMMARY

We developed a grain-based, mechanistic model for an oil/water displacement under capillary control in the fractionally wet media. The model invokes the two types of irreversible pore-level events: Haines jumps (single meniscus in a throat) and Melrose mergers (two menisci on adjacent throats merging). We implemented and illustrated the model in the two dimensional media, solving analytically for stable configuration of the meniscus held between pairs of grains of arbitrary and unequal contact angle. We carried out drainage and imbibition simulations that yield *a priori* predictions of the grain-scale configurations of water/oil interfaces (menisci) within the fractionally wet porous medium.

We used this grain-based and mechanistic model to predict macroscopic properties (e.g.  $P$ - $S$  curve for imbibition and drainage) of a fractionally wet porous medium that are qualitatively in agreement with experimental data. The experimental data and simulation results show a nonlinear behavior between the position of  $P$ - $S$  curves and fraction of oil-wet grains.

## **CHAPTER 4: UNIFIED MODEL OF DRAINAGE AND IMBIBITION IN 3D FRACTIONALLY WET POROUS MEDIA**

### **4.1. ABSTRACT**

We develop a grain-based model for capillary controlled displacement within 3D fractionally wet porous media. The model is based on a novel local calculation of the position of stable interfaces in contact with multiple grains. Each grain can have a different, arbitrary contact angle with the interface. The interface is assumed to be locally spherical for menisci separating the non-wetting and wetting phases. The interfaces between pairs of grains (pendular rings) are assumed toroidal. Because the calculation of interface position is entirely local (grain-based), it provides a single, generalized criterion that applies to drainage as well as to imbibition events. This generality is essential for modeling displacements in fractionally wet media. Pore filling occurs when an interface becomes unstable in a pore throat (analogous to Haines condition for drainage in a uniformly wet throat), or when two or more interfaces come into contact and merge to form a single interface (the Melrose condition for imbibition).

The concept of tracking the fluid/fluid interface on each grain (i.e. grain-based modeling) allows the model to be independent of the definition of pores. As a result, the pore space can be divided to pores and throats by any approach (e.g. Delaunay tessellation, Voronoi tessellation, and medial axis methods).

The analytical solution for stable interface locations generalizes the Melrose and Haines criteria previously validated for pore-level imbibition and drainage events in uniformly wet media. The results yield a set of purely geometric, mechanistic criteria for interface movement in 3D porous media when each grain has arbitrary contact angle.

We validate our model by comparing the simulation result with experimental data on fractionally wet porous media prepared by mixing oil-wet grains with water-wet grains. In both experimental and simulation results, the drainage/imbibition curves shift to lower capillary pressure with increasing fraction of oil-wet grains.

## 4.2. INTRODUCTION

The fundamental event in a grain-based approach to capillary controlled fluid displacement is the filling of an individual pore, just as in traditional pore network models. In this work, we establish criteria for such events in terms of grain locations and contact angles, rather than in terms of the geometry of idealized pores and throats. For invasion of a pore by a single meniscus passing through a throat, the grain-based and pore network models arrive at essentially the same result, namely the criterion for a Haines jump. For invasion of a pore by the merger of two (or more) interfaces, the grain-based approach offers a significant advantage. The correct geometry and location of pendular rings (at contacts between pairs of grains) and of menisci (between three or more grains) are readily determined in a grain-based model. We are unaware of any mechanistic way to account for these phenomena in a traditional pore network model. As a result, in traditional network models, *ad hoc* parameters and rules were used to describe invasion of a pore by the merger of two (or more) interfaces [27-29, 158, 159]. Haines jumps and mergers of two (or more) interfaces both occur during any cycle of drainage or imbibition in a fractionally wet medium. Consequently, using a grain-based approach for modeling of fluid flow within fractionally wet media seems natural.

In our grain-based model we are looking for the stable position of menisci on the grains. As a result, our model is independent of the approach of dividing pore space into the pore bodies and pore throats. The pore space can be divided into a network of pore

bodies and pore throats by any approach (e.g. Delaunay tessellation [38, 42], Voronoi tessellation [103, 105], and medial axis [130, 154] methods). The pore network in our model functions as tool to track the position of the menisci within the pore space, but all pore-filling criteria are developed based on the grains. For instance, two menisci which are not located in the same pore (e.g. they are located in two neighboring pores), still can merge if they touch each other on a common grain. The common grain should be common between two throats that hold the two menisci. When the two menisci touch, both pores will be filled by invading fluid.

We conclude that a grain-based approach is essential for obtaining a mechanistic understanding of fluid displacements in fractionally wet media. This assertion is supported by the successful prediction of imbibition curves in uniformly wet media [80]

### **4.3. MODEL**

#### **4.3.1. Model of Pore Space**

To study the movement in menisci through 3D fractionally wet porous media, we use a dense random packing of equal spheres generated by cooperative rearrangement algorithm (see Chapter 1 for more details; see also ref. [191]). The sphere pack is composed of 7000 equal size spheres (Fig. 4.1a). Each sphere can be made either water-wet or oil-wet.

We use the approach of Bryant *et al.* [42] to obtain simple network models from the sphere pack. We use a Delaunay tessellation of the spheres centers to subdivide the pore space into pore bodies and pore throats. The tessellation yields tetrahedra (Fig. 4.1b). Each tetrahedron has four faces and each face is the narrowest local path between outside and inside of the tetrahedron. Each face of a tetrahedron therefore corresponds to a pore throat. The space inside each tetrahedron (excluding the grain's portion) is the

pore body (Fig. 4.2). Each tetrahedron has four faces. Consequently, each pore has four throats and is connected to four neighboring pores through its throats.

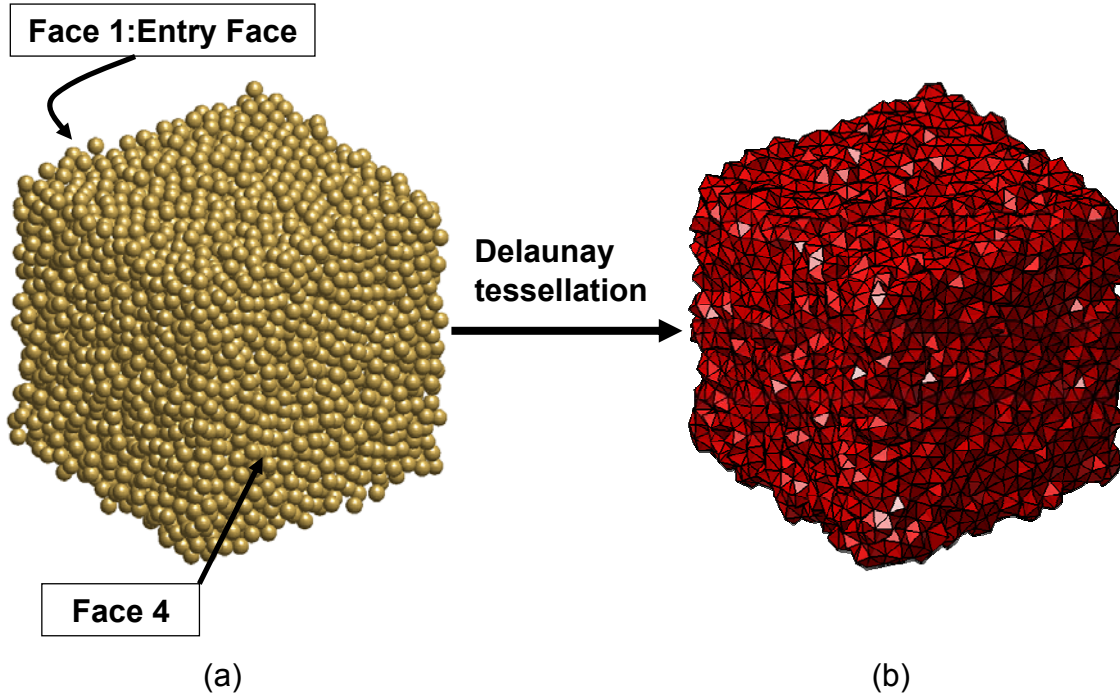


Figure 4.1. (a) Schematic of a dense random packing of equal spheres. The face 1 is used as the entry face during simulation. The exit face(s) can be only face 4 or all faces other than face 1. (b) Schematic of network of tetrahedra extracted from the sphere pack (Fig. 4.1a). The pore space within the sphere pack can be divided into pore bodies and pore throats using Delaunay tessellation. The network of pore bodies and pore throats is extracted from network of tetrahedra.

### 4.3.2. Assumptions

In this chapter, we do not take into account the existence of thin wetting films on the surface of grains. Also, the interface is assumed to be locally spherical for menisci separating the non-wetting and wetting phases. The surface of minimum energy corresponds to the surface with constant curvature, and sphere is the simplest surface with constant curvature. The interfaces between pairs of grains (pendular rings) are

assumed to be toroidal. Though the toroid does not have constant curvature, Gladkikh et. al [78] shows that the toroid model is a good approximation of the nodoid (model of fluid/fluid interface with surface of constant curvature) when calculating the properties of pendular rings relevant to our application (e.g. volume, filling angle). Here, we do not explicitly solve for the minimum surface energy, but developed our model based on the finding from studies regarding the stability of a fluid/fluid interface within the porous media [87, 88, 144]. However, Deng and Lake [62] used minimization of free energy to calculate fluid distribution of two immiscible phases in a porous medium.

### 4.3.3. Terminology

Pore: one pore (Delaunay cell) is constructed from four grains (spheres). In Fig. 4.2, the pore body is the space inside tetrahedron  $O_1O_2O_3O_4$  (exclude the grains portion). The centers of grains are the vertices of the tetrahedron (Delaunay cell).

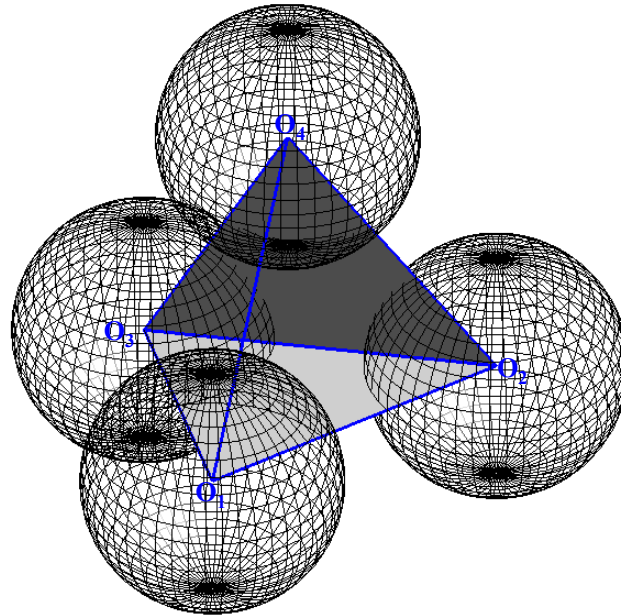


Figure 4.2. Schematic of a pore (Delaunay cell) in a random packing of equal spheres.



Throat: Three grains in a Delaunay cell define a pore throat. Thus each face of a Delaunay cell (pore) corresponds to a pore throat. A throat plane is a plane connecting the center of grains that define the throat. For instance, plane  $\triangle O_1O_2O_3$  in Fig. 4.2 is a throat plane.

**Edge:** Each edge of the tetrahedron (Fig. 4.2) corresponds to a grain-grain contact (if the spheres touch) or a gap between grains (if the spheres do not touch). Each edge connects the centers of two grains (spheres). For instance, line  $\overline{O_1O_3}$  and  $\overline{O_1O_2}$  are two edges of a pore. The grain 1 and grain 3 are in a grain-grain contact, while there is a gap between grain 1 and grain 2.

**Nomenclature:** We use a grain-based nomenclature through the text for referring to pores, throats and edges. For instance, pore 1234 in Fig. 4.2 is defined by grain 1, grain 2, grain 3 and grain 4. In the same way throat 123 is composed of grain 1, grain 2 and grain 3.

There are two morphologies for fluid/fluid interfaces within a porous medium: menisci and pendular rings.

**Meniscus:** we model a meniscus with the spherical cap. Fig. 4.3 shows a throat and a meniscus located on the throat. The throat is constructed by three grains (grain 1, grain 2, and grain 3). For a meniscus with the constant curvature, the geometry of the meniscus is defined by the center of the meniscus ( $O$ ), the radius of meniscus, and the intersections with the solid surface. The intersections of the meniscus with the grains are forced to be at the contact angle of each surface. In Fig. 4.3, the meniscus is the cap part of yellow sphere. The radius and the center of the yellow sphere and the meniscus are the same. However, the meniscus is limited to inside of the tetrahedron  $OO_1O_2O_3$ , where the vertices of the tetrahedron are the centers of the meniscus and the three grains, respectively. At zero contact angle, the meniscus is tangent to each of the three grains.

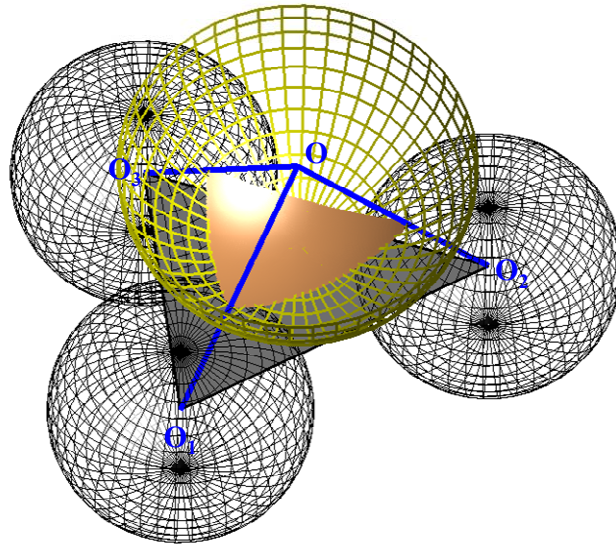


Figure 4.3. Schematic of a meniscus (brown triangular patch) located on three grains (spheres) with zero contact angles (fully water-wet).  $O$  indicates the center of the meniscus and  $O_1$ ,  $O_2$ , and  $O_3$  indicate centers of spheres constructing the throat. The meniscus is the cap part of the yellow sphere, limited to inside of the tetrahedron  $OO_1O_2O_3$ , where the vertices of the tetrahedron are the centers of the meniscus and three grains.

**Filling angle of a meniscus:** In Fig. 4.4, the filling angle of meniscus ( $\psi_2$ ) on grain 2 is the angle between the throat plane  $\triangle O_1O_2O_3$  and the line connecting the center of grain 2 ( $O_2$ ) to the contact point ( $P_2$ ). Point  $P_2$  is the point where the meniscus touches grain 2.

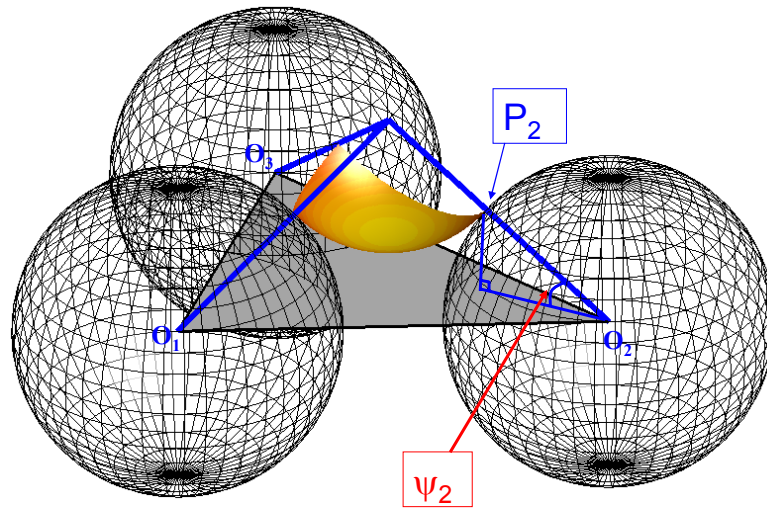


Figure 4.4. Schematic of a meniscus (yellow cap) located on three grains (spheres) with zero contact angles.  $O_1$ ,  $O_2$ , and  $O_3$  indicate centers of the grains constructing the throat. Point  $P_2$  is the point where the meniscus touches grain 2. The filling angle of meniscus ( $\psi_2$ ) on grain 2 is the angle between line  $\overline{O_2P_2}$  and plane  $\triangle O_1O_2O_3$ .

**Pendular ring/ liquid bridge:** the edges of Delaunay tetrahedra within a sphere pack can hold pendular rings and liquid bridges of wetting phase, if both grains associated with the edge have the same wettability. If the edge has a grain-grain contact, it holds the wetting phase as a pendular ring. An edge with a gap between its grains holds the wetting phase as a liquid bridge. The main difference between pendular rings and liquid bridges is stability of the pendular rings and liquid bridges. For instance, the pendular rings are always stable on the water-wet edges at positive capillary pressure, while the liquid bridges could be ruptured at high capillary pressure (For more detail, see Appendix A). The morphology of pendular rings held in the crevices associated with grain-grain contacts is qualitatively similar to the morphology of liquid bridges held on the gap between two grains. In this chapter, for simplicity we will use the terms "pendular ring" to refer to any of these morphologies.

Fig. 4.5 shows the schematic of a water-wet edge holding a pendular ring of the water phase. The contact angles between the water phase and grains are zero degrees. Pendular rings between pairs of grains are assumed toroidal. Note, only edges with the same wettability grains can hold pendular rings. For instance, a water-wet edge composed of two water-wet grains can hold a pendular ring of the water phase, while a oil-wet edge composed of two oil-wet grains can hold a pendular ring of the oil phase. A fractionally wet edge, where one of the grains is oil-wet (contact angle above  $90^\circ$ ) and the other grain is water-wet (contact angle below  $90^\circ$ ) cannot hold any pendular ring.

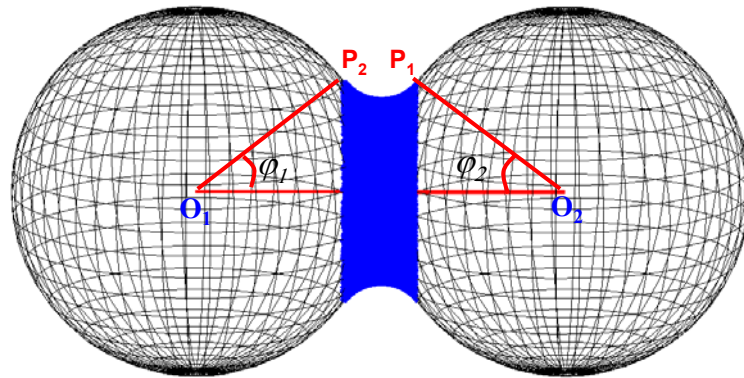


Figure 4.5. Schematic of a water-wet edge holding a pendular ring of the water phase.  $O_1$  and  $O_2$  indicate centers of grains constructing the edge. Points  $P_1$  and  $P_2$  are the points where the pendular rings touches grain 1 and grain 2 respectively. The contact angle between the water phase and grains is zero degrees.  $\phi_1$  and  $\phi_2$  are the filling angles of the pendular ring on grain 1 and grain 2 respectively.

**Filling angle of pendular ring:** The pendular ring filling angle  $\phi$  is the angle between the line connecting the centers of the two grains defining the edge (line  $\overline{O_1O_2}$  in Fig. 4.5) and the line connecting a grain center and any point at which the pendular ring touches the grain (line  $\overline{O_1P_1}$  and  $\overline{O_2P_2}$  in Fig. 4.5).

**Capillary pressure/ curvature:** Because the solid surfaces in a fractionally wet porous medium have different wettability, the terms "wetting" and "non-wetting" phase

are ambiguous. Hence we define capillary pressure to be the pressure of the non-aqueous phase (oil) minus pressure of the aqueous phase (water or brine).

$$P_c = P_o - P_w . \quad (4.1)$$

This macroscopic capillary pressure is proportional to the curvature of the microscopic interfaces through the Young Laplace equation,

$$P_c = \sigma_{ow} \left( \frac{1}{r_1} + \frac{1}{r_2} \right) = 2C\sigma_{ow} , \quad (4.2)$$

where  $r_1, r_2$  are radii of curvature and  $C$  is the mean curvature. The curvature is essentially a scaled capillary pressure. Thus, when the pressure of oil phase exceeds the water phase pressure, the capillary pressure and curvature are positive and consequently the interface curves toward the oil phase, and when the capillary pressure and curvature are negative the interface curves toward the water phase. These curved interfaces are referred to as menisci. We report the value of the curvature as dimensionless curvature by normalizing the grains radii to be unity.

***Drainage/ imbibition:*** Along these lines and following Morrow [149], we define drainage to be when the water saturation is decreasing, and imbibition to be when the water saturation is increasing.

#### **4.3.4. Grain-Based Mechanistic Criteria for Menisci Movement**

The essential features of a grain-based approach are (i) the locations of the grains and (ii) the wettability (contact angle) of each grain. The former data allow an unambiguous identification of pores and throats, without recourse to sampling a distribution or specifying a shape. The latter data lead to criteria for stable configurations of the fluid /fluid interfaces (i.e. menisci and pendular rings).

In fractionally wet porous media, a fluid/fluid interface can become unstable if any of the criteria below is met.

1. The curvature of meniscus exceeds the critical curvature for the throat holding the meniscus (corresponds to Haines criterion for drainage in uniformly wet throat).
2. Two menisci merge and become a single meniscus (analogous to Haines criterion for imbibition in uniformly wet pore).
3. A meniscus touches a pendular ring inside a pore (analogous to Melrose criterion for imbibition in uniformly wet pore).
4. Two pendular rings touch each other inside a pore (corresponds to Melrose criterion for coalescence of pendular rings).
5. A meniscus associated with three grains touches a fourth grain located in front of the meniscus (meniscus-4<sup>th</sup> grain criterion).

### ***Generalized Haines Drainage Criterion***

Haines [87] defines the drainage critical curvature of a throat as the curvature of the biggest sphere that can pass through the opening of the throat. In the case of a strongly water-wet medium (i.e. contact angles of the grains equal to zero degrees), when the radius of the meniscus becomes smaller than the inscribed radius of the throat, the throat cannot hold the meniscus and the meniscus passes through the throat. However, when the contact angle between meniscus and grains which define the throat is non zero, the above rule cannot be applied. We develop a general rule for the drainage critical curvature of a throat with arbitrary contact angle on each grain defining the throat.

For a throat composed of three grains with arbitrary contact angle, the drainage critical curvature is given by the curvature of the meniscus when the center of the meniscus (cf. Fig. 4.3) is located on the throat plane (cf. Fig. 4.2). As curvature increases, the center of the meniscus approaches the throat plane. When the center of the meniscus reaches the throat plane, the throat cannot hold the meniscus after any further increment in curvature. Thus, the curvature at which the meniscus center reaches the throat plane is

identified as the critical curvature for passing through the throat. This criterion reduces to the Haines criterion for drainage in the case that all three grains make contact angle of zero with the meniscus. Thus, we refer to a generalized Haines drainage criterion. We develop this criterion based on the analytical solution for the position and stability of a meniscus on a throat with arbitrary contact angle.

Here, the focus is more concept and demonstration of how this criterion works. For illustration we examine the drainage critical curvature on a 2D throat. A 2D throat is composed of two disks, and the 2D meniscus is part of a circle (Fig. 4.6 and Fig. 4.7). Fig. 4.6a shows the meniscus (blue curve) located on a water-wet throat. The curvature of the meniscus is smaller than the drainage critical curvature for that throat. As a result, the center of the meniscus is located above line  $\overline{O_1O_2}$ , which connects the centers of two disks. In Fig. 4.6b, the curvature of meniscus equals the drainage critical curvature. At this curvature, the center of the meniscus is positioned on line  $\overline{O_1O_2}$  at point  $O$ , and at any larger curvature there is no stable location for the meniscus.

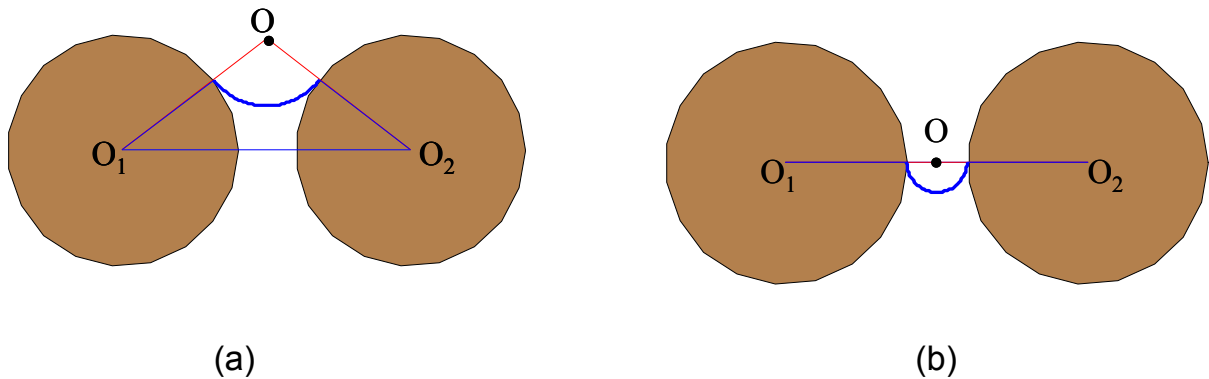


Figure 4.6. Schematic of meniscus (blue curve) located on two disks with zero contact angles (fully water-wet).  $O$  indicates the center of the meniscus and  $O_1$  and  $O_2$  indicate the center of disks constructing the throat. a) Curvature of the meniscus is smaller than the drainage critical curvature for the throat. (b) Curvature of the meniscus equals the drainage critical curvature.  $O$  (center of meniscus) is located on line  $\overline{O_1O_2}$ .

In Fig. 4.7, the throat which holds the meniscus is fractionally wet. In Fig. 4.7a, the curvature of meniscus is smaller than the drainage critical curvature for that throat. As a result, the center of meniscus is located above line  $\overline{O_1O_2}$ , which connects the centers of two disks. In the Fig. 4.7b, the center of the meniscus is positioned on line  $\overline{O_1O_2}$ . Thus the curvature of the meniscus equals the drainage critical curvature.

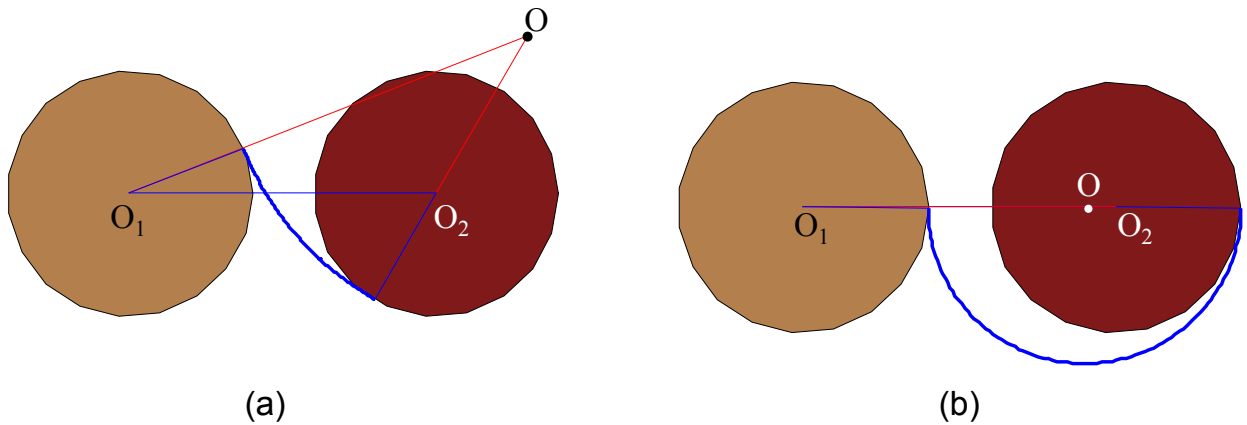


Figure 4.7. Schematic of meniscus (blue curve) located on a fractionally wet throat.  $O$  indicates the center of the meniscus and  $O_1$  is the center of water-wet disk (contact angle= $0^\circ$ ) and  $O_2$  is the center of oil-wet disk (contact angle= $180^\circ$ ) the center of disks constructing the throat. (a) Curvature of the meniscus is smaller than the drainage critical curvature for the throat. (b) Curvature of the meniscus equals the drainage critical curvature.  $O$  (center of the meniscus) is located on line  $\overline{O_1O_2}$ .

Similar criteria will be applied to a 3D throat; if the center of the meniscus is positioned on the throat plane, then the curvature of the meniscus equals the drainage critical curvature for that throat. Fig. 4.8a shows the meniscus (yellow cap) located on a water-wet throat. The curvature of meniscus is smaller than the drainage critical curvature for that throat. As a result, the center of meniscus stands above plane  $\triangle O_1O_2O_3$  (throat plane). However, in Fig. 4.8b, the curvature of meniscus equals the



drainage critical curvature of the throat. Thus, the center of the meniscus (brown cap) is positioned on the plane  $\triangle O_1O_2O_3$ .

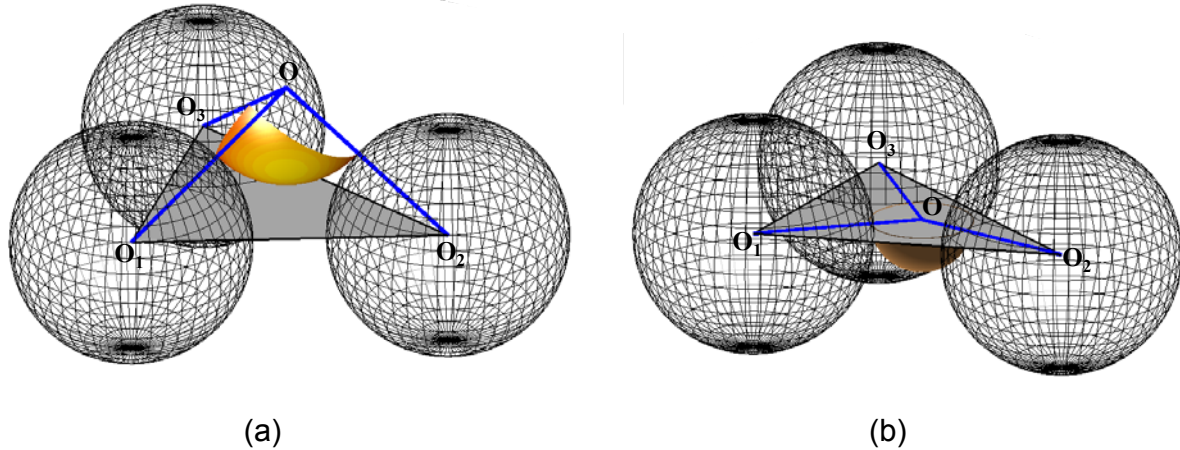


Figure 4.8. Schematic of a meniscus (yellow cap in (a), brown cap in (b)) located on three grains (spheres) with zero contact angles (fully water-wet).  $O$  indicates the center of the meniscus and  $O_1$ ,  $O_2$ , and  $O_3$  indicate the center of spheres constructing the throat. (a) Curvature of the meniscus is smaller than the drainage critical curvature for the throat. (b) Curvature of the meniscus equals the drainage critical curvature of the throat.  $O$  (center of meniscus) is located on plane  $\triangle O_1O_2O_3$ .

In Fig. 4.9 the throat which holds the meniscus is fractionally wet. In Fig. 4.9a, the curvature of the meniscus is smaller than the drainage critical curvature for that throat. As a result, the center of meniscus stands above plane  $\triangle O_1O_2O_3$  (throat plane). The  $O_1$ ,  $O_3$  are the centers of water-wet grains and  $O_2$  is center of the oil-wet grain. In Fig. 4.9b, the curvature of meniscus equals the drainage critical curvature. Thus, the center of the meniscus is positioned on the plane  $\triangle O_1O_2O_3$ .

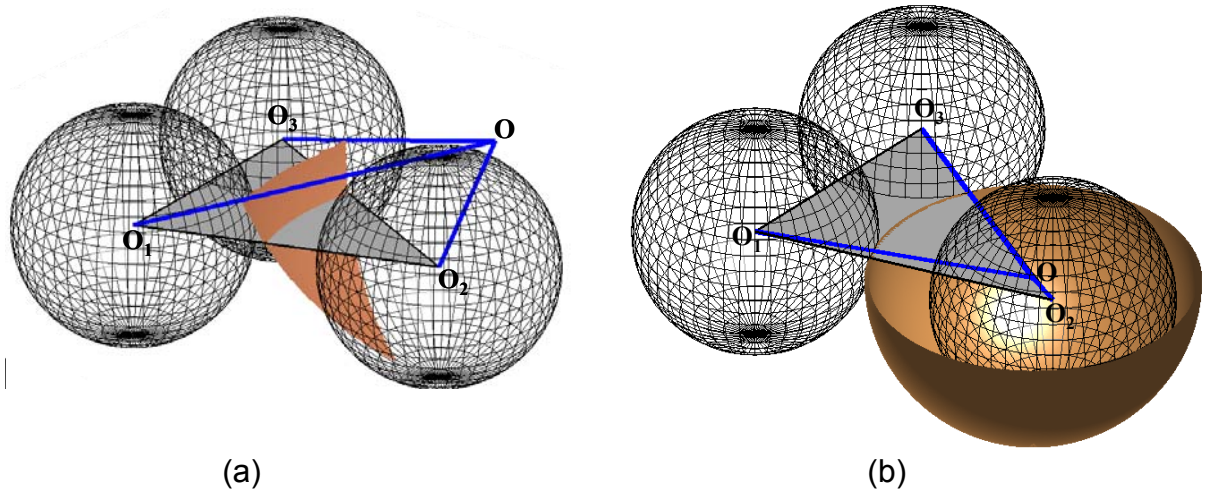


Figure 4.9. Schematic of a meniscus (light brown cap in (a), brown hemisphere in (b)) located on a fractionally wet throat.  $O$  indicates the center of the meniscus and  $O_1$  and  $O_3$  is the center of water-wet grains (contact angle= $0^\circ$ ) and  $O_2$  is the center of oil-wet grain (contact angle= $180^\circ$ ). (a) Curvature of the meniscus is smaller than the drainage critical curvature for the throat. (b) Curvature of the meniscus equals the drainage critical curvature.  $O$  (center of meniscus) is located on the plane of  $\triangle O_1O_2O_3$ .

### ***Generalized Haines Imbibition Criterion***

Haines [87] defines imbibition critical curvature of a pore as the curvature of the biggest sphere that can be held inside a pore. In the case of a strongly water-wet medium (i.e. contact angle equal to zero degree), the imbibition critical curvature of the pore equal to curvature of the sphere inscribed in the pore. However, when the contact angle between menisci and grains which define the pore is non zero, the above rule cannot be applied. We develop a general rule for the imbibition critical curvature of a pore with arbitrary contact angle.

We define the imbibition critical curvature of a pore as the curvature of a meniscus that results from merging two menisci located on two adjacent throats in a pore. The merging of two menisci occurs when centers of two menisci merge to the same point.

This criterion reduces to the Haines criterion for imbibition in the case that all four grains of the pore make contact angle of zero with the menisci. Thus, we call this a generalized Haines imbibition criterion. No direct analogy for Haines imbibition criterion exists in 2D media. However, there is similarity between merging two menisci within 2D media (Melrose event, see Chapter 3 for more details) and merging two menisci within 3D media (generalized Haines imbibition criterion). Two menisci in a 2D pore are distinct, disconnected interfaces, and ignoring sub-pore-scale features of wetting films, the merger of two (or more) menisci is geometrically well defined and corresponds to a Melrose event. In contrast, two menisci in a 3D pore are connected, e.g. by an interface where wetting phase is held at a grain-grain contact. In the example of Fig. 4.10, the red and blue menisci are connected by the interface in the crevice between grains 2 and 3. The connecting interface has a different shape (toroidal) from the menisci (spherical), but the situation does not correspond to the notion of merging two previously disconnected interfaces. Consequently, merging two (or more) menisci in 3D cannot properly be called Melrose event. Nevertheless, a closely analogous geometric criterion can be deduced.

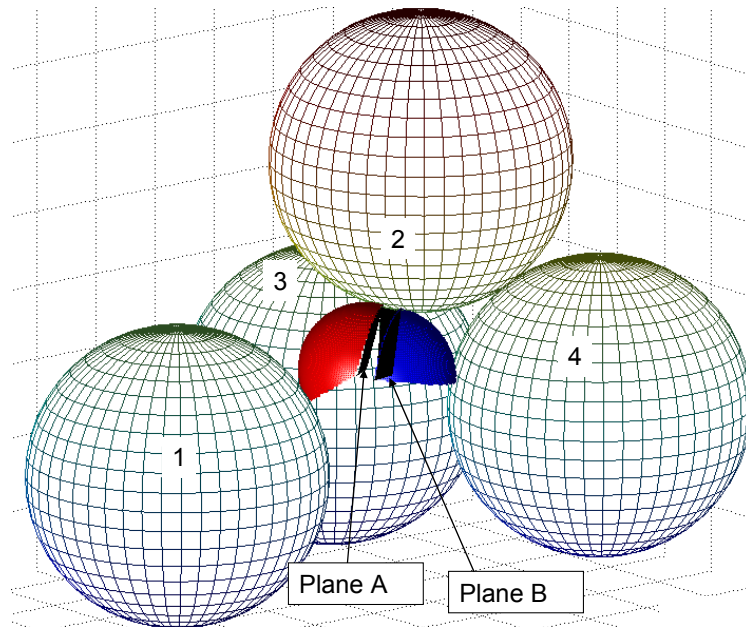


Figure 4.10. Schematic of two menisci located on two adjacent throats. The red meniscus sits on throat 123 and the blue meniscus sits on throat 234. All grains make zero contact angles with the two menisci. The menisci are connected by a wedge of wetting phase between grains 2 and 3.

Fig. 4.10 shows a pore composed of four grains (1, 2, 3, and 4). Two menisci (blue and red) are located in two adjacent throats (throat 123 and throat 234). Throat 123 is defined by grains (1, 2, and 3) and throat 234 is defined by grains (2, 3, and 4). The red meniscus sits on throat 123 and the blue meniscus sits on throat 234. All grains make zero contact angles with the two menisci. During imbibition, as the curvature decreases, the centers of these two menisci become closer to each other. Hence, the angle between plane A and plane B get smaller. Plane A connects the center of red meniscus and centers of grain 2 and 3. Plane B connects the center of blue meniscus and centers of grain 2 and 3. In Fig. 4.10, the blue meniscus and red meniscus have different centers. As a result, the angle between plane A and plane B is non zero. We regard this as a stable configuration, analogous to Fig. 4.6a and Fig. 4.8a.

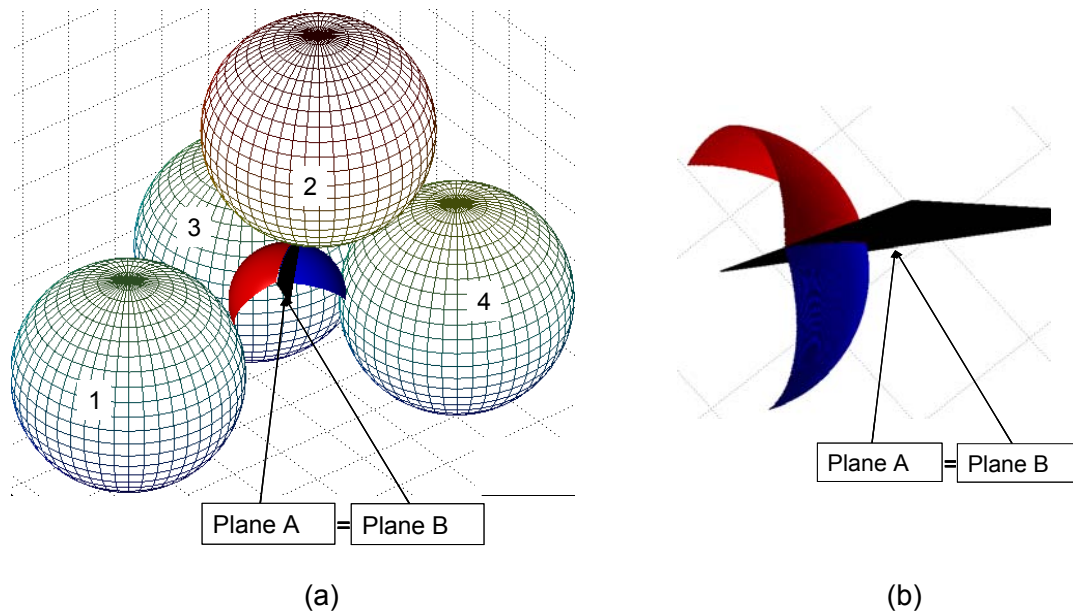


Figure 4.11 (a) Schematic of merging of two menisci located on two adjacent throats. The red meniscus sits on throat 123 and the blue meniscus sits on throat 234. All grains make zero contact angles with the two menisci. Throat 123 and throat 234 share an edge composed of grain 2 and grain 3. (b) Plane A and plane B are on the same plane (the angle between plane A and plane B equal zero degree). The Haines imbibition critical curvature equals the curvature of this merged meniscus.

As curvature decreases, centers of these two menisci get closer together, until the centers of the two menisci are located at the same point. When this occurs, plane A and plane B are the same. In other words, the angle between plane A and plane B equals zero (Fig. 4.11). Hence two menisci become the part of a single, spherical surface. Since in this example the contact angles are zero, this sphere is the inscribed sphere of the pore. The moment the menisci touch, they become unstable and merge into one meniscus. As a result, a generalized Haines imbibition event occurs and the pore will be filled with the invading phase.

The main difference between our criterion developed above and criterion for imbibition developed by Haines is that in Haines development, a pore will imbibe if the

applied curvature is smaller than the curvature of the inscribed sphere. This criterion can be computed *a priori* from the pore geometry, independent of the number of menisci within the pore during displacement. In contrast, our generalized Haines imbibition criterion requires the merger of two menisci centers. Thus, if a pore has only one meniscus, it will not imbibe even if the curvature of the meniscus becomes smaller than the curvature of inscribed sphere of the pore. In other words, a pore must have at least two menisci located in its throats before it can be imbibed. During drainage or imbibition, the existence of two menisci on two adjacent throats belonging to a given pore is contingent on the particular sequence of local filling events. Consequently, our criterion for imbibition cannot be calculated *a priori* to the drainage/imbibition simulation.

### ***Melrose Criterion for Imbibition***

A Melrose event occurs when two or more separated interfaces come into contact and merge to form a single interface [144]. As discussed in the previous section, when two menisci merge to a single meniscus, we call the event a generalized Haines imbibition (Fig. 4.11). Note that two menisci located on adjacent throats are not separated interfaces, even though we model them as two separated spherical caps. Here we operate under the understanding that the only separated interfaces are the pendular rings. As a result, when a pendular ring touches a meniscus, or when two pendular rings touch each other (coalescence in a pore throat), then a Melrose event occurs.

#### **A pendular ring and a meniscus touch (Melrose event):**

Fig. 4.12 shows a schematic of a pore that holds a meniscus in one of its pore throats (throat 234). In addition it holds a pendular ring in one of its edges (edge 13) which is not associated with throat 234. A Melrose event occurs, when a meniscus touches a pendular ring. Previously Gladkikh [78] developed numerical implementation for Melrose criterion. According to his development, when the meniscus and the pendular

ring touch, then the summation of filling angles of pendular rings and meniscus is bigger than or equal to angle between edge 13 and its projection on the plane of throat 234 (angle  $\alpha$  in Fig. 4.13).

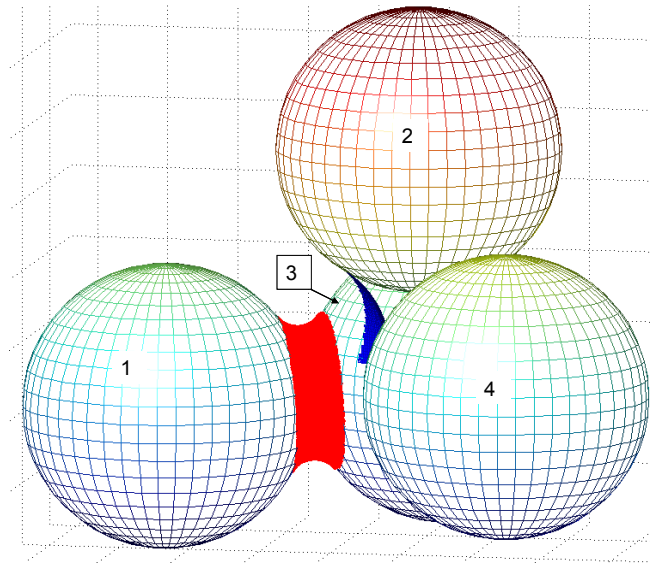


Figure 4.12. A meniscus (blue) does not touch a pendular ring (red) inside a pore; hence this is a stable configuration not satisfying the condition for a Melrose event. The pore is composed of four grains (1, 2, 3, and 4). The pendular ring (red) located on edge 13 composed of grain 1 and grain 3. The meniscus is located on throat 234 which is composed of three grains (2, 3, and 4).

Fig. 4.13 shows a 2D slice by the plane  $\triangle ADN$ , which  $A$  is the center of grain 3 in Fig. 4.12,  $D$  is the center of grain 1 in Fig. 4.12 and  $N$  is the point, equidistant from the grain centers of throat 234. The grain 3 is common between edge 13 and throat 234. The pendular ring filling angle  $\varphi$ , is the angle between the line connecting the two grain centers of the edge ( $\overline{AD}$  in Fig. 4.13) and line connecting a center of grain 3 and the contact point where the pendular ring touches grain 3 ( $P_r$  in Fig. 4.13). The meniscus filling angle  $\psi$  is the angle between line  $\overline{AN}$  (in Fig. 4.13) and line  $\overline{AP_m}$ .  $\overline{AP_m}$  is a line which connect center of grain 3 to the contact point where meniscus touch grain 3 ( $P_m$  in Fig. 4.13).

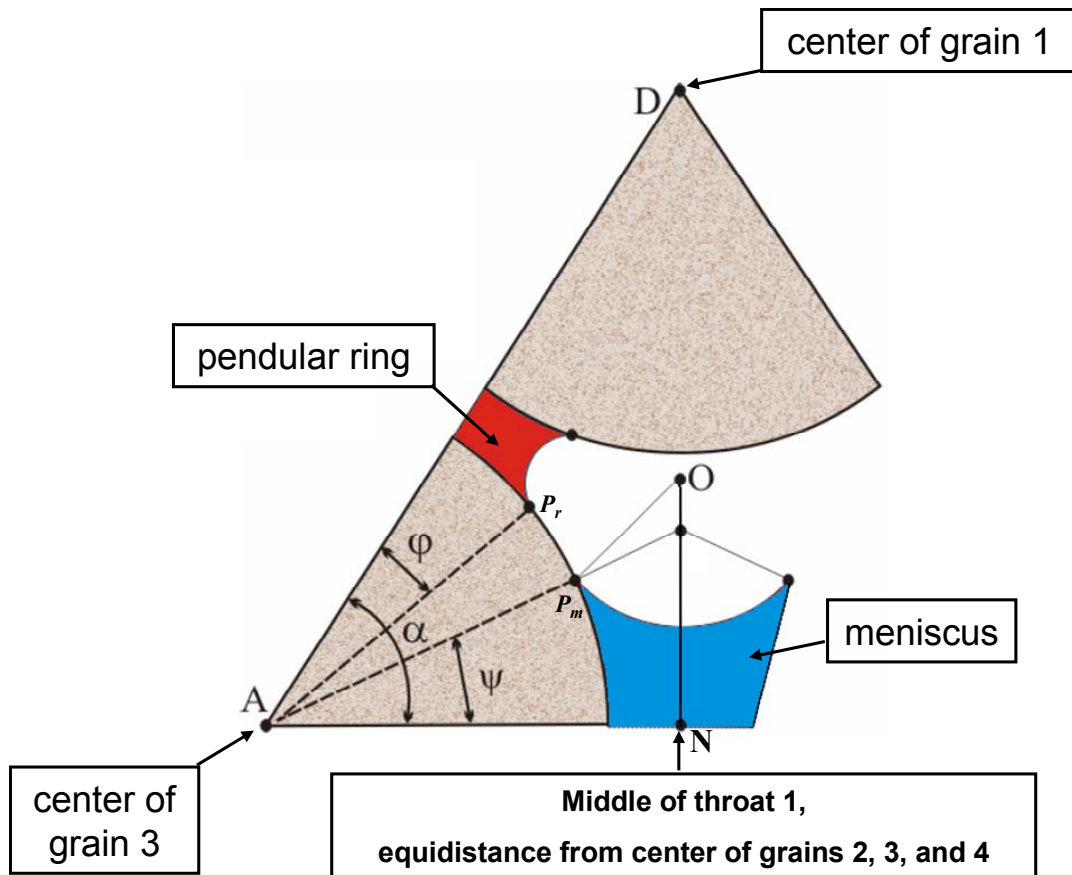


Figure 4.13. A 2D slice through the plane  $\triangle AON$ , which  $A$  is the center of grain 3 in Fig. 4.12,  $D$  is the center of grain 1 in Fig. 4.12 and  $N$  is the point, equidistant from the grain centers of throat 234. The grain 3 is common between edge 13 and throat 234.  $\varphi$  is the pendular ring filling angle and  $\psi$  is the meniscus filling angle. The meniscus and pendular ring do not touch, as a result the angle  $\alpha$  is greater than summation of angle  $\varphi$  and  $\psi$ . This figure is modified from the figure presented in Ref. [78].

The above argument is true only if point  $D$  (center of grain 1) is located in plane  $\triangle AON$ . In other words, plane  $\triangle AON$  and  $\triangle AOD$  are the same plane. As we show next, this statement is not always true. Plane  $\triangle AOD$  is a plan connecting the center of grain 1, the center of grain 3, and the center of the meniscus. Plane  $\triangle AON$  is a plane connecting the center of the meniscus, the middle point of throat holding meniscus, and the center of grains common between the edge holding a pendular ring and the throat



holding a meniscus. Fig. 4.14 shows that the planes  $\triangle AON$  (brown) and  $\triangle AOD$  (green) are not the same and they make a nonzero angle with each other.

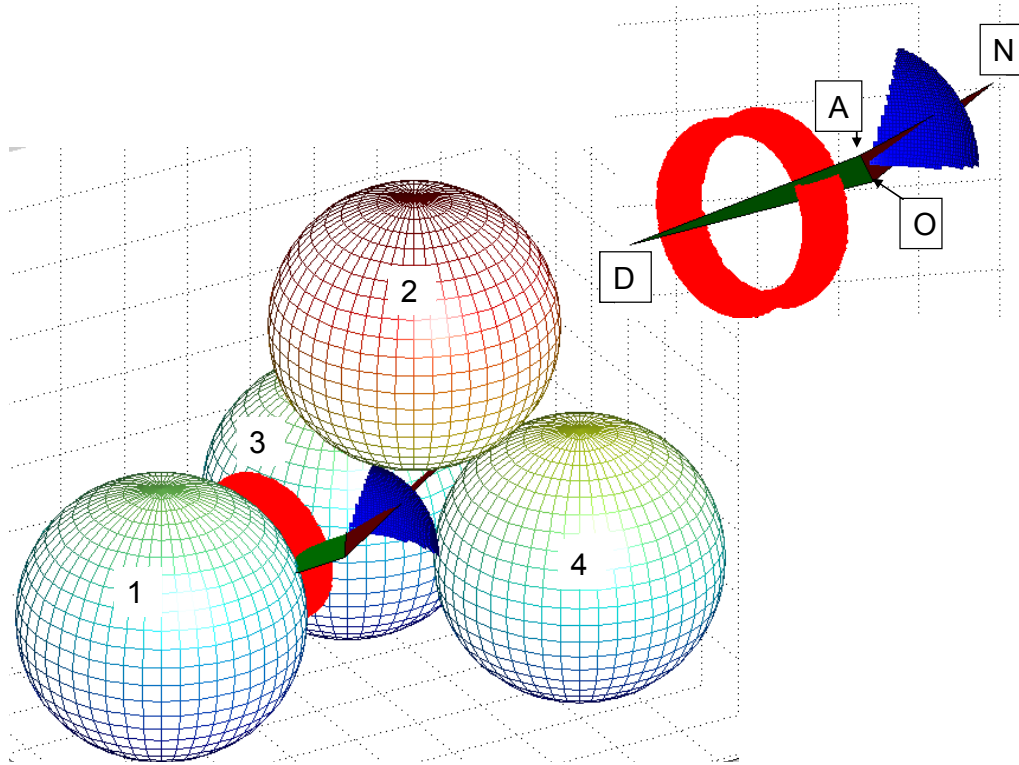


Figure 4.14. The edge holding pendular ring ( $\overline{AD}$ ) is not located on the  $\triangle AON$  plane. Planes  $\triangle AON$  (brown) and  $\triangle AOD$  (green) are not in the same plane. They intersected with a nonzero angle with each other.  $A$  is the center of grain 3. Grain 3 is common between the edge holding a pendular ring (red) and the throat holding a meniscus (blue).  $D$  is the center of grain 1.  $O$  is the center of the meniscus.  $N$  is the point that is equidistant from the grain centers of the throat holding the meniscus.

The assumption that planes  $\triangle AON$  (brown) and  $\triangle AOD$  (green) are the same leads to overestimating the curvature in which the Melrose event occurs. For instance, for a pore in Fig. 4.15, the Gladkikh development of the Melrose criterion predicts that the meniscus and the pendular ring touch at dimensionless curvature of 2.85 (Fig. 4.15a). However, Fig. 4.15a shows that the meniscus and the pendular ring do not touch at the

curvature predicted by the Gladkikh development of Melrose criterion. The meniscus and the pendular ring touch at the dimensionless curvature of 2.15 which is lower than the predicted curvature (Fig. 4.15b)

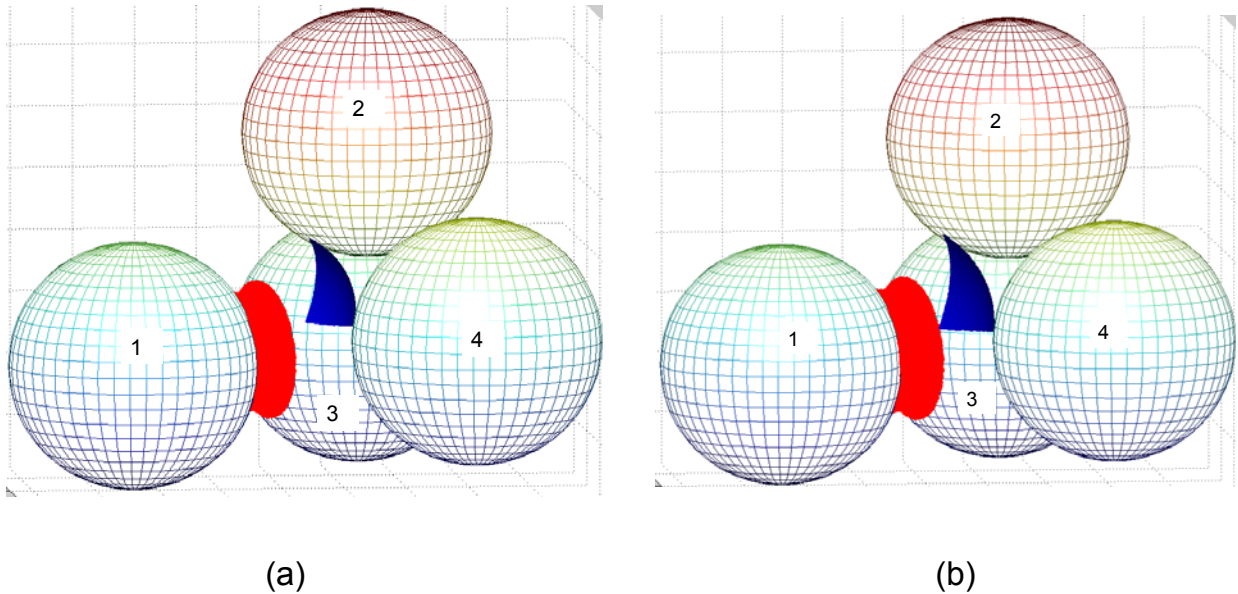


Figure 4.15. (a) A pendular ring (red) and a meniscus (blue) at the curvature of 2.85. The pendular ring and meniscus do not touch at this curvature. (b) A pendular ring (red) and a meniscus (blue) at curvature of 2.15. The pendular ring and meniscus touch at this curvature. The Gladkikh development of Melrose criterion predicts that the two interfaces touch at curvature of 2.85 which is an overestimate of the real critical curvature for the Melrose event.

In order to develop a correct Melrose criterion, the mathematical implementation should apply in a plane. We choose plane  $\triangle AON$  as reference plane (gray plane in Fig. 4.16). We project the center of grain 1 (point  $D$ ) on to the plane  $\triangle AON$ . The projection of the center of grain 1 (point  $D$ ) on the plane  $\triangle AON$  is point  $D'$ .

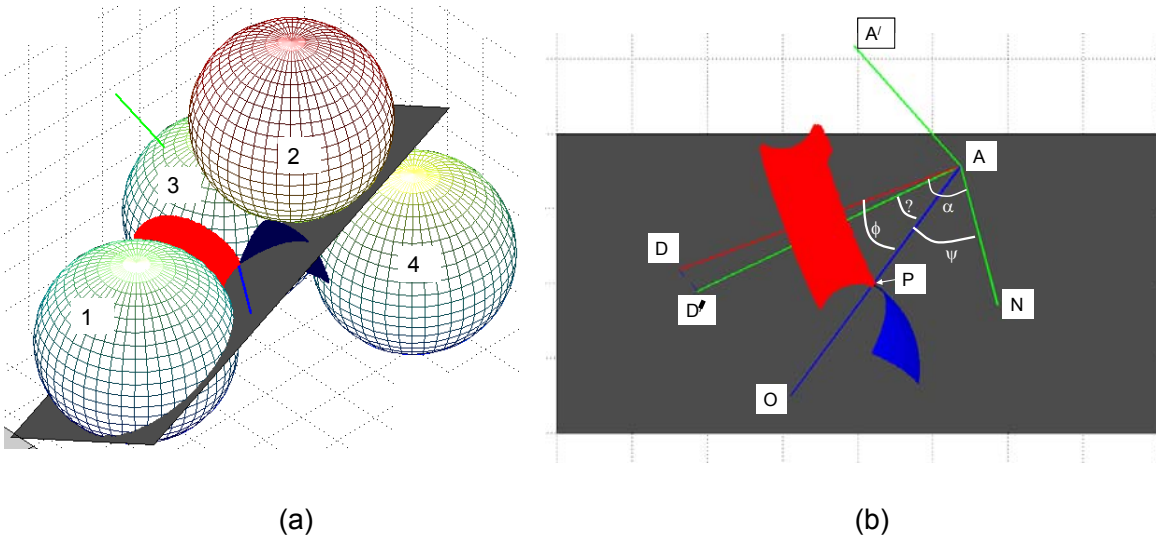


Figure 4.16. (a) Fluid configuration when a meniscus (blue) touch a pendular ring (red) inside a pore. The gray plane is the plane  $\triangle AON$  which connects the middle of throat 234 and the center of the meniscus and the center of grain common between throat 234 and edge 13. The blue line connect the center of grain 3 to the center of meniscus. The blue line passes through the touching point between the pendular ring and meniscus. The green line is the line normal to the gray plane ( $\triangle AON$ ). (b) Demonstrate development of new Melrose criterion.  $\overline{AD}$  is the edge holding a pendular ring (red).  $\overline{AA'}$  is the normal vector to plane  $\triangle AON$ , where  $A$  is the center of grain 3.  $D'$  is the projection of the center of grain 1 (point  $D$ ) on the plane  $\triangle AON$ .  $O$  is the center of the meniscus.  $N$  is the point, equidistant from the grain centers of the throat holding the meniscus.  $P$  is the point which the pendular ring and the meniscus touch each other on grain 3.  $\phi$  is the filling angle of the pendular ring and  $\psi$  is the filling angle of the meniscus.

The gray plane in Fig. 4.16 shows the plane  $\triangle AON$ . In the plane  $\triangle AON$ , line  $\overline{AO}$  connects the center of grain 3 to the center of the meniscus, this line pass through the contact point between the meniscus and grain 3 (point  $P$ ). As a result, the filling angle of the meniscus ( $\psi$ ) is equal to angle between line  $\overline{AN}$  and line  $\overline{AO}$ . The angle between line  $\overline{AN}$  and  $\overline{AD'}$  is angle  $\alpha$  in Fig. 4.16 and it can be calculated based on the coordinate of points  $A$ ,  $N$ , and  $D'$ . The angle  $\alpha$  is the angle between throat 234 and the projection of edge 13 on the plane  $\triangle AON$ . Now it is important to calculate the angle between line

$\overline{AO}$  and line  $\overline{AD'}$  (angle  $\phi'$ ). Because, when the meniscus and the pendular ring touch each other on the grain 3, the angle  $\alpha$  equals to summation of angle between line  $\overline{AN}$  and  $\overline{AO}$  (angle  $\psi$ ) and angle between line  $\overline{AO}$  and line  $\overline{AD'}$  (angle  $\phi'$ ). In other words, the Melrose event occurs if the summation of  $\phi'$  and  $\psi$  is equal to  $\alpha$  (the angle between line  $\overline{AN}$  and  $\overline{AD'}$ ).

The angle between line  $\overline{AO}$  and line  $\overline{AD'}$  can be calculated by knowing the filling angle of the pendular ring (angle  $\phi$ ). First we choose an arbitrary vector  $\vec{a}$  on line  $\overline{AD}$  (it can be vector with size equal to 1). Then, we decompose the vector  $\vec{a}$  to three principle vectors ( $a_1$ ,  $a_2$  and  $a_3$ ) which  $a_1$  lay on line  $\overline{AO}$ ,  $a_3$  lay on line  $\overline{AA'}$  ( $\overline{AA'}$  is a normal to the plane  $\triangle AON$ ), and  $a_2$  lay on the line perpendicular to both  $\overline{AO}$  and  $\overline{AA'}$ . The detail is shown in Fig. 4.17. The vector  $a$  is indicated by black vector in Fig. 4.17, and vectors  $a_1$ ,  $a_2$  and  $a_3$  are indicated by white vector in Fig. 4.17.

$$|a_1| = |a| \times \cos(\phi), \quad (4.3)$$

$$|a_3| = |a| \times \cos(\gamma), \quad (4.4)$$

$$|a_2| = \sqrt{|a|^2 - (|a_1|^2 + |a_3|^2)}, \quad (4.5)$$

$$\phi' = \tan^{-1} \left( \frac{|a_2|}{|a_1|} \right). \quad (4.6)$$

Where, angle  $\gamma$  is the angle between line  $\overline{AA'}$  and  $\overline{AD}$ . The angle  $\gamma$  can be calculated from the angle between line  $\overline{AD}$  and plane  $\triangle AON$ .

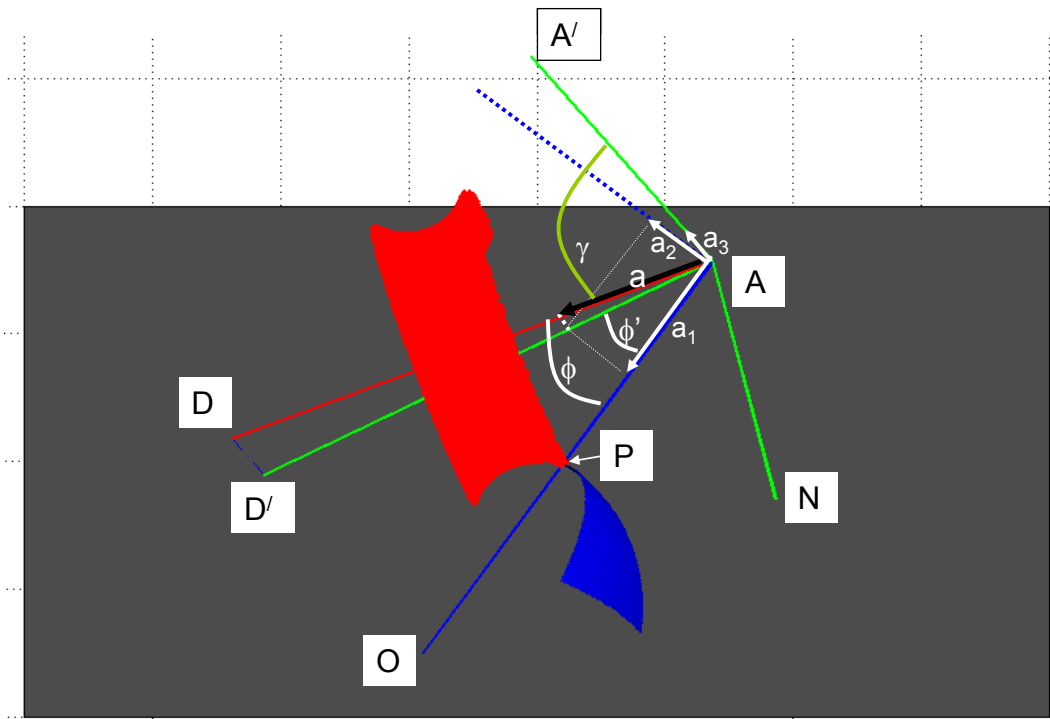


Figure 4.17. A Melrose event occurs if the summation of  $\phi$  and  $\psi$  (see Fig. 4.16) is bigger than  $\alpha$  (the angle between line  $\overline{AN}$  and  $\overline{AD'}$ ).  $D'$  is the projection of the center of grain 1 (point  $D$ ) on plane  $\triangle AON$ .  $O$  is the center of the meniscus.  $N$  is the point equidistant from the grain centers of throat holding the meniscus.  $P$  is the point at which the pendular ring and the meniscus touch each other on grain 3. Vector  $a$  is indicated by a black vector, and vectors  $a_1$ ,  $a_2$  and  $a_3$  are indicated by the white vectors.

In summary, a Melrose event occurs when a pendular ring touches a meniscus inside a pore. As a result, a pore will be filled with the invading phase and the critical curvature for imbibition of the pore equals to the curvature of the meniscus. For simplicity, we call this event a Melrose event.

**Two pendular rings touch (coalescences event):**

As curvature decreases, pendular rings grow inside pores and at some curvature two adjacent pendular rings will touch each other. As a result, the coalescence of two pendular rings occurs and results in closure of a pore throat to the non-wetting phase. Fig.

4.18 and Fig. 4.19 show the stage of coalescence of pendular rings on a pore throat. Fig. 4.18 shows a 2D slice of a pore throat and pendular rings, while Fig. 4.19 shows 3D view of the pore throat and the pendular rings. The numerical implementation of pendular rings coalescences is as follows. First, we compute the filling angle of each pendular ring ( $\varphi_1$  and  $\varphi_2$  in Fig. 4.18). If the summation of two pendular rings filling angles is bigger than the angle between the two edges holding pendular rings ( $\alpha$  in Fig. 4.18), then the two pendular rings touch each other and as a result the coalescence occurs (Fig. 4.18c). For simplicity, we call this event a coalescence event. In the uniformly wet medium, the coalescence event can result in disconnecting of the non-wetting phase (snap off). As a result, this event called snap off in several literatures [25, 146].

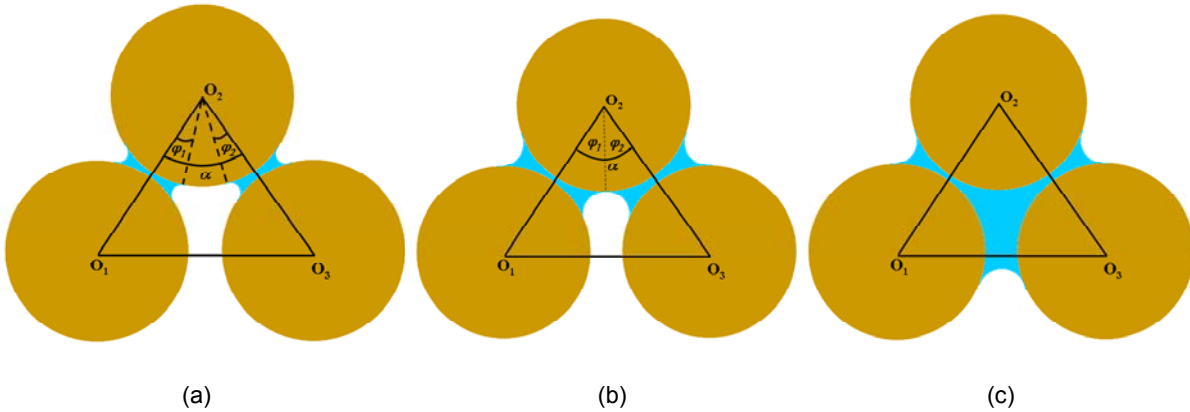


Figure 4.18. Stage of coalescence of pendular rings on a pore throat in 2D view. A 2D slice of a pore throat by the plane connecting center of grains ( $O_1$ ,  $O_2$ , and  $O_3$ ). (a) Curvature of pendular rings is smaller than the critical curvature for coalescence to occur. Summation of pendular rings filling angle ( $\varphi_1$  and  $\varphi_2$ ) is smaller than angle  $\alpha$ . (b) Curvature of pendular rings equal to the critical curvature for coalescence to occur. Summation of pendular rings filling angles ( $\varphi_1$  and  $\varphi_2$ ) equals to angle  $\alpha$ . (c) The coalescence occurs and the pore throat is closed by the wetting phase.

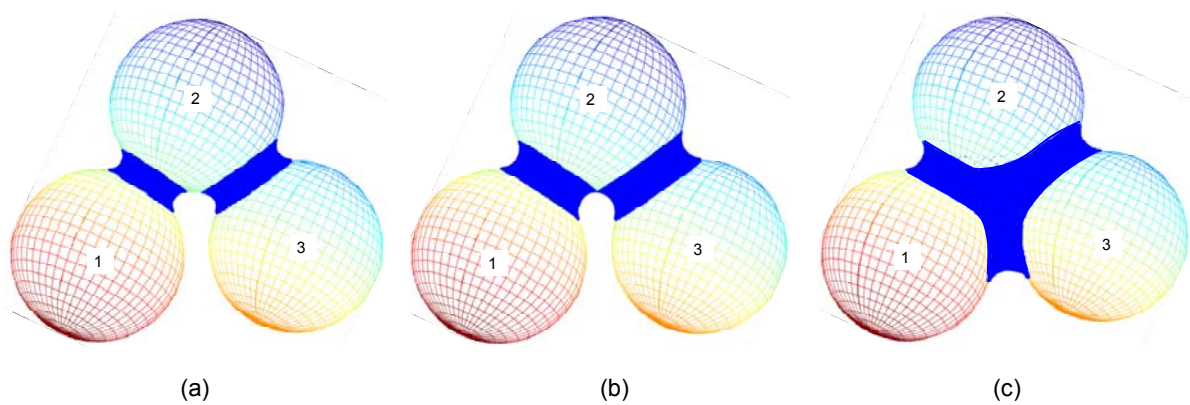


Figure 4.19. The stages of coalescence of pendular rings on a pore throat in 3D view. (a) Curvature of pendular rings is smaller than the critical curvature for coalescence to occur. Summation of pendular rings filling angle is smaller than angle between two edges holding pendular rings (angle  $\alpha$ ). (b) Curvature of pendular rings equal to the critical curvature for coalescence to occur. Summation of pendular rings filling angles equals to angle  $\alpha$ . (c) The coalescence occurs and the pore throat is closed by the wetting phase.

From all four events described in this section (i.e. generalized Haines drainage, generalized Haines imbibition, Melrose, and coalescence), the first three events are pore-filling events. However, coalescence is not a pore-filling event. Upon occurrence of coalescence only a pore throat will be filled by invading fluid.

#### ***A Meniscus-4<sup>th</sup> Grain Contact***

Another event that causes instability of a meniscus is when the meniscus touches a fourth grain located in front of the meniscus. We develop a mechanistic criterion for the encounter of a meniscus with a fourth grain not involved in the throat holding the meniscus. To our knowledge this criterion has not been previously considered in pore-scale modeling of fluid displacement. A Meniscus-4<sup>th</sup> grain event is not a pore-filling event *per se*, but it leads to several events that result in a pore-filling event. For better understanding of this event (a meniscus 4<sup>th</sup> grain contact), we use an example.

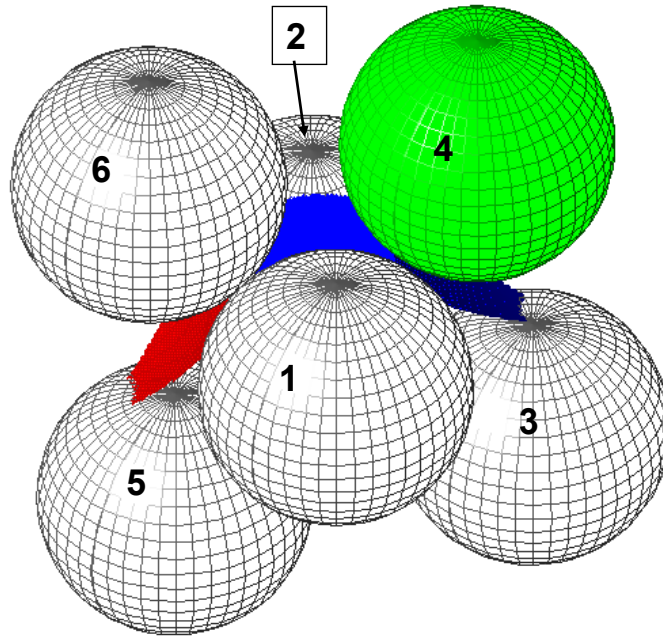


Figure 4.20. Fluid configuration within two pores (pore 1234, and pore 1256), before a meniscus–4<sup>th</sup> grain contact during imbibition. Throat 123 and throat 125 hold menisci which are colored dark blue and red, respectively. A light blue interface connects the two menisci. All grains are water-wet and they make a contact angles of  $30^\circ$  with the menisci. The water phase is located below the menisci, and the oil phase is located above. The fourth grain of pore 1234 (grain 4) which comes in contact with the meniscus in throat 123 is colored green.

Fig. 4.20 shows a schematic of two pores (pore 1234 and pore 1256). Throat 123 and Throat 125 hold menisci which are colored red and a dark blue, respectively. A light blue interface connects these two menisci. All grains are water-wet and they make contact angles of  $30^\circ$  with the menisci. During imbibition, the menisci advance farther into pore 1234 and pore 1256 as the curvature decreases. As a result of menisci movement, the dark blue meniscus in throat 123 eventually touches the fourth grain located in front of the meniscus (grain 4). This grain (grain 4) is one of four grains which construct pore 1234, but this grain does not belong to throat 123.



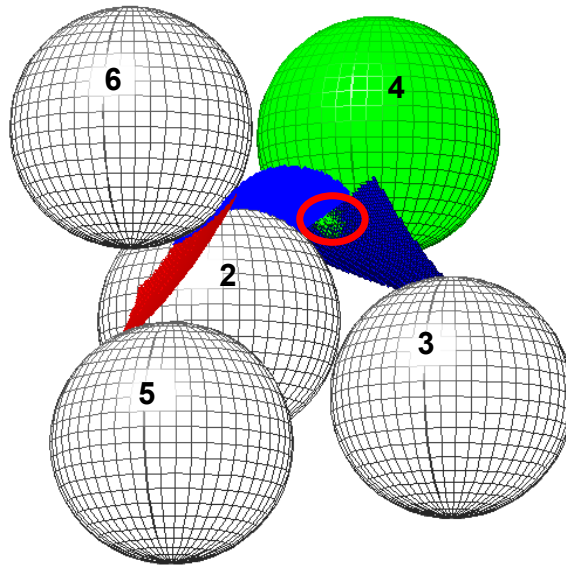


Figure 4.21. Reducing the curvature in Fig. 4.20 leads to this fluid configuration (different view point than Fig. 4.20) in which the meniscus (dark blue) touches the green fourth grain (grain 4). Grain 1 has been removed to expose the region of the meniscus and the fourth grain contact (this region is highlighted by red circle).

Fig. 4.21 shows the evolution of the fluid configuration of Fig. 4.20 when the curvature is small enough for the meniscus (dark blue) to touch the 4<sup>th</sup> grain (grain 4). When this happens, the water phase which is located below the meniscus becomes in contact with water-wet grain 4. Consequently, the water phase rises along the surface of grain 4. As a result, two pendular rings form on edge 14 and edge 24 (Fig. 4.22). To generalize, when the meniscus touches a fourth grain (e.g. grain 4) near an edge joining two grains (e.g. grain 1 and grain 2), all three grains (e.g. grain 1, grain 2 and grain 4) must have the same wettability in order for the invading phase to rise on the touched grain.

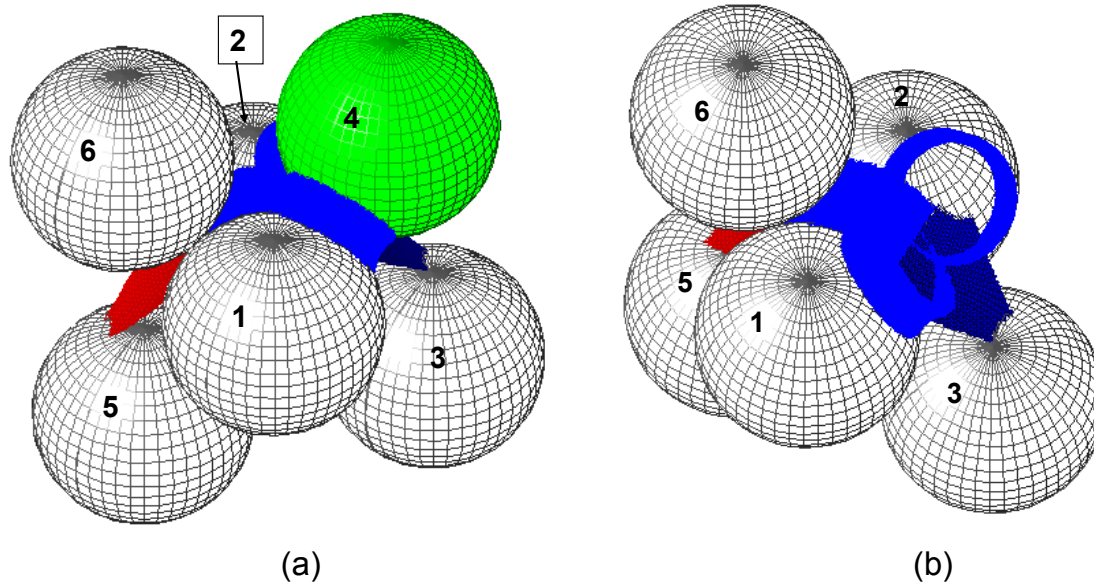


Figure 4.22. Fluid configuration within two pores (pore 1234, and pore 1256), after the meniscus (dark blue) touches the 4<sup>th</sup> grain (grain 4) (cf. Fig. 4.21). (a) The water phase rises on the surface of grain 4, and as a result two pendular rings are formed on edge 14 and edge 24. (b) Grain 4 is removed in order to reveal rings (light blue) and meniscus (dark blue) contacts.

The pendular rings which form on edge 14 and edge 24 are touched by the dark blue meniscus (Fig. 4.22b). Consequently, Melrose events occur, and pore 1234 will be filled with the water phase (Fig. 4.23).

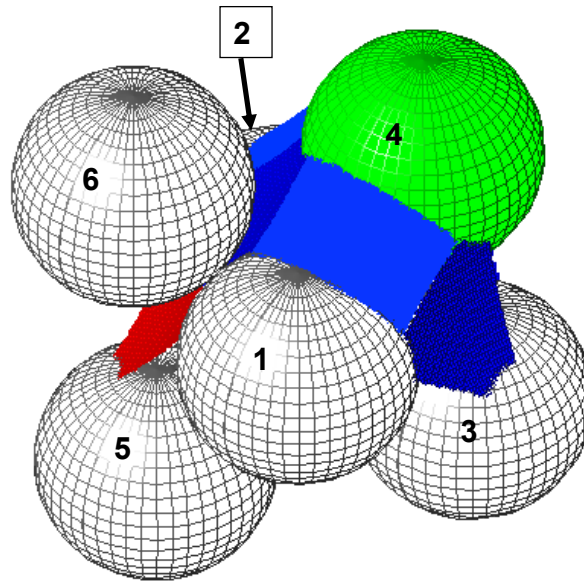


Figure 4.23. The fluid configuration within two pores (pore 1234, and pore 1256), after the meniscus touches the 4<sup>th</sup> grain (grain 4) (final stage). Three new menisci (dark blue) are formed on the throat corresponding to pore 1234 (throat 124, throat 134, and throat 243). The light blue interface is not a pendular ring, but a surface that connects adjacent menisci.

In summary, when a meniscus touches a nearby grain that is not one of the three grains holding the meniscus (4<sup>th</sup> grain), but has the same wettability as at least two grains holding the meniscus, then the invading fluid rises on the touched grain and forms two pendular rings on the edges composed of the touched grain and two other grains. Subsequently, the formed pendular rings touch the original meniscus, and a Melrose event occurs, causing the pore to be filled with invading fluid. A grain can touch a meniscus during imbibition or drainage. In the dense random packings of spheres studied here, this event occurs only when the absolute value of dimensionless curvature is small (approximately less than 1.5).

#### **4.4. SIMULATION**

We simulate the menisci motion within fractionally wet media during drainage and imbibition using the invasion percolation algorithm. We change curvature in small increments then compute the stable meniscus locations in all pores. At any given curvature (capillary pressure), all pores that are connected to the inlet (via invading fluid) will be in a candidate list for invasion. We check the candidate pores for criteria of invasion (Melrose, generalized Haines and meniscus-4<sup>th</sup> grain criteria). If a candidate meets the criteria of invasion and it also connected to the outlet, we invade the candidate and add the neighboring pores to the list of candidates. We continue until no more candidates remain in the list. Candidates that are not connected to the outlet are labeled “trapped” and removed from further consideration of events. Then we increase or decrease the curvature incrementally and we repeat the procedure.

We emphasize that by checking generalized Haines and Melrose criteria developed in Sec. 4.3 for all pores, the algorithm has generalized the notion of simulating drainage and imbibition. Indeed, the only difference inside the code between drainage and imbibition is the sign of the increment in curvature. In contrast, traditional pore network models have algorithms specific to drainage and different algorithms specific to imbibition; only the machinery of invasion percolation is common to both.

#### **4.5. RESULT**

In this section, we focus on the result for drainage and imbibition for a fractionally wet porous medium. In the next section, we compare the simulation results for both water-wet and fractionally wet media with experimental data. Fig. 4.24 shows the imbibition and drainage curves for a porous medium with 50% of its grains oil-wet. The porous medium is composed of 7000 equal size grains. For this and subsequent figures, the curvature is dimensionless such that a curvature of 2 corresponds to the

curvature of the grains surface. The radii of the grains are normalized to have value of unity.

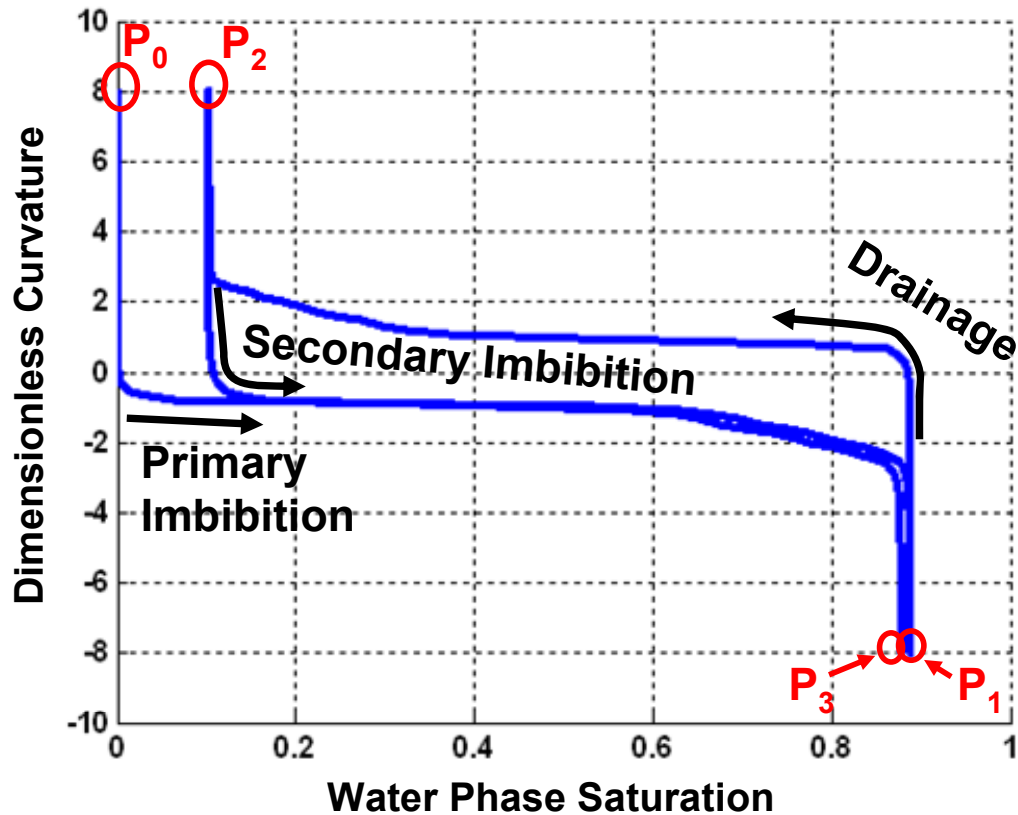


Figure 4.24. Imbibition and drainage curves for a porous medium with 50% of grains oil-wet. The porous medium was filled with the oil phase initially: first, the water phase pushes the oil out by decreasing capillary pressure (primary imbibition), second the oil phase drains the water out of the porous medium by increasing capillary pressure (drainage), and finally the water phase pushes into the porous medium and replaces the oil phase (secondary imbibition). In all three curves, the curvature ranges from positive to negative values and thus passes through zero curvature. All three curves are produced from the same code applying the same criteria for pore-filling events. The different behavior arises entirely from the different values of starting and ending applied curvature.

Initially, the porous medium was filled with the oil phase (Fig. 4.24, point  $P_0$ ), so the first process is primary imbibition where the water phase imbibes to the porous

medium until residual oil phase saturation (imbibition end point). At the imbibition end point, the residual oil phase exists in two morphologies: The oil phase trapped inside the pores and the oil phase in the form of pendular rings at grain-grain contact of two oil-wet grains. Note that the calculation for water saturation reported in Fig. 4.24 does not account for the volume of the oil phase held by oil-wet grains nor the volume of the water phase hold by water-wet grains, as these are both very minimal. The drainage starts from imbibition endpoint (Fig. 4.24, point  $P_1$ ) with increasing applied curvature (capillary pressure) and decreasing water saturation. Finally, the secondary imbibition starts from drainage endpoint (Fig. 4.24, point  $P_2$ ) and the water phase imbibe to the porous medium to the new value of residual oil phase saturation (Fig. 4.24, point  $P_3$ ). The model allows seamless movements of interfaces and filling events even through the zero curvature level. Both generalized Haines and Melrose events can occur with a change in the applied curvature. All menisci are tested for all pore-filling events depending on their local circumstances. Thus the critical curvature for local events is dynamic and cannot be pre-calculated. This is unlike traditional invasion percolation models.

As we mention in the simulation section, our modeling approach considers both Haines and Melrose events on imbibition and drainage, as is necessary for fractionally wet media. This gives the model an inherent robustness in the sense that all grains, throats, and pore bodies are considered equivalent, just with a different contact angle for each grain. This robustness can be seen by considering a 25% oil-wet medium, and the equivalent 75% oil-wet medium in which all of the oil-wet grains are made water-wet and vice-versa. By reversing the wettability of each grain, the capillary pressure curve should also be reversed. Fig. 4.25a shows the 25% oil-wet capillary pressure curve obtained with the model, and Fig. 4.25b shows the 75% oil-wet capillary pressure curve. The symmetry is evident, as the drainage in the 25% oil-wet medium is identical to the imbibition in the

75% oil-wet medium. This shows that the model is performing as expected. Note that this symmetry is only seen if each grain's wettability is reversed. If the position of the grains is different, or the pattern of the oil-wet grains is different, the model will show slightly different capillary pressure curves.

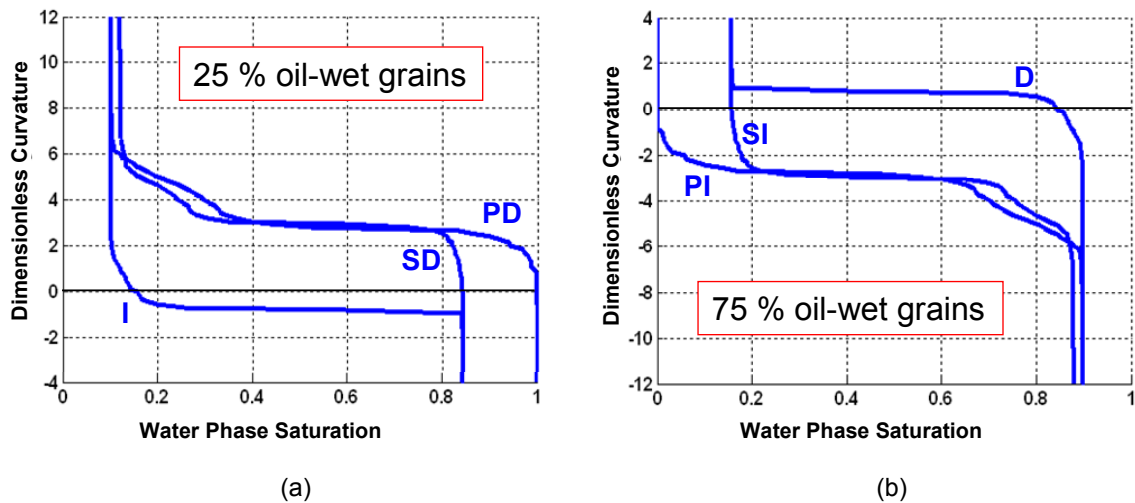


Figure 4.25. (a) The primary drainage (PD), imbibition (I) and secondary drainage (SD) curves for a porous medium with 25% oil-wet grains. (b) The primary imbibition (PI), drainage (D) and secondary imbibition (SI) curves for a porous medium with 75% oil-wet grains. The curves on the Figs. 4.21a and 4.21b are vertically symmetric, so if the Fig. 4.25b rotates 180°, the curves will overlies the curves on Fig. 4.25a.

We can now use the model to study how the drainage and imbibition curves vary with the change in the fraction of oil-wet grains. Fig. 4.26 shows the primary drainage curves for porous media with different fraction of oil-wet grains. The oil-wet grains have a contact angle of 150° and the water-wet grains have a contact angle of 30°. For simplicity, we ignore the trapping of the receding phase for the results presented in the Fig. 4.26. As a result, the advancing phase can displace receding phase even though the receding phase is not connected to exit pores through the bulk phase. Consequently, the curves in Fig. 4.26 show no residual saturation for the receding phase.

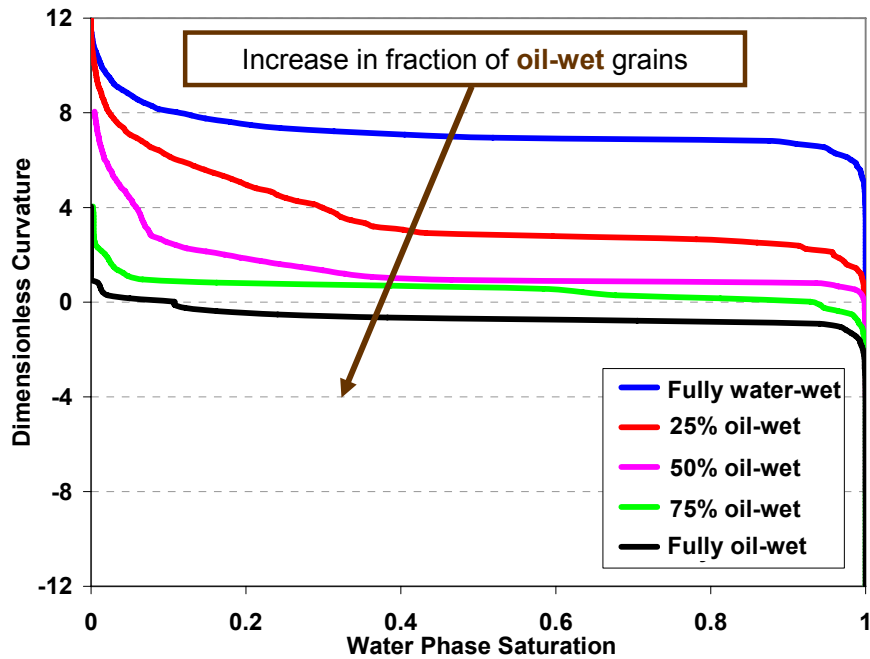


Figure 4.26. Comparison between primary drainage curves for the porous media with different fractions of oil-wet ( $\theta_{ow} = 150^\circ$ ) grains distributed randomly among water-wet ( $\theta_{ww} = 30^\circ$ ) grains. The porous media was originally filled with water. The oil phase pushes the water phase out as the capillary pressure (curvature) increases.

Generally, the drainage curves move to lower capillary pressures (curvatures) as fraction of oil-wet grains in the media increases. In other words, the curvature corresponds to the percolation threshold decreases monotonically in all curves. When the applied curvature is increased, the water saturations go from near 100% saturated to less than 50% saturated at a specific curvature, this curvature correspond to the percolation threshold. The invading fluid breaks through the porous medium when the curvature reaches percolation threshold value. What is interesting is in the fact, that the movement of  $P$ - $S$  curves is not linear function of fraction of oil-wet grains. The significant change in the position of the drainage curve occurs from the fully water-wet case to the 25% oil-wet case. The second significant change in the position of the drainage curve occurs from of



the drainage curve for the 25% oil-wet case to the drainage curve for the 50% oil-wet case. The position of drainage curve for the 75% oil-wet case is slightly lower compared to the position of drainage curve for the 50% oil-wet case. The percolation threshold value for the drainage curves of fully oil-wet case is negative. For all other cases (i.e. fully water-wet, 25% oil-wet, 50% oil-wet, 75% oil-wet), the invading fluid percolate through the porous medium at positive curvature.

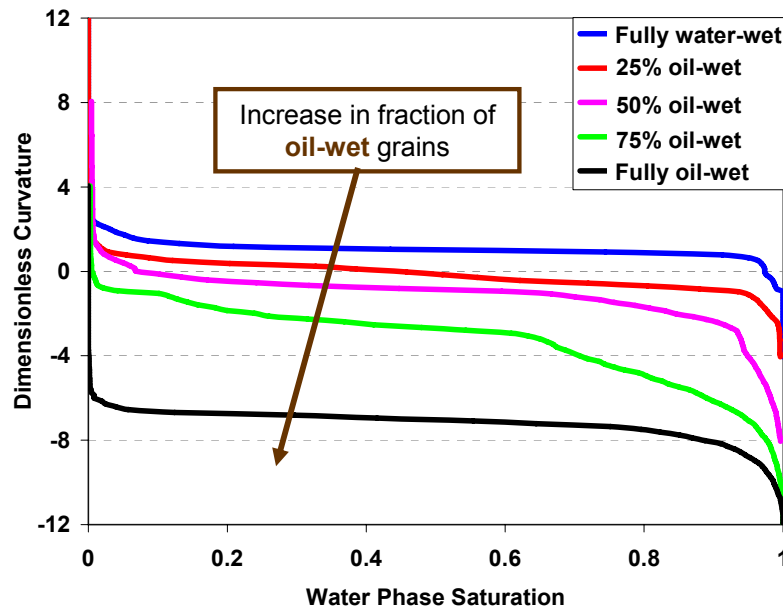


Figure 4.27. Comparison between secondary imbibition curves for the porous media with different fractions of oil-wet grains; the contact angles on water-wet and oil-wet grains are  $\theta_{ww} = 30^\circ$  and  $\theta_{ow} = 150^\circ$ , respectively. The imbibition curves start from drainage endpoint of the curves in Fig. 4.26. The water phase pushes the oil phase out as the capillary pressure (curvature) decreases. As the fraction of oil-wet grains within porous medium increases the value for curvature which the water phase percolates through porous medium decreases.

Fig. 4.27 shows the model results for the secondary imbibition curves for porous media with different fraction of oil-wet grains. The imbibition curves move to lower capillary pressures (curvatures) with increasing fraction of oil-wet grains in the media.

Again, the change in the position of the curves is not linear. The change in position of imbibition curves is minor from the fully water-wet case to the 25% oil-wet case and from the 25% oil-wet case to the 50% oil-wet case. A moderate change in the position of imbibition curves from the 50% oil-wet case to the 75% oil-wet case. Finally, the position of curve in the fully oil-wet case move lower significantly compared to the 75% oil-wet case.

## **4.6. MODEL VALIDATION**

In this section, first we compare the simulation results for the fully water-wet case with the experimental data by Haines [89]. Second, we compare the simulation results for the fractional wet cases with the experimental data by Ashouripashaki [14], Ustohal *et al.* [204] and O'Carroll *et al.* [153].

### **4.6.1. Water-Wet Case**

Haines [89] performed a series of drainage experiments followed by imbibition experiments in a packing of 0.038 cm glass beads. The imbibition experiments were started from the endpoints of the drainage experiments. Haines used water as the wetting phase and air as the non-wetting phase. His capillary pressure data were reported in terms of the as dimensionless curvature by normalizing the glass beads radii to be unity. He also reported existence of thin films of water phase on grains during experiments. As a result, we assume the contact angle of zero degrees for water-wet grains. However, we assume that the thin film of water is not thick enough to be hydraulically conductive. Consequently, we do not simulate the growing of pendular ring and coalescence of the pendular rings during imbibition. During drainage, a pendular ring gets frozen after all of its neighboring pores are drained. During imbibition, this pendular ring remains frozen

until one of its neighboring pores is imbibed. In the discussion section, we will assess the effect of coalescence on the  $P$ - $S$  curves for a fully water-wet medium.

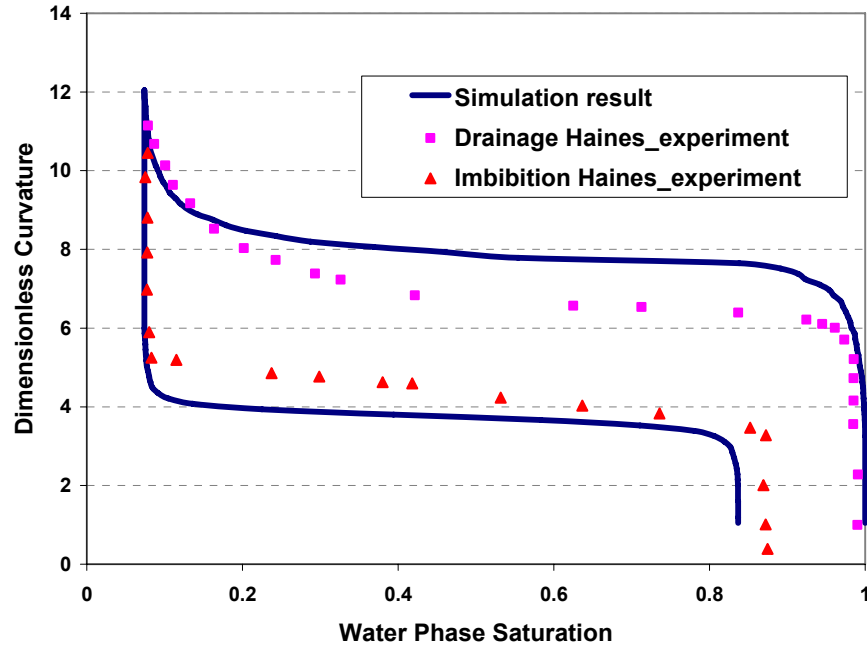


Figure 4.28. Comparison between simulation results for a fully water-wet medium and Haines experimental data for packing of glass beads. The contact angles on water-wet grains are  $\theta_{ww} = 0^\circ$ . The imbibition curve starts from the drainage endpoint of the drainage curves. The drainage curve is a primary drainage curve.

In order to simulate primary drainage, the oil phase enters to the sphere pack from entrance face (face 1 in the Fig. 4.1) as the curvature increases. The displaced water phase can exit from all faces except the entrance face (face 1). In the discussion section, we will elaborate on the effect of number of exit faces on the residual oil and water phases. The secondary imbibition starts from the drainage end point. During secondary imbibition, we decrease the applied curvature. As a result, the water phase invades the porous medium and pushes the oil phase out of the porous medium through all faces except face 4 (opposite side of face 1, see Fig. 4.1).

The overall capillary pressure match between experimental data and simulation results are very good, but the simulation results for drainage curve overestimate the value of curvature corresponding to the percolation threshold for the primary drainage. This over estimation is due to use of Haines drainage criterion. According to Haines drainage criterion, we assume a meniscus that passes through a throat plane is cap part of sphere that is inscribed to the grains forming the throat. Other researchers also report the over estimation in value of capillary pressure corresponding to the percolation threshold for primary drainage, when they use Haines drainage criterion in their model [110, 140]. The spherical approximation is easily calculated and provides semi-quantitative agreement in the  $P$ - $S$  curve; the essential point here is that it correctly captures the sequence of throat filling events, and this is the main objective of the modeling. The model also underestimates the curvature in which the water phase breaks through the porous medium during imbibition. We hypothesize, the assumption of menisci being part of spheres results in this under estimation, in the same way that the spherical approximation overestimates the drainage critical curvature in a throat. The spherical approximations thus degrade the quantitative prediction, but the overall agreement between experimental data and simulation results is satisfactory. The agreement between simulation results (our *a priori* prediction) and experimental data shows that our model captures the essential of the fluid flow within the uniformly wet media.

#### **4.6.2. Fractional-Wet Case**

Ashouripashaki [14] performed laboratory experiments to obtain octane/water pressure-saturation curves for primary drainage, and primary imbibition within fractionally wet sand packs (see Chapter 3 for more detail about the experimental procedure).

## Drainage

Fig. 4.29a shows the measured  $P$ - $S$  curves for primary drainage for 5 different sands of varying oil-wet fraction. The primary drainage measured for octane/water system. The drainage curves move monotonically lower with increasing oil-wet fraction. We simulate the primary drainage for the media with the same fraction of oil-wet grains as experimental data (e.g. 0, 25%, 50%, etc.). We multiply the dimensionless curvature by the known interfacial tension and divide by grains radii to obtain the capillary pressure in Pascal for simulation results. Fig. 4.29b shows the simulation results for 3D fractionally wet porous media. In the model, the contact angles on water-wet and oil-wet grains are  $\theta_{ww} = 30^\circ$  and  $\theta_{ow} = 150^\circ$ , respectively.

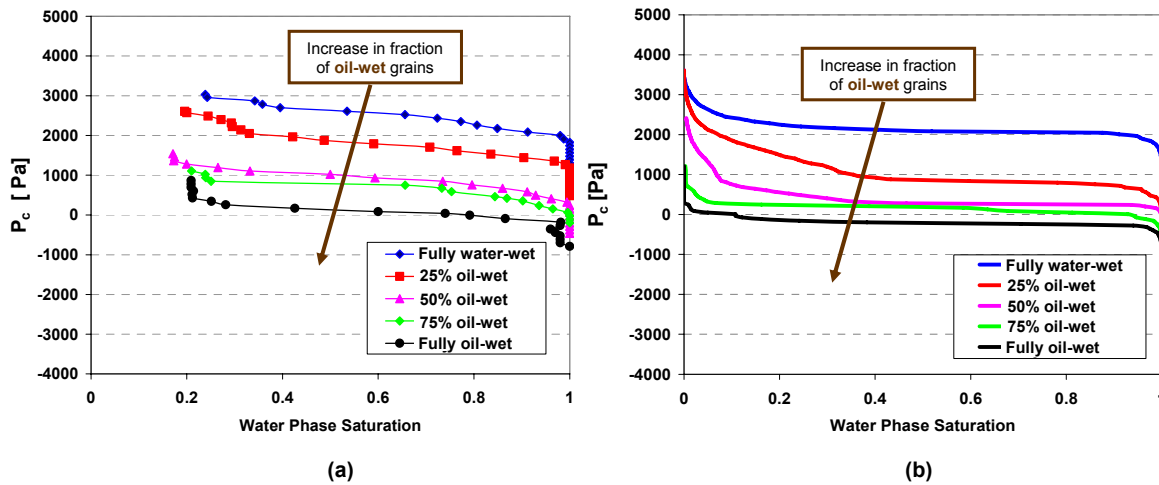


Figure 4.29. (a) Measured octane/water drainage curve for the fractionally wet media. The primary drainage curves move monotonically lower with increasing oil-wet fraction. (b) Simulation results for drainage of fractionally wet media. The contact angles on water-wet and oil-wet grains are  $\theta_{ww} = 30^\circ$  and  $\theta_{ow} = 150^\circ$ , respectively. For the model, we multiply the curvature by the known interfacial tension and divide by the grains radii to obtain the capillary pressure in Pascal

The similarity of the trend with increasing oil-wet fraction between experimental data and simulation results is very good. The capillary pressure corresponding to the

percolation threshold decreases monotonically in both figures (Fig. 4.29a and Fig. 4.29b). The percolation threshold changes nonlinearly with fraction of oil-wet grains in both experimental data and simulation results. Looking at the model results (Fig. 4.29b), starting from 0% oil-wet fraction (fully water-wet), the transition capillary pressure (percolation threshold) decreases significantly up to about 50% oil-wet fraction; between 50% and 75% oil-wet fraction there is a small decrease in the transition capillary pressure; finally, a moderate change of the transition capillary pressure between 75% and 100% oil-wet fraction. The transition capillary pressure for 100% oil-wet case occurs at negative capillary pressure. In experimental data (Fig. 4.29a), a moderate change of the transition capillary pressure between 0% and 25% oil-wet fraction; a moderate change of the transition capillary pressure between 25% and 50% oil-wet fraction; a slight change between 50% and 75%, and finally a moderate change between 75% and 100%. In both experimental data and simulation results, the transition capillary pressure for all of drainage curves (except 100% oil-wet) located above zero capillary pressure. In experimental measurement, half of the drainage curves for the fully oil-wet (100% oil-wet) medium locate below zero capillary pressure. However, in simulation results, most of the drainage curves for the fully oil-wet (100% oil-wet) medium curves are located below the zero capillary pressure.

Despite the similarity between experimental data and simulation results, the drainage curves in simulation results are located at lower capillary pressures compared to the experimental measurements. The model is robust enough to handle the different contact angles in calculating the movement of the menisci. If we change the contact angle for the water-wet and oil-wet grains within the model, the overall match between experimental data and simulation results will be improved. Fig. 4.30b shows the simulation results for fractionally wet porous media in which the contact angles on its

water-wet and oil-wet grains are  $\theta_{ww} = 0^\circ$  and  $\theta_{ow} = 120^\circ$ , respectively. Because no independent measurement of the contact angles on the sand is available, we conclude that the model captures the overall behavior reasonably well.

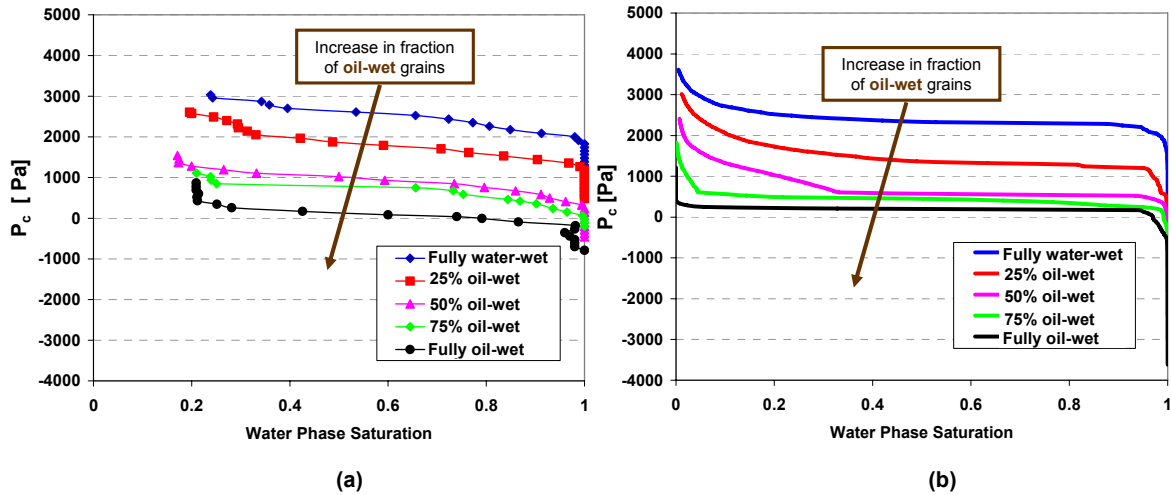


Figure 4.30. (a) Measured octane/water drainage curve for the fractionally wet media. The primary drainage curves move monotonically lower with increasing oil-wet fraction. (b) Simulation results for drainage of fractionally wet media. The contact angles on water-wet and oil-wet grains are  $\theta_{ww} = 0^\circ$  and  $\theta_{ow} = 120^\circ$ , respectively. For the model, we multiply the curvature by the known interfacial tension and divide by the grains radii to obtain the capillary pressure in Pascal

The primary drainage curves in experimental data from other sources [153, 204] qualitatively show the same behavior as Fig. 4.29a. O’Carroll *et al.* [153] present primary drainage of PCE/water for fractional water-wet and oil-wet sands (Fig. 4.31). PCE (tetrachloroethene) was used as the representative of the oil phase. The value of water saturation in Fig. 4.31 are normalized. The minimum measured water saturation equate to value of zero for the apparent water phase saturation. The maximum measured water saturation equate to the value of one for the apparent water phase saturation.

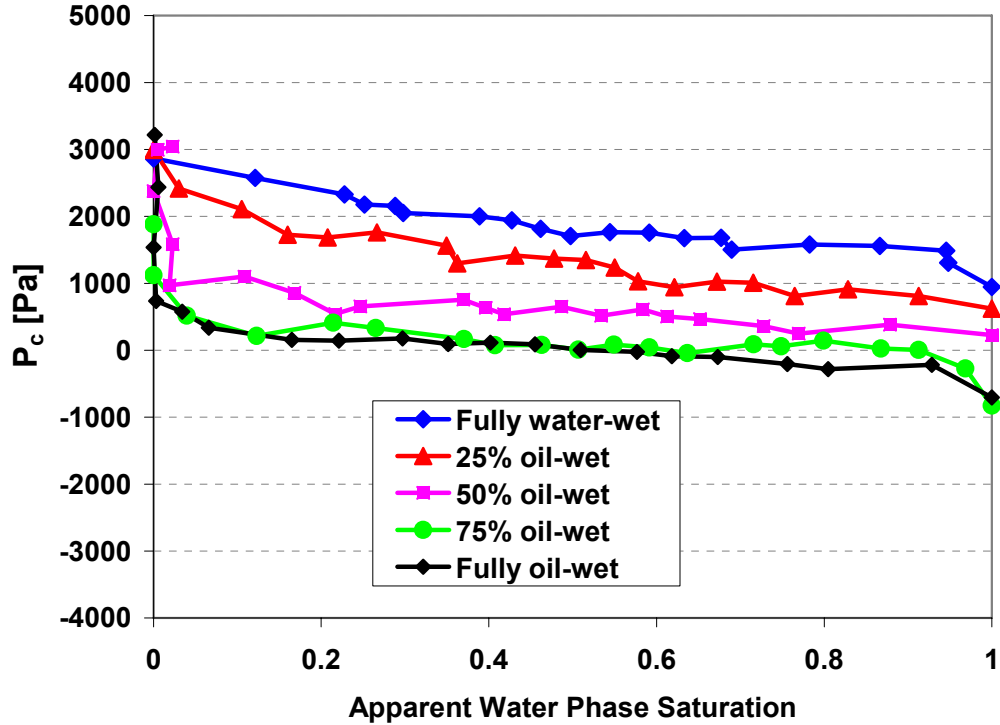


Figure 4.31. Measured PCE/water drainage curve for the fractionally wet media [153]. The primary drainage curves move monotonically lower with increasing oil-wet fraction. The value of water saturation is normalized. The apparent water phase saturation is zero at the minimum measured water saturation. The apparent water phase saturation is unity at the maximum measured water saturation.

The trend of the experimental data in Fig. 4.29a and Fig. 4.31 with increasing oil-wet fraction is very similar. In addition, in both sets of experiments half of the drainage curve for the fully oil-wet (100% oil-wet) medium locate below zero capillary pressure.



## Imbibition

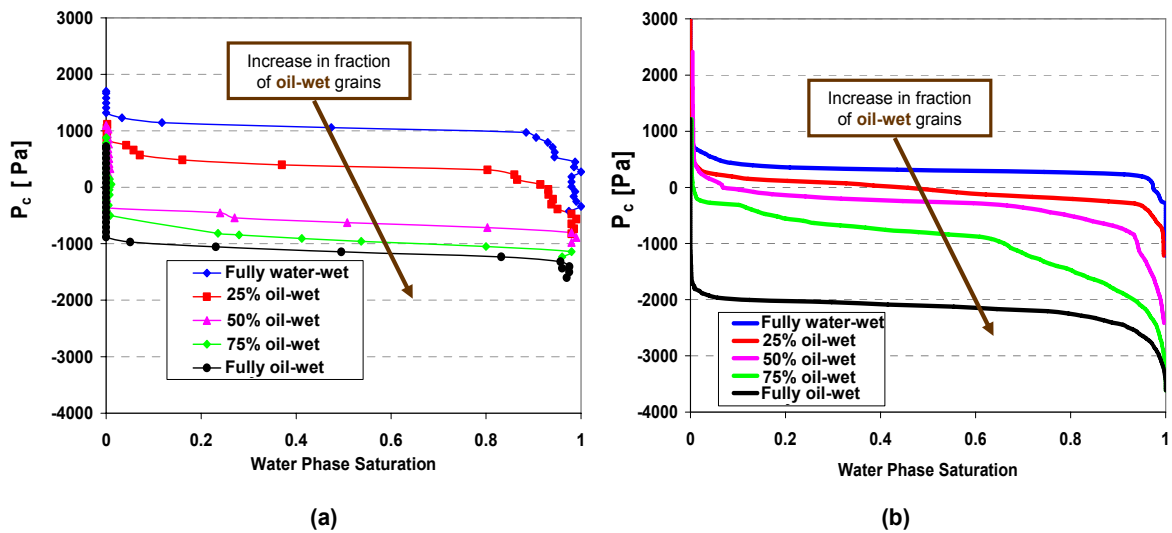


Figure 4.32. (a) Measured octane/water imbibition curve for the fractionally wet media. The primary imbibition curves move monotonically lower with increasing oil-wet fraction. (b) Simulation results for imbibition of fractionally wet media. The contact angles on water-wet and oil-wet grains are  $\theta_{ww} = 30^\circ$  and  $\theta_{ow} = 150^\circ$ , respectively. For the model, we multiply the curvature by the known interfacial tension and divide by the grains radii to obtain the capillary pressure in Pascal.

Fig. 4.32a shows the measured  $P$ - $S$  curves for primary imbibition for 5 different sands of varying oil-wet fraction. The primary imbibition was measured for octane/water system. The imbibition curves move monotonically lower with increasing oil-wet fraction. We simulate the imbibition with the same fraction of oil-wet grains as experimental data. We multiply the dimensionless curvature by the known interfacial tension and divide by grains radii to obtain the capillary pressure in Pascal for simulation results. Fig. 4.32b shows the simulation results for fractionally wet porous media in which the contact angles on its water-wet and oil-wet grains are  $\theta_{ww} = 30^\circ$  and  $\theta_{ow} = 150^\circ$ , respectively.

In the imbibition curves, Fig. 4.32a (experiment) and Fig. 4.31b (model), the transition capillary pressure (percolation threshold) decreases monotonically with increasing oil-wet fraction in both figures. More interestingly, the transition capillary pressure does not change linearly with oil-wet fraction in either figure. Looking at the model results (Fig. 4.32b), starting from 0% oil-wet fraction, the transition capillary pressure decreases only slightly up to about 50% oil-wet fraction; between 50% and 75% oil-wet fraction, there is a moderate decrease in the transition capillary pressure; finally between 75% and 100% the transition capillary pressure decreases significantly. Looking at the experimental results (Fig. 4.32a), different patterns are observed: a slight change of the transition capillary pressure between 0% and 25% oil-wet fraction; a large change between 25% and 75%, and finally a slight change between 75% and 100%. In addition, the imbibition curves in simulation results located at lower capillary pressure compared to the experimental measurements.

To examine the sensitivity of the model to contact angles, which are not reported for the experiments, we repeated the simulation with the contact angles for water-wet and oil-wet grains  $\theta_{ww}=0^\circ$  and  $\theta_{ow}=120^\circ$ , respectively. The results are shown in Fig. 4.33.

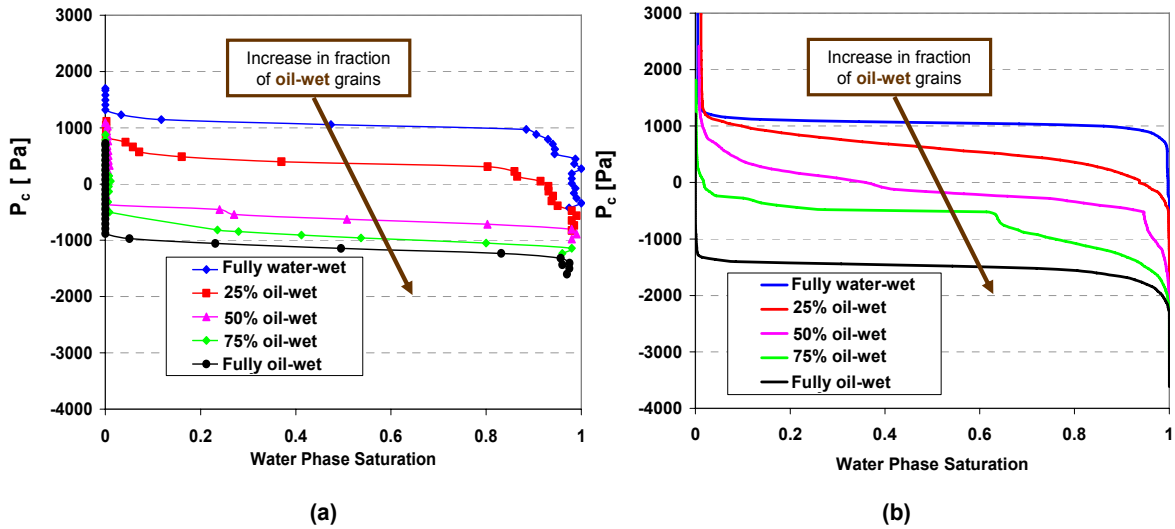


Figure 4.33. (a) Measured octane/water imbibition curve for the fractionally wet media. The primary imbibition curves move monotonically lower with increasing oil-wet fraction. (b) Simulation results for imbibition of fractionally wet media. The contact angles on water-wet and oil-wet grains are  $\theta_{ww} = 0^\circ$  and  $\theta_{ow} = 120^\circ$ , respectively. For the model, we multiply the curvature by the known interfacial tension and divide by the grains radii to obtain the capillary pressure in Pascal.

Despite the overall match between experimental data (Fig. 4.33a) and simulation results (Fig. 4.33b), several trends in the data are not captured by the simulation. For instance, in experimental data (Fig. 4.33a), the entire imbibition curve for 50% oil-wet fraction is positioned at negative capillary pressure. However, in simulation results (Fig. 4.33b), half of the imbibition curve for 50% oil-wet fraction located above zero capillary pressure line. In addition, in experimental data, the position of imbibition curve for the fully oil-wet case is slightly lower than the position of imbibition curve for the 75% oil-wet case. In contrast, in the simulation results, the position of imbibition curve for the fully oil-wet case is significantly lower compared to the position of imbibition curve for the 75% oil-wet case.

We hypothesize that the difference between experimental data and simulation results for imbibition can be contributed from the spatial correlation (clustering) of oil-wet grains. There is no spatial correlation between oil-wet grains in our model (i.e. the grains are randomly made oil-wet). However, in fractionally wet media built in laboratory, the mixing of oil-wet grains and water-wet grains can result in nonrandom distribution of oil-wet grains. The oil-wet grains have the similar weight and surface energy, while the surface properties of oil-wet grains and water-wet grains are different. Consequently, the oil-wet grains can bundle together and make a layer of oil-wet grains during the creation of the packing. This oil-wet layer prevents the water phase from imbibing to the porous medium at the positive capillary pressure. As a result, the entire imbibition curve will be located at the negative capillary pressure (see Fig. 4.33a, 50%, 75% and 100% oil-wet fraction cases).

In addition, there are discrepancies between experimental data reported for imbibition experiments of fractionally wet media, while the measurements reported for drainage experiments of fractionally wet are qualitatively similar [14, 153]. For instance, Ustohal *et al.* [204] performed imbibition experiments on fractionally wet porous media. They constructed fractionally wet media by mixing different fraction of silanized quartz sand and pure quartz sand. The silanized quartz grains were oil-wet grains and the pure quartz grains were water-wet grains. Fig. 4.34a shows measured air/water imbibition curve for fractionally wet media made by Ustohal *et al.* They reported the contact angle of  $0^\circ$  for the pure quartz sand grains (water-wet grains) and contact angle of  $110^\circ$  for silanized quartz grains (oil-wet grains). There are several qualitative differences between experimental data presented by Ashouripashaki [14] and Ustohal *et al.* [204]. For instance, in experimental data presented by Ashouripashaki (Fig. 4.33a), the entire imbibition curve for 50% oil-wet fraction is positioned at negative capillary pressure.

However, in experimental data presented by Ustohal *et al.* (Fig. 4.34a), half of the imbibition curve for 50% oil-wet fraction located above zero capillary pressure line. In addition, in experimental data presented in Fig. 4.33a, the position of imbibition curve for the fully oil-wet case is slightly lower than the position of imbibition curve for the 50% oil-wet case. In contrast, in experimental data presented in Fig. 4.34a, the position of imbibition curve for the fully oil-wet case is lower significantly compare to the position of imbibition curve for the 50% oil-wet case.

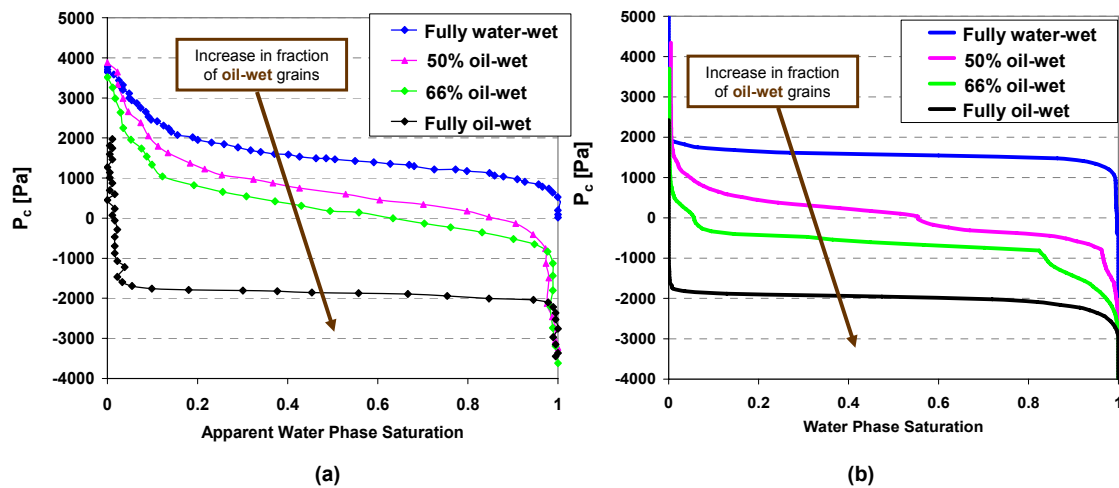


Figure 4.34. (a) Measured air/water imbibition curve for the fractionally wet media [204]. The primary imbibition curves move monotonically lower with increasing oil-wet fraction. The value of water saturation is normalized. The minimum measured water saturation equate to a value of zero for the apparent water phase saturation. The maximum measured water saturation equate to the value of one for the apparent water phase saturation. (b) Simulation result for imbibition of the fractionally wet media. The contact angles on water-wet and oil-wet grains are  $\theta_{ww} = 0^\circ$  and  $\theta_{ow} = 110^\circ$ , respectively. For the model, we multiply the curvature by the known interfacial tension and divide by the grains radii to obtain the capillary pressure in Pascal.

We simulated the imbibition for fractionally wet media, where the fluid/fluid interfaces make  $0^\circ$  contact angle with the water-wet grains and  $110^\circ$  contact angle with oil-wet grains. As shown in Fig. 4.34, the overall match between experimental data and

simulation results are satisfactory. However, several trends within the experiments are not captured by the simulations. For instance, in experimental data, the imbibition curves for 50% oil-wet case and 66% oil-wet case are located at higher capillary pressure compared to corresponding imbibition curves in simulation results.

## **4.7. DISCUSSION**

In this section, the main goal is to understand which of the five pore and throat filling processes dominate as a function of wettability and capillary pressure. We also study the effect of wettability on the fluid configuration during drainage and imbibition. We vary the wettability of a medium by changing the fraction of oil-wet grains within the medium. The first step is to analyze the effect of individual pore or throat filling event on drainage and imbibition of a fully water-wet medium.

### **4.7.1. Effect of Each Event Type on Drainage/ Imbibition within a Water-Wet Medium**

The Haines drainage event is the only pore-filling event occurs during the drainage of water-wet medium. However, several events (i.e. Melrose, generalized Haines imbibition, ring coalescence, meniscus-4<sup>th</sup> grain) could occur during imbibition within a water-wet medium. In this section we study effect of each event on the imbibition of a fully water-wet medium. For research purposes, the drainage/imbibition simulation code allows us to turn off a particular type of pore or throat filling event during the drainage/imbibition simulation (see Fig. 4.35).

#### ***Effect of Melrose Events versus Generalized Haines Imbibition Events***

First, we study the effect of generalized Haines imbibition events by simulating imbibition with other events turned off in the code. At least two menisci must merge in order for a generalized Haines imbibition event to occur. However, at the beginning of

imbibition (drainage end point), very few pores have at least two menisci on their pore throats. As a result, if we ignore pendular rings and consider only the occurrence of generalized Haines imbibition (i.e. no Melrose events), very little imbibition occurs, even when the curvature is reduced to zero. As a result, the water phase does not percolate across the medium (Fig. 4.35, light blue curve).

Next we study the effect of Melrose events. If we only allow the occurrence of the Melrose events and turn off all other events in the drainage/imbibition simulation code, the water phase does percolate through the porous medium and fill all the pores. (Here we ignore the trapping of the oil phase). During imbibition, Melrose events are essential for initially establishing enough pores with at least two menisci located in their pore throats for generalized Haines imbibition to occur subsequently. Fig. 4.35 compares the imbibition curve for the case that only Melrose event occurs (red curve) with the case that both Melrose and generalized Haines imbibition events occur (green curve). The occurrence of generalized Haines imbibition moves the imbibition curve to a higher value of the curvature.

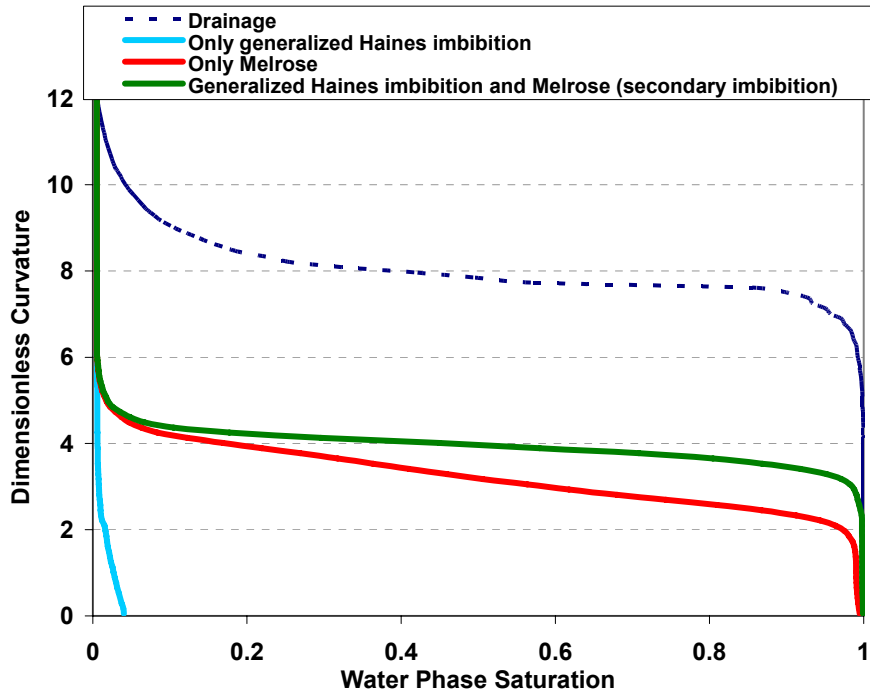


Figure 4.35. Compares the simulation results for imbibition of a water-wet medium when only generalized Haines imbibition events occur (light blue curve), only Melrose events (red curve) occur, both generalized Haines imbibition and Melrose events occur (green curve). The imbibition starts from the drainage end point. Here we ignore the trapping of the oil phase.

Fig. 4.36a plots the fraction of each type of event (i.e. Melrose and generalized Haines imbibition) versus water phase saturation during imbibition. Fig. 4.36b plots the number of total events during imbibition versus water phase saturation. Fig. 4.36 shows that more than 20% of the events occur during imbibition are Haines imbibition events. In addition, it shows when most of events occur ( $S_w=0.4$ ), more than 30% of the events are Haines imbibition events. In conclusion, even though the generalized Haines imbibition events are not dominate during imbibition of a water-wet medium, the occurrence of these events affect the imbibition. As a result, the occurrence of generalized Haines imbibition cannot be ignored.



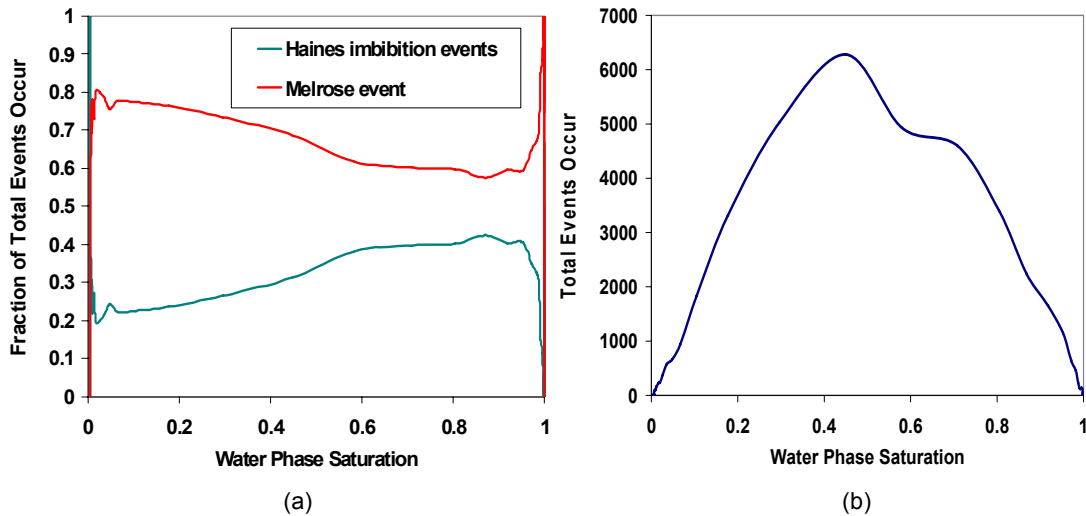


Figure 4.36. (a) Fraction of each event (i.e. Melrose and generalized Haines imbibition) during imbibition of a water-wet medium. (b) Total events during imbibition versus the water phase saturation.

Fig. 4.35 and Fig. 4.36 show the importance of the occurrence of Melrose events for imbibition of a water-wet medium. The occurrence of the Melrose events is necessary to initiate a chain of events which results in percolating the water phase through the porous medium. In addition, more than 60% of the events occur during imbibition are Melrose events.

#### ***Effect of Melrose Events versus Meniscus-4<sup>th</sup> Grain Events***

The existence of pendular rings is necessary for the occurrence of Melrose events. Consequently, the existence of pendular rings is necessary for the imbibition within a water-wet medium. However, at the beginning of the primary imbibition, the medium is completely filled with the oil (or gas) phase. As a result, no water phase pendular ring exists initially. Hence, the only possible event at high values of dimensionless curvature (above 2) is a generalized Haines imbibition event. In the absence of Melrose events, the water phase does not percolate through the medium until the applied curvature reaches a

small value. At lower dimensionless curvature (smaller than 2), some of menisci touch 4<sup>th</sup> grains (meniscus-4<sup>th</sup> grain event), and these events lead to pore-filling events (i.e. generalized Haines imbibition events). These pore-filling events initiate a chain of events that results in percolating the water phase through the porous medium. In conclusion, the occurrence of meniscus-4<sup>th</sup> grain events results in percolating the water phase through the porous medium at a lower curvature compare to occurrence of Melrose events.

Fig. 4.37 compares the *P-S* curve for primary imbibition (purple curve) and secondary imbibition (green curve). The main events occur in secondary imbibition are Melrose events. During secondary imbibition, the water phase percolates through porous medium at the curvature much higher than two due to the occurrence of the Melrose events at the high value of curvature. As a result, there is no chance for occurrence of meniscus-4<sup>th</sup> grain events. In contrast, in the absence of the pendular ring, the main events that occur in the primary imbibition are meniscus-4<sup>th</sup> grain. The meniscus-4<sup>th</sup> grain event occurs at lower value of the dimensionless curvature compared to the Melrose events. As a result, the primary imbibition curve is positioned at lower value of the curvature compared to the secondary imbibition curve. The difference between the primary and secondary imbibition curves in Fig. 4.37 show the importance of the pendular rings and its role during imbibition.

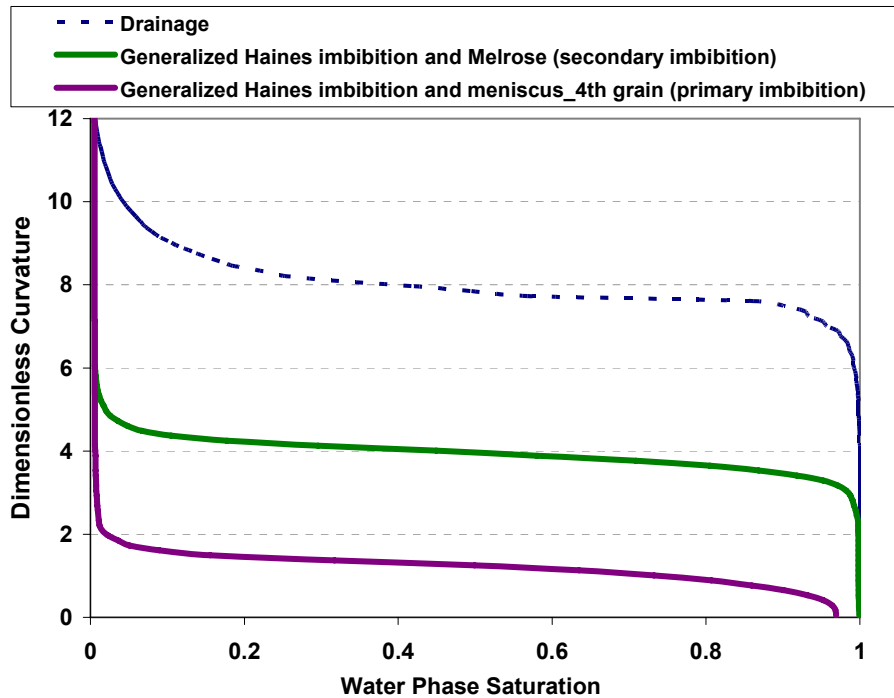


Figure 4.37. Compares the simulation results for primary imbibition of a water-wet medium (purple curve) with secondary imbibition of a water-wet medium (green curve). Haines imbibition event can occur in both primary and secondary imbibition. During secondary imbibition, pendular ring exist. Consequently, the Melrose events can occur. In contrast, in primary imbibition, no Melrose event occurs due to the lack of existence of pendular rings. During primary imbibition, the meniscus-4<sup>th</sup> grain event occurs at a small value of dimensionless curvature.

For the purpose of comparison between experimental data and simulation results, we assume that the pendular ring exist in front of the advancing menisci, even though the experimental data was measured for primary imbibition. The moisture within the porous media allows the formation of thin films. These thin films can carry small amounts of water through the roughness of the grains surfaces and build pendular rings in front of the advancing menisci. As a result, Melrose events can occur during primary imbibition experiments.

### Effect of Coalescence Events

Another type of event that can occur during imbibition within a water-wet medium is the pendular ring coalescence. In the water-wet medium, the coalescence event results in disconnecting of the oil (or gas) phase. As a result, this event called snap off in several literatures [25, 146]. Fig. 4.38 shows the effect of coalescence on the imbibition curves of the water-wet medium. The simulation results in Fig. 4.38a ignore the trapping of oil and water phase, while the simulation results in Fig. 4.38b accounts for the trapping of receding phase (oil or water). The imbibition curves with and without accounting for the coalescence events are the same in Fig. 4.38a. Hence the coalescence event does not change the position of imbibition curves. However, the coalescence event affects the saturation of the trapped water phase at the end of imbibition (Fig. 4.38b).

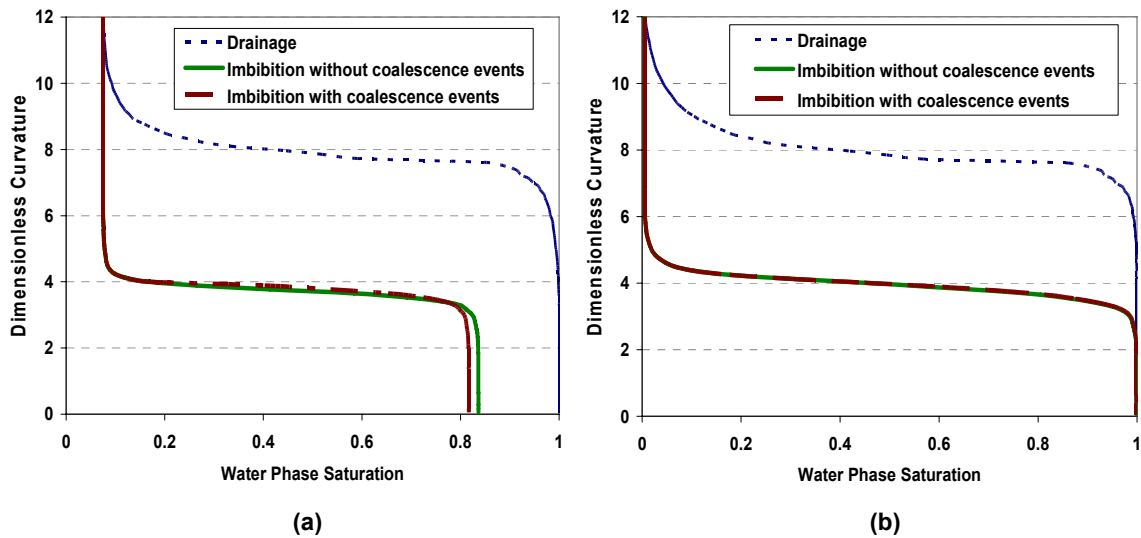


Figure 4.38. Compares the simulation results for the primary imbibition of a water-wet medium with and without accounting for the coalescence of pendular rings. (a) We ignore the trapping of the oil and water phases. (b) We take into account the trapping of the oil and water phases.

Fig. 4.38 shows that we can ignore the effect of coalescence events on the imbibition curves for the unconsolidated water-wet medium. Note that the porous

medium we use as a model rock has porosity of 36%. The coalescence of pendular rings affects imbibition in consolidated rocks (see Chapter 2 for more details). The occurrence of pendular rings coalescence during drainage and imbibition within fractionally wet media is less probable compared to the water-wet case. In fractionally wet media, not all edges can hold a pendular ring, because some edges join two grains with different wettability.

#### **4.7.2. Compare Occurrence of Each Event during Drainage /Imbibition within a Fractionally Wet Medium**

In a water-wet medium, the Haines drainage is the only event that occurs during the drainage. The generalized Haines imbibition and the Melrose events only occur during the imbibition. The Haines drainage event does not occur during imbibition within the water-wet medium. However, all pore-filling events (i.e. generalized Haines drainage, generalized Haines imbibition and Melrose events) can occur during both drainage and imbibition of a fractionally wet medium. Fig. 4.39b shows the fraction of each event during drainage of a fractionally wet medium with 25 % oil-wet grains. Fig. 4.39a shows the corresponding *P-S* curve for drainage of that medium. Fig. 4.39b shows that majority of events occur during drainage of the medium with 25% oil-wet grains are generalized Haines drainage events. Fig. 4.39b also shows some generalized Haines imbibition and meniscus-4th grain events also occur during drainage of that medium. In contrast, in a water-wet medium, the only event occur during drainage is Haines drainage event. The Melrose event hardly occurs during drainage of the medium with 25% oil-wet grains. In contrast the Melrose event is important for drainage of the medium with 75% oil-wet grains. Fig. 4.40b shows the fraction of each event during drainage of fractionally wet medium with 75 % oil-wet grains. The main events at negative curvature are the Melrose and generalized Haines imbibition. The saturation of the water phase at zero curvature is

0.6. At positive curvature, the main events are generalized Haines drainage and meniscus-4<sup>th</sup> grain. Hardly any Melrose or generalized Haines imbibition events occur at positive capillary pressure.

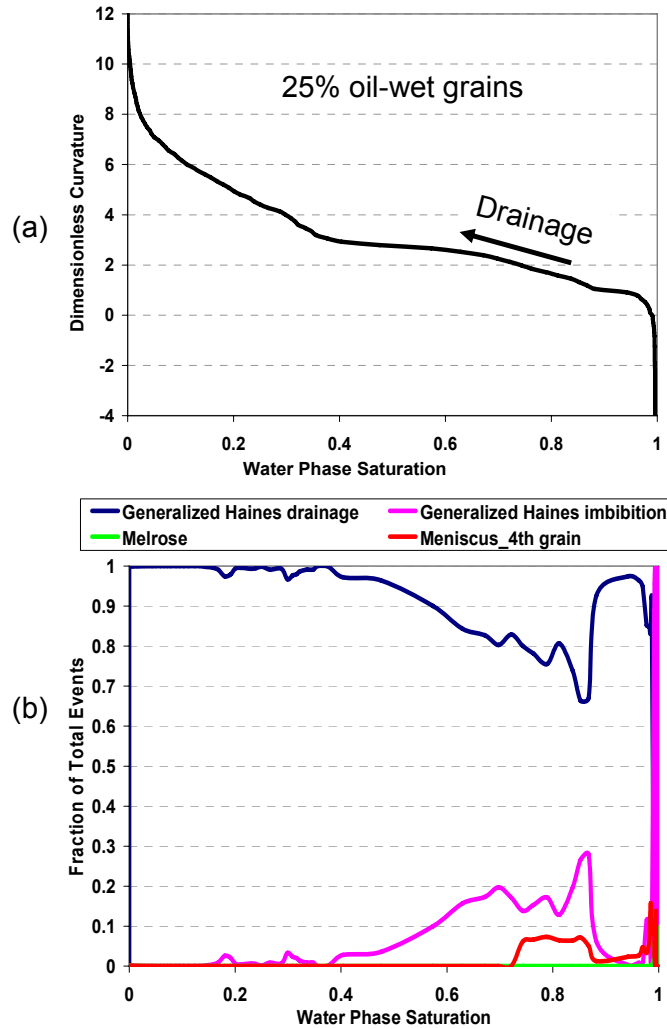


Figure 4.39. (a)  $P$ - $S$  curve for drainage of a fractionally wet medium with 25% oil-wet grains. The contact angles on water-wet and oil-wet grains are  $\theta_{ww} = 30^\circ$  and  $\theta_{ow} = 150^\circ$ , respectively. (b) Fraction of each event occur during drainage of the fractionally wet medium with 25% oil-wet grains.

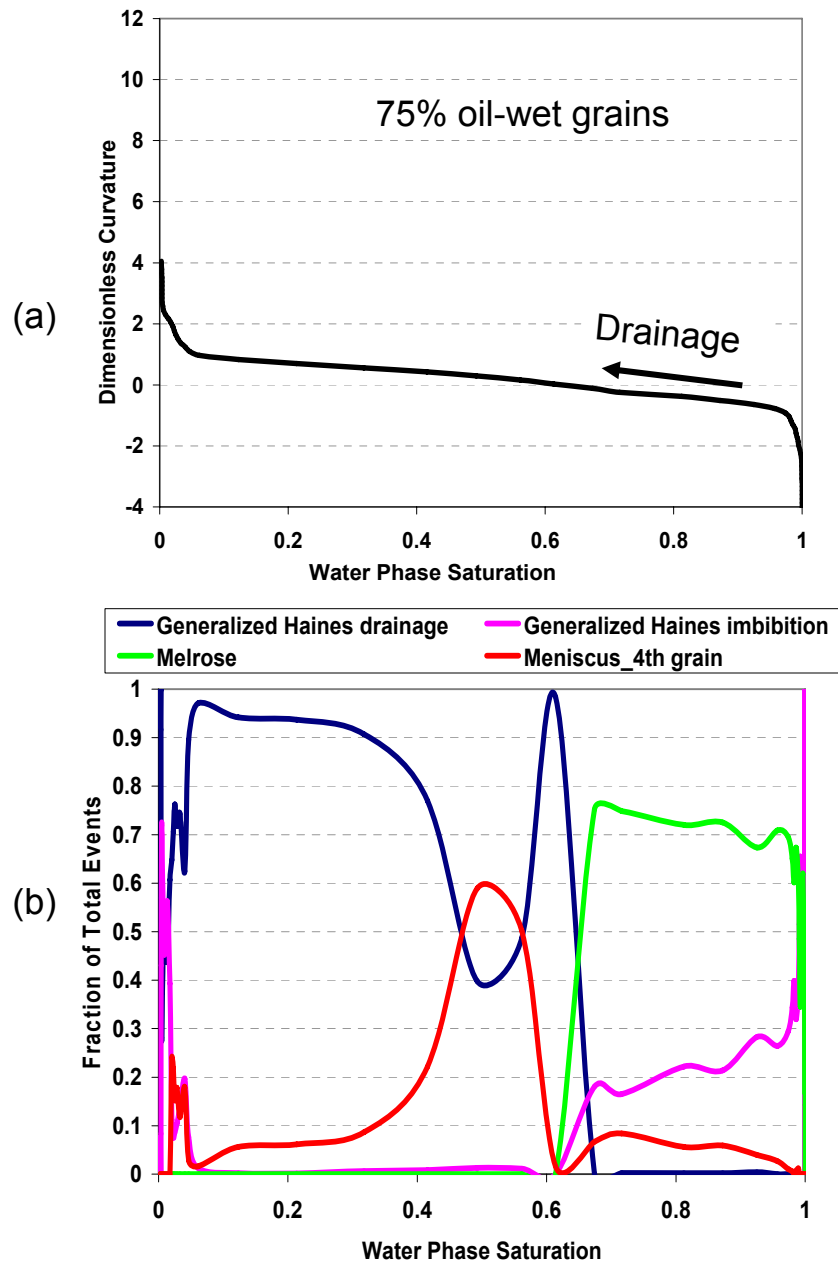


Figure 4.40. (a)  $P$ - $S$  curve for drainage of a fractionally wet medium with 75% oil-wet grains. The contact angles on water-wet and oil-wet grains are  $\theta_{ww} = 30^\circ$  and  $\theta_{ow} = 150^\circ$ , respectively. (b) Fraction of each event during drainage of the fractionally wet medium with 75% oil-wet grains.

The distribution of the event for imbibition of the medium with 25% oil-wet grains is approximately the mirror image of the distribution of the events for drainage of the medium with 75% oil-wet grains. Fig. 4.41b shows the fraction of each event during imbibition of the fractionally wet medium with 25% oil-wet grains. Fig. 4.41a shows the corresponding *P-S* curve for imbibition of that medium. During the imbibition within the fractionally wet medium with 25% oil-wet grains, Melrose and generalized Haines imbibition are the main events at positive curvature. At negative curvature, the main events are generalized Haines drainage and meniscus-4<sup>th</sup> grain. The saturation of the water phase at zero curvature is 0.4. The main events at positive curvature are Melrose and generalized Haines imbibition.

The distribution of the event for the imbibition of the medium with 75% oil-wet grains is approximately the mirror image of the distribution of the events for the drainage of the medium with 25% oil-wet grains. Fig. 4.42b shows the fraction of each events occur during imbibition of the fractionally wet medium with 75 % oil-wet grains. Fig. 4.42a shows the corresponding *P-S* curve for imbibition of that medium. Fig. 4.42b shows that majority of events occur during imbibition of the medium with 75% oil-wet grains are generalized Haines drainage events. Fig. 4.42b also show some generalized Haines imbibition and meniscus-4<sup>th</sup> grain events also occur during imbibition of the medium with 75% oil-wet grains. The Melrose event hardly occurs during imbibition of the medium with 75% oil-wet grains.



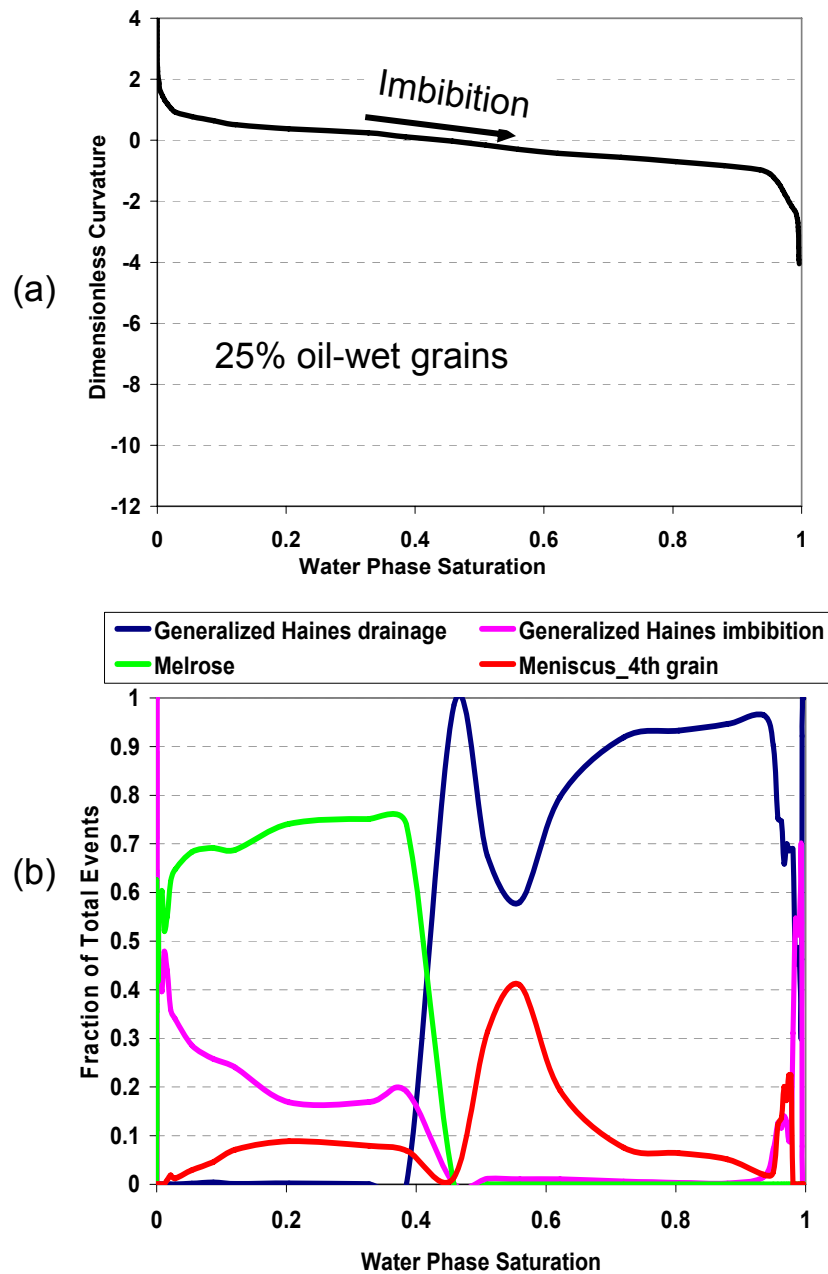


Figure 4.41. (a)  $P$ - $S$  curve for imbibition of a fractionally wet medium with 25% oil-wet grains. The contact angles on water-wet and oil-wet grains are  $\theta_{ww} = 30^\circ$  and  $\theta_{ow} = 150^\circ$ , respectively. (b) Fraction of each events occur during imbibition of the fractionally wet medium with 25% oil-wet grains.

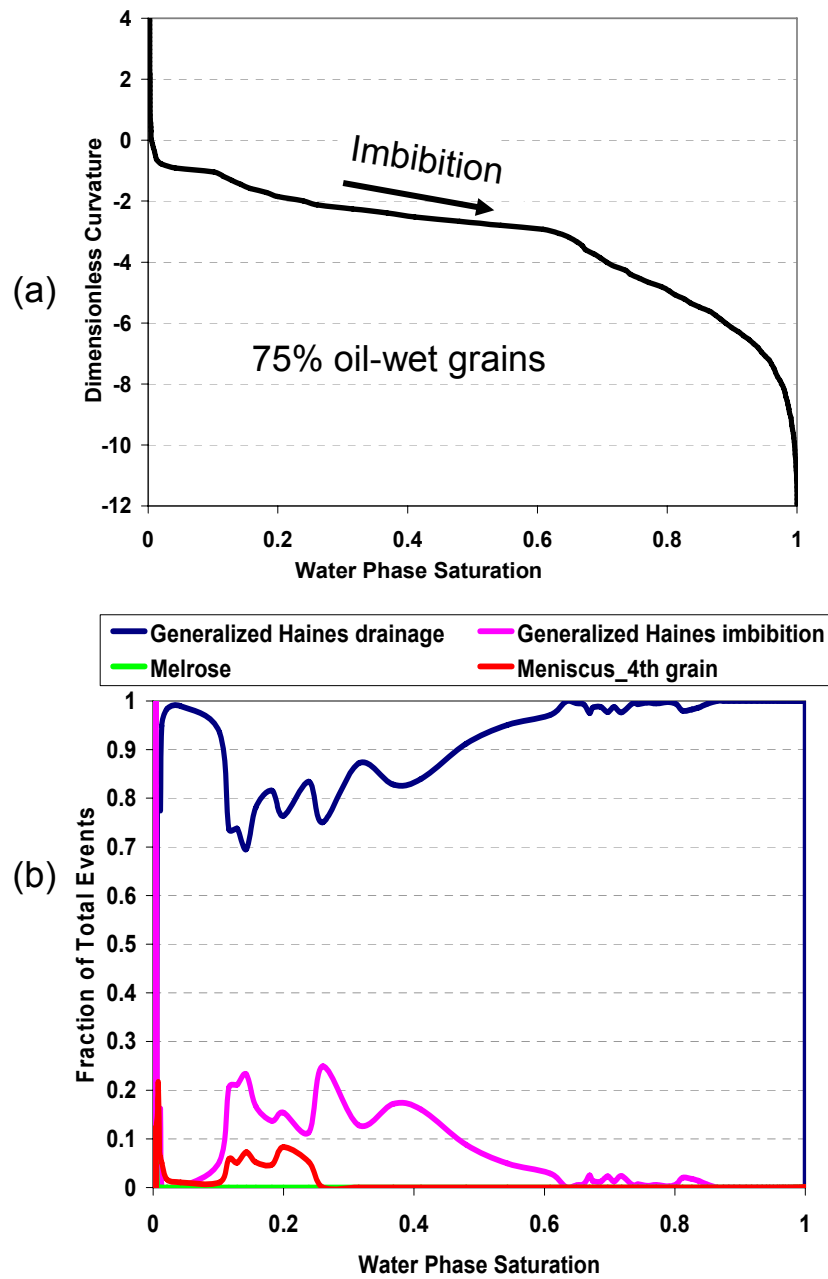


Figure 4.42. (a)  $P$ - $S$  curve for imbibition of a fractionally wet medium with 75% oil-wet grains. The contact angles on water-wet and oil-wet grains are  $\theta_{ww} = 30^\circ$  and  $\theta_{ow} = 150^\circ$ , respectively. (b) Fraction of each events occur during imbibition of the fractionally wet medium with 75% oil-wet grains.

### 4.7.3. Effect of Oil-Wet Grain Positions on Drainage/Imbibition Curves

The drainage and imbibition curves presented in previous sections are only corresponding to one realization of the fractionally wet media. For instance, for modeling a fractionally wet medium with 25% oil-wet grains, we randomly choose 25% of grains and assign the oil-wet wettability to them. As result of randomness in choosing which grain to be oil-wet, the position of oil-wet grains will change in each realization of the fractionally wet medium with 25% oil-wet grains. Fig. 4.43 shows the simulation results of primary drainage within different realization of fractionally wet media with 25% oil-wet grains.

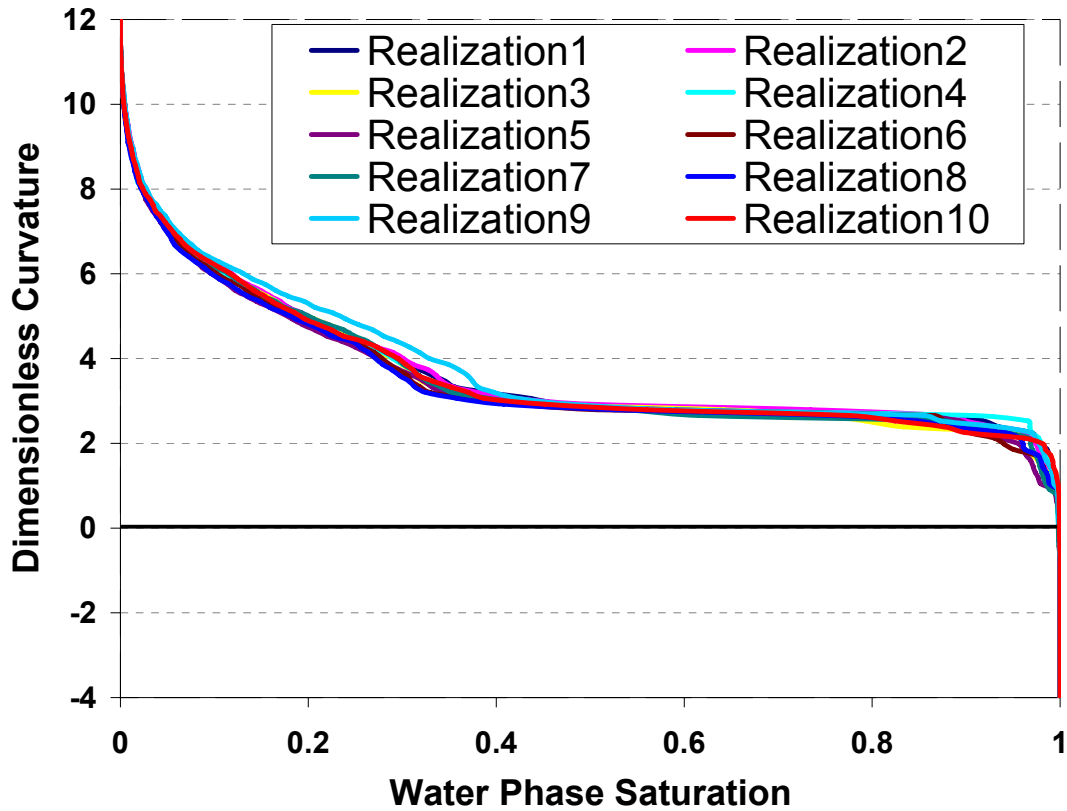


Figure 4.43. *P-S* curve for the primary drainage of different realization of the fractionally wet media with 25% oil-wet grains. The contact angles on water-wet and oil-wet grains are  $\theta_{ww} = 30^\circ$  and  $\theta_{ow} = 150^\circ$ , respectively.

In Fig. 4.43, the positions of drainage curves for different realization of the fractionally wet media are almost the same. To investigate the effect of oil-wet grain positions on drainage/imbibition curves, we study the effect of oil-wet grain positions on the criteria for pore-filling events. Among all the criteria for pore-filling events, only generalized Haines drainage criterion is an *a priori* criterion. Such a criterion can be calculated prior to and independent from the drainage/imbibition simulation. In other words, *a priori* criterion is independent of the position of menisci within the medium during drainage/imbibition simulation. Therefore, we focus our discussion on the effect of oil-wet grain position on the critical curvature for generalized Haines drainage event.

The positions of oil-wet grains within two different realizations of media with same fraction of oil-wet grains are different. Consequently, the critical curvature for each individual throat is different. However, the overall distribution (e.g. CDF, PDF) for the critical curvature of both realizations is almost the same (Fig. 4.44). As a result, the drainage curve for both realizations is quite similar. Fig. 4.44 shows the CDF (cumulative distribution function) and histograms for Haines critical curvature of two realizations of media with 25% oil-wet grains. The CDF of those realization are similar, consequently the drainage curve for those realization will be similar. Note that generalized Haines drainage event is the main pore-filling event occur during primary drainage of the medium with 25% oil-wet grains.

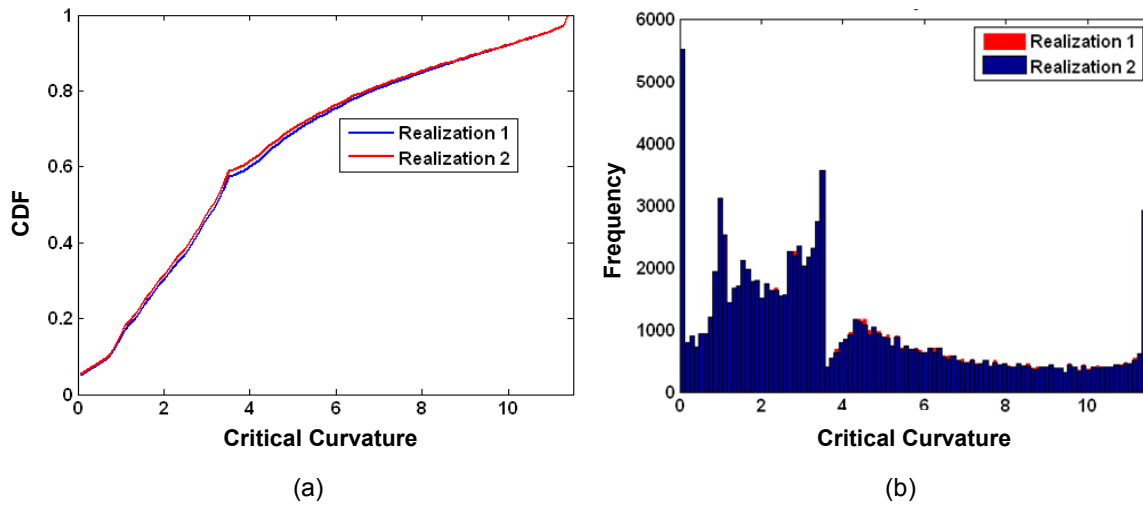


Figure 4.44. (a) CDF and (b) histograms for Haines critical curvature for drainage of two realizations of the media with 25% oil-wet grains. The CDF and histogram for the realization 1 and realization 2 are similar. The contact angles on water-wet and oil-wet grains are  $\theta_{ww} = 30^\circ$  and  $\theta_{ow} = 150^\circ$ , respectively.

Although the position of the oil-wet grains does not affect the distribution of Haines critical curvature, the fraction of oil-wet grains affects the distribution of Haines critical curvature and consequently affects the drainage process within the fractionally wet media. Fig. 4.45 compares the histogram of Haines critical curvature for the medium with all water-wet grains and the medium with 25% oil-wet grains. The peak in the histogram of Haines critical curvature for the fully water-wet medium is related to the throats with three point contacts between its grains. These throats have the smallest inscribed radius and highest value of Haines critical curvature. For convenience, we call them smallest throats. In the fractionally wet medium (e.g. medium with 25 % oil-wet grains), some of these smallest throats remain fully water-wet (i.e. three water-wet grains) and some of them become fractionally wet throat. A fractionally wet throat has either one or two oil-wet grains.

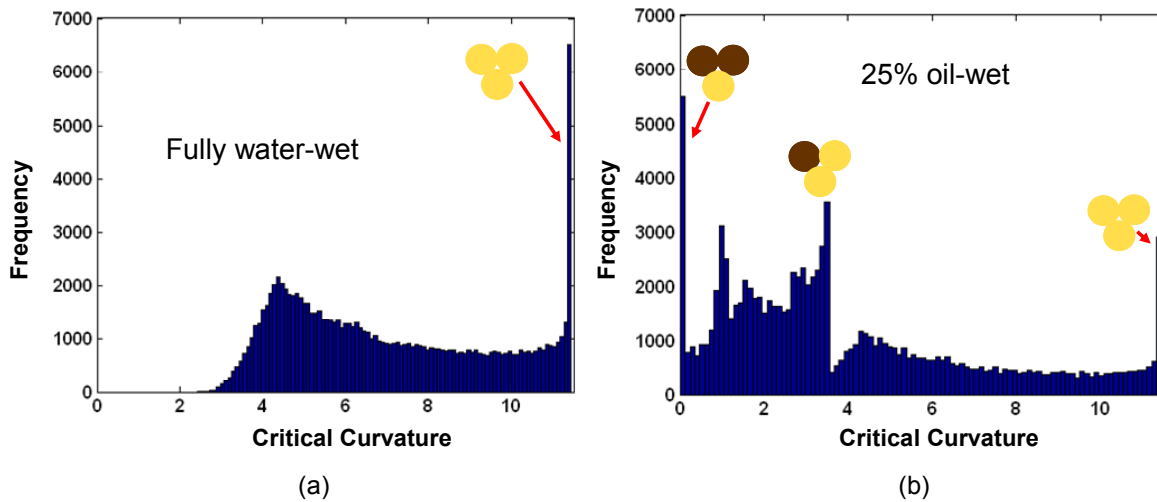


Figure 4.45. (a) Histograms for Haines critical curvature for drainage in a fully water-wet medium. The peak at the value of 11.5 is corresponding to the throats that have three point contacts between its grains. (b) Histograms for Haines critical curvature of the medium with 25% oil-wet grains. The peak at critical curvature of 11.5 associates with the throats defined by three water-wet grains that touch each other. The peak at critical curvature of 3.5 associates with throat composed of two water-wet grains and one oil-wet grain that touch each other. The peak at critical curvature of zero associates with throat composed of two oil-wet grains and one water-wet grain that touch each other. The contact angles on water-wet and oil-wet grains are  $\theta_{ww} = 30^\circ$  and  $\theta_{ow} = 150^\circ$ , respectively.

There are three peaks in Fig. 4.45b associated with these three configurations of throats in the medium with 25% oil-wet grains. The first peak is at critical curvature of 11.5. This peak associates with the throat composed of three water-wet grains that touch each other. The second peak is at critical curvature of 3.5. This peak associates with a throat composed of two water-wet grains and one oil-wet grain that touch each other. The third peak is at critical curvature of zero. This peak associates with a throat composed of two oil-wet grains and one water-wet grain that touch each other. The smallest throats with two oil-wet grains cannot hold menisci at positive curvature. As a result, the CDF of

Haines critical curvature for medium with 25% oil-wet grains shifts toward smaller value of critical curvature.

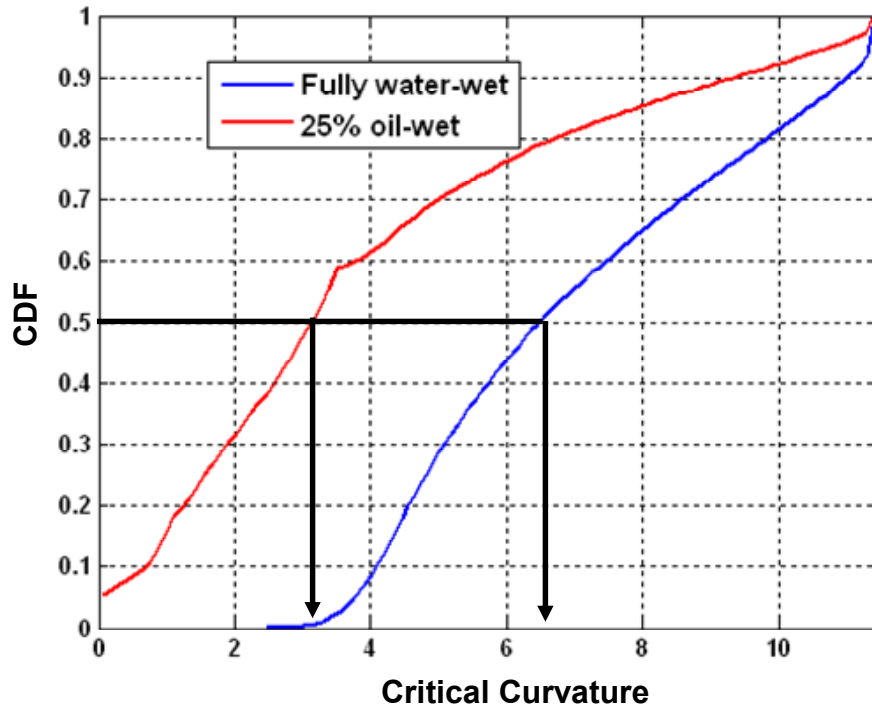


Figure 4.46. CDF of Haines critical curvature of a fully water-wet medium (blue curve) and the medium with 25% oil-wet grains (red curve). 50% of throats within the medium with 25% oil-wet grains have Haines critical curvature smaller than 3.5. 50% of throats within the fully water-wet medium have Haines critical curvature smaller than 6.5. The value of 50% corresponds to the bond percolation threshold of the random sphere pack [143]

Fig. 4.46 compares the CDF of Haines critical curvature for the fully water-wet medium with the fractionally wet medium with 25% oil-wet grains. 50% of throats within the medium with 25% oil-wet grains have Haines critical curvature smaller than 3.5. The value of 50% corresponds to the bond percolation threshold of the random sphere pack [143]. During primary drainage of the medium with 25% oil-wet grains, when the applied curvature is increased above bond percolation threshold for Haines critical curvature (3.5), then the oil phase percolates through the medium (Fig. 4.26). As a result, the oil

phase accesses almost all the pores. Therefore, the drainage curve for the curvature above 3.5 looks like the drainage curve obtained from the bundle of tubes model. Note that in bundle of tubes model, all pores are accessible and the critical curvature for drainage of the pore is inversely proportional to the radius of the tubes. In the fully water-wet medium, 50% of throats have Haines critical curvature smaller than 6.5 (Fig. 4.46). Consequently, the oil phase percolates through the medium at applied curvature above 6.5 (Fig. 4.26).

In conclusion, the position of oil-wet grains does not affect the  $P-S$  curve of fractionally wet media. However, the fraction of oil-wet grain affects the  $P-S$  curve of fractionally wet media. Note that, the positions of oil-wet grains within the fractionally wet media are randomly chosen. Effect of spatial correlation for oil-wet grains on the drainage/imbibition is not within the scope of this study.

#### **4.7.4. Effect of Meniscus-4<sup>th</sup> Grain Criterion on the Primary Drainage Curves of Fractionally Wet Media**

In Section 4.4.3.4, we develop a novel and mechanistic criterion for the meniscus motion within a porous medium. When a meniscus touches a grain located in front of the meniscus, pore-filling events occur and the meniscus advances. To our knowledge, this criterion was not considered in other study of fluid flow within a porous medium. Fig. 4.47 compares the primary drainage simulation results without considering this criterion (Fig. 4.47a) with the primary drainage simulation results including this criterion (Fig. 4.47b). Fig. 4.47a shows that primary drainage curves for the fully oil-wet medium, the medium with 75% oil-wet grains, and the medium with 50% oil-wet grains are positioned at the same curvature. In other words, the curvature corresponding to the percolation threshold of their primary drainage curves are the same.



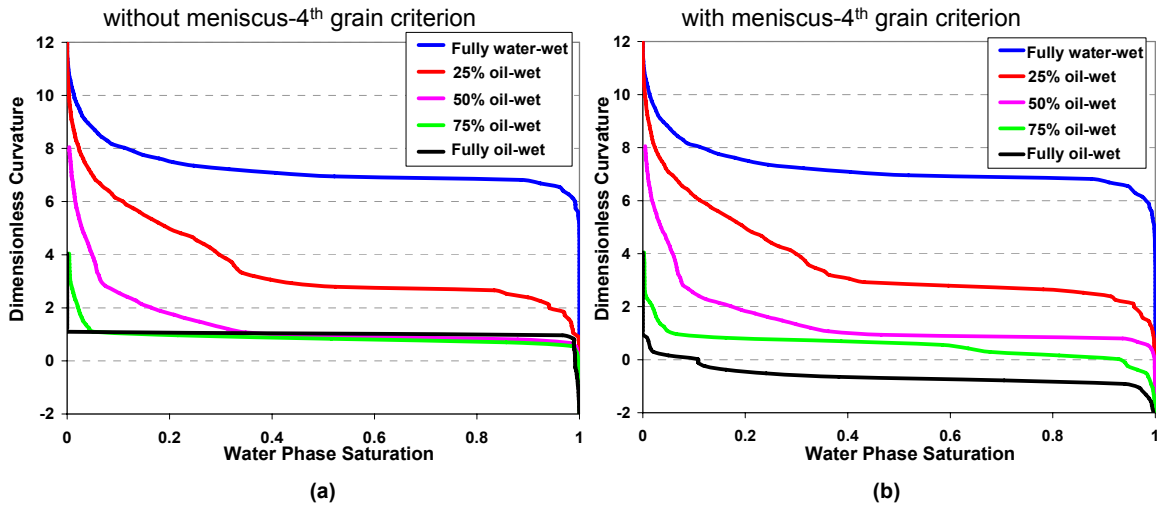


Figure 4.47. (a) Primary drainage curves for the porous media with different fractions of oil-wet ( $\theta_{ow} = 150^\circ$ ) grains distributed randomly among water-wet ( $\theta_{ww} = 30^\circ$ ) grains. The meniscus-4<sup>th</sup> grain event is not considered. (b) Primary drainage curves for the porous media with different fractions of oil-wet ( $\theta_{ow} = 150^\circ$ ) grains distributed randomly among water-wet ( $\theta_{ww} = 30^\circ$ ) grains. The meniscus-4<sup>th</sup> grain event is considered.

During drainage, the oil phase invades to the porous medium and when a meniscus touches an oil-wet grain, the oil phase then climbs through the rough surface of the grain and creates pendular rings on the edges, which results in pore-filling events. However, if the meniscus touches a water-wet grain, the oil phase does not climb the grain and does not create pendular rings. Consequently, no pore-filling event occurs. As a result, the effect of meniscus-4<sup>th</sup> grain events on primary drainage curve decreases as the fraction of oil-wet grains decreases. We can observe this trend in the Fig. 4.47. The position of primary drainage curve for the fully-water-wet medium, the medium with 25% oil-wet grains, and the medium with 50% oil-wet grains are the same in both Fig. 4.47a and Fig. 4.47b. The position of primary drainage curve for the fully oil-wet medium and the medium with 75% oil-wet grains are different in Fig. 4.47a and Fig. 4.47b.

During the primary drainage of the fully oil-wet medium, the oil phase percolates at negative curvature if the menisci touch grain criterion is considered, while the oil phase does not percolate until the curvature increase to positive value as shown in Fig. 4.47a. The primary imbibition of the fully water-wet medium is mirror image of primary drainage of the fully oil-wet medium. Therefore, the meniscus-4<sup>th</sup> grain criterion is important to be considered for simulation of primary imbibition of the fully water-wet medium. Without this consideration, the water phase does not percolate through the medium at positive capillary pressure.

#### **4.7.5. Residual Phase Saturation**

In this section, we study the effect of wettability on the residual phase saturation. The residual phase saturation exists in two morphologies: trapped phase inside pores and trapped phase as isolated pendular rings. The saturation of later morphology (pendular rings) is small and negligible compare to the saturation of trapped phase inside pores. Hence, we study the effect of wettability on the saturation of trapped phase inside pores.

Wettability is one of the phenomena that affect the trapped phase saturation, but it is not the only phenomenon. For instance, the boundary conditions (e.g. number of pores available for the receding phase to exit the porous medium) also affect the trapped phase saturation.

##### ***Effect of Number of Exit Pores on Trapped Phase Saturation***

We use a spherical pack with cube dimension to study the fluid flow through fractionally wet media. If more sides of the cube are open as exits, more pores are available for receding phase to exit. This must affect the trapped phase saturation. For instance, in our simulations of primary drainage, the oil phase enters from one side (side

1 Fig. 4.1) to the porous medium. The water phase can either exit from one side (side 4 Fig. 4.1) or exits from five sides (all side except side 1, Fig. 4.1).

Fig. 4.48 compares the drainage and imbibition curves for the fully water-wet medium which only one of its side open as exit side for the receding phase (red curve) with the fully water-wet medium which has five exit sides (blue curve).

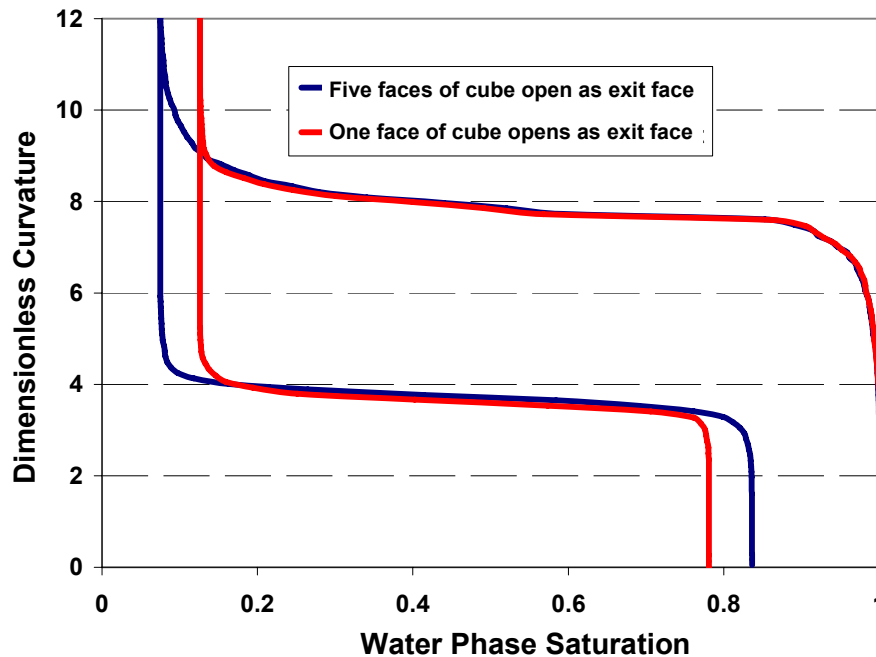


Figure 4.48. Shows the difference in the trapped phase saturation at the end of drainage and imbibition for a water-wet medium with two different boundary conditions. The red curve shows the result for drainage/imbibition when only one side of the medium is open as an exit side. The blue curve shows the result for drainage/imbibition when five sides of the medium are open as the exit sides.

Fig. 4.48 shows that as the number of sides open for exiting phase increases, the residual saturation for the water phase decreases. The same trend was observed by Behseresht *et al.* [20].

### Effect of Wettability on Trapped Phase Saturation

In this section, we study the effect of wettability on the residual phase saturation. Hence, we keep the boundary condition consistence. In all simulation results below, only one side of the porous medium is available as the exit side. Fig. 4.49 shows the primary drainage curves for porous media with different fraction of oil-wet grains. The oil-wet grains have a contact angle of  $150^\circ$  and the water-wet grains have a contact angle of  $30^\circ$ . The water phase gets trapped when disconnected from the bulk phase.

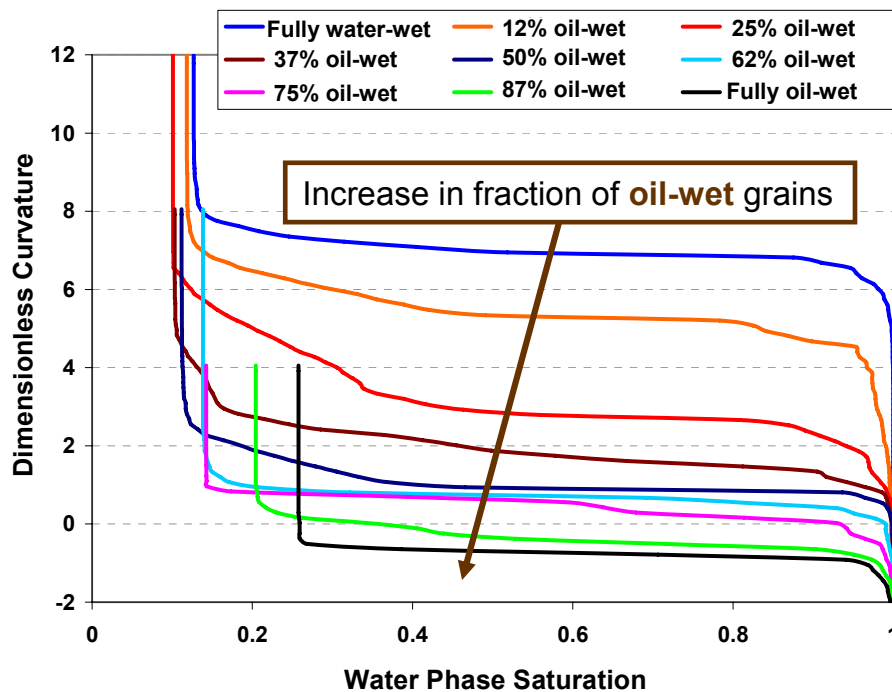


Figure 4.49. Comparison between primary drainage curves for the porous media with different fractions of oil-wet ( $\theta_{ow} = 150^\circ$ ) grains distributed randomly among water-wet ( $\theta_{ww} = 30^\circ$ ) grains. The water phase gets trapped when disconnected from the bulk phase.

Initially, the residual water saturation decreases when the fraction of oil-wet grains increases from 0% to 25%. Further increase in the fraction of oil-wet grains (i.e. from 25% to 100%) increases the residual water saturation.

The primary drainage curves shown in Fig. 4.49 correspond to only one realization of each fractionally wet medium. The position of the oil-wet grains affects the residual saturation of receding phase. As a result, the value of the residual receding phase saturation for a medium with specific fraction of oil-wet grains is a range, not an exact number. Fig. 4.50 compares the residual water phase saturation at the end of primary drainage for porous media with different fraction of oil-wet grains.

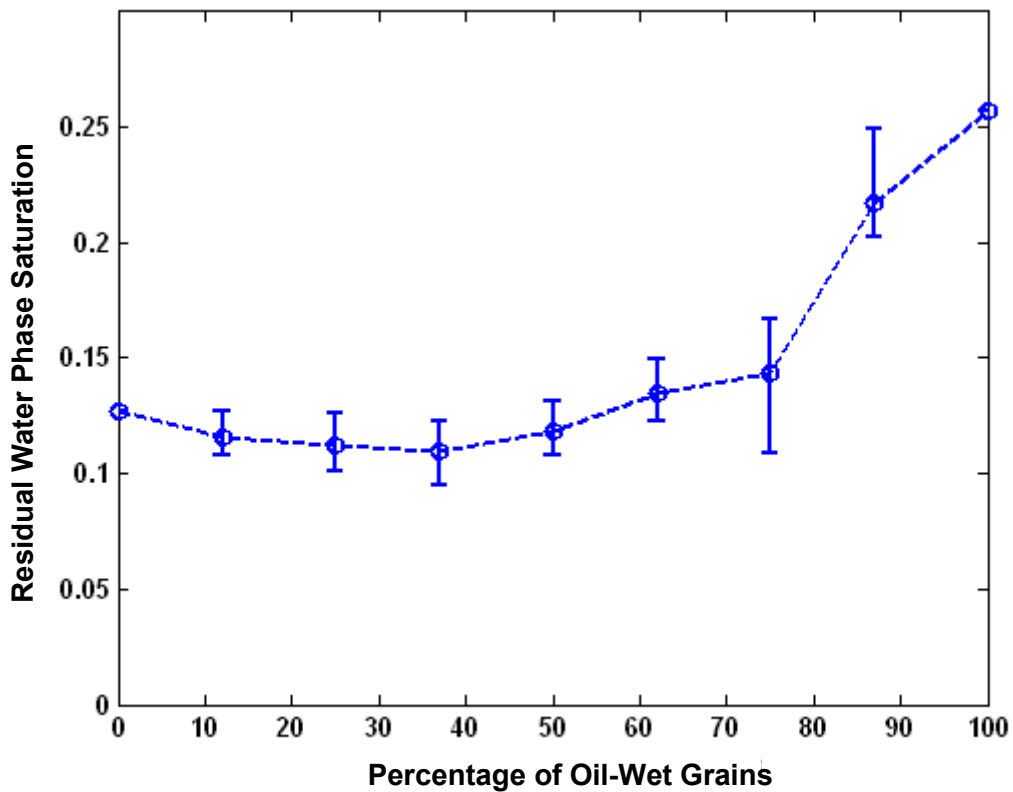


Figure 4.50. Compares the residual water phase saturation at the end of primary drainage for porous media with different fraction of oil-wet ( $\theta_{ow} = 150^\circ$ ) grains distributed randomly among water-wet ( $\theta_{ww} = 30^\circ$ ) grains. The marker 'O' shows the average value of the residual water saturation for primary drainage of different realization of fractionally wet media. The bar shows the maximum and minimum values for residual water saturation achieved for simulation of 10 realizations.

## 4.8. CONCLUSIONS

We developed a grain-based and mechanistic model for oil/water displacement under capillary control in the fractionally wet media. This is done by generalizing the grain-based criteria previously developed for fully water-wet media (i.e. the Haines and Melrose criteria) to be used for fractionally wet media. A novel criterion (i.e. meniscus-4<sup>th</sup> grain criterion) is proposed for the instability of a meniscus when the meniscus touches a grain located in front of it. We implemented and illustrated the model in a dense disordered packing of spheres, solving analytically for stable configuration of the meniscus held between grains of arbitrary and unequal contact angle. Using the model, we carried out drainage and imbibition simulations that yield *a priori* predictions of the grain-scale configurations of water/oil interfaces (menisci) within the fractionally wet porous medium. The predictions of macroscopic properties (e.g. *P-S* curve for imbibition and drainage) agree semi-quantitatively with experimental data. The experimental data and simulation result both show a nonlinear behavior between the position of *P-S* curves and fraction of oil-wet grains.

The model allows an understanding and prediction of how pore-filling processes change as a function of the initial wetting state, the wettability of each grain and the fraction of each type of grain. We found that for a water-wet medium, the difference between *P-S* curves of primary and secondary imbibition is due to the existence of pendular rings during secondary imbibition which allows Melrose events to take place. In contrast, for primary imbibition, the meniscus-4<sup>th</sup> grain events are necessary to initiate imbibition, causing the imbibition to take place at a lower capillary pressure.

For fractional wettability, the grain-based model of displacement has no criteria developed specifically for drainage or for imbibition. Instead, we developed generalized grain-based criteria for five types of pore/throat filling events. As a result, our model

unifies the simulation of drainage and imbibition processes. In this approach, the familiar hysteresis of the  $P$ - $S$  curves between drainage and imbibition in uniformly wet media is due to the difference in the type of pore/throat filling events that occur during each part of the cycle. The only event that occurs during drainage of a fully water-wet medium is the generalized Haines drainage event. The main events that occur during imbibition of a fully water-wet medium are the generalized Haines imbibition and Melrose events. In contrast, all types of pore/throat filling events can occur during drainage and imbibition of fractionally wet media. Consequently, the unified grain-based model is the only mechanistic way to simulate capillary controlled displacement (i.e. drainage and imbibition) in fractionally wet media.

## CHAPTER 5: CONCLUDING REMARKS

We used a dense random sphere packing as a model of sediment. We geometrically modified this model sediment to simulate a rock forming process (i.e. isopachous quartz cementation). By simulating thick cement layers, we obtained a simple model for low porosity-low permeability rocks. We extracted a physically representative network from this rock model. Using this network to compute phase permeability, we quantified the effect in this simple model rock at very low saturations (less than 6% wetting phase) by considering the geometry of pendular rings and liquid bridges held at grain contacts and near-contacts. The rings/bridges reduce the area open to flow of gas phase. This reduces the effective radius of these throats and thus reduces the effective permeability to the gas phase. For small porosity, the rings/bridges can coalesce in throats as the wetting phase saturation increases, causing snap off of the gas phase. This reduces the connectivity of the gas phase and thus amplifies the reduction in effective permeability. Coalescence occurs much less often in model rocks of larger porosity. This difference contributes to the greater sensitivity of tight gas sandstones to water saturation.

The model also provides a quantitative explanation for the disproportionately large reduction in gas permeability caused by injection of dry gas into a brine-saturated core. The salt precipitated from the initial brine saturation; builds porous obstructions corresponding to the locations of pendular rings/liquid bridges. In this manner a small volume of solid salt can obstruct a large enough volume of pore space to reduce permeability disproportionately.

We also developed a grain-based, mechanistic model for oil/water displacement under capillary control in 2D and 3D fractionally wet media. We implemented and illustrated the model by solving analytically for the stable configuration of the meniscus



held between grains of arbitrary and unequal contact angle. We generalized the grain-based criteria previously developed for fully water-wet media (i.e. Haines and Melrose criteria) to be used for fractionally wet media. We also developed a previously unrecognized criterion (i.e. meniscus-4<sup>th</sup> grain criterion) for instability of a meniscus when the meniscus touches a grain located in front of it.

Our model of displacement has no criteria developed specifically for drainage events or for imbibition events. Instead, we developed generalized grain-based criteria for five types of pore/throat filling events. In any simulation of capillary controlled displacement, we simply check for the occurrence of each of the five pore/throat filling events. As a result, our model unified the algorithm for simulation of drainage and imbibition. That is, we have established a single modeling approach within which drainage and imbibition are special cases. In this approach, the familiar hysteresis of  $P$ - $S$  curves between drainage and imbibition in uniformly wet media is due to difference in the type of pore/throat filling events that occur during each part of the displacement cycle. The only event that occurs during drainage of a fully water-wet medium is the generalized Haines drainage event and the main events that occur during imbibition of a fully water-wet medium are both generalized Haines imbibition and Melrose events. However, all types of pore/throat filling events can occur during drainage and imbibition of fractionally wet media. Consequently, use of the unified grain-based model is the only mechanistic way to simulate capillary controlled displacement (i.e. drainage and imbibition) in fractionally wet media. The criteria applied in fractionally wet porous media are not fundamentally different from criteria applied in mixed wet porous media. As a result, we expect that the grain-based approach should be well suited for modeling of capillary controlled displacement within mixed wet media, which are of great practical interest in petroleum engineering.

## APPENDIX A: TOROID APPROXIMATION FOR CALCULATING VOLUME AND CROSS-SECTION AREA OF PENDULAR RINGS/LIQUID BRIDGES

In this section, we develop the numerical implication of toroid approximation for the calculation of volume and cross-section area of pendular rings. Fig. A.1 shows the schematic of a pendular ring that makes non-zero contact angle ( $\theta$ ) with grains. The radii of both grains equal  $R$ .

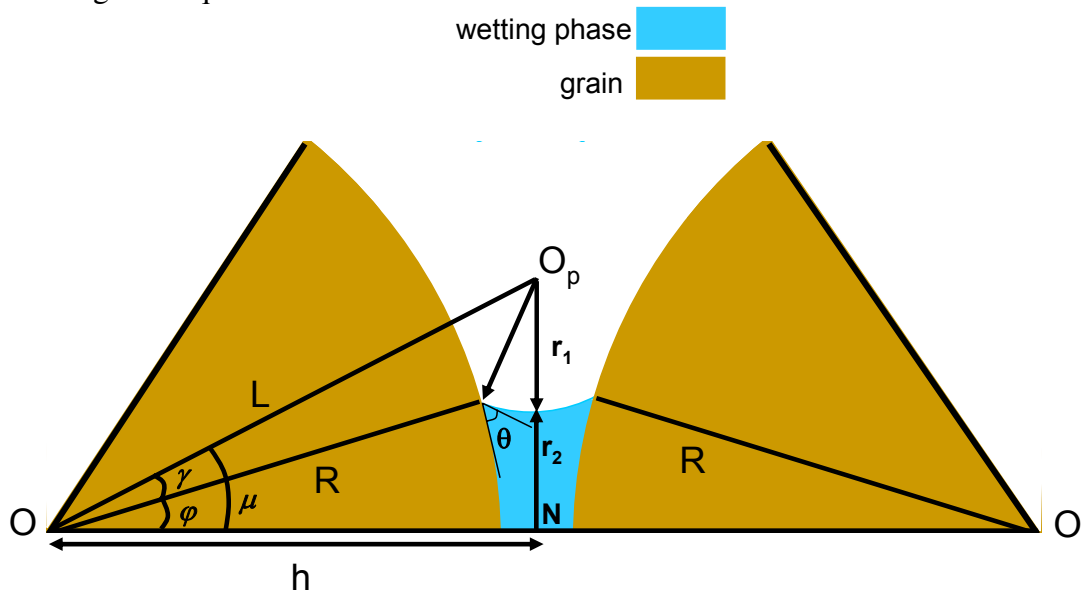


Figure A.1. Schematic of a toroidal liquid bridge of the wetting phase between two grains with radius  $R$ . The contact angle between the pendular ring and grains is  $\theta$ . The vertices  $O$  and  $O'$  correspond to the sphere centers. Line  $\overline{OO'}$  that joins the sphere centers is the axis of symmetry for the liquid bridge. For the toroid approximation, the surface of the liquid bridge has radii of curvature  $r_1$  and  $r_2$ . The grain centers are separated by distance  $2h$ . Point  $N$  is the equidistance from grain centers.

Geometry of pendular rings/liquid bridges depends on the geometry of grains (e.g. radii of grain,  $R$ , distance between the grains center,  $(2h)$ , and the wettability of grains (contact angle,  $\theta$ ). The geometry of pendular rings/liquid bridges will be known if the values of radii of curvature ( $r_1$  and  $r_2$ ) are calculated. From definition of mean curvature, we can write

$$\frac{1}{r_1} - \frac{1}{r_2} = C. \quad (\text{A.1})$$

We also write cosine rule for triangle  $\triangle OO_pN$

$$L^2 = R^2 + r_1^2 - 2Rr_1 \cos(\pi - \theta) = R^2 + r_1^2 + 2Rr_1 \cos(\theta). \quad (\text{A.2})$$

Another form of Eq. A.2 can be express as

$$L = \sqrt{R^2 + r_1^2 + 2Rr_1 \cos(\theta)}. \quad (\text{A.3})$$

From trigonometry of triangle  $\triangle OO_pN$ , we can write

$$h^2 + (r_1 + r_2)^2 = L^2. \quad (\text{A.4})$$

Substituting Eq. A.1 and A.3 in Eq. A.4 results in a cubic equation.

$$r_2^3 + pr_2 + q = 0. \quad (\text{A.5})$$

Eq. A.5 has three real roots if  $\left(\frac{p}{3}\right) + \left(\frac{q}{2}\right) < 0$ , where

$$\begin{aligned} p &= \frac{3n - m^2}{3}, \\ q &= t + \frac{2m^3}{27} - \frac{mn}{3}, \\ n &= \frac{C(h^2 - R^2) - 2R \cos(\theta)}{C}, \\ m &= \frac{3}{C}, \\ t &= \frac{h^2 - R^2}{C}. \end{aligned}$$

When two grains touch, then the value of  $h$  (half length between grains center) and the value of  $R$  (radii of grains) are equal. As a result,  $r_2$  has only one positive root which it

exists for all value of curvature. In contrast,  $r_2$  has two positive roots, when there is gap between grains constructing the edge holding the liquid bridge. In addition, for each gap size, there is maximum value of curvature in which  $r_2$  has at least one positive root. The liquid bridge at curvature higher than this critical curvature is not stable and will be ruptured. When  $r_2$  has two positive roots, we choose larger value of  $r_2$ . Larger value of  $r_2$  yields to smaller surface area to volume ratio and is favorable thermodynamically.

In summary, we calculate value of  $r_2$  from Eq. A.5, value of  $r_1$  from Eq. A.1, and value of  $L$  from Eq. A.3. From these values, we can calculate the value of filling ( $\varphi$ ) angle of the rings/bridges. The rings/bridges filling angle  $\varphi$ , is the angle between the line connecting the two grains centers of the edge (line  $\overline{OO'}$  in Fig. A.1) and line connecting a center of grains and the point that pendular ring touch the grains. From trigonometry of triangle  $\triangle OO_p N$ , the rings/bridges filling angle  $\varphi$  equals to

$$\varphi = \mu - \gamma,$$

where

$$\mu = \sin^{-1}\left(\frac{r_1 + r_2}{L}\right),$$

$$\gamma = \cos^{-1}\left(\frac{R^2 + L^2 - r_1^2}{2RL}\right).$$

These values define the geometry of the pendular rings/liquid bridges. Now, we can calculate the cross-section area and volume of the rings/ bridges from their geometry.

### A.1.CROSS-SECTION AREA

The cross-section area of rings/bridges is calculated based on the value of rings/bridges filling angle, radii of curvature ( $r_1$  and  $r_2$ ), grain radius ( $R$ ), and the distance between two grains center ( $2h$ ).

$$Area = \left[ (r_1 + r_2)h - R^2\varphi - r_1^2\left(\frac{\pi}{2} - \varphi\right) \right].$$

## A.2. VOLUME

In order to calculate the volume of a pendular ring, we calculate volume of a solid revolution of surface of the rings/bridges around axis of  $\overline{OO'}$ . We calculate this volume by integration using method of cylindrical shells [65]. Gvirtzman and Roberts [85] use this method to calculate volume and surface area of pendular rings (i.e.  $h=R$ ). We extended this method to calculate the volume of the pendular rings/liquid bridges when there is gap between grains holding the liquid bride (i.e.  $h>R$ ) or when two grains overlap (i.e.  $h<R$ ). The volume of pendular rings/liquid bridges is calculated from Eq. A.6 if  $h \geq R$  and it is calculated from Eq. A.7 if  $h < R$ .

If  $h \geq R$ :

$$volume = 4\pi \left[ \frac{R^3}{3} (1 - \cos^3 \varphi) + \frac{R^2 h}{2} \sin^2 \varphi + \frac{(h - R \cos \varphi)^3}{3} - \frac{a}{2} \left( (R \sin \varphi - a)(h - R \cos \varphi) + r_1^2 \left( \frac{\pi}{2} - \varphi \right) \right) \right], \quad (A.6)$$

if  $h < R$ :

$$volume = 4\pi \left[ \frac{h^3}{6} + R^2 \cos^2 \varphi \left( \frac{h}{2} - \frac{R \cos \varphi}{3} \right) + \frac{(h - R \cos \varphi)^3}{3} - \frac{a}{2} \left( (R \sin \varphi - a)(h - R \cos \varphi) + r_1^2 \left( \frac{\pi}{2} - \varphi \right) \right) \right], \quad (A.7)$$

where  $a = r_1 + r_2$ ,  $r_1$  and  $r_2$  are radii of curvature,  $j$  is the filling angle of the ring/bridge, and  $h$  is half length between grains center.

## APPENDIX B: EFFECT OF GRAIN SURFACE ROUGHNESS

In this appendix, we study the effect of grain surface roughness on the effect of low wetting phase saturation held in the rings/bridges on the non-wetting phase permeability (see Chapter 2).

The grain surface in real rocks is rough, creating nooks and crannies that can be occupied by wetting phase. In our model (see Chapter 2) grains are smooth spheres and thus we neglect the contribution of this wetting phase morphology. In this appendix, we evaluate the contribution of this form of wetting phase, combining our model with the ideas of Moulu *et al.* [151]. We anticipate that the small cavities on the rough surface contribute little to gas flow, so filling them with wetting phase affects saturation but not gas phase permeability.

Moulu *et al.* [151] present a fractal model for the roughness of pore walls (grain surfaces). The fractal dimension  $D_L$  is a measure of roughness. During a drainage experiment the effect of roughness on the wetting phase becomes most pronounced near the drainage endpoint. Thus the fractal dimension can be estimated from the drainage curve at low  $S_w$  (Moulu *et al.*):

$$P_c \propto S_w^{\left(\frac{1}{D_L-2}\right)}. \quad (\text{B.1})$$

Our simulated capillary pressure curve for low  $S_w$ , Fig. 2.8, is re-plotted as curvature versus wetting phase saturation on log-log scales in Fig. B.1. All the curves have slopes smaller than 0.6.

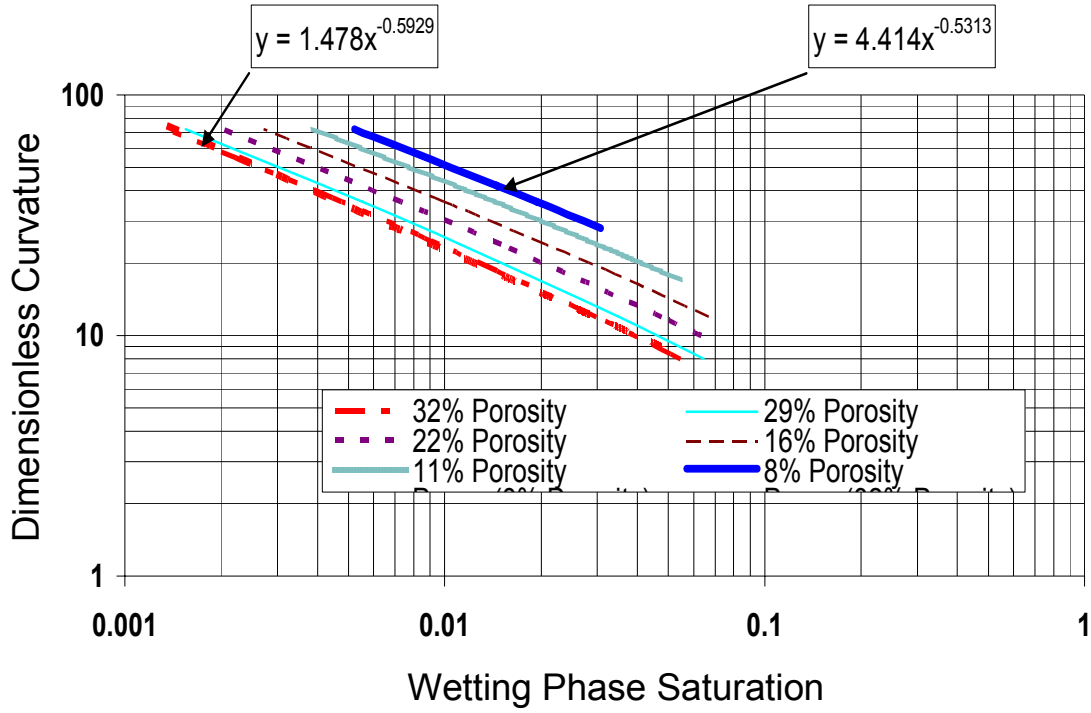


Figure B.1. Capillary pressure (divided by interfacial tension to yield curvature) exhibits a power law dependence on wetting phase saturation in our model rocks. The exponents have magnitudes between 0.53 and 0.6, corresponding to fractal dimension  $D_L$  between 0.1 and 0.34.

We use Eq. B.1 to estimate the  $D_L$  for our simulation result. The maximum value for  $D_L$  for our model rocks is small, about 0.34. Small values would be expected since the models have smooth grains.

Moulu *et al.* [151] also calculate the effective gas permeability using fractal dimension of medium,  $D_L$ :

$$k_{rg} = k_{rg \max} \left( 1 - S_L^{\left( \frac{1}{2-D_L} \right)} \right)^4. \quad (\text{B.2})$$

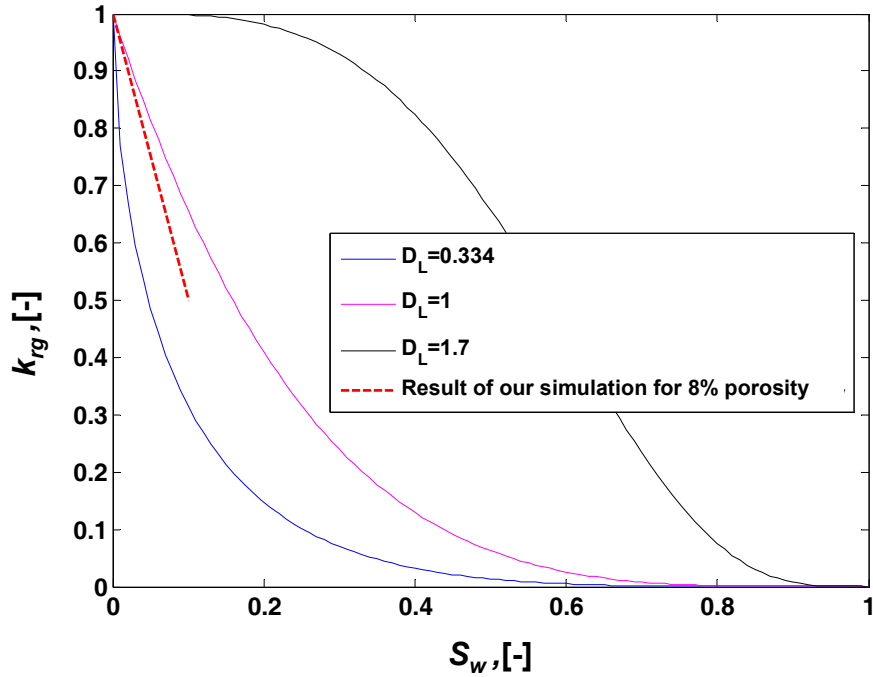


Figure B.2. As fractal dimension increases corresponding to increasingly rough grain surfaces, Eq. B.2 predicts that gas relative permeability is less sensitive to small saturations of water. We assume  $k_{rg,max} = 1$  for all curves. At a fractal dimension of 1.7, which corresponds to a strongly water-wet rock [151], the gas phase permeability is almost independent of water saturation for  $S_w < 0.1$ . This indicates that the pore space associated with surface roughness in this rock makes a negligible contribution to the gas phase permeability. Thus, when water occupies that pore space, it contributes to  $S_w$  but does not change  $k_{rg}$ . For comparison, a fractal dimension 0.334 corresponds to our high porosity model rock; Eq. B.2 predicts greater sensitivity to low  $S_w$  than observed in experiments or predicted by our model.

Fig. B.2 compares the gas relative permeability curves computed from Eq. B.2 for porous media with different fractal dimension. Moulu *et al.* [151] report  $D_L$  of 1.7 for a strongly water-wet rock. The weak dependence of  $k_{rg} / k_{rg,max}$  on  $S_w$  at low  $S_w$  for this value of fractal dimension makes intuitive sense. Very rough surfaces can have a substantial volume of pore space associated with the surface, even though the characteristic length scale for the surface roughness is too small to make a substantial contribution to flow. Thus, filling the associated pore space with the wetting phase increases  $S_w$  without



altering  $k_{rg}$ . This treatment of surface roughness supports our conclusion that the volume of wetting phase held as pendular rings and liquid bridges is the cause of reduced gas phase permeability at low  $S_w$ .

As indicated in Fig. 2.10, our model predicts greater sensitivity to low  $S_w$  than observed in tight gas sandstones. Accounting for surface roughness would improve the prediction. At any given curvature the value of  $S_w$  would be greater than in our model, because the volume associated with “nooks and crannies” would be added to the volume of pendular rings. But only the pendular rings affect pore throat hydraulic conductance and thus gas phase permeability. Thus the slope of  $k_{rg}$  vs.  $S_w$  would be less steep.

## APPENDIX C: STABILITY AND POSITION OF MENISCI WITHIN FRACTIONALLY WET POROUS MEDIA

### C.1. STABILITY OF A MENISCUS (HAINES CRITERION)

In this appendix, we find an analytical solution for the position of the stable meniscus on a two-dimensional fractionally wet throat. The fractionally wet throat is composed of two disks with arbitrary radii. The intersections of the meniscus with the disks are forced to be at the contact angle of each surface. The contact angles can be varied from  $0^\circ$  to  $180^\circ$ . For a meniscus with constant curvature, the geometry of the meniscus is defined by the center of the meniscus  $(x_0, y_0)$ , the radius of meniscus, and the intersections with the solid surface. The geometry of meniscus is calculated based on the geometry of disks forming the fractionally wet throat. Since the geometry of these disks is known, the position of center of each disks (e.g.  $x_1, y_1$ ), the radius of each disks ( $R_1, R_2$ ), and the gap width ( $D$ ) between two disks are also known. In addition, the contact angle between each disk and the meniscus ( $\theta_1, \theta_2$ ) is also pre-defined. Thus, we assume in the two dimensional media, the meniscus with constant curvature is the arc of circle with radius equal to reciprocal of mean curvature. Together, these constraints yield a trigonometry problem to be solved for the center of meniscus.

Fig. C.1. shows the schematic of a meniscus positioned on the fractionally wet throat. The point  $O$  is the center of the meniscus, and the center of disk 1 and disk 2 are  $O_1$  and  $O_2$  respectively.  $r$  is the radius of the meniscus.  $L_1$  and  $L_2$  are the distance of the center of meniscus from the center of disk 1 and disk 2 respectively.  $P_1$  and  $P_2$  are the contact point of the meniscus with the disk 1 and disk 2 respectively.

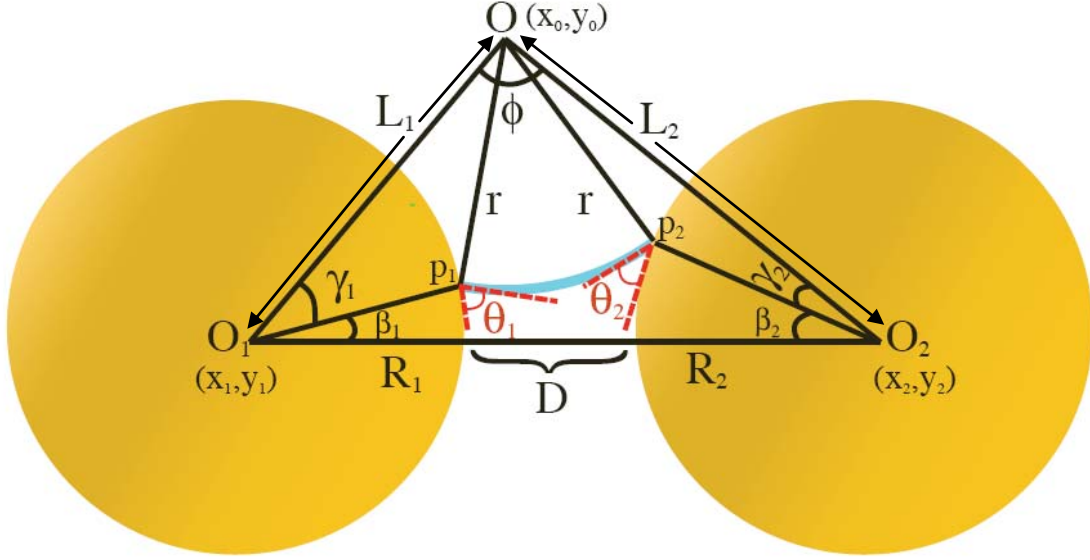


Figure C.1. Schematic of a meniscus (blue) with radius of  $r$ , located on two disks with different contact angle  $(\theta_1, \theta_2)$ . The disks have different radii  $(R_1, R_2)$ .  $L_1$  and  $L_2$  are distance of center of meniscus from center of disk 1 and disk 2 respectively.  $P_1$  and  $P_2$  are the contact point of the meniscus with the disk 1 and disk 2 respectively.

The first step is to find the criteria for the stability of the meniscus. We write cosine rule for triangle  $\triangle O_1P_1O$

$$L_1^2 = R_1^2 + r^2 - 2R_1r \cos(\pi - \theta_1) = R_1^2 + r^2 + 2R_1r \cos(\theta_1), \quad (\text{C.1})$$

another form of Eq. C.1 can be expressed as

$$L_1 = \sqrt{R_1^2 + r^2 + 2R_1r \cos(\theta_1)}. \quad (\text{C.2})$$

Now we write cosine rule for triangle  $\triangle O_2P_2O$

$$L_2^2 = R_2^2 + r^2 - 2R_2r \cos(\pi - \theta_2) = R_2^2 + r^2 + 2R_2r \cos(\theta_2), \quad (\text{C.3})$$

$$L_2 = \sqrt{R_2^2 + r^2 + 2R_2r \cos(\theta_2)}. \quad (\text{C.4})$$

Eq. C.2 and C.1 express the distance between centers of meniscus to the center of the disks based on the radii of the disks, radius of meniscus, and the contact angle each disk

makes with the meniscus. If the meniscus is stable on the fractionally wet throat, there exists a center for a meniscus. As a result, the triangle  $\triangle O_1O_2O$  which connecting center of disks to the center of meniscus exists. The cosine rule for triangle  $\triangle O_1O_2O$  leads to

$$(D + R_1 + R_2)^2 = L_1^2 + L_2^2 - 2L_1L_2 \cos \varphi, \quad (\text{C.5})$$

where  $\varphi$  is the angle between line  $\overline{OO_1}$  and  $\overline{OO_2}$ .  $L_1$  and  $L_2$  are the length of lines  $\overline{OO_1}$  and  $\overline{OO_2}$  respectively. Re-working of the right-hand side of Eq. C.5 leads to

$$L_1^2 + L_2^2 - 2L_1L_2 + 2L_1L_2(1 - \cos \varphi) = (L_1 - L_2)^2 + 2L_1L_2(1 - \cos \varphi). \quad (\text{C.6})$$

As a result the Eq. C.5 can be written as

$$1 - \cos \varphi = \frac{(D + R_1 + R_2)^2 - (L_1 - L_2)^2}{2L_1L_2}. \quad (\text{C.7})$$

The Eq. C.7 leads to criterion for stability of the meniscus located on the fractionally wet throat. Since  $\cos \varphi$  is bounded between -1 and 1, therefore  $1 - \cos \varphi$  is bounded between 0 and 2. As a result the Eq. C.7 leads to the inequality of

$$0 \leq \frac{(D + R_1 + R_2)^2 - (L_1 - L_2)^2}{2L_1L_2} \leq 2. \quad (\text{C.8})$$

Inequality C.8 can be simplified by taking into account the trigonometry of triangle  $\triangle O_1O_2O$ . In triangle  $\triangle O_1O_2O$ , the length of one side,  $\overline{O_1O_2}$ , is bigger or equal to the difference between the length of two other sides ( $\overline{OO_1}$  and  $\overline{OO_2}$ ). In other words,  $(D + R_1 + R_2) \geq (L_1 - L_2)$ . In addition the length of each side is positive (i.e.  $L_1 \geq 0$ ,  $L_2 \geq 0$ ). This consideration leads to

$$\frac{(D + R_1 + R_2)^2 - (L_1 - L_2)^2}{2L_1L_2} \geq 0. \quad (\text{C.9})$$

The lower limit of Eq. C.9 occurs when value of  $\varphi$  equals to zero. This situation occurs when the curvature of the meniscus equals to zero. As a result, the center of the meniscus has a distance of infinity relative to the center of disk 1 and disk 2. Consideration of Eq C.9 simplifies the inequality of C.8 to

$$\frac{(D + R_1 + R_2)^2 - (L_1 - L_2)^2}{2L_1L_2} \leq 2. \quad (\text{C.10})$$

If the criterion of Eq. C.10 is satisfied, then the meniscus is stable on the fractionally wet throat. The upper limit of Eq. C.10 occurs when value of  $\varphi$  equals to  $180^\circ$ , and arises when the center of the meniscus ( $O$ ) is located on the line  $\overline{O_1O_2}$ . In this situation, the meniscus is unstable and the Haines' jump occurs. Fig. 4.6b and Fig. 4.7b are example of this situation.

In the next step, we calculate an important geometrical parameter, such as filling angles for the meniscus (i.e.  $\beta_1, \beta_2$ ). The filling angle is the angle between the line connecting the contact point of a meniscus and a disk to the center of the disk and the line connecting two centers of the disks composing the throat holding the meniscus. The line connecting two disks center refers to throat line in this text

$$\beta_1 = \mu_1 - \gamma_1,$$

$$\beta_2 = \mu_2 - \gamma_2,$$

where

$$\begin{aligned} \cos(\mu_1) &= \frac{(D + R_1 + R_2)^2 - L_2^2 + L_1^2}{2(D + R_1 + R_2)L_1}, & \cos(\mu_2) &= \frac{(D + R_1 + R_2)^2 - L_1^2 + L_2^2}{2(D + R_1 + R_2)L_2}, \\ \cos(\gamma_1) &= \frac{R_1^2 - r^2 + L_1^2}{2R_1L_1}, & \cos(\gamma_2) &= \frac{R_2^2 - r^2 + L_2^2}{2R_2L_2}. \end{aligned}$$

Eq. C.10 is a general criterion for any two disks with different contact angles and different radii. We illustrate it for two specific cases that are frequently observed in the fractionally wet medium. First, we study the stability of a meniscus located on a water-wet throat. Fig. C.2 shows the schematic of a meniscus positioned on two disks of equal size ( $R_1=R_2=R$ ) with zero contact angles  $\theta_1=\theta_2=0^\circ$ .

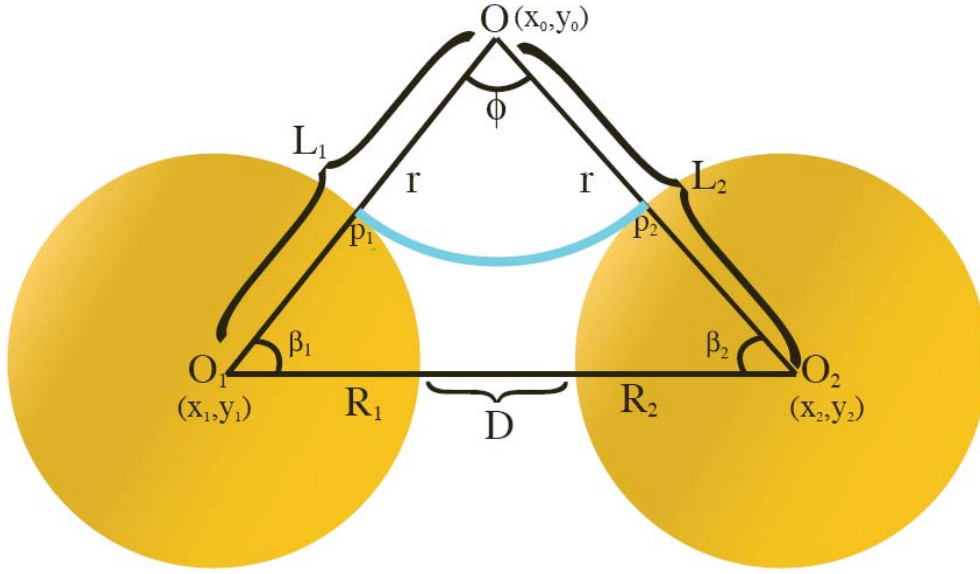


Figure C.2. Schematic of a meniscus (blue) with radii of  $r$ , located on two disks with zero contact angles ( $\theta_1=\theta_2=0$ ). The disks have same radius ( $R_1=R_2=R$ ) and are separated by a gap of width  $D$ .

The main difference between Fig. C.2 and Fig. C.1 is the position of the contact point between the meniscus and disks (points  $p_1$  and  $p_2$ ). In the Fig. C.2, the point  $p_1$  and  $p_2$  located on line  $\overline{OO_1}$  and  $\overline{OO_2}$  respectively. As a result, all triangles merge to only one triangle ( $\triangle O_1O_2O$ ). In Fig. C.2, the distances from center of each disk to the center of meniscus are equal:

$$L_1 = L_2 = r + R, \quad (\text{C.11})$$

and substituting Eq. C.11 in the Eq. C.10 simplifies the criterion for a meniscus to be stable on the water-wet throat. The Eq. C.12 is the criterion for stability of a meniscus on the water-wet throat.

$$(D + 2R)^2 \leq 4(R + r)^2, \quad (\text{C.12})$$

The Eq. C.12, can be simplified more to Eq. C.13.

$$r \geq \frac{D}{2}. \quad (\text{C.13})$$

Eq. C.13 defines a minimum radius of the stable meniscus for a given gap width  $D$ . In Fig. C.2 the meniscus will be stable if the radius of meniscus is bigger than half of the gap. Thus, as soon as the radius of the meniscus becomes smaller than half of the gap width, the meniscus becomes unstable, and a Haines' jump occurs.

Fig. C.3 shows the stable and unstable value for the radius of meniscus located on the water-wet throat composed of two equal size disks. In the Fig. C.3, the minimum radii of the stable menisci are plotted versus half the gap size of water-wet throats. The radii of menisci and gap size are normalized to the radii of the disks. The data points in the Fig. C.3 are computed from Eq. C.10. These data points create a straight line with slope of 1 and intercept of zero. As a result, this line represents the Eq. C.13.

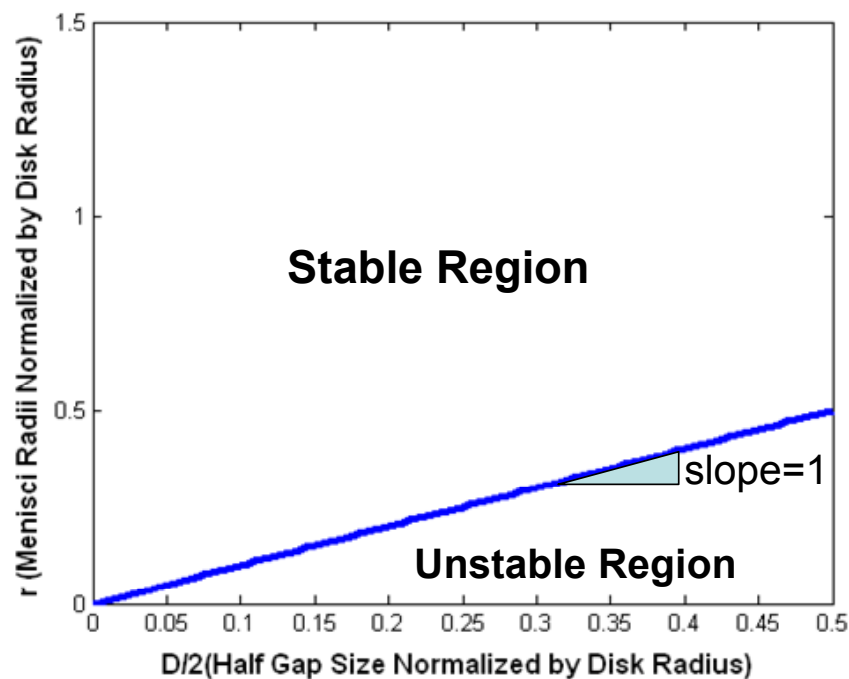


Figure C.3. Stable and unstable values for radii of menisci located on the water-wet throat composed of two equal size disks. The area above the blue line is the region of stable menisci. The area below the blue line is the region of unstable menisci. The slope of blue line is one and its intercept is zero.

The other specific case of interest is when two disks have the same radii and opposite wetting preference. These two disks form a fractionally wet throat. Fig. C.4 shows the schematic of a meniscus positioned on two disks of equal size with  $0^\circ$  and  $180^\circ$  contact angles ( $\theta_1=0^\circ$ ,  $\theta_2=180^\circ$ ).

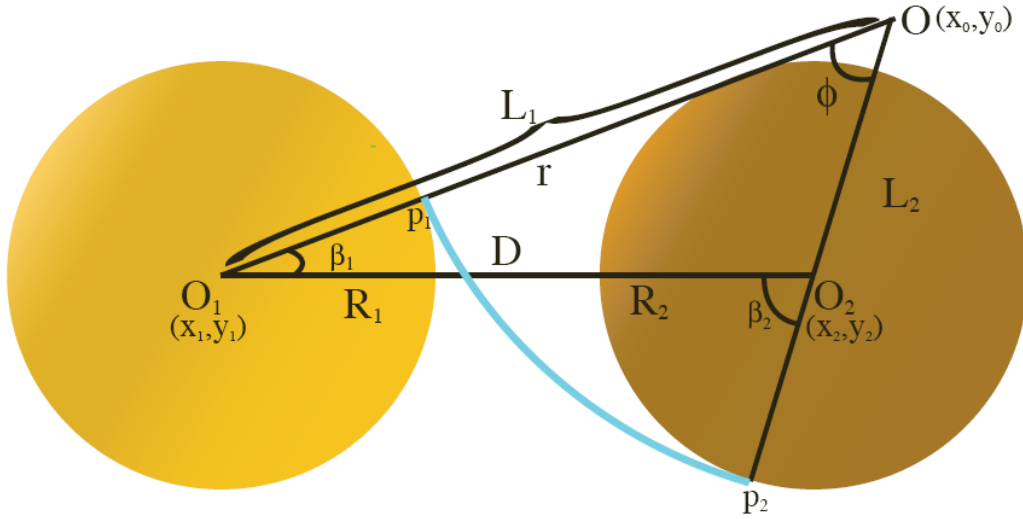


Figure C.4. Schematic of a meniscus (blue) with radii of  $r$ , located on two disks with zero and  $180^\circ$  contact angles ( $\theta_1=0$ ,  $\theta_2=180^\circ$ ). The disks have same radius ( $R_1=R_2=R$ ).

In Fig. C.4, the distances from the center of the meniscus to the center of disk 1 and disk 2 are  $L_1$  and  $L_2$ , where

$$L_1 = r + R, \quad L_2 = r - R. \quad (\text{C.14})$$

Substituting Eq. C.14 in to Eq. C.10 leads to

$$D + 2R \leq 2r. \quad (\text{C.15})$$

Eq. C.15 can be re-arranged to

$$r \geq \frac{D}{2} + R. \quad (\text{C.16})$$

Eq. C.16 defines a minimum radius of the stable meniscus for a given gap width  $D$ . In Fig. C.4 the meniscus will be stable if the radius of the meniscus is bigger than the



summation of half of the gap size and the radius of the disk. Comparing the inequality of C.16 and C.13 shows that the minimum radius of the stable meniscus located on the fractionally wet throat is bigger than the minimum radius of the stable meniscus located on the water-wet throat. Both throats have the same size gap of  $D$ . In addition, the radius of meniscus and the curvature of meniscus are inversely proportional. Therefore, the meniscus located on fractionally wet throat will be unstable at lower curvature compare to the meniscus located on water-wet throat.

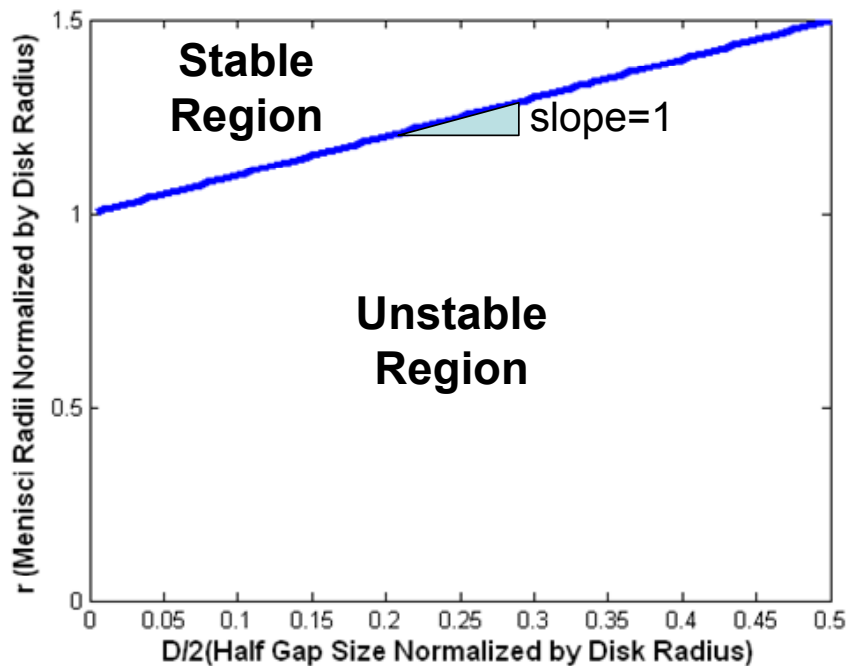


Figure C.5. Stable and unstable values for radii of menisci located on the fractionally wet throat composed of two equal size disks with zero and  $180^\circ$  contact angles ( $\theta_1=0, \theta_2=180^\circ$ ). The area above the blue line is the region of stable menisci. The area below the blue line is the region of unstable menisci. The slope of blue line is one and its intercept is one.

Fig. C.5 shows the stable and unstable value for the radius of meniscus located on the fractionally wet throat composed of two equal size disks with zero and  $180^\circ$  contact angles ( $\theta_1=0, \theta_2=180^\circ$ ). In Fig. C.5, the minimum radii of stable menisci are plotted

versus half the gap size of fractionally wet throats. The radii of menisci and the gap size are normalized to the radius of disk. The data points in the Fig. C.5 are computed from Eq. C.10. These data points create a straight line with slope of one and intercept of one. As a result, this line represents the Eq. C.16. Comparing Fig. C.5 and Fig. C.3 shows that the region of stable menisci located on the fractionally wet throats is much smaller than the region of stable menisci located on water-wet throats.

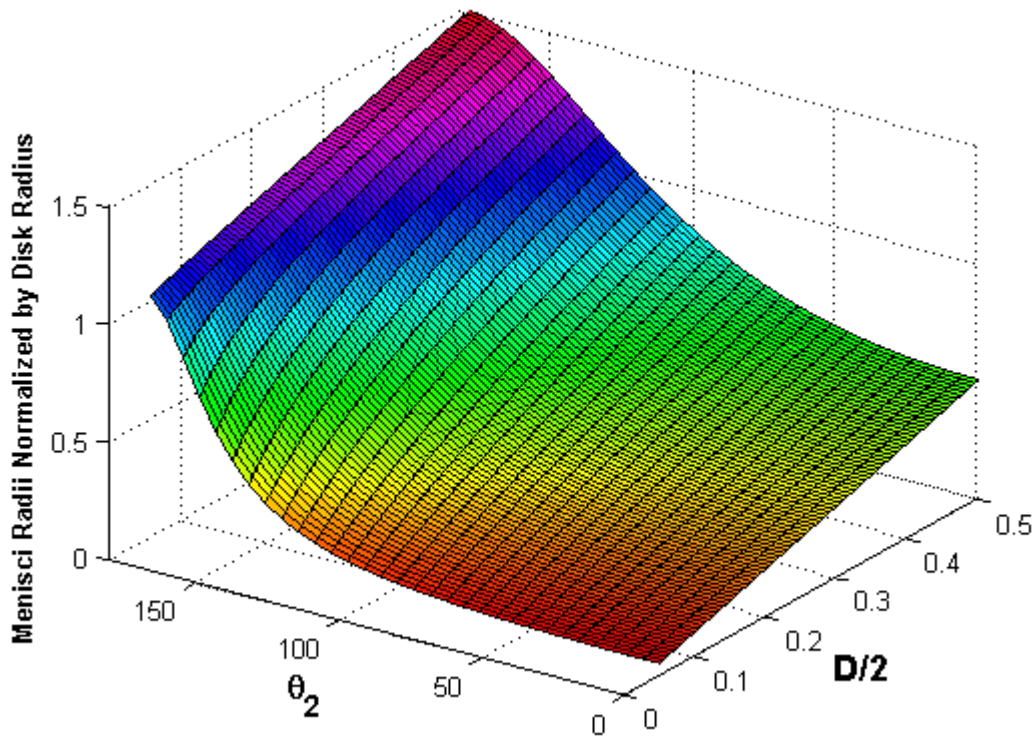


Figure. C.6. Surface of minimum radii of stable menisci at different gap size of fractionally wet throats. The fractionally wet throats are composed of two equal size disks, where the contact angle of disk 1 and menisci remains constant at zero degree ( $\theta_1=0^\circ$ ) and the contact angle of disk 2 and menisci varies between 0 and 180° ( $0^\circ \leq \theta_2 \leq 180^\circ$ ). The region above the plotted surface is the region of stable menisci. The region below the plotted surface is the region of unstable menisci.

To generalize Fig. C.3 and Fig. C.5, we calculate the minimum radii of stable menisci for throats composed of two equal size disks, where the contact angle of disk 1 and menisci remains constant at zero degree ( $\theta_1=0^\circ$ ) and the contact angle of disk 2 and menisci varies between 0 and  $180^\circ$  ( $0^\circ \leq \theta_2 \leq 180^\circ$ ). Fig. C.6 shows the surface of minimum radii of stable menisci at different gap size of throats described above. The radii of menisci and the gap size are normalized by the radius of disk. The data points in the Fig. C.6 are computed from Eq. C.10. In the Fig. C.6, the region above the plotted surface is the region of the stable menisci. The region below the plotted surface is the region of the unstable menisci.

## C.2. POSITION OF A MENISCUS

In two dimensional media, we represent the meniscus with the arc part of a circle. The geometry and position of a meniscus is defined by the radius of the meniscus and the coordination of center of the meniscus. In the Fig. C.1, the point  $O$  is the center of the stable meniscus located on a fractionally wet throat. The coordination of point  $O$  is  $(x_0, y_0)$ . The equation for the length of line  $\overline{OO_1}$  and  $\overline{OO_2}$  is represent by Eq. C.17 and C.18 respectively.

$$(x_1 - x_0)^2 + (y_1 - y_0)^2 = L_1^2, \quad (\text{C.17})$$

$$(x_2 - x_0)^2 + (y_2 - y_0)^2 = L_2^2. \quad (\text{C.18})$$

In the Eq. C.17 and C.18,  $L_1$  and  $L_2$  are the length of line  $\overline{OO_1}$  and  $\overline{OO_2}$  respectively. The  $(x_1, y_1)$  and  $(x_2, y_2)$  are the coordinate of center of disk 1 ( $O_1$ ) and center of disk 2 ( $O_2$ ) respectively. The values of  $L_1$  and  $L_2$  are calculated from Eq. C.2 and C.4. Since, the position of two disks is known, the value of  $(x_1, y_1)$  and  $(x_2, y_2)$  are known. Therefore, in order to find the coordinate of center of the meniscus, we solve system of Eq. C.17 and C.18. As a result, the coordinate of the center of meniscus equals to:

$$x_0 = -\frac{p}{2} \pm \sqrt{\left(\frac{p}{2}\right)^2 - q}, \quad (\text{C.19})$$

$$y_0 = B - Ax_0. \quad (\text{C.20})$$

The parameters  $p$ ,  $q$ ,  $A$  and  $B$  used in Eq. C.19 and C.20, are defined as below

$$P = \frac{2(y_1 - B)A - x_1}{1 + A^2},$$

$$q = \frac{x_1^2 + (y_1 - B)^2 - L_1^2}{1 + A^2},$$

$$A = \frac{x_1 - x_2}{y_1 - y_2},$$

$$B = \frac{x_1^2 - x_2^2 + y_1^2 - y_2^2 - (L_1^2 - L_2^2)}{2(y_1 - y_2)}.$$

### C.3. STABILITY OF TWO ADJACENT MENISCI (MELROSE CRITERION)

In this section, we develop the numerical implementation of Melrose event described in Chapter 3. We consider two menisci at adjacent throats in a single pore. To develop the numerical implementation of the Melrose event, we consider a uniformly wet pore, shown in Fig. C.7. The pore has three uniformly wet throats. In Fig. C.7, originally two menisci are located at adjacent throats (throat 1 and throat 2). The throat 1 is composed of disk 1 and disk 2, and represent by line  $\overline{O_1O_2}$  in the Fig. C.7. The throat 2 is composed of disk 1 and disk 3, and represent by line  $\overline{O_1O_3}$  in the Fig. C.7. In the Fig. C.7a, the points  $p_1$  and  $p_2$  are point contact between meniscus 1 and meniscus 2 with disk 1.  $\beta_1$  and  $\beta_2$  are the filling angle of meniscus 1 and meniscus 2 respectively. The value of the filling angle of a meniscus is calculated based on the geometry of disks and the geometry of meniscus (see section C.1 for more details)

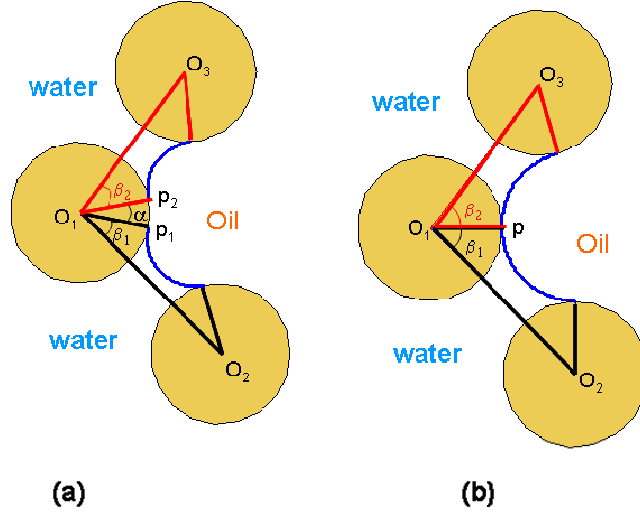


Figure C.7. Two menisci are located at adjacent throats (throat 1 ( $\overline{O_1O_2}$ ) and throat 2 ( $\overline{O_1O_3}$ )). The menisci and grains make zero contact angles.  $\beta_1$  and  $\beta_2$  are the filling angle of meniscus 1 and meniscus 2 respectively. (a) The points  $p_1$  and  $p_2$ , contact points between meniscus 1 and meniscus 2 with disk 1, are distinct. As a result, two menisci are separated by angle  $\alpha$ . (b) Points  $p$  is the contact point between meniscus 1, meniscus 2 and disk 1. The angle  $\alpha$  equal zero. Two menisci merge and become a single meniscus. This situation results in occurrence of the Melrose event.

In order to develop Melrose criterion, we calculate the angle  $\alpha$ . Angle  $\alpha$  is the angle between lines connecting center of disk 1 to the contacting points ( $p_1$  and  $p_2$ ). The value of angle  $\alpha$  equal to

$$\alpha = \sphericalangle o_1o_2o_3 - (\beta_1 + \beta_2). \quad (C.21)$$

The angle  $\sphericalangle o_1o_2o_3$  is the angle between line  $\overline{O_1O_2}$  and line  $\overline{O_1O_3}$ . We calculate this angle based on the coordinate of center of disk 1, disk 2, and disk 3. If the value of angle  $\alpha$  is bigger than zero, then two menisci are two separated interfaces. When value of angle  $\alpha$  reaches to zero, then two menisci merge to a single meniscus. This situation is unstable and the meniscus leave disk 1. As a result of this instability the Melrose event occurs and a pore will be filled with invading fluid.

The same principles developed in this section also apply to fractionally wet throats. Fig. C.8. shows the stage of a Melrose event within a fractionally wet pore. In Fig. C.8, two menisci are located at adjacent throats (throat 1 and throat 2). The throat 1 is composed of disk 1 and disk 2, and represent by line  $\overline{O_1O_2}$  in the Fig. C.8. The throat 2 is composed of disk 1 and disk 3, and represent by line  $\overline{O_1O_3}$  in the Fig. C.8. In the Fig. C.8a, the points  $p_1$  and  $p_2$  are point of contact between meniscus 1 and meniscus 2 with disk 1.  $\beta_1$  and  $\beta_2$  are the filling angle of meniscus 1 and meniscus 2 respectively. In Fig. C.8b, the point contacts between menisci and grains are merged to the one point ( $p$ ). As a result, the angle  $\alpha$  equal zero. Two menisci merge and become a single meniscus. This situation is unstable and the meniscus leave disk 1.

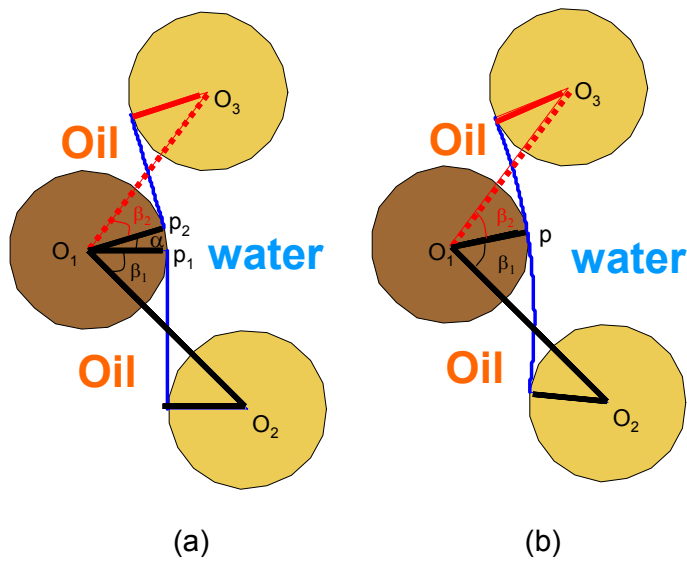


Figure C.8. Two menisci are located at adjacent throats (throat 1 ( $\overline{O_1O_2}$ ) and throat 2 ( $\overline{O_1O_3}$ )). The menisci and water-wet grains make zero contact angles and the menisci and oil-wet grains make  $180^\circ$  contact angles.  $\beta_1$  and  $\beta_2$  are the filling angle of meniscus 1 and meniscus 2 respectively. (a) The points  $p_1$  and  $p_2$  (contact points between meniscus 1 and meniscus 2 with disk 1) are distinct. As a result, two menisci are separated by angle  $\alpha$ . (b) Points  $p$  is the contact point between meniscus 1, meniscus 2 and disk 1. The angle  $\alpha$  equal zero. Two menisci merge and become a meniscus. This situation results in occurrence of the Melrose event.

## APPENDIX D: VISUALIZATION OF MENISCI MOTION WITHIN FRACTIONALLY WET POROUS MEDIA

In this appendix, we illustrate the menisci motion within the uniformly wet and fractionally wet porous media. For visualization purposes, we use a small porous medium composed of twelve equal size disks (Fig. D.1 and Fig. D.10). The disks cannot overlap but otherwise are randomly located. To facilitate the movement of water and oil through the network, we create an oil-wet membrane made of smaller sized oil-wet disks on the right hand side, and a similar water-wet membrane on the left hand side of the porous medium (Fig. D.1 and Fig. D.10). We use a Delaunay tessellation of the disks centers to subdivide the pore space into pores and throats. In the Fig. D.1, the pores are represented by the space in each triangle, where the disks do not exist. The throats are represented by a line connecting two disks.

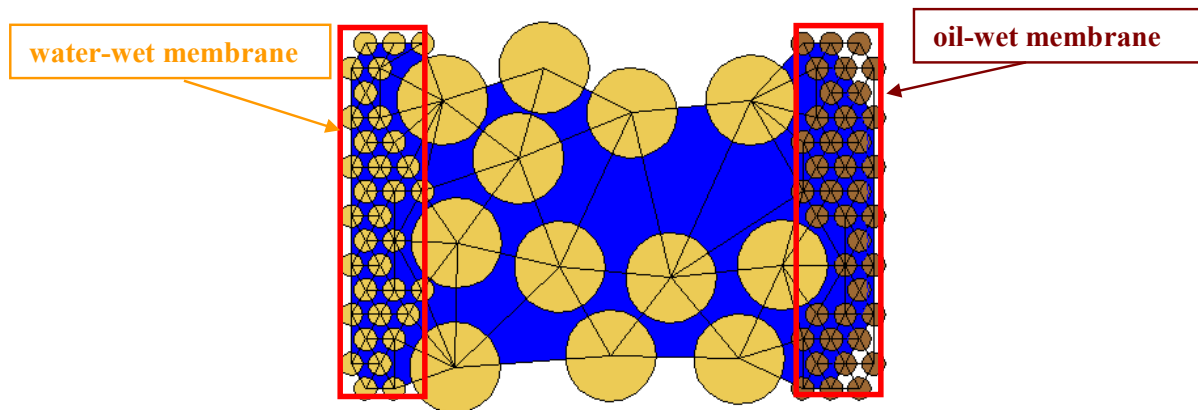


Figure D.1. Schematic of a water-wet porous medium at the beginning of primary drainage. The porous medium is filled with the water phase (blue). The oil phase (white) is connected to the oil-wet membrane.

## D. 1. MENISCI MOTION IN A WATER-WET POROUS MEDIUM

First, we present the menisci motion during primary drainage and secondary imbibition of a water-wet porous medium. During primary drainage, we increase the applied curvature (dimensionless capillary pressure). As a result, the oil phase invades to the porous medium from the right hand side and pushes the water out of the porous medium from the left hand side. Consequently, the fluid/fluid interfaces (menisci) move from right to left. We simulate the menisci motion using the invasion percolation algorithm (see the Chapter 3 for more details). At beginning of primary drainage, the porous medium is filled with the water phase (Fig. D.1) and the oil phase is connected to the oil-wet membrane. Moreover, the curvature is smaller than zero. As a result, the oil-wet membrane is filled with water phase. During primary drainage, we increase the curvature in small increments then computing the stable menisci locations in all pores (Fig. D.2a).

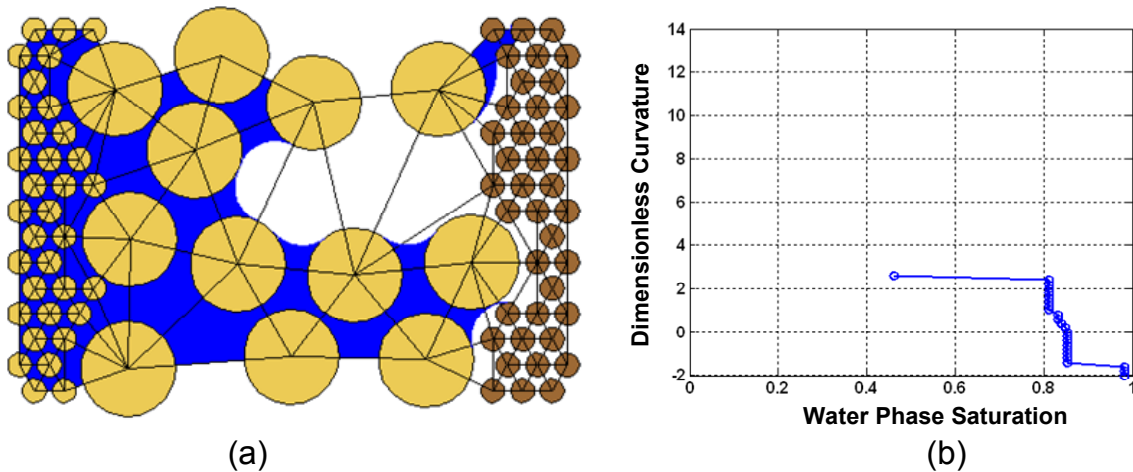


Figure D.2. (a) Schematic of a water-wet porous medium and fluid/fluid interfaces (menisci) during primary drainage. The dimensionless curvature of the interface equals 2.6. (b) Change of the water phase saturation versus change of applied curvature from value of -2 to 2.6.



Fig. D.2a shows the location of fluid/fluid interfaces (menisci) within the porous medium, when the applied curvature equal to 2.6. Fig. D.2b shows change of water phase saturation versus change of applied curvature from value of -2 to 2.6. In Fig. D.2b, the value of water phase saturation ( $S_w$ ) equal to the volume of pores completely filled with water phase divided by the total volume of the porous medium. As a result,  $S_w$  does not change until a pore-filling event (e.g. Haines event) occurs. Hence, the movement of a meniscus on a throat does not change the  $S_w$  in the Fig. D.2b until a pore-filling event occurs.

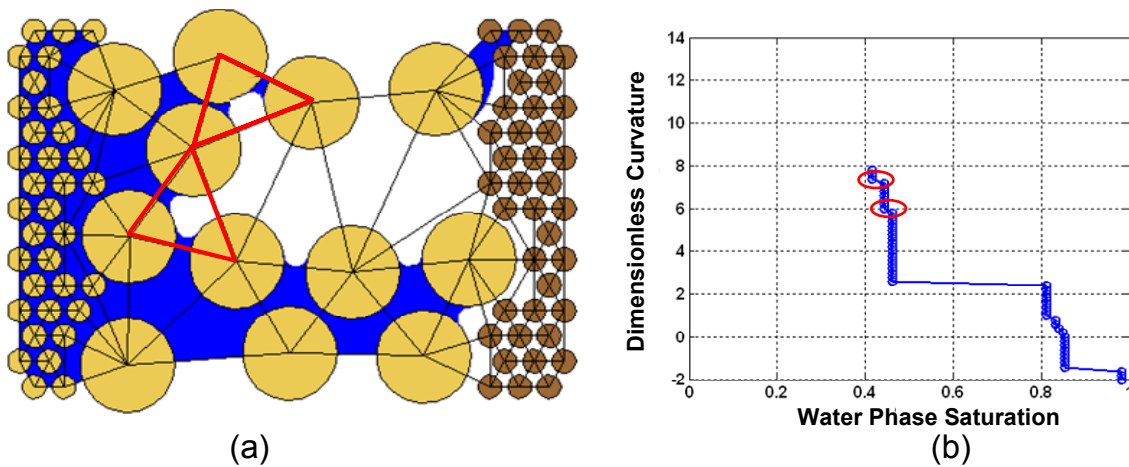


Figure D.3. (a) Schematic of a water-wet porous medium and fluid/fluid interfaces (menisci) during primary drainage. The dimensionless curvature of the interface equals 7.8. The value of curvature is normalized by radius of disks composing the porous medium. The pores highlighted by red triangles are filled by the oil phase, whereas they were filled with water phase in the Fig. D.2a. (b) Change in the water phase saturation with change in the applied curvature from value of -2 to 7.8. Two red circle highlight the  $S_w$  change correspond to filling event of two pores highlighted in Fig. D.3a.

During drainage, as the applied dimensionless capillary pressure increases, the curvature of menisci increases. The oil phase advances toward the center of pores candidate for invasion, but no pore-filling event (i.e. Haines event) occurs until menisci passes through the biggest throats available. The candidate pores for invasion are pores in

which at least one of their throats holds a meniscus. Fig. D.3a, highlight the only two pores filled by the oil phase (red triangles), while the applied curvature increase from 2.6 to 7.8. In the Fig. D.3b, two red circles highlight the  $S_w$  change which corresponds to filling events of two pores highlighted in Fig. D.3a.

The drainage process can continue until the drainage end point where most of the water phase exists in the form of trapping phase (Fig. D.4). The trapped water phase exists in two morphologies: water phase trapped in a cluster of pores, or water phase trapped in a throat. After the water phase is trapped in a throat (box A and B in the Fig. D.4a) or cluster of pores, the trapped water phase gets disconnected from the bulk fluids and its corresponding menisci become frozen. As a result, the curvatures of menisci remain constant throughout the rest of primary drainage.

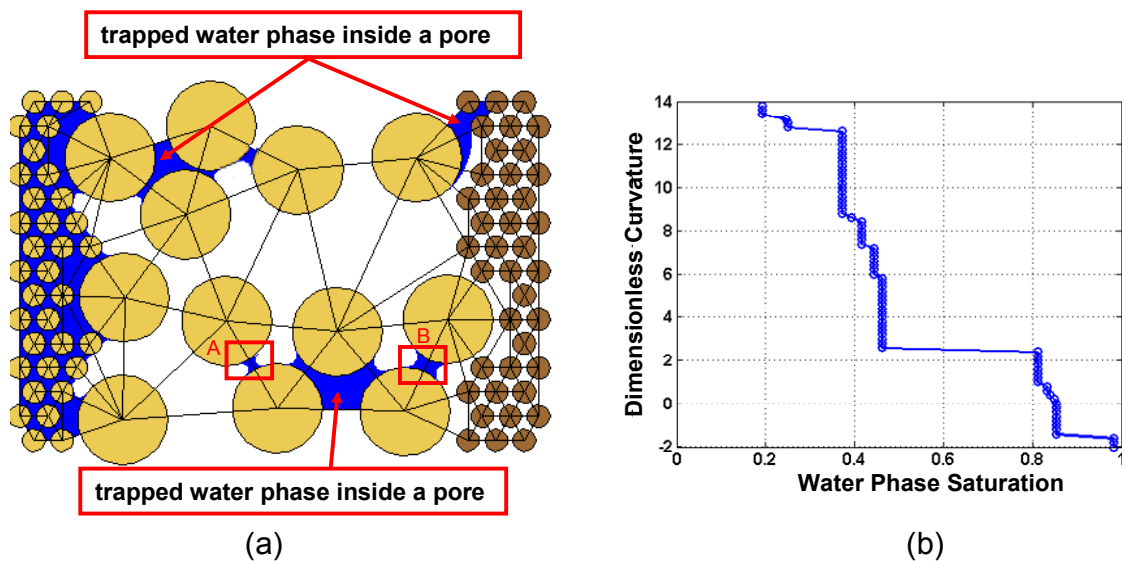


Figure D.4. (a) Schematic of a water-wet porous medium and fluid configuration at drainage end point. The dimensionless curvature of the interface equals 13.8. The red boxes (box A and B) highlight the trapped water phase in a throat. The trapped water phase in the pores is indicated by red arrows. (b) Change in the water phase saturation with change in the applied curvature from value of -2 to 13.8.

The secondary imbibition starts from the drainage end point. During secondary imbibition, we decrease the applied curvature (dimensionless capillary pressure). As a result, the water phase invades to the porous medium from the left hand side and pushes the oil phase out of the porous medium from the right hand side. Consequently, the fluid/fluid interfaces (menisci) move from left to right.

During imbibition of a water-wet medium, the pore-filling events occur only when two or more menisci come into contact and merge to form a single meniscus (Melrose event). Fig. D.5a and Fig. D.5b shows the fluid configuration before and after a Melrose event occurs. The red box A highlights the pore in which the Melrose event occur within. As the two menisci touch (Fig. D.5a), they become unstable and merge into a single meniscus. As a result, the corresponding pore is filled with the water phase and the meniscus locates on a new pore throat (Fig. D.5b).

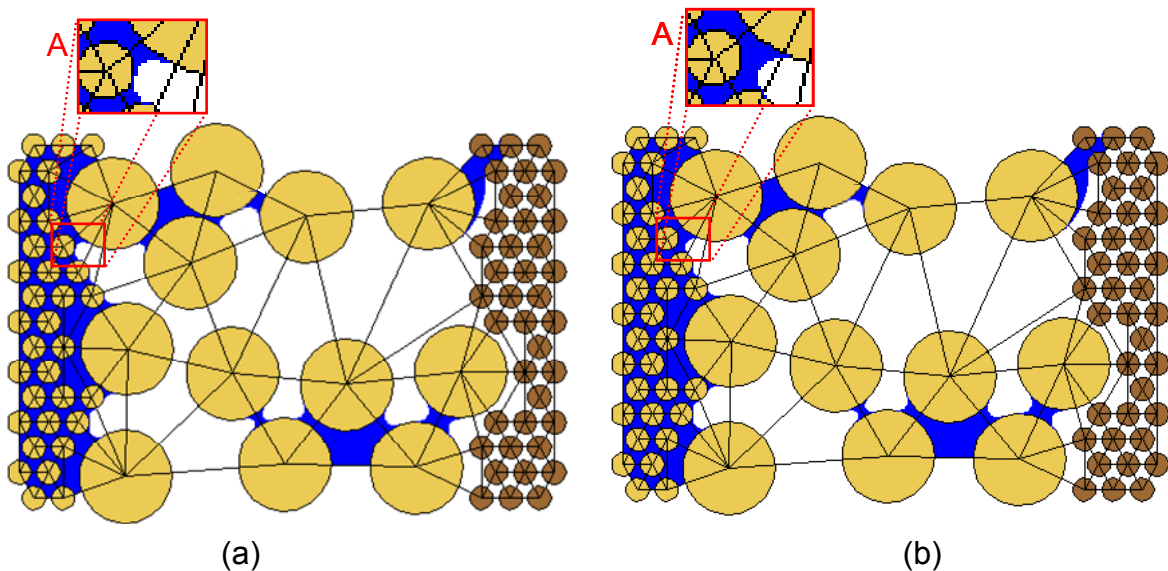


Figure D.5. Schematic of a water-wet porous medium and fluid/fluid interface (menisci) during secondary imbibition. (a) The fluid configuration before the Melrose event: Two menisci touch inside a pore highlighted by the red box. (b) The fluid configuration after the Melrose event: a pore highlighted by the red box is filled with a water phase and a meniscus locates on a new pore throat.

During secondary imbibition, the trapped water phase can be reconnected to the bulk water phase. As a result, the menisci which correspond to the trapped water phase get unfrozen, and their curvatures adjust to the applied curvature. Fig. D.6a and Fig. D.7a show configuration and location of menisci before and after reconnection of the trapped water phase to the bulk water phase. In Fig. D.6a, the red box A highlights two pores in which a Melrose event occurs within. The two pores fill with water phase consequent of Melrose event. As a result of this pore-filling event, the trapped water phase connects to the bulk water phase. The red box B in Fig. D.6a highlights a frozen meniscus corresponded to trapped water phase. The curvature of this frozen meniscus is higher than applied curvature. The curvature of the meniscus adjusts to applied curvature after the trapped phase reconnects to the bulk water phase (Fig. D.7a red box B).

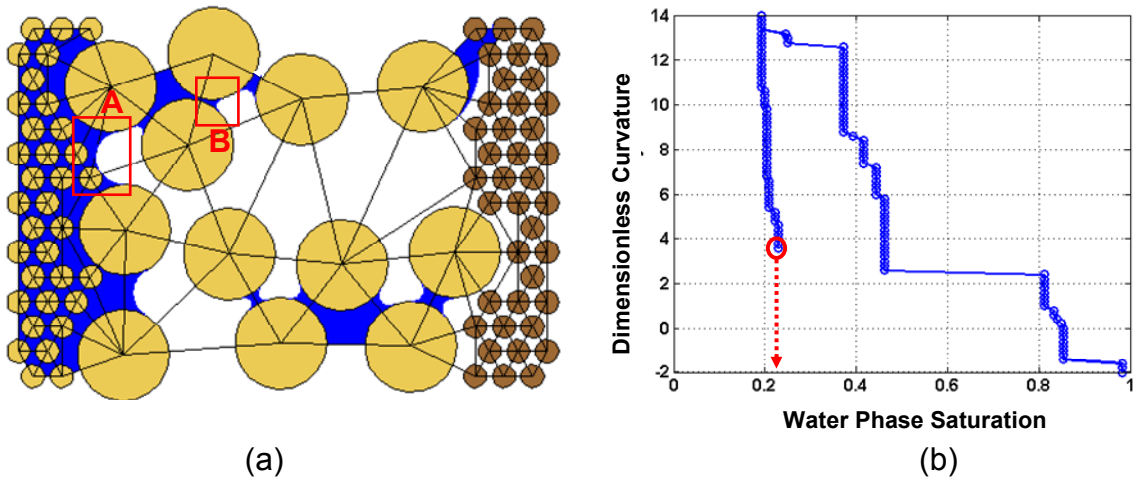


Figure D.6. (a) Schematic of a water-wet porous medium and fluid/fluid interfaces (menisci) during secondary imbibition. The dimensionless curvature of the interface equals 3.6. The red box A highlights two pores in which a Melrose event occur within. The red box B highlights a frozen meniscus corresponded to the trapped water phase (b) Change of water phase saturation versus change of applied curvature for the primary drainage and the secondary imbibition. In the secondary imbibition the value of the curvature changed from 13.8 to 3.6.

The red circle in Fig. D.6b shows the value of  $S_w$  before reconnection of the trapped phase to the bulk water phase occur, while the red circle in Fig. D.7b shows the value of  $S_w$  after the trapped phase reconnects to the bulk water phase.

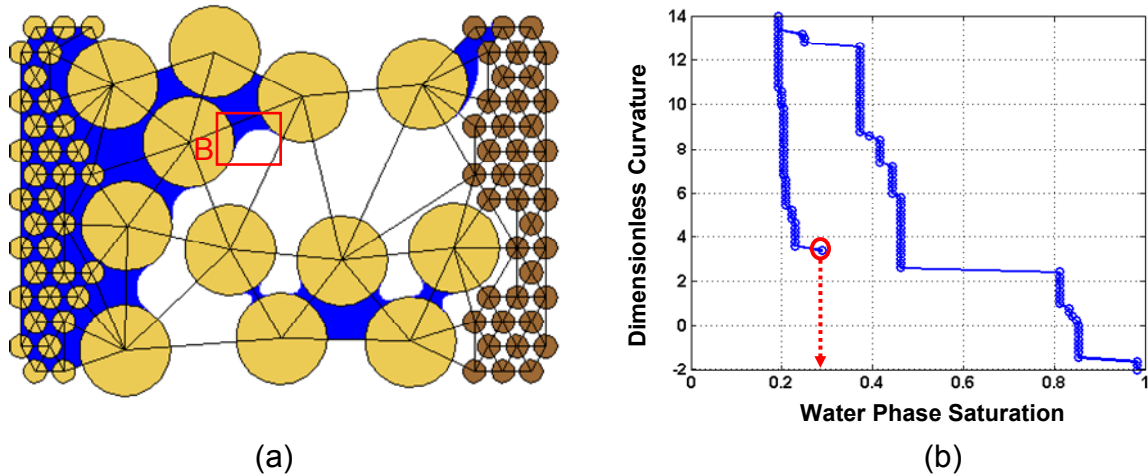


Figure D.7. (a) Schematic of a water-wet porous medium and fluid/fluid interfaces (menisci) during secondary imbibition. The dimensionless curvature of the interface equals 3.4. The red box B highlights a meniscus in which get unfrozen after reconnection of trapped water phase to bulk water phase (b) Change in the water phase saturation with change in the applied curvature for primary drainage and secondary imbibition. In the secondary imbibition the value of the curvature changed from 13.8 to 3.4.

As we decrease the applied curvature (from 3.4 to 0.8), the menisci advance towards the candidate pores for invasion, however no pore-filling event occurs. At the curvature of 3.4, three menisci merge and become unstable (Fig. D.8a). As a result, Melrose events occur and porous medium (exclude oil-wet membrane) is completely filled with the water phase (Fig. D.9a). The red box in the Fig. D.8b shows that the water phase saturation ( $S_w$ ) does not change while the applied curvature decreases from 3.4 to 0.8. The unchanged  $S_w$  shows that no pore-filling event occurs. The red circles in the Fig. D.9b shows the value of  $S_w$  after the Melrose events occur and the porous medium is completely filled with the water phase.

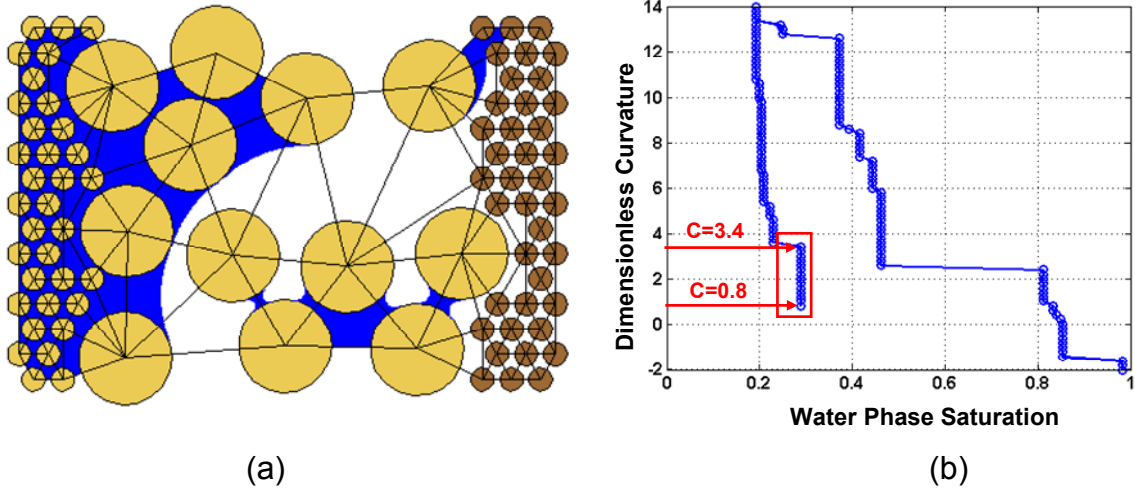


Figure D.8. (a) Schematic of a water-wet porous medium and fluid/fluid interfaces (menisci) during secondary imbibition. The dimensionless curvature of the interface equals 0.8. (b) Change in the water phase saturation with change in the applied curvature for primary drainage and secondary imbibition. In the secondary imbibition the value of the curvature changed from 13.8 to 0.8. The red box shows that the water phase saturation ( $S_w$ ) does not change while the applied curvature decreases from 3.4 to 0.8.

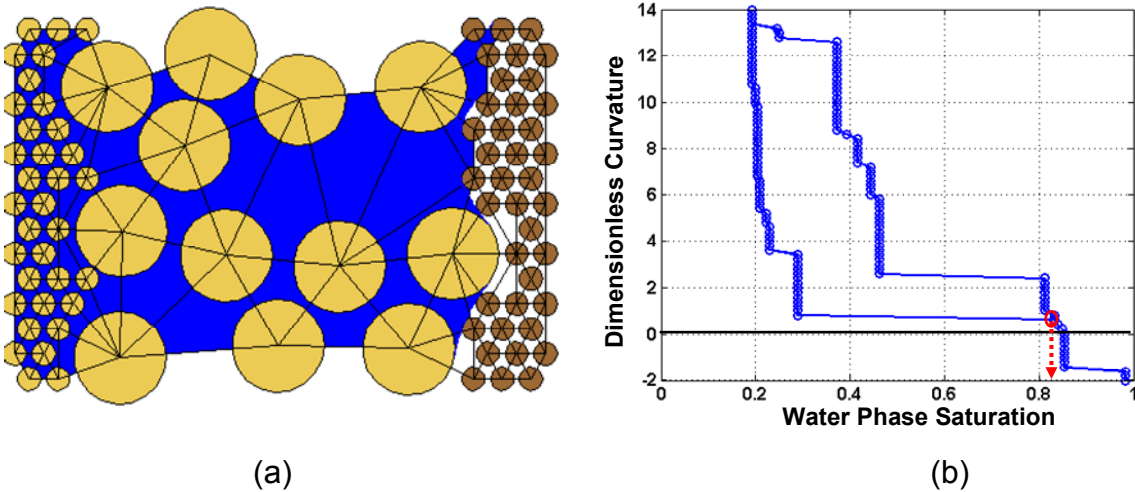


Figure D.9. (a) Schematic of a water-wet porous medium and fluid/fluid interfaces (menisci) during secondary imbibition. The dimensionless curvature of the interface equals 0.6. (b) Change in the water phase saturation with change in the applied curvature for primary drainage and secondary imbibition. In the secondary imbibition the value of the curvature changed from 13.8 to 0.4.

## D. 2. MENISCI MOTION IN A FRACTIONALLY WET POROUS MEDIUM

Second, we present the menisci motion during primary drainage and secondary imbibition of a fractionally wet porous medium. In order to make the porous medium fractionally wet, we replace one of the water-wet disks with an oil-wet disk (Fig. D.10). Similar to the water-wet porous medium, during primary drainage we increase the applied curvature (dimensionless capillary pressure). As a result, the oil phase invades to the porous medium from the right hand side and pushes water out of the porous medium from the left hand side. Hence, the fluid/fluid interfaces (menisci) move from right to left. At the beginning of primary drainage, the porous medium is filled with the water phase (Fig. D.10) and the oil phase is connected to the oil-wet membrane. In addition, the curvature is smaller than zero. As a result, the oil-wet membrane is filled with the water phase. We increase the curvature in small increments then computing the stable menisci locations in all pores (Fig. D.11a).

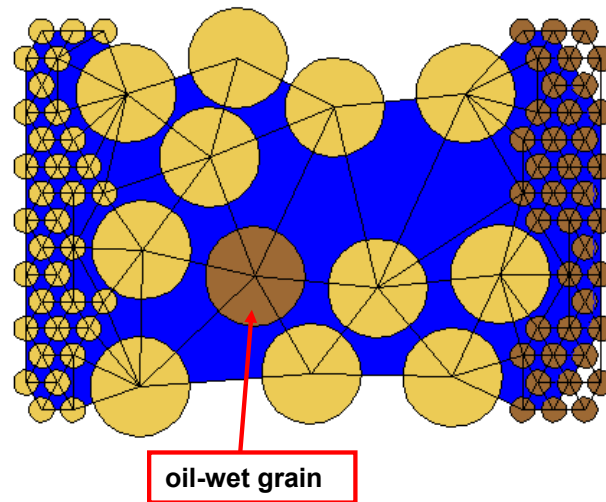


Figure D.10. Schematic of a fractionally wet porous medium at the beginning of primary drainage. The porous medium is filled the with the water phase (blue). The oil phase (white) is connected to the oil-wet membrane.

Fig. D.11a shows the location of fluid/fluid interfaces (menisci) within the porous medium, when the applied curvature equal to 2.4. Fig. D.11b shows change of the water phase saturation versus change of applied curvature from value of -2 to 2.4. At this curvature, the oil phase push the water phase out of oil-wet membrane but the porous medium is filled with the water phase. Until this stage there is no difference between fluid configuration in the water-wet medium and the fractionally wet medium.

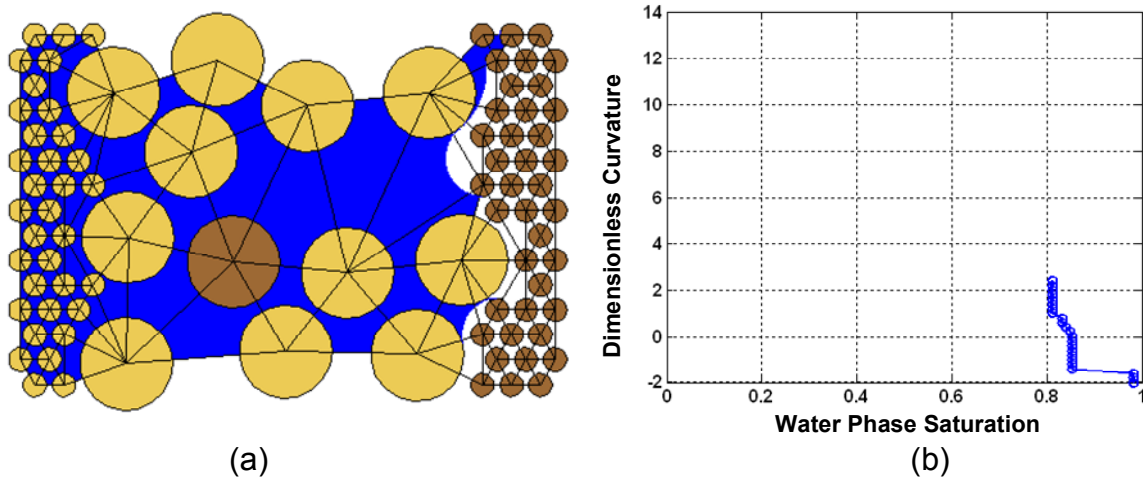


Figure D.11. (a) Schematic of a fractionally wet porous medium and fluid/fluid interfaces (menisci) during primary drainage. The dimensionless curvature of the interface equals 2.4. (b) Change of the water phase saturation versus change of applied curvature from value of -2 to 2.4.

Fig. D.12a show the location of fluid/fluid interfaces (menisci) within the fractionally wet porous media, when the applied curvature equal to 2.6. Fig. D.12b shows change of the water phase saturation versus change of the applied curvature from value of -2 to 2.6. At this curvature, the menisci reach to the oil-wet disk, and the menisci are not stable on the fractional-wet throats at this curvature. As a result, the Haines events occur and menisci pass the fractional-wet throats. Comparing Fig. D.2a and Fig. D. 12a, we observe that an oil-wet disk causes the oil phase to push more water out of the



fractionally wet porous medium. Note that both Fig. D.2a and Fig. D.12a show the menisci location, when the applied curvature equal 2.6. In addition, the comparison of Fig. D.2a and Fig. D.12a shows that the existence of oil-wet disks can change the topology of the trapped water phase.

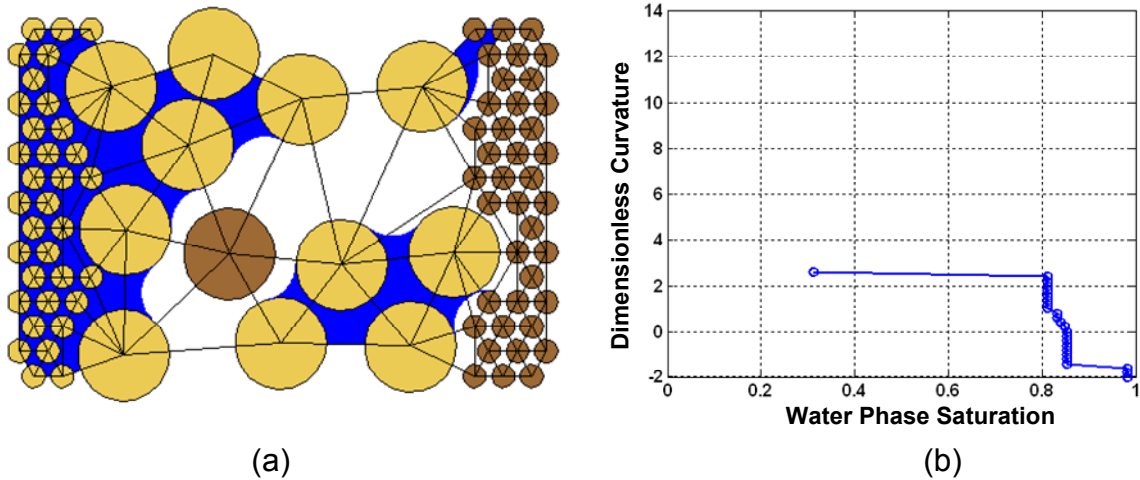


Figure D.12. (a) Schematic of a fractionally wet porous medium and fluid/fluid interfaces (menisci) during primary drainage. The dimensionless curvature of the interface equals 2.6. (b) Change of the water phase saturation versus change of applied curvature from value of -2 to 2.6.

The drainage process can continue until the drainage end point, where most of the water phase exists in the form of trapping phase (Fig. D.13). At the drainage end point of this fractionally wet porous medium, the trapped phase occupies different pores compare to the drainage end point of the water-wet porous medium. The curvatures of the frozen menisci correspond to the trapped water phase (inside Red box, Fig. D.13a) are smaller compared to the curvatures of the trapped water phase at the drainage end point of the water-wet porous medium (Fig. D.4a). The above observation shows that the water phase trapped at the lower applied curvature in the fractionally wet porous medium compared to the water-wet porous medium.

Fig. D.13b plots the dimensionless curvature versus water phase saturation for a primary drainage of the fractionally wet porous medium.

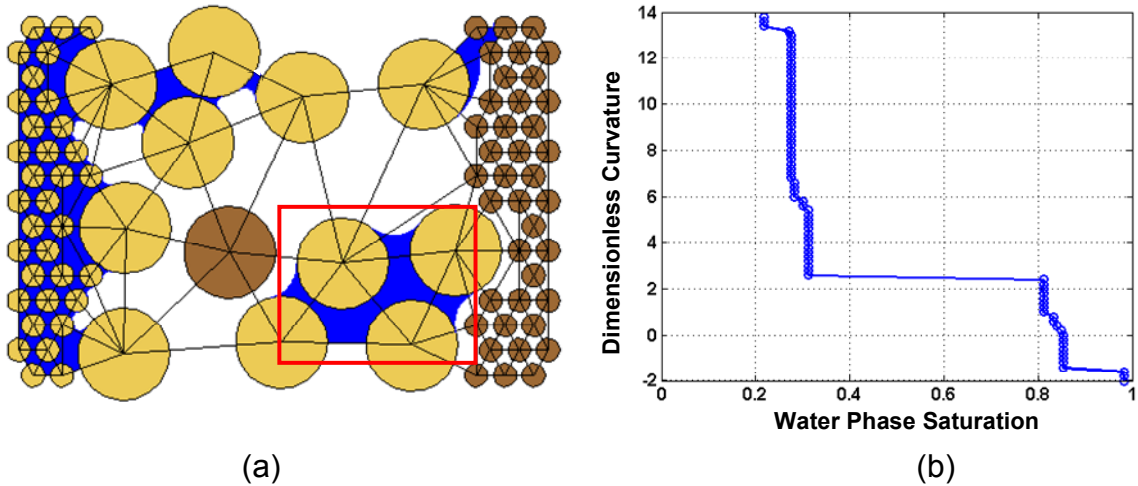


Figure D.13. (a) Schematic of a fractionally wet porous medium and fluid configuration at drainage end point. The dimensionless curvature of the interface equals 13.8. (b) Change of the water phase saturation versus change of applied curvature from value of -2 to 13.8.

The secondary imbibition starts from the drainage end point. During secondary imbibition, we decrease the applied curvature (dimensionless capillary pressure). As a result, the water phase invades the porous medium from the left hand side and pushes the oil phase out of the porous medium from the right hand side. Thus, the fluid/fluid interfaces (menisci) move from left to right.

The movement of menisci in the fractionally wet porous medium is no different than the menisci movement in the water-wet medium until the menisci (fluid/fluid interfaces) touch the oil-wet disk. In the water-wet medium, after the Melrose events occur at the curvature of 0.8, the porous medium is completely filled with the water phase. In contrast, the oil-wet disk in the fractional-wet medium prevents the

advancement of the menisci (fluid/fluid interfaces) after the Melrose events occur at the curvature of 0.8 (Fig. D.14a).

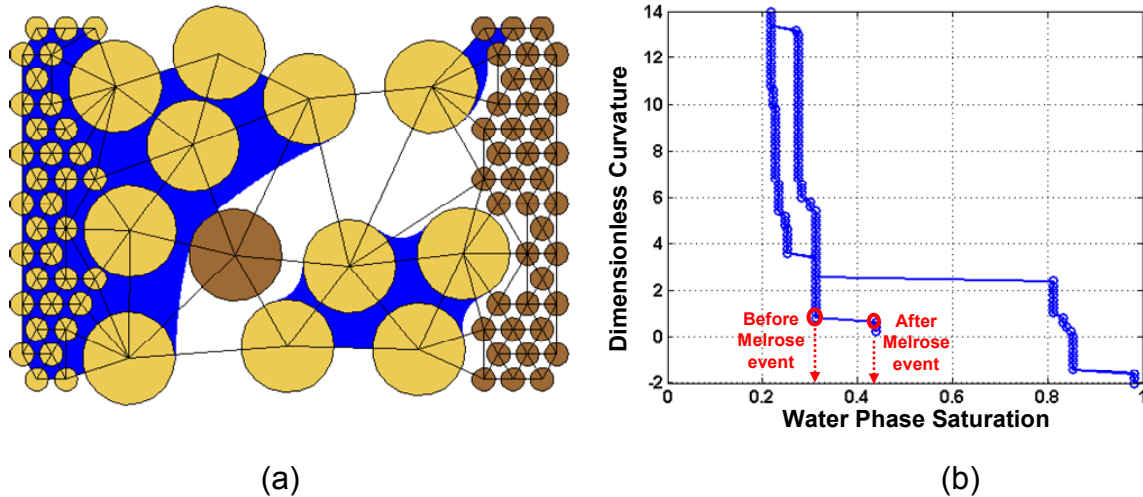


Figure D.14. (a) Schematic of a fractionally wet porous medium and fluid/fluid interfaces (menisci) during secondary imbibition. The dimensionless curvature of the interface equals 0.2. (b) Change in the water phase saturation with change in the applied curvature for primary drainage and secondary imbibition. In the secondary imbibition the value of the curvature changed from 13.8 to 0.2.

Fig. D.14a shows the location of fluid/fluid interfaces (menisci) within the fractionally wet porous media, when the applied curvature equals to 0.2. The menisci are stable at the fractionally wet throats at this curvature. The red circles in Fig. D.14.b shows the water phase saturation ( $S_w$ ) before and after the Melrose events.

The further decrease of applied curvature causes a switching sign of curvature. The change from a positive curvature to a negative curvature causes the menisci (fluid/fluid interfaces) to curve towards the water phase (Fig. D.15a). In this situation, the pressure inside the water phase is higher than pressure of the oil phase. As a result, the capillary pressure is negative (see Chapter 3 for definition of capillary pressure). Fig. D.15a shows that the oil-wet disk holds the two menisci and prevents any pore-filling event. Consequently, the oil-wet disk prevents the porous media to be filled with the

water phase at applied curvature of  $-0.8$ . The red box in the Fig. D.15b shows that the saturation of water phase remains constant while the applied curvature decrease from a positive value to a negative value.

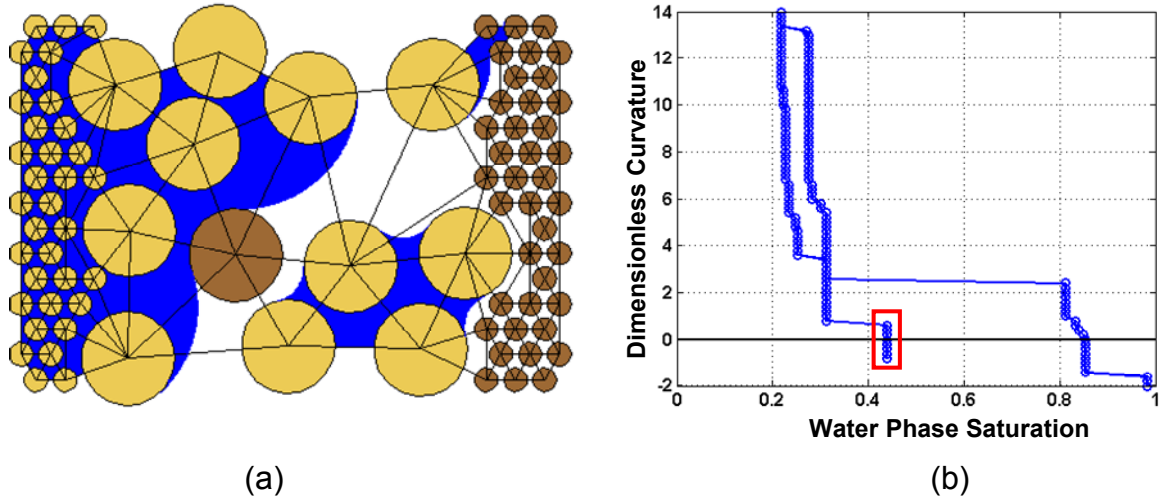


Figure D.15. (a) Schematic of a fractionally wet porous medium and fluid/fluid interfaces (menisci) during secondary imbibition. The dimensionless curvature of the interface equals  $-0.8$ . (b) Change in the water phase saturation with change in the applied curvature for primary drainage and secondary imbibition. In the secondary imbibition the value of the curvature changed from  $13.8$  to  $-0.8$ .

Further decrease of applied curvature causes instability of the meniscus located on the fractionally wet throat (highlighted with red box in the Fig. D.16a). As a result, the Haines event occurs, which leads to series of pore-filling events (i.e. Haines events). Consequently, the water phase fills the porous medium except a part which remains as trapped oil phase (Fig. D.16a). The red circle in the Fig. D.16b shows the value of  $S_w$  after series of Haines events occur and porous medium is filled with the water phase.

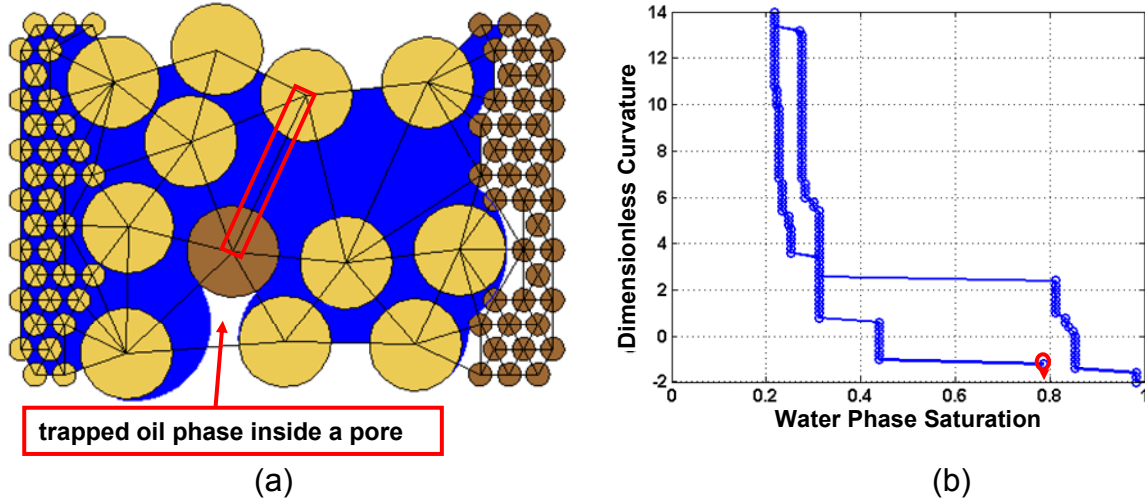


Figure D.16. (a) Schematic of a fractionally wet porous medium and fluid/fluid interfaces (menisci) during secondary imbibition. The dimensionless curvature of the interface equals -1.2. (b) Change in the water phase saturation with change in the applied curvature for primary drainage and secondary imbibition. In the secondary imbibition the value of the curvature changed from 13.8 to -1.2.

In conclusion, comparison of movement of menisci within fractionally wet and water-wet media during primary drainage shows that the oil-wet disks open a path for the oil phase to invade the fractionally wet medium. Consequently, the oil phase can breakthrough the fractionally wet medium at lower applied curvature (dimensionless capillary pressure). In addition, comparison of movement of menisci within fractionally wet and water-wet media during secondary imbibition shows that the oil-wet disks prevent the water phase from advancing towards the oil phase. As a result, the water phase breakthrough the fractionally wet medium at lower applied curvature.

## NOMENCLATURE

$C$  = curvature of fluid/fluid interface

$D$  = gap size

$D_L$  = fractal dimension

$g_{hydr}$  = hydraulic conductance of throat

$h$  = half length between two grain centers

$k_{rg}$  = gas relative permeability

$k_{rgmax}$  = maximum gas relative permeability

$P$  = pressure

$P_c$  = capillary pressure

$P_o$  = pressure of the oil phase

$P_w$  = pressure of the water phase

$P_{mw}$  = pressure of the non-wetting phase

$P$ - $S$  = pressure saturation curve

$q$  = flow rate

$r_1$  = normal radius of the curvature

$r_2$  = tangential radius of the curvature

$r_c$  = inscribed radius of a throat

$r_e$  = equivalent radius of a throat

$r_{ef}$  = effective radius

$R$  = grain radius

$S_w$  = water phase saturation

$\theta$  = contact angle

$\theta_{ww}$  = contact angles between water-wet grains and fluid/fluid interfaces

$\theta_{ow}$  = contact angles between oil-wet grains and fluid/fluid interfaces

$\Delta P$  = pressure difference

$\mu$  = viscosity of fluid

$\varphi$  = filling angle of pendular rings

$\psi$  = filling angle of menisci

$\sigma_{AS}$  = interfacial tension between solid surface and air

$\sigma_{WS}$  = interfacial tension between solid surface and water

$\sigma_{OS}$  = interfacial tension between solid surface and oil

$\sigma_{WA}$  = the surface tension of water

$\sigma_{WO}$  = interfacial tension between water and oil

$\sigma_{AO}$  = the surface tension of oil

## REFERENCES

1. Adler, P.M., C.G. Jacquin, and J.A. Quiblier, *Flow in simulated porous-media*. International Journal of Multiphase Flow, 1990. 16(4): p. 691-712.
2. Adler, P.M., C.G. Jacquin, and J.F. Thovert, *The formation factor of reconstructed porous-media*. Water Resources Research, 1992. 28(6): p. 1571-1576.
3. Al-Futaisi, A. and T.W. Patzek, *Impact of wettability alteration on two-phase flow characteristics of sandstones: A quasi-static description*. Water Resources Research, 2003. 39(2).
4. Al-Futaisi, A. and T.W. Patzek, *Three-phase hydraulic conductances in angular capillaries*. SPE Journal, 2003. 8(3): p. 252-261.
5. Al-Futaisi, A. and T.W. Patzek, *Secondary imbibition in NAPL-invaded mixed-wet sediments*. Journal of Contaminant Hydrology, 2004. 74(1-4): p. 61-81.
6. Al-Gharbi, M.S. and M.J. Blunt, *Dynamic network modeling of two-phase drainage in porous media*. Physical Review E, 2005. 71(1): 016308.
7. Al-Raoush, R.I. and C.S. Willson, *Extraction of physically realistic pore network properties from three-dimensional synchrotron X-ray microtomography images of unconsolidated porous media systems*. Journal of Hydrology, 2005. 300(1-4): p. 44-64.
8. Al-Raoush, R.I. and C.S. Willson, *A pore-scale investigation of a multiphase porous media system*. Journal of Contaminant Hydrology, 2005. 77(1-2): p. 67-89.
9. Al-Raoush, R., K.E. Thompson, and C.S. Willson, *Comparison of network generation techniques for unconsolidated porous media*. Soil Science Society of America Journal, 2003. 67: p. 1687-1700.
10. Anderson, W.G., *Wettability literature survey: Part 4. Effects of wettability on capillary-pressure*. Journal of Petroleum Technology, 1987. 39(10): p. 1283-1300.
11. Anderson, W.G., *Wettability literature survey: Part 5. The effects of wettability on relative permeability*. Journal of Petroleum Technology, 1987. 39(11): p. 1453-1468.
12. Arriola, A., G.P. Willhite, and D.W. Green. *Mobilization of an oil drop trapped in a noncircular pore throat upon contact with surfactants*, SPE 9405 presented at SPE Annual Technical Conference and Exhibition. 1980. Dallas, Texas.
13. Arriola, A., G.P. Willhite, and D.W. Green, *Trapping of oil drops in a non-circular pore throat and mobilization upon contact with a surfactant*. Society of Petroleum Engineers Journal, 1983. 23(1): p. 99-114.
14. Ashouripashaki, M., *The effect of fractional wettability on two phase capillary pressure-saturation curves in drainage, imbibition and secondary imbibition*, MS thesis, 2008, The University of Texas at Austin.



15. Bakke, S. and P.E. Øren, *3D pore-scale modeling of sandstones and flow simulations in the pore networks*. SPE Journal, 1997. 2: p. 136-149.
16. Basu, S. and M.M. Sharma, *Effect of dielectric saturation on disjoining pressure in thin-films of aqueous-electrolytes*. Journal of Colloid and Interface Science, 1994. 165(2): p. 355-366.
17. Basu, S. and M.M. Sharma, *Measurement of critical disjoining pressure for dewetting of solid surfaces*. Journal of Colloid and Interface Science, 1996. 181: p. 443-455.
18. Basu, S. and M.M. Sharma, *Characterization of mixed-wettability states in oil reservoirs by atomic force microscopy*. SPE Journal, 1997. 2(4): p. 427-435.
19. Bauters, T.W.J., T.S. Steenhuis, D.A. DiCarlo, J.L. Nieber, L.W. Dekker, C.J. Ritsema, J.Y. Parlange, and R. Haverkamp, *Physics of water repellent soils*. Journal of Hydrology, 2000. 231: p. 233-243.
20. Behseresht, J., S. Bryant, and K. Sepehrnoori. *Infinite-acting physically representative networks for capillarity-controlled displacements*, SPE 110581 presented at SPE Annual Technical Conference and Exhibition. 2007. Anaheim, California.
21. Bekri, S., K. Xu, F. Yousefian, P.M. Adler, J.F. Thovert, J. Muller, K. Iden, A. Pysillos, A.K. Stubos, and M.A. Ioannidis, *Pore geometry and transport properties in North Sea chalk*. Journal of Petroleum Science and Engineering, 2000. 25(3-4): p. 107-134.
22. Berkowitz, B. and I. Balberg, *Percolation theory and its application to groundwater hydrology*. Water Resources Research, 1993. 29(4): p. 775-794.
23. Bernal, J. and J. Mason, *Co-ordinate of randomly packed spheres*. Nature, 1960. 188: p. 910-11.
24. Biswal, B., C. Manwart, R. Hilfer, S. Bakke, and P.E. Oren, *Quantitative analysis of experimental and synthetic microstructures for sedimentary rock*. Physica A-Statistical Mechanics and Its Applications, 1999. 273(3-4): p. 452-475.
25. Blunt, M., M.J. King, and H. Scher, *Simulation and theory of two-phase flow in porous-media*. Physical Review A, 1992. 46(12): p. 7680-7699.
26. Blunt, M.J., *Physically based network modeling of multiphase flow in intermediate-wet porous media*. Journal of Petroleum Science and Engineering, 1998. 20: p. 117-125.
27. Blunt, M.J., *Flow in porous media - pore-network models and multiphase flow*. Current Opinion in Colloid & Interface Science, 2001. 6(3): p. 197-207.
28. Blunt, M.J., M.D. Jackson, M. Piri, and P.H. Valvatne, *Detailed physics, predictive capabilities and macroscopic consequences for pore-network models of multiphase flow*. Advances in Water Resources, 2002. 25(8-12): p. 1069-1089.
29. Blunt, M.J. and H. Scher, *Pore-level modeling of wetting*. Physical Review E, 1995. 52(6): p. 6387-6403.
30. Bradford, S.A. and L.M. Abriola, *Dissolution of residual tetrachloroethylene in fractional wettability porous media: Incorporation of interfacial area estimates*. Water Resources Research, 2001. 37(5): p. 1183-1195.

31. Bradford, S.A. and F.J. Leij, *Fractional wettability effects on two-fluid and three-fluid capillary pressure-saturation relations*. Journal of Contaminant Hydrology, 1995. 20(1-2): p. 89-109.
32. Bradford, S.A. and F.J. Leij, *Estimating interfacial areas for multi-fluid soil systems*. Journal of Contaminant Hydrology, 1997. 27(1-2): p. 83-105.
33. Broadbent, S.R. and J.M. Hammersley, *Percolation processes, I. crystals and mazes*. Proceedings of Cambridge Philosophical Society, 1957. 53: p. 629-641.
34. Broadbent, S.R. and J.M. Hammersly, *Percolation processes, II. the connective constant*. Proceedings of Cambridge Philosophical Society, 1957. 53: p. 642-645.
35. Brown, R.J.S. and I. Fatt. *Measurements of fractional wettability of oil fields rocks by the nuclear magnetic relaxation method*, SPE 743 presented at Fall Meeting of the Petroleum Branch of AIME. 1956. Los Angeles, California.
36. Bryant, S., C. Cade, and D. Mellor, *Permeability prediction from geologic models*. AAPG Bulletin, 1993. 77(8): p. 1338-1350.
37. Bryant, S., G. Mason, and D. Mellor, *Quantification of spatial correlation in porous media and its effect on mercury porosimetry*. Journal of Colloid and Interface Science, 1996. 177(1): p. 88-100.
38. Bryant, S., D. Mellor, and C. Cade, *Physically representative network models of transport in porous media*. AIChE Journal, 1993. 39: p. 387-396.
39. Bryant, S. and N. Pallatt, *Predicting formation factor and resistivity index in simple sandstones*. Journal of Petroleum Science and Engineering, 1996. 15(2-4): p. 169-179.
40. Bryant, S.L. and M. Blunt, *Prediction of relative permeability in simple porous media*. Physical Review A, 1992. 46: p. 2004-2011.
41. Bryant, S.L. and A. Johnson, *Wetting phase connectivity and irreducible saturation in simple granular media*. Journal of Colloid and Interface Science, 2003. 263: p. 572-579.
42. Bryant, S.L., P.R. King, and D.W. Mellor, *Network model evaluation of permeability and spatial correlation in a real random sphere packing*. Transport in Porous Media, 1993. 11(1): p. 53-70.
43. Bryant, S.L. and N. Pallatt, *Predicting formation factor and resistivity index in simple sandstones*. Journal of Petroleum Science and Engineering, 1996. 15: p. 169-179.
44. Burdine, N.T., *Relative permeability calculation from pore size distribution data*. AIME Pet. Trans., 1953. 198: p. 71-78.
45. Byrnes, A.P., K. Sampath, and P.L. Randolp. *Effect of pressure and water saturation on permeability of western tight sandstones*, presented at DOE Symposium on Enhanced Oil and Gas Recovery and Improved Drilling Technology. 1979. Tulsa, Oklahoma.
46. Calhoun, J.C., M. Lewis, and R.C. Newman, *Experiment on the capillary properties of porous solids*. AIME Pet. Trans., 1949. 186: p. 189-196.
47. Cargill, G.S., *Radial distribution function and microgeometry of dense random packing of hard sphere*. AIP Conf. Proc., 1984. 107(1): p. 20-36.

48. Celia, M.A., P.C. Reeves, and L.A. Ferrand, *Recent advances in pore scale models for multiphase flow in porous-media*. Reviews of Geophysics, 1995. 33: p. 1049-1057.
49. Chandler, R., J. Koplik, K. Lerman, and J.F. Willemsen, *Capillary displacement and percolation in porous-media*. Journal of Fluid Mechanics, 1982. 119(JUN): p. 249-267.
50. Chen, S. and G.D. Doolen, *Lattice Boltzmann method for fluid flows*. Annual Review of Fluid Mechanics, 1998. 30: p. 329-364.
51. Cheng, Y.F., S.J. Guo, and H.Y. Lai, *Dynamic simulation of random packing of spherical particles*. Powder Technology, 2000. 107(1-2): p. 123-130.
52. Chowdiah, P., *Influence of water-desaturation technique and stress on laboratory measurement of hydraulic properties of tight sandstones*. SPE Formation Evaluation, 1988. 3(4): p. 679-685.
53. Clarke, A.S. and J.D. Wiley, *Numerical-simulation of the dense random packing of a binary mixture of hard-spheres - amorphous metals*. Physical Review B, 1987. 35(14): p. 7350-7356.
54. Coles, M.E., R.D. Hazlett, E.L. Muegge, K.W. Jones, B. Andrews, B. Dowd, P. Siddons, A. Peskin, P. Spanne, and W. Soll, *Developments in synchrotron X-ray microtomography with applications to flow in porous media*. SPE Reservoir Evaluation & Engineering, 1998. 1(4): p. 288-296.
55. Coles, M.E., R.D. Hazlett, P. Spanne, W.E. Soll, E.L. Muegge, and K.W. Jones, *Pore level imaging of fluid transport using synchrotron X-ray microtomography*. Journal of Petroleum Science and Engineering, 1998. 19(1-2): p. 55-63.
56. Dahle, H.K., M.A. Celia, and S.M. Hassanizadeh, *Bundle-of-tubes model for calculating dynamic effects in the capillary-pressure-saturation relationship*. Transport in Porous Media, 2005. 58(1-2): p. 5-22.
57. Dalla, E., M. Hilpert, C. Miller, and D. Pitea, *Modelling the dissolution of non-aqueous phase liquid blobs in sphere packings*. Annali Di Chimica, 2003. 93(7-8): p. 631-638.
58. Dalla, E., M. Hilpert, and C.T. Miller, *Computation of the interfacial area for two-fluid porous medium systems*. Journal of Contaminant Hydrology, 2002. 56(1-2): p. 25-48.
59. de Gennes, P.G., F. Brochard-Wyart, and D. Quere, *Capillarity and wetting phenomena: drops, bubbles, pearls, waves*. 1ed. 2003, New York: Springer-Verlag.
60. Dekker, L.W. and C.J. Ritsema, *How water moves in a water repellent sandy soil, I. potential and actual water repellency*. Water Resources Research, 1994. 30(9): p. 2507-2517.
61. Demond, A.H., F.N. Desai, and K.F. Hayes, *Effect of cationic surfactants on organic liquid water capillary-pressure saturation relationships*. Water Resources Research, 1994. 30(2): p. 333-342.
62. Deng, Y. and L.W. Lake, *Thermodynamic study of capillary pressure curves based on free minimization*. Geofluid, 2001. 1: p. 183-193.
63. Dullien, F.A.L., *Porous media; fluid transport and pore structure*. 2 ed. 1992, San Diego, California: Academic Press.

64. Dunsmuir, J.H., S.R. Ferguson, K.L. D'Amico, and J.P. Stokes. *X-ray microtomography: a new tool for the characterization of porous media*, SPE 22860 presented at SPE Annual Technical Conference and Exhibition. 1991. Dallas, Texas.
65. Edwards, C.H. and D.E. Penney, *Calculus and analytic geometry*. 1982, Prentice Hall: Englewood Cliffs, N. J. p. 239-288.
66. Ellies, A. and K.H. Hartge, *Veränderung der Benetzungseigenschaften von Böden durch verschiedene Kulturen und Kulturdauern*. Z. Kulturtechnik Landentw, 1994. 350: p. 358-364.
67. Fatt, I., *The network model of porous media, I. Capillary pressure characteristics*. AIME Pet. Trans., 1956. 207: p. 144-159.
68. Fatt, I., *The network model of porous media, II. Dynamic properties of a single size tube network*. AIME Pet. Trans., 1956. 207: p. 160-163.
69. Fatt, I., *The network model of porous media, III. Dynamic properties of networks with tube radius distribution*. AIME Pet. Trans., 1956. 207: p. 164-181.
70. Fatt, I. and W.A. Klikoff, *Effect of fractional wettability on multiphase flow through porous media*. Journal of Petroleum Technology, 1959. 11(10): p. 71-76.
71. Fenwick, D.H. and M.J. Blunt, *Three-dimensional modeling of three phase imbibition and drainage*. Advances in Water Resources, 1998. 21(2): p. 121-143.
72. Finney, J., *Random packing and structure of the liquid state*, PhD dissertation, 1968, University of London.
73. Fischer, U. and M.A. Celia, *Prediction of relative and absolute permeabilities for gas and water from soil water retention curves using a pore-scale network model*. Water Resources Research, 1999. 35(4): p. 1089-1100.
74. Fisher, R.A., *On the capillary forces in an ideal soil; correction of formulae given by W. B. Haines*. Journal of Agriculture Science, 1926. 16: p. 492-503.
75. Flannery, B.P., H.W. Deckman, W.G. Roberge, and K.L. Damico, *Three-dimensional X-ray microtomography*. Science, 1987. 237(4821): p. 1439-1444.
76. Flory, P.J., *Molecular size distribution in three dimensional polymers*. Journal of the American Chemical Society, 1941. 63: p. 3083-3100.
77. Ghassemzadeh, J. and M. Sahimi, *Pore network simulation of fluid imbibition into paper during coating: II. Characterization of paper's morphology and computation of its effective permeability tensor*. Chemical Engineering Science, 2004. 59(11): p. 2265-2280.
78. Gladkikh, M., *A Priori prediction of macroscopic properties of sedimentary rocks containing two immiscible fluids*, PhD dissertation, 2005, The University of Texas at Austin.
79. Gladkikh, M. and S. Bryant, *Prediction of interfacial areas during imbibition in simple porous media*. Advances in Water Resources, 2003. 26(6): p. 609-622.
80. Gladkikh, M. and S. Bryant, *Prediction of imbibition in unconsolidated granular materials*. Journal of Colloid and Interface Science, 2005. 288(2): p. 526-539.
81. Gladkikh, M. and S. Bryant, *Prediction of imbibition from grain-scale interface movement*. Advances in Water Resources, 2007. 30(2): p. 249-260.

82. Gladkikh, M. and S.L. Bryant, *Influence of wettability on petrophysical properties during imbibition in a random dense packing of equal spheres*. Journal of Petroleum Science and Engineering, 2006. 52(1-4): p. 19-34.
83. Glantz, R. and M. Hilpert, *Invasion percolation through minimum-weight spanning trees*. Physical Review E, 2008. 77(3): 031128.
84. Gunstensen, A.K. and D.H. Rothman, *Lattice-Boltzmann studies of immiscible two-phase flow through porous-media*. Journal of Geophysical Research-Solid Earth, 1993. 98(B4): p. 6431-6441.
85. Gvirtzman, H. and P.V. Roberts, *Pore scale spatial-analysis of two immiscible fluids in porous-media*. Water Resources Research, 1991. 27(6): p. 1165-1176.
86. Hackett, F.E. and J.S. Strettan, *The capillary pull of an ideal soil*. Journal Agriculture Science, 1928. 18: p. 671 - 681.
87. Haines, W.B., *Studies in the physical properties of soils. II. A note on the cohesion developed by capillary forces in an ideal soil*. Journal Agriculture Science, 1925. 15: p. 529-535.
88. Haines, W.B., *Studies in the physical properties of soils. IV. A further contribution to the theory of capillary phenomena in soil*. Journal Agriculture Science, 1927. 17: p. 264 - 290.
89. Haines, W.B., *Studies in the physical properties of soils. IV. The hysteresis effect in capillary properties and the modes of moisture distribution associated therewith*. Journal Agriculture Science, 1930. 20: p. 97-116.
90. Han, J., Y. Jin, and C. Willson, *Virus retention and transport in chemically heterogeneous porous media under saturated and unsaturated flow conditions*. Environmental Science & Technology, 2006. 40: p. 1547-1555.
91. He, X.Y. and L.S. Luo, *Theory of the lattice Boltzmann method: From the Boltzmann equation to the lattice Boltzmann equation*. Physical Review E, 1997. 56(6): p. 6811-6817.
92. Heiba, A.A., H.T. Davis, and L.E. Scriven. *Effect of wettability on two-phase relative permeabilities and capillary pressures*, SPE 12172 presented at SPE Annual Technical Conference and Exhibition. 1983. San Francisco, California.
93. Held, R.J. and M.A. Celia, *Pore-scale modeling extension of constitutive relationships in the range of residual saturations*. Water Resources Research, 2001. 37(1): p. 165-170.
94. Hilpert, M. and W.B. Lindquist, *Pore-scale modeling*. Advances in Water Resources, 2007. 30(2): p. 169-170.
95. Hilpert, M. and C.T. Miller, *Pore-morphology-based simulation of drainage in totally wetting porous media*. Advances in Water Resources, 2001. 24(3-4): p. 243-255.
96. Hirasaki, G.J., *Wettability: fundamentals and surface forces* SPE Formation Evaluation, 1991. 6(2): p. 217-226.
97. Hoshen, J., P. Klymko, and R. Kopelman, *Percolation and cluster distribution, 3. algorithms for the site-bond problem*. Journal of Statistical Physics, 1979. 21(5): p. 583-600.

98. Hoshen, J. and R. Kopelman, *Percolation and cluster distribution, I. cluster multiple labeling technique and critical concentration algorithm*. Physical Review B, 1976. 14(8): p. 3438-3445.
99. Hoshen, J., R. Kopelman, and E.M. Monberg, *Percolation and cluster distribution. II. layers, variable-range interactions, and exciton cluster model*. Journal of Statistical Physics, 1978. 19(3): p. 219-242.
100. Hui, M. and M.J. Blunt. *Pore-scale modeling of three-phase flow and the effects of wettability*, SPE 59309 presented at SPE/DOE Improved Oil Recovery Symposium. 2000. Tulsa, Oklahoma.
101. Ioannidis, M.A. and I. Chatzis, *On the geometry and topology of 3D stochastic porous media*. Journal of Colloid and Interface Science, 2000. 229(2): p. 323-334.
102. Ioannidis, M.A., I. Chatzis, and M.J. Kwiecien, *Computer enhanced core analysis for petrophysical properties*. Journal of Canadian Petroleum Technology, 1999. 38(3): p. 18-24.
103. Jerauld, G.R., J.C. Hatfield, L.E. Scriven, and H.T. Davis, *Percolation and conduction on the 3D Voronoi and regular networks: a case study in topological disorder*. Journal of Physics C-Solid State Physics, 1984. 17(9): p. 1519-1529.
104. Jerauld, G.R. and S.J. Salter, *The effect of pore-structure on hysteresis in relative permeability and capillary pressure: Pore-level modeling*. Transport in Porous Media, 1990. 5(2): p. 103-151.
105. Jerauld, G.R., L.E. Scriven, and H.T. Davis, *Percolation and conduction on the 3D Voronoi and regular networks: a second case-study in topological disorder*. Journal of Physics C-Solid State Physics, 1984. 17(19): p. 3429-3439.
106. Jia, X. and R.A. Williams, *A packing algorithm for particles of arbitrary shapes*. Powder Technology, 2001. 120(3): p. 175-186.
107. Jin, G., T.W. Patzek, and D.B. Silin. *Physics-based reconstruction of sedimentary rocks*, SPE 83587 presented at SPE Western Regional/AAPG Pacific Section Joint Meeting. 2003. Long Beach, California.
108. Jin, G.D., C. Torres-Verdin, S. Devarajan, E. Toumelin, and E.C. Thomas, *Pore-scale analysis of the Waxman-Smits shaly-sand conductivity model*. Petrophysics, 2007. 48(2): p. 104-120.
109. Johns, M.L. and L.F. Gladden, *Magnetic resonance imaging study of the dissolution kinetics of octanol in porous media*. Journal of Colloid and Interface Science, 1999. 210(2): p. 261-270.
110. Johnson, A.S., *Pore level modeling of interfacial area in porous media*, MS thesis, 2001, The University of Texas at Austin.
111. Jones, F.O. and W.W. Owens, *A laboratory study of low-permeability gas sands*. Journal of Petroleum Technology, 1980. 32(9): p. 1631-1640.
112. Kovscek, A.R., H. Wong, and C.J. Radke, *A pore-level scenario for the development of mixed wettability in oil-reservoirs*. AIChE Journal, 1993. 39(6): p. 1072-1085.
113. Laroche, C., O. Vizika, and F. Kalaydjian, *Network modeling as a tool to predict three-phase gas injection in heterogeneous wettability porous media*. Journal of Petroleum Science and Engineering, 1999. 24(2-4): p. 155-168.

114. Larson, R.G., H.T. Davis, and L.E. Scriven, *Displacement of residual non-wetting fluid from porous-media*. Chemical Engineering Science, 1981. 36(1): p. 75-85.
115. Larson, R.G. and N.R. Morrow, *Effects of sample-size on capillary pressures in porous-media*. Powder Technology, 1981. 30(2): p. 123-138.
116. Larson, R.G., L.E. Scriven, and H.T. Davis, *Percolation theory of residual phases in porous-media*. Nature, 1977. 268(4): p. 409-413.
117. Larson, R.G., L.E. Scriven, and H.T. Davis, *Percolation theory of two phase flow in porous-media*. Chemical Engineering Science, 1981. 36(1): p. 57-73.
118. Legait, B., *Laminar-flow of two phases through a capillary-tube with variable square cross-section*. Journal of Colloid and Interface Science, 1983. 96(1): p. 28-38.
119. Lenormand, R. and S. Bories, *Description of a bond percolation mechanism used for the simulation of drainage with trapping in porous-media*. Comptes Rendus Hebdomadaires Des Seances De L Academie Des Sciences Serie B, 1980. 291(12): p. 279-282.
120. Lenormand, R., E. Touboul, and C. Zarcone, *Numerical-models and experiments on immiscible displacements in porous-media*. Journal of Fluid Mechanics, 1988. 189: p. 165-187.
121. Lenormand, R. and C. Zarcone. *Role of roughness and edges during imbibition in square capillaries*, SPE 13264 presented at 59th Annual Technical Conference and Exhibition of the Society of Petroleum Engineers of AIME. 1984. Houston, Texas.
122. Lenormand, R. and C. Zarcone, *Invasion percolation in an etched network - measurement of a fractal dimension*. Physical Review Letters, 1985. 54(20): p. 2226-2229.
123. Lenormand, R. and C. Zarcone, *Two-phase flow experiments in a two-dimensional permeable medium*. Physicochemical Hydrodynamics, 1985. 6(5-6): p. 497-506.
124. Lenormand, R. and C. Zarcone, *Capillary fingering - percolation and fractal dimension*. Transport in Porous Media, 1989. 4(6): p. 599-612.
125. Lenormand, R., C. Zarcone, and A. Sarr, *Mechanisms of the displacement of one fluid by another in a network of capillary ducts*. Journal of Fluid Mechanics, 1983. 135(OCT): p. 337-353.
126. Leverett, M.C., *Capillary behavior in porous solids*. AIME Pet. Trans., 1941. 142: p. 152-169.
127. Liang, Z.R., C.P. Fernandes, F.S. Magnani, and P.C. Philippi, *A reconstruction technique for three-dimensional porous media using image analysis and Fourier transforms*. Journal of Petroleum Science and Engineering, 1998. 21(3-4): p. 273-283.
128. Liang, Z.R., P.C. Philippi, C.P. Fernandes, and F.S. Magnani, *Prediction of permeability from the skeleton of three-dimensional pore structure*. SPE Reservoir Evaluation & Engineering, 1999. 2(2): p. 161-168.
129. Lin, C. and M.H. Cohen, *Quantitative methods for micro-geometric modeling*. Journal of Applied Physics, 1982. 53(6): p. 4152-4165.

130. Lindquist, W.B., S.M. Lee, D.A. Coker, K.W. Jones, and P. Spanne, *Medial axis analysis of void structure in three-dimensional tomographic images of porous media*. Journal of Geophysical Research-Solid Earth, 1996. 101(B4): p. 8297-8310.
131. Lindquist, W.B., A. Venkatarangan, J. Dunsmuir, and T.F. Wong, *Pore and throat size distributions measured from synchrotron X-ray tomographic images of Fontainebleau sandstones*. Journal of Geophysical Research-Solid Earth, 2000. 105(B9): p. 21509-21527.
132. Lowry, M.I. and C.T. Miller, *Pore-scale modeling of nonwetting-phase residual in porous-media*. Water Resources Research, 1995. 31(3): p. 455-473.
133. Man, H.N. and X.D. Jing, *Network modelling of wettability and pore geometry effects on electrical resistivity and capillary pressure*. Journal of Petroleum Science and Engineering, 1999. 24(2-4): p. 255-267.
134. Man, H.N. and X.D. Jing, *Pore network modelling of electrical resistivity and capillary pressure characteristics*. Transport in Porous Media, 2000. 41(3): p. 263-286.
135. Man, H.N. and X.D. Jing, *Network modelling of strong and intermediate wettability on electrical resistivity and capillary pressure*. Advances in Water Resources, 2001. 24(3-4): p. 345-363.
136. Man, H.N. and X.D. Jing, *Network modelling of mixed-wettability on electrical resistivity, capillary pressure and wettability indices*. Journal of Petroleum Science and Engineering, 2002. 33(1-3): p. 101-122.
137. Masad, E., B. Muhunthan, and N. Martys, *Simulation of fluid flow and permeability in cohesionless soils*. Water Resources Research, 2000. 36(4): p. 851-864.
138. Mason, G., *Computer-simulation of hard disk packings of varying packing density*. Journal of Colloid and Interface Science, 1976. 56(3): p. 483-491.
139. Mason, G., *Determination of the pore-size distributions and pore-space interconnectivity of VYCOR porous-glass from adsorption desorption hysteresis capillary condensation isotherms*. Proceedings of the Royal Society of London Series A-Mathematical Physical and Engineering Sciences, 1988. 415(1849): p. 453-486.
140. Mason, G. and D.W. Mellor, *Simulation of drainage and imbibition in a random packing of equal spheres*. Journal of Colloid and Interface Science, 1995. 176(1): p. 214-225.
141. Mason, G.J., *A model of the pore space in a random packing of equal spheres*. Journal of Colloid and Interface Science, 1971. 35 p. 279-287.
142. McDougall, S.R. and K.S. Sorbie. *The prediction of waterflood performance in mixed-wet systems from pore-scale modeling and simulation*, SPE 25271 presented at SPE Symposium on Reservoir Simulation. 1993. New Orleans, Louisiana.
143. Mellor, D.W., *Random close packing (RCP) of equal spheres: Structure and implications for use as a model porous medium*. , PhD dissertation, 1989, Open University: Milton Keynes, UK.



144. Melrose, J.C., *Wettability as related to capillary action in porous media*. SPE Journal, 1965. 5: p. 259 - 271.
145. Mogensen, K. and E.H. Stenby, *A dynamic two-phase pore-scale model of imbibition*. Transport in Porous Media, 1998. 32(3): p. 299-327.
146. Mohanty, K.K., H. Davis, and L.E. Scriven, *Physics of oil entrapment in water-wet rock*. SPE Reservoir Engineering, 1987. 2(1): p. 113-128.
147. Mohanty, K.K. and S.J. Salter. *Multiphase flow in porous media: III. Oil mobilization, transverse dispersion, and wettability*, SPE 12127 presented at SPE Annual Technical Conference and Exhibition 1983. San Francisco, California.
148. Morrow, N.R., *Effects of surface-roughness on contact angle with special reference to petroleum recovery*. Journal of Canadian Petroleum Technology, 1975. 14(4): p. 42-53.
149. Morrow, N.R., *Wettability and its effect on oil-recovery*. Journal of Petroleum Technology, 1990. 42(12): p. 1476-1484.
150. Motealleh, S. and S.L. Bryant, *Quantitative mechanism for permeability reduction by small water saturation in tight gas sandstones*. SPE Journal, 2009. 14(2): p. 252-258.
151. Moulu, J.-C., O. Vizika, F. Kalaydjian, and J.-P. Duquerroix. *A new model for three-phase relative permeabilities based on a fractal representation of the porous medium*, SPE 38891 presented at SPE Annual Technical Conference and Exhibition. 1997. San Antonio, Texas.
152. Nourgaliev, R.R., T.N. Dinh, T.G. Theofanous, and D. Joseph, *The lattice Boltzmann equation method: theoretical interpretation, numerics and implications*. International Journal of Multiphase Flow, 2003. 29(1): p. 117-169.
153. O'Carroll, D.M., L.M. Abriola, C.A. Polityka, S.A. Bradford, and A.H. Demond, *Prediction of two-phase capillary pressure-saturation relationships in fractional wettability systems*. Journal of Contaminant Hydrology, 2005. 77(4): p. 247-270.
154. O'Rourke, J., *Computational geometry in C*. 2 ed. 1998, Cambridge: Cambridge University Press.
155. Øren, P.E. and S. Bakke, *Process based reconstruction of sandstones and prediction of transport properties*. Transport in Porous Media, 2002. 46: p. 311-343.
156. Øren, P.E., S. Bakke, and O.J. Arntzen, *Extending predictive capabilities to network models*. SPE Journal, 1998. 3: p. 324-336.
157. Pan, C., M. Hilpert, and C.T. Miller, *Lattice-Boltzmann simulation of two-phase flow in porous media*. Water Resources Research, 2004. 40(1).
158. Patzek, T.W., *Verification of a complete pore network simulator of drainage and imbibition*. SPE Journal, 2001. 6(3): p. 251-251.
159. Piri, M. and M.J. Blunt. *Pore-scale modeling of three-phase flow in mixed-wet systems*, SPE 77726 presented at SPE Annual Technical Conference and Exhibition. 2002. San Antonio, Texas.
160. Piri, M. and M.J. Blunt, *Three-phase threshold capillary pressures in noncircular capillary tubes with different wettabilities including contact angle hysteresis*. Physical Review E, 2004. 70(6): 061603.

161. Piri, M. and M.J. Blunt, *Three-dimensional mixed-wet random pore-scale network modeling of two- and three-phase flow in porous media. I. Model description*. Physical Review E, 2005. 71(2): 026301.
162. Piri, M. and M.J. Blunt, *Three-dimensional mixed-wet random pore-scale network modeling of two- and three-phase flow in porous media. II. Results*. Physical Review E, 2005. 71(2): 026302.
163. Powers, S.E., W.H. Anckner, and T.F. Seacord, *Wettability of NAPL-contaminated sands*. Journal of Environmental Engineering-Asce, 1996. 122(10): p. 889-896.
164. Prodanovic, M., W.B. Lindquist, and R.S. Seright, *3D image-based characterization of fluid displacement in a Berea core*. Advances in Water Resources, 2007. 30(2): p. 214-226.
165. Purcell, W.R., *Capillary pressures - their measurement using mercury and the calculation of permeability therefrom*. AIME Pet. Trans., 1949. 186: p. 39-48.
166. Rajaram, H., L.A. Ferrand, and M.A. Celia, *Prediction of relative permeabilities for unconsolidated soils using pore-scale network models*. Water Resources Research, 1997. 33(1): p. 43-52.
167. Reeves, P.C. and M.A. Celia, *A functional relationship between capillary pressure, saturation, and interfacial area as revealed by a pore-scale network model*. Water Resources Research, 1996. 32(8): p. 2345-2358.
168. Rodriguez, J., C.H. Allibert, and J.M. Chaix, *A computer method for random packing of spheres of unequal size*. Powder Technology, 1986. 47(1): p. 25-33.
169. Rose, W. and W.A. Bruce, *Evaluation of capillary character in petroleum reservoir rock*. AIME Pet. Trans., 1949. 186: p. 127-142.
170. Sahimi, M., *Critical exponents and thresholds for percolation and conduction*. Lecture Notes in Mathematics, 1983. 1035: p. 314-346.
171. Sahimi, M., *Flow phenomena in rocks - from continuum models to fractals, percolation, cellular-automata, and simulated annealing*. Reviews of Modern Physics, 1993. 65(4): p. 1393-1534.
172. Salathiel, R.A., *Oil recovery by surface film drainage in mixed-wettability rocks*. Journal of Petroleum Technology, 1973. 155: p. 1216-1224.
173. Sampath, K. and C.W. Keighinm, *Factors affecting gas slippage in tight sandstone of Cretaceous age in Unita basin*. Journal of Petroleum Technology, 1982. 34(11): p. 2715-2720.
174. Seright, R.S., J. Liang, W.B. Lindquist, and J.H. Dunsmuir, *Characterizing disproportionate permeability reduction using synchrotron X-ray computed microtomography*. SPE Reservoir Evaluation & Engineering, 2002. 5(5): p. 355-364.
175. Seright, R.S., J. Liang, W.B. Lindquist, and J.H. Dunsmuir, *Use of X-ray computed microtomography to understand why gels reduce relative permeability to water more than that to oil*. Journal of Petroleum Science and Engineering, 2003. 39(3-4): p. 217-230.
176. Seright, R.S., M. Prodanovic, and W.B. Lindquist, *X-ray computed microtomography studies of fluid partitioning in drainage and imbibition before*

- and after gel placement: Disproportionate permeability reduction.* SPE Journal, 2006. 11(2): p. 159-170.
177. Shanley, K.W., R.M. Cluff, and R.J. W., *Factors controlling prolific gas production from low-permeability sandstone reservoirs: Implications for resource assessment, prospect development and risk analysis.* AAPG Bulletin, 2004. 88(8): p. 1083-1121.
  178. Sharma, M.M., A. Garough, and H.F. Dunlap, *Effects of wettability, pore geometry, and stress on electrical conduction in fluid saturated rocks.* Log Analyst 1991. 32: p. 511-526.
  179. Shi, Y. and Y.W. Zhang, *Simulation of random packing of spherical particles with different size distributions.* Applied Physics A-Materials Science & Processing, 2008. 92(3): p. 621-626.
  180. Silin, D. and T. Patzek, *Pore space morphology analysis using maximal inscribed spheres.* Physica A-Statistical Mechanics and Its Applications, 2006. 371(2): p. 336-360.
  181. Silin, D.B., G.D. Jin, and T.W. Patzek, *Robust determination of the pore-space morphology in sedimentary rocks.* Journal of Petroleum Technology, 2004. 56(5): p. 69-70.
  182. Singhal, A.K. and W.H. Somerton, *Two-phase flow through a non-circular capillary at low Reynolds number* Journal of Canadian Petroleum Technology, 1970. July-Sept.: p. 197-205.
  183. Singhal, A.K. and W.H. Somerton, *Quantitative modeling of immiscible displacement in porous-media - network approach.* Revue De L Institut Francais Du Petrole, 1977. 32(6): p. 897-920.
  184. Slichter, C., *Theoretical investigations of the motions of groundwaters.* 1899, US Geol Surv Ann Rept. p. 306.
  185. Soppe, W., *Computer-simulation of random packings of hard-spheres.* Powder Technology, 1990. 62(2): p. 189-197.
  186. Stockmayer, W.H., *Theory of molecular size distribution and gel formation in branched-chain polymers.* Journal of Chemical physics, 1943. 11: p. 45-55.
  187. Suicmez, V.S., M. Piri, and M.J. Blunt, *Pore-scale simulation of water alternate gas injection.* Transport in Porous Media, 2007. 66(3): p. 259-286.
  188. Suicmez, V.S., M. Piri, and M.J. Blunt, *Effects of wettability and pore-level displacement on hydrocarbon trapping.* Advances in Water Resources, 2008. 31(3): p. 503-512.
  189. Svirsky, D.S., M.I.J. van Dijke, and K.S. Sorbie, *Prediction of three-phase relative permeabilities using a pore-scale network model anchored to two-phase data.* SPE Reservoir Evaluation & Engineering, 2007. 10(5): p. 527-538.
  190. Swanson, B.F., *A simple correlation between permeabilities and mercury capillary pressures.* Journal of Petroleum Technology, 1981. 33(12): p. 2498-2504.
  191. Thane, C., *Geometry and topology of model sediments and their influence on sediment properties,* MS thesis, 2006, The University of Texas at Austin.
  192. Thomeer, J.H., *Air permeability as a function of three pore-network parameters.* Journal of Petroleum Technology, 1983. 35(4): p. 809-814.

193. Thomeer, J.H.M., *Introduction of a pore geometrical factor defined by the capillary pressure curve*. AIME Pet. Trans., 1960. 213: p. 354-358.
194. Thompson, K.E. and H.S. Fogler, *Modeling flow in disordered packed beds from pore-scale fluid mechanics*. AIChE Journal, 1997. 43: p. 1377-1389.
195. Toumelin, E., *Pore-scale petrophysical model for the simulation and combined interpretation of nuclear magnetic resonance and wide-band electromagnetic measurement of saturated rocks*, PhD dissertation, 2006, The University of Texas at Austin.
196. Toumelin, E. and C. Torres-Verdin, *2D pore-scale simulation of wide-band electromagnetic dispersion of saturated rocks*. Geophysics, 2007. 72(3): p. F97-F110.
197. Toumelin, E., C. Torres-Verdin, and S. Chen, *Modeling of multiple echo-time NMR measurements for complex pore geometries and multiphase saturations*. SPE Reservoir Evaluation & Engineering, 2003. 6(4): p. 234-243.
198. Toumelin, E., C. Torres-Verdin, B. Sun, and K.J. Dunn, *Random-walk technique for simulating NMR measurements and 2D NMR maps of porous media with relaxing and permeable boundaries*. Journal of Magnetic Resonance, 2007. 188(1): p. 83-96.
199. Toumelin, E., C. Torres-Verdin, B.Q. Sun, and K.J. Dunn, *Limits of 2D NMR interpretation techniques to quantify pore size, wettability, and fluid type: A numerical sensitivity study*. SPE Journal, 2006. 11(3): p. 354-363.
200. Tsakiroglou, C.D. and M. Fleury, *Resistivity index of fractional wettability porous media*. Journal of Petroleum Science and Engineering, 1999. 22(4): p. 253-274.
201. Tsakiroglou, C.D. and A.C. Payatakes, *Characterization of the pore structure of reservoir rocks with the aid of serial sectioning analysis, mercury porosimetry and network simulation*. Advances in Water Resources, 2000. 23(7): p. 773-789.
202. Tschapek, M., *Criteria for determining the hydrophilicity / hydrophobicity of Soils*. Z. Pflanzenern. Bodenk., 1984. 147: p. 137-145.
203. Turner, M.L., L. Knufing, C.H. Arns, A. Sakellariou, T.J. Senden, A.P. Sheppard, R.M. Sok, A. Limaye, W.V. Pinczewski, and M.A. Knackstedt, *Three-dimensional imaging of multiphase flow in porous media*. Physica A-Statistical Mechanics and Its Applications, 2004. 339(1-2): p. 166-172.
204. Ustohal, P., F. Stauffer, and T. Dracos, *Measurement and modeling of hydraulic characteristics of unsaturated porous media with mixed wettability*. Journal of Contaminant Hydrology, 1998. 33(1-2): p. 5-37.
205. Valvatne, P.H. and M.J. Blunt. *Predictive pore-scale network modeling*, SPE 84550 presented at SPE Annual Technical Conference and Exhibition. 2003. Denver, Colorado.
206. Valvatne, P.H. and M.J. Blunt, *Predictive pore-scale modeling of two-phase flow in mixed wet media*. Water Resources Research, 2004. 40(7).
207. Valvatne, P.H., M. Piri, X. Lopez, and M.J. Blunt, *Predictive pore-scale modeling of single and multiphase flow*. Transport in Porous Media, 2005. 58(1-2): p. 23-41.

208. van Dijke, M.I.J., M. Piri, J.O. Helland, K.S. Sorbie, M.J. Blunt, and S.M. Skjaeveland, *Criteria for three-fluid configurations including layers in a pore with nonuniform wettability*. Water Resources Research, 2007. 43(12).
209. van Dijke, M.I.J. and K.S. Sorbie. *A process-based approach for three-phase capillary pressure and relative permeability relationships in mixed-wet systems*, SPE 59310 presented at SPE/DOE Improved Oil Recovery Symposium. 2000. Tulsa, Oklahoma.
210. van Dijke, M.I.J. and K.S. Sorbie, *Pore-scale network model for three-phase flow in mixed-wet porous media*. Physical Review E, 2002. 66(4): 046302.
211. van Dijke, M.I.J. and K.S. Sorbie, *Pore-scale modelling of three-phase flow in mixed-wet porous media: multiple displacement chains*. Journal of Petroleum Science and Engineering, 2003. 39(3-4): p. 201-216.
212. van Kats, F.M. and P.J.P. Egberts, *Simulation of three-phase displacement mechanisms using a 2D lattice-Boltzmann model*. Transport in Porous Media, 1999. 37(1): p. 55-68.
213. Visscher, W.M. and M. Bolstereli, *Random packing of equal and unequal spheres in two and three dimensions*. Nature, 1972. 239: p. 504-508.
214. Vogel, H.J. and K. Roth, *Quantitative morphology and network representation of soil pore structure*. Advances in Water Resources, 2001. 24(3-4): p. 233-242.
215. Walls, J.D., A.M. Nur, and T. Bourbie, *Effect of pressure and partial water saturation on gas permeability in tight sand: experimental results*. Journal of Petroleum Technology, 1982. 34(4): p. 930-936.
216. Wang, X., F. Thauvin, and K.K. Mohanty, *Non-Darcy flow through anisotropic porous media*. Chemical Engineering Science, 1999. 54(12): p. 1859-1869.
217. Ward, J. and N.R. Morrow, *Capillary pressure and gas relative permeabilities of low-permeability sandstone*. SPE Formation Evaluation, 1987. 2(3): p. 345-356.
218. Wildenschild, D., J.W. Hopmans, M.L. Rivers, and A.J.R. Kent, *Quantitative analysis of flow processes in a sand using synchrotron-based X-ray microtomography*. Vadose Zone Journal, 2005. 4(1): p. 112-126.
219. Wildenschild, D., J.W. Hopmans, C.M.P. Vaz, M.L. Rivers, D. Rikard, and B.S.B. Christensen, *Using X-ray computed tomography in hydrology: systems, resolutions, and limitations*. Journal of Hydrology, 2002. 267(3-4): p. 285-297.
220. Wilkinson, D. and J.F. Willemsen, *Invasion percolation - A new form of percolation theory*. Journal of Physics A-Mathematical and General, 1983. 16(14): p. 3365-3376.
221. Yeong, C.L.Y. and S. Torquato, *Reconstructing random media. II. Three-dimensional media from two-dimensional cuts*. Physical Review E, 1998. 58(1): p. 224-233.
222. Zuluaga, E. and L.W. Lake. *Semi-analytical model for water vaporization in gas producers*, SPE 93862 presented at SPE Western Regional Meeting. 2005. Irvine, California.

## VITA

Siyavash Motealleh received his B.Sc. degree in chemical engineering as a first ranked student from Shiraz University, Iran, on September of 2001. He pursued his M.Sc. degree in Applied Earth Science from Delft University of Technology, The Netherlands where he graduated with honors in 2004. From September 2004 to January 2005 he worked at the Delft University of technology as research assistant. In 2005 he began his PhD level graduate studies with Dr. Steven Bryant where he worked on grain based modeling of two phase flow in a porous media. Siyavash worked as petrophysicist intern for Baker Hughes, Inc. and BP America, Inc. in Houston, Texas and as reservoir engineer for Calsep, in Dubai, UAE. He was member of Senate of Collage Council and served on President Student Advisory Council (PSAC). He is recipient of 2005 SIPES (Society of Independent Professional Earth Scientists) scholarship, 2006 SPWLA (Society of Petrophysicists & Well Log Analysts) scholarship, and 2009 Graduate Student Leadership award. He is author of more than seven report and technical articles. His research interests include petrophysics, log analysis, and pore-scale petrophysics.

Permanent address: 410 West 37<sup>th</sup> Street, Austin, Texas, 78705

This dissertation was typed by Siyavash Motealleh